University of Southampton

Faculty of Engineering and Physical Sciences
Institute of Sound and Vibration Research

Understanding the micromechanics of the cochlea

by

Riccardo Marrocchio

ORCiD: 0000-0001-5269-4620

A thesis for the degree of
Doctor of Philosophy

January 2022

University of Southampton

Abstract

Faculty of Engineering and Physical Sciences
Institute of Sound and Vibration Research

Doctor of Philosophy

Understanding the micromechanics of the cochlea

by Riccardo Marrocchio

The function of the cochlea is to convert the sound waves that reach our ears into neural signals that can be interpreted by the brain. Its mechanics can be modelled as two fluid chambers separated by the basilar membrane (BM), on which the Organ of Corti (OoC) sits. The OoC is the cochlear sensory organ composed of different cells and tissues, including the reticular lamina, the tectorial membrane (TM), the outer and inner hair cells and other supporting cells. The process of transduction is achieved through two mechanisms: a passive and an active one. The passive mechanism is responsible for the tonotopic map of the cochlea, while the active mechanism determines the high sensitivity and frequency selectivity of our hearing.

This thesis contributes to the understanding of the passive and the active mechanism of the cochlea. First an analytical solution to the equations governing the cochlear mechanics is derived, in the case of a passive, locally reacting BM, including fluid compressibility and viscosity. The solution is expressed in terms of only a few nondimensional parameters and it is shown that one of these, a phase-shift parameter, has the greatest influence on the cochlear response, as it determines the form of coupling between the fluid and the BM.

In terms of the active mechanism, an existing elemental model is extended (e.g. Elliott and Ni 2018) to include the micromechanical structure of the OoC, as described in a detailed Finite Element Model (FEM) of the cochlea developed by Grosh's laboratory (e.g. Sasmal and Grosh 2019). The use of an elemental method, instead of a detailed FEM, provides insight into the study of the active mechanism by dividing it into two terms; one due to the dynamics of the BM, including longitudinal coupling within the OoC, and one due to various types of fluid coupling. The effects of the various type of longitudinal coupling are discussed and it is shown that the most important one in determining the amplification and stability of the cochlea is the longitudinal coupling in the TM. To better understand the effect of longitudinal coupling, a method is developed to derive, from the elemental model, the wavenumber distribution associated with the different types of waves that can propagate in the cochlea. In particular, it is shown that, for a model with TM longitudinal coupling only, the wavenumber distribution associated with the main travelling wave is characterized by an imaginary part which is positive in a small region just before the frequency at which the BM peaks, indicating a distributed amplification of the response in this region.

Contents

List of Figures

List of Tables

Declaration of Authorship

I, Riccardo Marrocchio, declare that this thesis titled "Understanding the micromechanics of the cochlea" and the work presented in it is my own and has been generated by me as the result of my own original research.

I confirm that:

1. This work was done wholly or mainly while in candidature for a research degree at this University;
2. Where any part of this thesis has previously been submitted for a degree or any other qualification at this University or any other institution, this has been clearly stated;
3. Where I have consulted the published work of others, this is always clearly attributed;
4. Where I have quoted from the work of others, the source is always given. With the exception of such quotations, this thesis is entirely my own work;
5. I have acknowledged all main sources of help;
6. Where the thesis is based on work done by myself jointly with others, I have made clear exactly what was done by others and what I have contributed myself;
7. Parts of this work have been published as:

   R. Marrocchio and S.J. Elliott. Including fluid compressibility and viscosity in the WKB solution to the wave equation of the cochlea. *Mechanics of Hearing Workshop 2020*, 5-10 July 2020 - Postponed to 13-18 June 2022;

   R. Marrocchio, A. Karlos and S.J. Elliott. WKB solutions to the wave equation for the cochlea and for acoustic rainbow sensors. *American Physical Society March Meeting 2021*, 15-19 March 2021;

   R. Marrocchio, A. Karlos and S.J.Elliott. Waves in the cochlea and in acoustic rainbow sensors. *Wave Motion*, 106:102808, November, 2021.

Signed:..... Date:.....

Acknowledgements

I would like to thank my supervisor Professor Steve Elliott, not only for his scientific advice and support but also for amplifying my passion, dedication, and resilience to research and professional life.
I owe special thanks to Professor Karl Grosh, for welcoming me in his research group and for his extraordinary availability to work together during our collaboration.
I wish to thank my co-supervisor Dr Ben Lineton, for his precious suggestions and continuous advice.
I would also like to express my gratitude to my parents, my sister, who always encouraged me to pursue my objectives, especially during the most difficult times.
Finally, I want to thank my partner Chiara, whose love is a constant support in my life.

Abbreviations

BM	Basilar Membrane
TM	Tectorial Membrane
RL	Reticular Lamina
OHC	Outer Hair Cell
HB	Hair Bundle
OoC	Organ of Corti
WKB	Wentzel-Kramers-Brillouin
CF	Characteristic Frequency
ST	Scala Tympani
SV	Scala Vestibuli
FEM	Finite Element Method
OCT	Optical Coherence Tomography
LR	Locally-reacting
MET	Mechano-Electrical Transduction
1D	one-dimensional
2D	two-dimensional
3D	three-dimensional
DOF	Degree of Freedom
FFT	Fast Fourier Transform

Chapter 1

Introduction

1.1 Active mechanism of the cochlea

The overall aim of this research project is to contribute to the understanding of the active mechanism of the cochlea, the sensitive organ of hearing. In the last fifty years, numerous experiments and modelling studies have investigated the functioning of the hearing organ, that is how it converts sound into induced vibrations within the cochlea and hence into electrical signals that can be interpreted by the brain. To understand the complete function of the cochlea, its micromechanics must be taken into consideration; that is how the components of a specific element of the cochlea, the Organ of Corti (OoC), move relative to each other. The Organ of Corti is the sensory epithelium lining the inner surface of the basilar membrane and contains: the tectorial membrane, the reticular lamina and the inner and outer hair cells. Studies demonstrate that the remarkable sensitivity and frequency selectivity of the mammalian hearing cannot be explained by passive gradient properties alone (Cooper and Rhode, 1992; Khanna and Leonard, 1982; Rhode, 1971) but these must rely on an active mechanism, the cochlear amplifier (Davis, 1983), which generates forces from within the Organ of Corti that amplify and sharpen the cochlear response.

Numerous theoretical models have been proposed to explain how the different components of the Organ of Corti contribute to the hearing sensations (Allen, 1980; Neely, 1985; Neely and Kim, 1986; Neely, 1993), but until recently they could not be properly validated by experimental evidence because there was no measurement method able to adequately distinguish the movements of each part of the Organ. Optical coherence tomography has recently been applied to the study of the cochlea, however, which allows data to be obtained on the differential motion of the components of the Organ of Corti in vivo, without the need to open the cochlea. This is especially important since the functioning of the cochlear amplifier has been showed to be highly sensitive to the mechanical properties and the normal metabolism of the cochlea. Furthermore, with optical coherence tomography, the axial resolution is not limited by small physical aperture that can be obtained within the cochlear bone but is imposed, at around 10 μm, by

the short coherence length of the laser. Therefore, optical coherence tomography is able to distinguish the motions between the different parts of the Organ of Corti.

The conclusions that can be drawn from this recent experimental data are not conclusive. In particular, (Chen et al., 2011) suggested that a local feedback mechanism is sufficient to explain the active mechanism of the cochlea, as measured in their data. On the other hand, (He et al., 2018) proposed a global hydro-mechanical model, to explain their data, in which they emphasize the importance of longitudinal coupling. To better understand the experimental discrepancies and the implications of the proposed theories, (Sasmal and Grosh, 2019) developed a detailed finite element model of the cochlea and simulated the basilar membrane response. The predicted amplitude and phase response of the BM at basal locations are in agreement with data obtained by (He et al., 2018) in gerbils and by (Ren et al., 2016b) in mice, while the predictions of the same variables at apical locations agree with data obtained by (Recio-Spinoso and Oghalai, 2017) in guinea pigs. A research collaboration has been established with Karl Grosh's laboratory, with the aim to gain further insight from this model by recasting the Finite Element Model into an elemental formulation. This led to the study of the contribution to the BM admittance from the various type of longitudinal coupling and a method of calculating the wavenumber distribution in the case of a model with a longitudinally coupled Organ of Corti.

1.2 Wavenumber distribution in a longitudinal coupled Organ of Corti

Many properties of the cochlea can be understood in terms of the propagation of a single type of wave. This wave is generated by the interaction between the inertia of the fluid in the chambers and the dynamics of the basilar membrane (de Boer, 1996). The properties of the wave can be characterised by a complex wavenumber, whose real part, called propagation function, determines the wave speed and wavelength while the imaginary part, called gain function, determines the regions in which power is dissipated or gained by the Organ of Corti. The wavenumber distribution can be calculated from a model or estimated by using an inverse method from measurements (Shera, 2007).

In the case of a model of the passive cochlea which includes a locally reacting BM with 1D fluid coupling, only one type of wave is present (de Boer, 1996). This is characterised by a wavenumber distribution whose real part starts out with a small value at low frequencies and then increases up to the frequency ω_n, giving a pass band in this frequency range. ω_n is the characteristic frequency, that is the frequency at which the response peaks at a specific point along the cochlea. The imaginary part, on the other hand, is for the most part very small. The rising value of the real part of the wavenumber with an increasing slope is also correlated to a decrease of the phase and group velocity, given respectively by $c_{ph} = w/k$ and $c_{gr} = \frac{dw}{dx}$, leading to the wave being slowed so that its amplitude is concentrated near the characteristic frequency. The gain

function is very small over most of the pass band and starts to increase in magnitude only at frequencies slightly before the peak of the real part, leading to a stop band, where the wavenumber remains high in absolute terms and the wave is greatly attenuated.

When 2D or 3D fluid coupling is included, the models predict an infinite number of wavenumber distributions, corresponding to multiple wave types (Steele and Taber, 1979b; Taber and Steele, 1981). As notice by Steele and Taber, only one wavenumber distribution corresponds to a travelling wave, while the others describe non propagation modes, which generally do not have a significant effect on the coupled response. To verify that only one wave type is sufficient to describe the cochlear response, the Wentzel-Kramers-Brillouin (WKB) method, which provides an analytical approximation to differential equations (Mathews, 1964, p.23), can be used to derive the response of the BM from the wavenumber distribution. Then this can be compared to either the full numerical solutions or to experimental results. Using this method, (Steele and Taber, 1979b) have shown that there is a difference between the WKB approximation and the full numerical solution, just above the peak response. (Watts, 2000) showed that by using a linear superposition of the travelling wave mode and a second cut off mode is possible to obtain a solution that is in better agreement with the full numerical predictions at frequencies above the peak response. This was also confirmed by (Elliott et al., 2013), who used the wave finite element (WFE) method to show that, for a passive cochlear model with 3D fluid coupling, the response beyond the peak involves multiple waves, which are identified as higher-order acoustic waves in the fluid coupling. The results by (Watts, 2000) and (Elliott et al., 2013) were confirmed by (Parthasarathi, 2000) and (Cheng, 2007) in their PhD thesis for a passive model which includes longitudinal coupling by the BM. Also in this case, the main travelling wave dominates the response up to the peak, while additional non-propagating modes are necessary to obtain a better agreement with experimental results for higher frequencies.

In the active cochlea, the propagation and gain functions are similar in shape to those of the travelling wave in the passive case, apart from two main differences (Shera, 2007). The propagation function has a higher peak, indicating a smaller wavelength and the gain function is positive just before the peak of the real part. This is shown in Fig. 1.1, were the real and imaginary part of the wavenumber are obtained by Shera from experimental measurements of the cochlea, by using an inverse method. The propagation and gain function in Fig. 1.1 are plotted as a function of a local scaling variable, v, defined as $f/CF(x)$, where $CF(x)$ is the characteristic frequency at location x, as given by the cochlear position-frequency map. Shera also noted that a positive value of the imaginary part indicates that the wave is amplified, as a positive sign of the imaginary part of the wavenumber near the response peak corresponds to a power transfer to the travelling wave and to an amplification of the response around the characteristic frequency. This is in agreement with (Dewey et al., 2019) in which it shown, from experimental measurements, that the amplification of the cochlear wave occurs before the characteristic frequency. At the highest frequency, the real part of the wavenumber

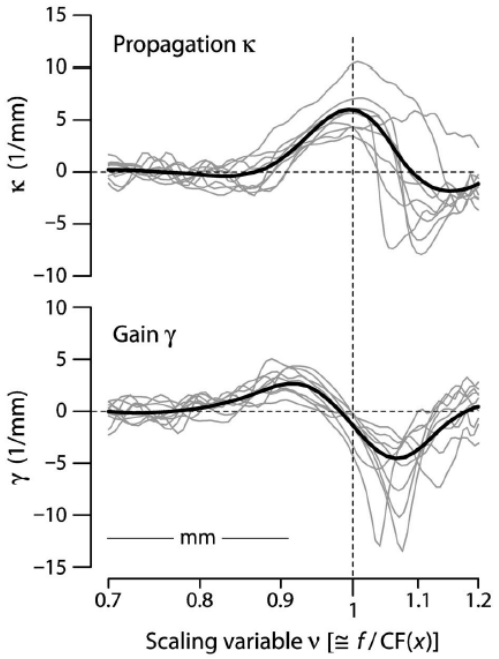

Figure 1.1: (Upper) real and (lower) imaginary part of the wavenumber as a function of the generalised local scaling variable v, derived using the inverse method. f is the frequency while $CF(x)$ is the characteristic frequency at the location x. Gray lines show individual distributions, black lines trends obtained by a fitting procedure. Reprinted with permission from (Shera, 2007). Copyright 2007, Acoustic Society of America.

in Fig. 1.1 becomes negative but, as noted by Shera, these results are not reliable as the inverse method, in this frequency region, is characterised by a great relative error. This can be seen in Fig. 1.1 in the great variability of the individual wavenumber distributions, represented as grey lines, in the high frequency region.

In this thesis, after obtaining an equivalent elemental formulation of the finite element model developed by (Sasmal and Grosh, 2019), we present a method to derive the wavenumber distribution of the various wave types, when longitudinal coupling is present.

1.3 Outline of the thesis

In Chapter 2 we review the anatomy and physiology of the ear, focusing in particular on the cochlea and on its active system. In Chapter 3 the Wentzel–Kramers–Brillouin (WKB) method is used to derive an approximation to the solution of the cochlear wave equation, including both fluid viscosity and compressibility. The solution is expressed in terms of a few nondimensional parameters and their physical effects on the wavenumber distribution and on the BM response are discussed. In Chapter 4 we review the experimental techniques that have been used to record the movements within the cochlea, underling the contribution of each approach to the understanding of the main features of the Organ of Corti: passive and active mechanics, non-linearity, high frequency selectivity. Then we show how recent experiments have demonstrated the importance of

fluid longitudinal coupling and mechanical and electrical longitudinal coupling, within the Organ of Corti, in the understanding of the active mechanism of the cochlea. In Chapter 5 we develop an elemental formulation of the finite element model by (Sasmal and Grosh, 2019) in the simplified case of a locally reacting basilar membrane. The elemental formulation is extended in Chapter 6 to include the longitudinal coupling by the TM, the BM and the electrical cables and the effects of these forms of longitudinal coupling on the overall response are studied. Finally, in Chapter 7, a method is developed to derive the wavenumber distribution for a propagation in a longitudinally coupled Organ of Corti.

1.4 Contributions

The novel contributions of the work consists of:

- An explicit formulation of the WKB solution to the wave equation for the passive cochlea, with fluid compressibility and viscosity, and a parametric study of the response and of the wavenumber distribution in terms of nondimensional parameters;
- Interpretation of the discrepancies in recent experimental results regarding the differential motion between the reticular lamina and the basilar membrane;
- Improved insight into the results of a previous finite element model of the active cochlea, using an elemental formulation;
- An overall model of different forms of longitudinal coupling in terms of a non-locally reacting BM admittance;
- A method of deriving the wavenumber distribution for a longitudinally coupled Organ of Corti.

1.5 Publications

Parts of the work presented in this thesis have been published, including one journal article and two articles in conference proceedings:

- R. Marrocchio and S.J. Elliott. Including fluid compressibility and viscosity in the WKB solution to the wave equation of the cochlea. *Mechanics of Hearing Workshop 2020*, 5-10 July 2020 - Postponed to 13-18 June 2022;
- R. Marrocchio, A. Karlos and S.J. Elliott. WKB solutions to the wave equation for the cochlea and for acoustic rainbow sensors. *American Physical Society March Meeting 2021*, 15-19 March 2021;
- R. Marrocchio, A. Karlos and S.J.Elliott. Waves in the cochlea and in acoustic rainbow sensors. *Wave Motion*, 106:102808, November, 2021.

Chapter 2

Anatomy and Physiology of the cochlea

2.1 Introduction

In this chapter we review the anatomy and physiology of the ear, focusing in particular on the cochlea, in order to understand the basics of its function as a transducer of sound waves. There are several standard textbooks that address this topic. This review chapter is based on (Pickles, 2012; Berne et al., 2008; Martini and Nath, 2009).

The human ear is subdivided into three main parts: the external, the middle and the inner ear. The external and middle ear collect and convey the sound stimuli to the inner ear, where sound waves are transduced into signals that are analysed by the brain. Besides its auditory part, the inner ear also contains the vestibular apparatus, a collection of specialised sensors which informs the central nervous system about the position and the movements of the head.

2.2 Transmission of sounds in the external and middle ear

The external ear is formed by the auricle or pinna and the external auditory meatus (Fig. 2.1). The pinna collects sound waves which are then conveyed to the tympanic membrane through the meatus. At the end of the acoustic meatus, sound waves are gathered on the tympanic membrane which vibrates accordingly and transmits its vibration to the ossicular chain, formed by the malleus, the incus and the stapes.

The middle ear is an irregular cavity in the temporal bone filled by air. It is separated from the meatus by the tympanic membrane and it contains the ossicular chain, the tensor tympani and the stapedius muscles, through which it interacts with the inner ear. The middle ear works as an impedance adapter between the tympanic membrane and the cochlea. The middle ear amplifies the intensity of the sound so that low stimuli can be efficiently transmitted to the liquid inside the ear. The timpanic-ossicular chain amplifies the intensity of the sound stimuli through two mechanism. First, the ossicular chain is a system of levels that increase the amplitude of vibrations. Secondly, the surface of the

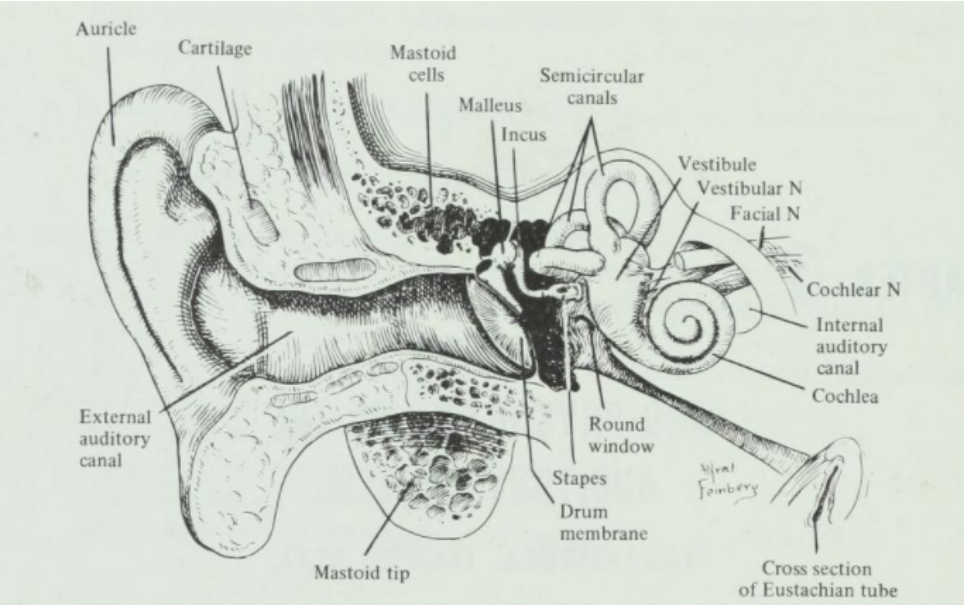

Figure 2.1: Anatomy of the human ear and its three main parts: the external, the middle and the inner ear. Republished with permission of Cengage Learning, from (Davis, 1970); permission conveyed through Copyright Clearance Center, Inc.

tympanic membrane is about twenty times larger than that of the footplate. Because the pressure is equal to the ratio between force and surface it follow that, given the same force, the pressure exerted by a stimulus on the footplate will be greater than that on the tympanic membrane. This mechanism is provided with a regulatory mechanism, called the stapedial reflex, constituted by two muscles: the tensor tympani and the stapedius. The tensor tympani is innervated by short fibres of the trigeminal nerve and is connected to the head of the malleus. Its contraction shifts laterally the head of the hammer increasing the tension of the tympanic membrane. The stapedius muscle is innervated by the facial nerve and is connected to the neck of the stapes. When it is contracted it applies a traction on the stapes decreasing their penetration in the oval window. The contraction of both muscles increases the rigidity of the tympanic-ossicular chain decreasing the conduction of sound waves, especially at low frequencies. Furthermore, this mechanism protects the inner ear from sound waves with excessive intensities. At the end of the stapes there is the footplate, which moves like a piston inside a hole on the lateral face of the temporal bone, called the oval window and transmits its vibration to the liquids inside the ear.

2.3 Transduction mechanism of the inner ear

The inner ear is composed of the osseous labyrinth, a series of interlinked cavities within the petrous temporal bone and the contained membranous labyrinth, a set of interconnected ducts. The osseous labyrinth has three cavities: the vestibule, the semicircular canals and the cochlea.

2.3.1 Anatomy of the cochlea

The cochlea is a spiral channel located in the anterior region of the bone labyrinth. In human it turns two and a half times on a length of 35 mm. Inside the cochlea there is a membranous labyrinth which forms three fluid chambers, or scale, that run parallel to each other. The scala vestibuli starts at the oval window and ends at the apex of the cochlea where, through a hole called helicotrema, it communicates with the scala tympani. The scala tympani ends at the base of the cochlea on the oval window, a hole in the temporal bone enclosed by an elastic membrane. Between these two scale there is the scala media. It has a triangular section with the apex directed towards the modiolus, the central bone axis of the cochlea, and it is formed by three membranes: the basilar membrane, which separates it from the scala tympani, the Reissner's membrane, which divide it from the scala vestibuli and the stria vascularis, which keep it apart from the external surface of the cochlea. The basilar membrane changes continuously in its width from the base, where is broad, to the apex, where is narrow while the scala media tapers in the opposite direction. The resulting space is filled by the spiral lamina. The scale tympani and vestibuli contains the perylimph, a fluid with a ionic composition similar to that of other extracellular fluid that is low in potassium and high in sodium and calcium, while the scala media contains the endolypmh, a fluid with a ionic composition like that of cytosol, high in potassium ions and low in sodium and calcium. Inside the scala media there is the Organ of Corti, the structure devoted to the

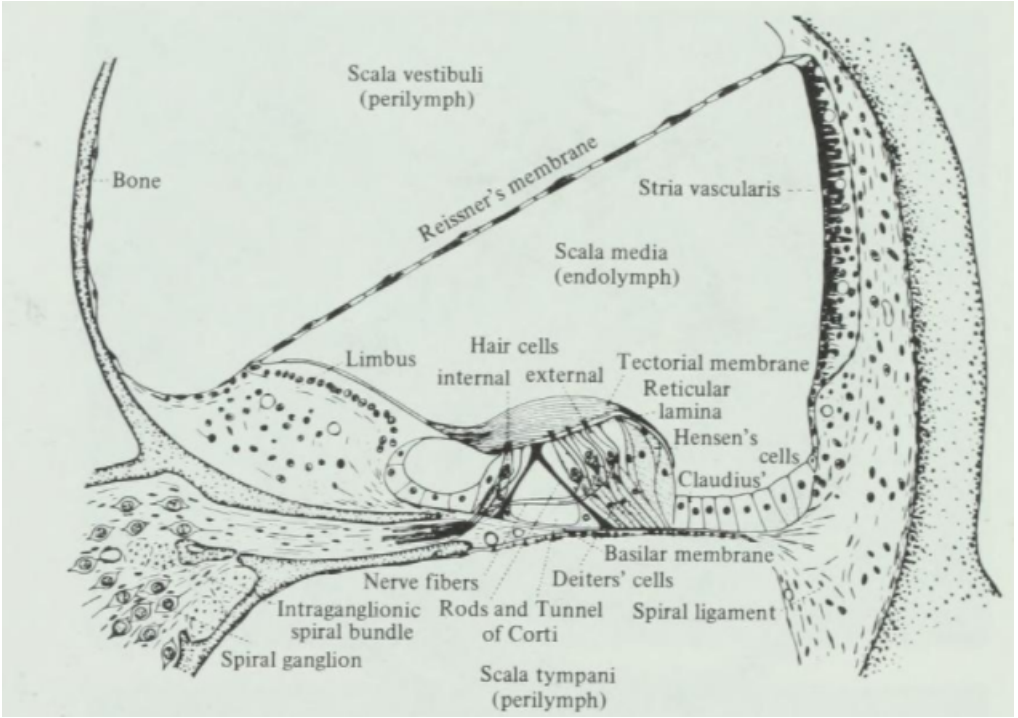

Figure 2.2: Structure of a cross section of the cochlea, with the main cells and tissues. Republished with permission of Cengage Learning, from (Davis, 1970); permission conveyed through Copyright Clearance Center, Inc.

transduction of sounds waves. It is composed of a sophisticated mechanism of sensors able to transduce, in less than a few microseconds, the sound stimuli into nerve impulses faithfully reproducing their intensity and frequencies. Furthermore, it is equipped with a powerful active amplification mechanism which further increases the performance of the ear in terms of its sensitivity and frequency selectivity.

The Organ of Corti contains support cells and acoustical receptors called hair cells. In the mammalian cochlea there are two types of hair cells: the outer and the inner hair cells, according to their position with respect to the modiolus. The apical portion of a receptor cell is composed of a complex transduction structure, the hair bundle of stereocilia, which is inside the scala media (Fig. 2.2). The free ends of the OHCs and the apical processes of the phalangeal cells form the reticular lamina, which acts as a chemical barrier between the ions in the scala media and the scala tympani. Above the hair bundles there is the tectorial membrane, which moves with the longest stereocilia of the outer hair cells. The transmission of the vibrations to the endocochlear fluid liquids is possible thanks to the round window whose movement is out of phase with those of the footplate, since the fluid in the chambers is almost incompressible. In this way the vibrations propagate through the perylimph of the scala vestibuli and tympani and is transmitted to the scala media.

2.3.2 Hair cells

Hair cells are epithelial structures specialised in the mechanoelectrical sensory transduction and are based in the organ of Corti. In mammals there are about 3500 inner hair cells arranged in a single row over the entire length of the basilar membrane while there are about 12000 outer hair cells arranged in three parallel rows. They are cylindrical in shape. The basal portion of the cell rests on support elements which have specialised structures for the synaptic transmission through the peripheral extensions of the neurons in the spiral ganglion or, in the case of the outer hair cells, through the efferent axon terminal from the central nervous system. The apical part is inside the scala media and it contains the hair bundles. The luminal surface which covers the scala media separates the two portion of the cells which are exposed to different external conditions. The apical part is immersed in the endolymph while the basal portion is surrounded by the perylimph.

These are the common characteristics of the outer and hair cells. They differ in other important details of their structure and innervations which reflects their distinct functional role. The hair cells have different afferent innervations through which they send signals to the central nervous system (CNS) and efferent innervations coming from the CNS through which their function is regulated. The inner hair cells transmit the sensory information to the peripheral extensions of type I neurons in the spiral ganglion. Type I neurons are about 30000 and represent 95% of the neuronal population of the ganglion. Every inner cell have about ten synaptic contact with an equal number of sensory neurons so that every neuron receives information from a single receptor. Furthermore, the

number of the peripheral extensions in contact with a single receptor cell is greater in the central part of the cochlea and decreases towards the apex. This suggests that the innervations is organised so that the transmission of particular frequencies important for the species is enhanced. The efferent innervations contact the post-synaptic elements of the peripheral extensions of the neurons of the spiral ganglion.

On the other hand, the outer hair cells are in contact with the peripheral extensions of afferent neurons which are just about 5% of the neurons in the spiral ganglion. Every peripheral extensions has then various branches that contact different receptors. The efferent connections of the OHCs contact directly the basal portion of the cells. The differences in innervation suggest that the inner hair cells play the role of receptor with high capacity of discrimination and analysis of the sensory stimulus. On the other hand, the innervations of the outer hair cells suggest that they play a different role acting as actuators that require a central control.

Mechanoelectrical transduction in the hair cells An important property of the outer hair cells is that they are based on the interface between the endolymph of the scala media and the perylmph, into which is inserted the basolateral portion of the receptor. The ionic composition of the endolymph is rich in potassium ions and low in sodium ions, maintained by sodium-potassium pumps in the membrane of the cells on the stria vascularis, which actively pumps potassium ions into the endolymph exchanging them with sodium ions. For this reason the potential difference between the endolymph and the extracellular liquid is about $+80\,\mathrm{mV}$. Furthermore, because the resting potential of the hair cells is about $-60\,\mathrm{mV}$ there is a potential difference of about $-140\,\mathrm{mV}$ between the interior of the receptors and the scala media (Purves et al., 2001). This potential difference is essential to the function of the inner ear because it provides the driving force for the mechanotransduction. The transduction is operated by the hair bundles: the mechanical stimulation produced by the sound wave deflects the bundle, which induce a variation of the ionic permeability of the membrane, which in turn changes the membrane potential of the receptor. Every bundle is formed by about ten stereocilia, rigid cytoplasmatic extroflexions, with a cylindrical shape and full of actin filaments which protrudes in the scala media. The stereocilia of a bundle have different lengths and they are arranged in parallel lines according to their length. The tip of every stereocilia is connected with the adjacent stereocilia of the next row through a proteic filament called tip-link. At its extremity the tip-link is connected with a channel protein called the transduction channel, which is based in the membrane of the stereocilia. The tip-link is a chain of cadherin-23 which form a filament with low extensibility, connected to the extremity of a ankyrin molecule, which is elastic. On the whole, the apparatus can be represented as a spring (Fettiplace, 2017): if it is contracted, the channel is opened and the ions flow through the pore; if it is relaxed the channel is closed. Because the stereocilia are arranged according to their length, when the bundle bends toward the row of longer stereocilia, the distance between the tip of the stereocilia of the next rows

increases, the tip-link is stretched and the channels are opened. On the other hand, a movement in the opposite direction results in a decrease of distance between the tips of the stereocilia, reducing the tension of the filament and in turn in the closure of the channel of transudction. Because the stereocilia are strictly connected through the tip-links, the bundles act as a unitary structure in which all the channels of transduction open and close at the same time. In this way small deflections of the bundle results in significant modifications of the membrane potential, so that the receptor can detect even the most fine temporal characteristics of the stimulus. When the bundle is at rest, the tip-links are not completely relaxed and the transduction channels are in part open. For this reason the receptor cell can detect deflections of the bundle in both directions. Deflections toward higher stereocilia results in a depolarization of the receptor while deflections in the opposite direction results in a hyperpolarizations. In this way the membrane potential of the receptor varies according to the movement of the stereocilia, reproducing the contracting and relaxing phases of the sound wave up to frequencies of tens of kHz. In the contraction phase the stimulus bends the bundles toward the rows of higher stereocilia so that the transduction channels are opened. The potential difference of $-140\,\mathrm{mV}$ between the interior of the outer hair cell and the endolymph produce a flux of potassium ions towards the interior of the receptor. The cell depolarises giving rise to the so called receptor potential. The variation of potential induces the opening of voltage-gated calcium channels that are in the basolateral membrane of the cell. This ion input increases further the depolarization triggering the release of the neurotransmitter at the synaptic level of the connections with the peripheral extension of the neurons of the spiral ganglion. Then, the mechanical stimulus bends the bundle towards the row of lower stereocilia closing the transduction channels and stopping the flows of potassium ions. The Ca^{2+} ions flown toward the interior of the hair cells inducing the opening of the potassium permeable channels on the basolateral membrane of the receptor. In this zone the hair cell is immersed in the extracellular liquid and the electrochemical gradient directs potassium ions towards the exterior of the cell. At the same time, Ca^{2+} ions are actively extruded by ionic pumps on the receptor membrane. In this way a flux of positive charge is directed toward the exterior hyperpolarizing the receptor membrane and stopping the synaptic transmission. The resting potential is restored at the end of the period of the sound wave when the stereocilia go back to the rest position and a new cycle began.

The variations of the membrane potential, the quantity of released neurotransmitter and the resulting activity of the neurons in the spiral ganglion are proportional to the deflections of the hair bundles which in turn are proportional to the stimulus. In this way the receptor measures the intensity of the mechanical stimulus and transduces it in a precise bioelectrical signal. It is important to note the high sensitivity of this mechanism which is able to respond to movements of the stereocilia up to few nanometers. For example, the tallest stereocilia movement produced by a stimulus at the threshold of hearing is about $0.3\,\mathrm{nm}$ (Purves et al., 2001).

2.3.3 Passive and active mechanisms of the cochlea

Since the first studies of the physiology of the hearing system it has been recognised that the fundamental sensory function of the cochlea is the spectral analysis of the frequencies that compose the sound stimulus. Herman von Helmotz suggested (von Helmoltz, 1874) that the basilar membrane was constituted by a series of elements, driven by the fluid pressure, able to resonate selectively at the different frequencies of the audible spectrum. Georg von Bekesy demonstrated (Békésy, 1960) that the sound stimulus induces a travelling wave that propagates along the basilar membrane. Because of the mechanical properties of the BM, rigid and narrow at the base of the cochlea and wider and more flexible as one goes toward the apex, a large change in stiffness exists along the BM so that the sound waves of different frequencies propagates for different distances. In particular, they reach a peak of maximum amplitude in precise locations, characteristic of each frequency. Accordingly, the frequencies of the audible spectrum are represented continuously along the basilar membrane: the high frequencies on the basal part, the low frequencies on the apical region. According to this model, the ability of a receptor to respond selectively to a particular frequency depends only on its position along the basilar membrane. However, the properties of the travelling waves, measured by Bekesy in the cochlea of human cadavers, cannot explain the high sensitivity and the exceptional discrimination abilities of the living hearing organ. For these reasons, the existence of an active mechanism that amplifies the mechanical stimulus and modifies the travelling wave to increase the sensitivity and the frequency selectivity of the receptors, was proposed by T. Gold (Gold, 1948). The basic hypothesis to explain the active amplification concerns the properties of the outer hair cells. In these cells the mechanoelectrical transduction, mediated by the hair bundle, is followed by an electromechanical transduction in which the variation of the membrane potential is transformed in vibrations of the length of the cells which then exert a force on the basilar membrane. In this way the OoC acts as a local feedback loop providing positive feedback to amplify the motion. However, it is not yet fully understood how the outer hair cells interact with each other and with the other parts of the Organ of Corti in order to provide a relatively stable system with a high performance in terms of sensitivity and frequency selectivity.

In the next Chapter we are going to study the passive mechanism of the cochlea, by deriving an analytical solution to the cochlear wave equation, when fluid viscosity and compressibility are included. Then, in Chapter 4 we will discuss experimental methods that have been used to characterize wave motion inside the cochlea, together with recent work measuring the relative motion of the various parts within the Organ of Corti, which emphasizes the importance of longitudinal coupling in understanding the active mechanism of the cochlea, as studied in the later chapters.

Chapter 3

Solution to the wave equation for the passive cochlea

3.1 Introduction

In this chapter we derive the Wentzel-Kramers-Brillouin (WKB) approximation to the cochlear wave equation, which results from the interaction between the passive dynamics of the basilar membrane and the 1D fluid coupling in the scale, including both fluid viscosity and compressibility. The solution is expressed only in terms of nondimensional parameters, the effect of which on the basilar membrane response and on the wavenumber distribution are then discussed. A nondimensional damping parameter and a nondimensional phase-shift parameter are shown to have the greatest influence on the response under normal conditions in the cochlea, with the fluid viscosity and compressibility only playing a minor role.

3.2 Wavenumber distribution in the passive cochlea including fluid compressibility and viscosity

The passive behaviour of the cochlea can be understood in terms of the interaction between the inertia of the fluid and the dynamics of the Organ of Corti which separates them. This can be modelled as a one-dimensional box model, represented in Fig. 3.1, which is based on some simplified assumptions with respect to the real geometry and cell's structure of the cochlea. First, it is assumed that the cochlea extends only along one dimension, the longitudinal coordinate x. Secondly, the Reissner's membrane is neglected because it is acoustically transparent, so that there are only two fluid chambers, denoted as scala vestibuli (SV) and scala tympani (ST). The boundaries of these chambers are considered to be rigid and to communicate with the external environment only through the membranes at the round and oval windows, at the base of the cochlea. Finally, the dynamic of the complex tissue and cell structure of the cochlear partition

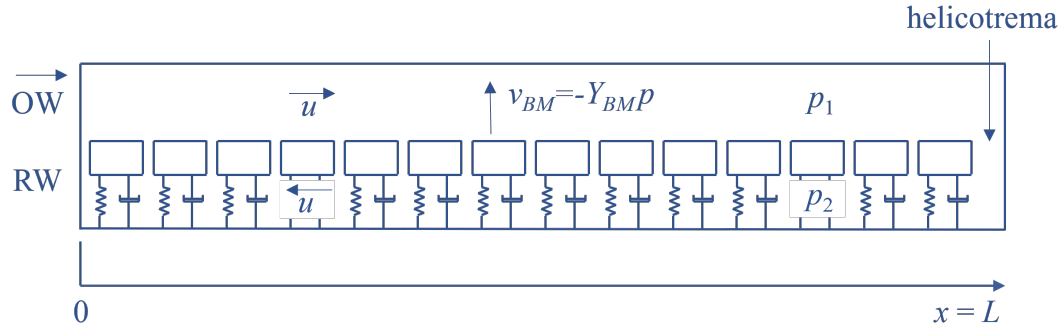

Figure 3.1: Schematic diagram of the box model of the uncoiled cochlea, showing two fluid chambers, divided by the BM, represented as N locally reacting single degree-of-freedom elements, consisting of a local mass, stiffness and damping, whose values vary with position along the cochlea. The upper chamber is driven by the middle ear via the oval window, OW, and the lower chamber is terminated at the basal end, $x = 0$, by the flexible round window, RW, which provides pressure release. The complex pressure difference $p = p_1 - p_2$ drives the locally reacting BM so that its velocity is v_{BM}, which produces equal and opposite longitudinal flow velocity u in the two fluid chambers, which are connected at the apical end, $x = L$, at the helicotrema.

is simplified as a single, elastic structure, the basilar membrane (BM), which moves in response to the difference in pressure between the two fluid chambers.

The dynamics of the system is described by a linear wave equation that is obtained using the conservation of mass and of momentum applied to an elemental volume of the fluid. Assuming a time dependence of the form $\mathrm{e}^{i\omega t}$, the continuity equations are given by:

$$\frac{\partial u(x)}{\partial x} + \frac{i\omega}{2\rho c_0^2} p(x) = \frac{v_{BM}(x)}{h}, \tag{3.1}$$

where $u(x)$ is the longitudinal fluid velocity averaged across the cross-sectional area, A, of the chamber; $p(x)$ is the pressure difference between the two scalae, averaged across the width, W, of the chamber; ρc_0^2 is the bulk modulus of the fluid, where ρ is its density and c_0 the velocity of sound in the fluid; v_{BM} is the transverse velocity of the BM, averaged across the width of the cochlea and h is the effective height of the chamber, given by $h = \pi^2 A/(8B)$ (Elliott and Ni, 2018), where B is the width of the basilar membrane. It is assumed that A, W and hence h are constant with x, giving a uniform cross section, as shown in Fig. 3.1.

The momentum equation is given by:

$$\frac{\partial p(x)}{\partial x} = -2i\omega\rho u(x) - \frac{4\nu}{h^2} u(x), \tag{3.2}$$

where ν is the dynamic viscosity of the fluid. The prefactor 4 is used to be consistent with the analysis in (Deepu, 2019), in which this term is derived by comparison with the solution of plane Poiseuille flow. Combining Eqs. (3.1) and (3.2) we obtain:

$$\frac{\partial^2 p(x)}{\partial x^2} + \frac{\omega^2}{c_0^2}\left(1 - \frac{2i\nu}{h^2\omega\rho}\right) p(x) = \frac{-2i\omega\rho}{h}\left(1 - \frac{2i\nu}{h^2\omega\rho}\right) v_{BM}, \tag{3.3}$$

which describes the relation between the movements of the BM and the pressure distribution of the fluid. As the BM is assumed to be locally reacting, the velocity of a point on the BM is equal to the negative value of the admittance, $Y(x)$, times the pressure difference $p(x)$, due to the sign convention:

$$v_{BM} = -Y(x,\omega)p(x), \tag{3.4}$$

so that Eq. (3.3) becomes:

$$\frac{\partial^2 p(x)}{\partial x^2} + k^2(x,\omega)p(x) = 0, \tag{3.5}$$

which is the wave equation of the cochlear model and k, the complex wavenumber, is given by:

$$k(x,\omega) = \pm\sqrt{\left(-\frac{2i\omega\rho}{h}Y + \frac{\omega^2}{c_0^2}\right)\left(1 - \frac{2i\nu}{h^2\omega\rho}\right)}. \tag{3.6}$$

A single degree-of-freedom model is used to model the dynamics of the passive BM, whose admittance, $Y(x)$, is given by:

$$Y(x) = \frac{i\omega}{i\omega R(x) + S(x) - \omega^2 M(x)}. \tag{3.7}$$

where $R(x,\omega)$, $S(x,\omega)$ and $M(x)$ are, respectively, the stiffness, mass and resistance per unit area of the BM. The term $M(x)$ includes a contribution from the entrained mass of the fluid (Neely, 1981). The longitudinal variation of the remaining variables is given by:

$$R(x) = \frac{m_0 w_n(x)}{Q}, \tag{3.8a}$$

$$S(x) = \omega_n^2(x) m_0, \tag{3.8b}$$

where Q is the quality factor of the BM local resonance, also assumed to be constant in x, and ω_n is its natural angular frequency at position x, and is assumed to vary exponentially along the cochlea as (de Boer, 1996):

$$\omega_n = \omega_b e^{-x/l}, \tag{3.9}$$

where ω_b is the natural angular frequency at the base of the cochlea and l the characteristic length. The expression of the wavenumber in Eq. (3.6) then becomes:

$$k = \pm\sqrt{\left(\frac{2\rho\omega^2}{h m_0 \omega_n^2}\frac{1}{\left(1 - \frac{w^2}{w_n^2} + \frac{i\omega}{\omega_n Q}\right)} + \frac{w^2}{c_0^2}\right)\left(1 - \frac{2i\nu}{h^2\omega\rho}\right)}. \tag{3.10}$$

This can be rewritten as:

$$k = k_{fc}\sqrt{\frac{G^2\omega_n^2 + \frac{\mathrm{i}\omega\omega_n}{Q} - \omega^2}{\omega_n^2 + \frac{\mathrm{i}\omega\omega_n}{Q} - \omega^2}}, \tag{3.11}$$

where k_{fc} is the complex wavenumber in the fluid domain, which takes into account the effect of viscosity, and is given by:

$$k_{fc} = \frac{\omega}{c_0}\sqrt{1 - 2\mathrm{i}V^2}, \tag{3.12}$$

and G is the bandgap ratio:

$$G = \sqrt{1 + \frac{16N^2}{C_n^2}}, \tag{3.13}$$

which is the ratio of the limiting frequencies of the corresponding stop band shown in Fig. 3.2a. In Eqs. (3.12) and (3.13) we have introduced the following nondimensional variables:

$$C = \frac{\omega l}{c_0}, \tag{3.14a}$$

$$V = \frac{\delta}{h}, \tag{3.14b}$$

$$N = \frac{l}{4h\sqrt{\mu}}, \tag{3.14c}$$

$$\mu = \frac{m_0}{2\rho h}, \tag{3.14d}$$

where C is the nondimensional compressibility; since C depends on the excitation frequency the parameter C_n, which is equal to $\omega_n l/c_0$, is also used and is called nondimensional compressibility at resonance; V is the nondimensional viscosity, which is the ratio of the viscous boundary layer thickness, δ, given by $\sqrt{\nu/\omega\rho}$, to the effective height of the fluid chambers, h; N is a constant introduced in (Zweig et al., 1976), called the phase-shift parameter and μ is the ratio of the mass per unit area of the BM and of the fluid in the chambers. The geometrical and physical values assumed for the cochlear model are listed in Table 3.1 and the corresponding nominal values of the nondimensional parameters (Q_0,N_0,C_0 and V_0), for an excitation frequency of 1 kHz, are listed in Table 3.2.

The real and imaginary parts of the wavenumber are plotted in Fig. 3.2 for different values of the nondimensional parameters, to show their effect on the wavenumber distribution. In Fig. 3.2a, it is shown that, for a nominal value of C_n, equal to C_0, a pass band is seen up to the natural frequency, for which $\omega/\omega_n = 1$. In this region the real part of the wavenumber is rising and also its slope is increasing, so that the phase and group velocities, given respectively by $c_{ph} = \omega/k$ and $c_{gr} = \frac{\partial w}{\partial k}$, decrease along this band, leading to the wave being slowed so that its amplitude is concentrated near the natural frequency. The imaginary part of the wavenumber is for the most part very small, corresponding to little energy loss. The imaginary part starts to increase in

magnitude at a frequency slightly before the peak of the real part. This leads to a stop band, where the imaginary part of the wavenumber remains high in absolute terms and the wave is greatly attenuated. For values of C_n much larger than the nominal one, a second pass band occurs, in which the wave again begins to propagate.

In Fig. 3.2b the real and imaginary parts of the wavenumber are plotted for different values of the nondimensional viscosity parameter V. Only for values of V that are very much larger than the nominal value do the real and the imaginary part of the wavenumber change significantly. In particular, the imaginary part increases and is non-zero even at the lowest frequencies, indicating a greater attenuation as V is increased.

In Fig. 3.2c the real and imaginary parts of the wavenumber are plotted for different values of the quality factor Q. The main effect is near the peaks of the real and imaginary parts, around the natural frequency. In particular, the peaks become sharper and shift slightly to higher frequencies for higher values of Q. The increase of the real part just before $\omega/\omega_n = 1$ corresponds to a decrease of the phase velocity c_{ph}, whereas the increase slope of the real part corresponds to a decrease of the group velocity c_{gr}. The imaginary part increases beyond $\omega/\omega_n = 1$, indicating a more abrupt dissipation of the response.

In Fig. 3.2d the real and imaginary parts of the wavenumber are plotted for different values of the nondimensional phase-shift parameter N. As this parameter increases, the magnitude of the real part increases, and thus the phase speed at a given frequency decreases, up to $\omega/\omega_n = 1$. The magnitude of the imaginary part and thus the attenuation of the wave, also increases beyond $\omega/\omega_n = 1$.

Table 3.1: Assumed geometrical and physical values of the one-dimensional cochlear box model (Elliott and Ni, 2018).

Parameter	Symbol	Value
Length of the cochlea	L	$3.5 \times 10^{-2}\,\mathrm{m}$
Characteristic length	l	$7.0 \times 10^{-3}\,\mathrm{m}$
Base natural frequency	$\omega_b/2\pi$	$2.0 \times 10^{4}\,\mathrm{Hz}$
Effective height of a fluid chamber	h	$4.1 \times 10^{-3}\,\mathrm{m}$
Density of the fluid	ρ	$1 \times 10^{3}\,\mathrm{kg/m^3}$
Mass per unit area of the BM	m_0	$3 \times 10^{-1}\,\mathrm{kg/m^2}$
Coefficient of viscosity	ν	$8.9 \times 10^{-6}\,\mathrm{Pas}$
Speed of sound	c_0	$1.5 \times 10^{3}\,\mathrm{m/s}$

Table 3.2: Nominal values of nondimensional parameters in the cochlear model corresponding to an excitation frequency of 1 kHz.

Parameter	Symbol	Value
Quality factor	Q_0	5
Nondimensional viscosity	V_0	2.9×10^{-3}
Nondimensional compressibility	C_0	2.1×10^{-2}
Phase-shift parameter	N_0	2.23

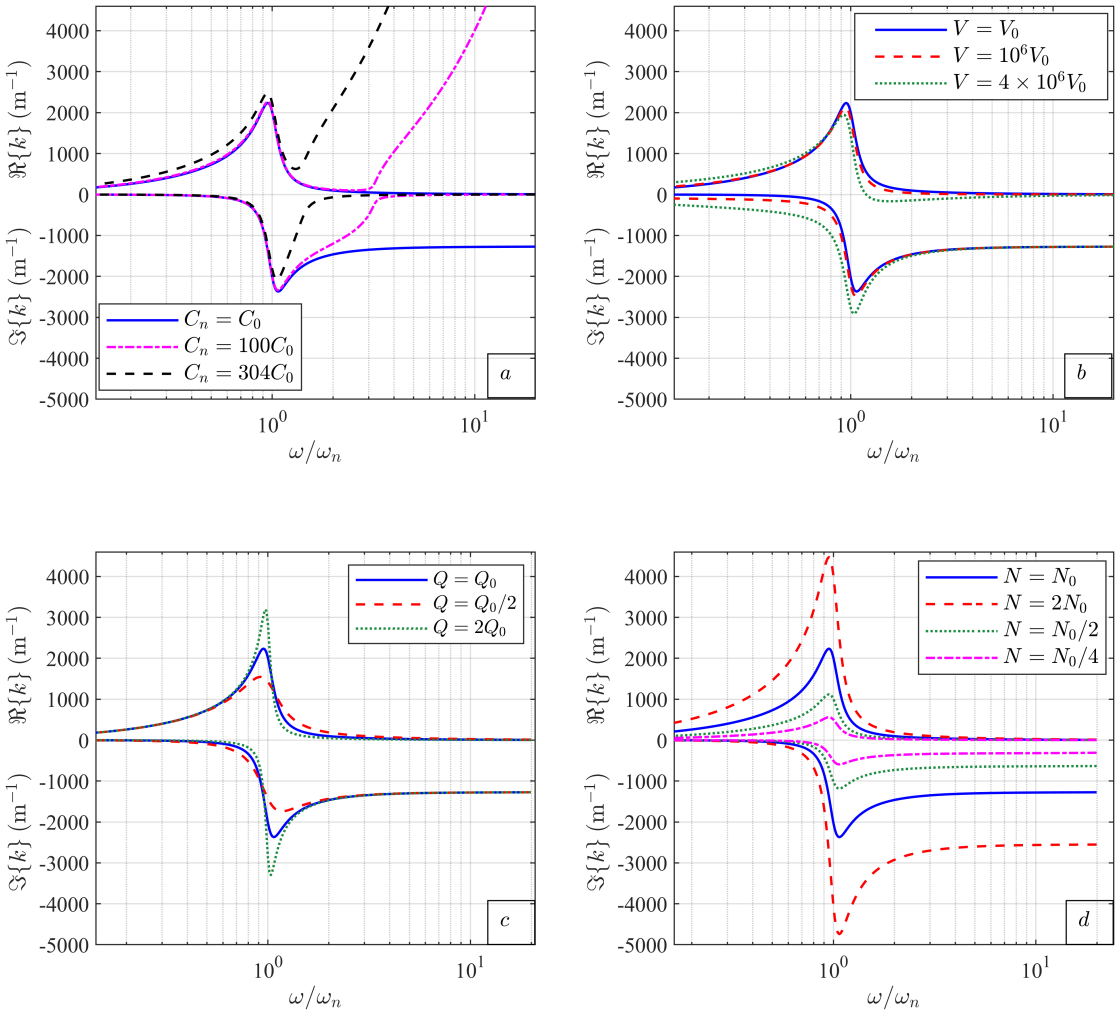

Figure 3.2: Variation of (upper) the real part and (lower) the imaginary part of the wavenumber as a function of normalised frequency, for (a) different values of the nondimensional compressibility parameter at resonance C_n, (b) the normalised viscosity V, (c) the quality factor Q and (d) the normalised phase-shift parameter N.

3.3 Analytic WKB solutions including compressibility and viscosity

We now derive an approximation to the exact solution of the wave equation Eq. (3.5) using the WKB method. The WKB method has been previously used to obtain closed-form solutions for 1D (Zweig et al., 1976), 2D (Steele and Miller, 1980) and 3D (Taber and Steele, 1981; Steele and Taber, 1979a) models. These solutions have been obtained in the case of an incompressible and inviscid fluid, by assuming light damping in the BM. In (Deepu, 2019) a semi-analytic solution is derived for the 1D case, including fluid compressibility and viscosity and with no approximation to the BM's damping. In this section we derive an analytical WKB solution in terms of the nondimensional parameters introduced in the previous section and then discuss their contribution to the amplitude and phase response of the BM.

The condition of validity for the WKB approximation is that:

$$\frac{|k'(x)|}{|k^2(x)|} \ll 1, \tag{3.15}$$

where $k(x)'$ is the derivative of k with respect to x. It has been shown that the approximate WKB solution differs from numerical solutions, given by the finite difference method (Neely, 1981), only for angular frequencies of excitation ω much lower than the value of the frequency at the base, ω_b, and for frequencies just above the natural frequency, where the WKB response drops off more quickly than the exact solution (de Boer and Viergever, 1982; Steele and Taber, 1979a; Steele and Miller, 1980). Although an assumption made in the WKB method is that only a single wave is propagating, the effects just above the natural frequency may be due to low amplitudes of an additional evanescent fluid wave (Elliott et al., 2013; Watts, 2000). Apart from these small differences, the WKB solution and the finite difference solutions are very similar around the characteristic frequency, which is the main region of interest in the study. The form of this response, with an increasing magnitude and falling phase up to the characteristic frequency, after which there is a rapid drop in amplitude with little additional phase shift, is consistent with that measured in the mammalian cochlea using laser methods, for example in (Robles and Ruggero, 2001) and recent optical coherence tomography techniques, as in (Ren et al., 2016b).

The general WKB solution to Eq. (3.5), with the boundary condition $p(x = L) = 0$, is given by:

$$p(x) = \frac{p(0)\sqrt{k(0)}}{\sqrt{k(x)}} \frac{\exp[-i\int_0^x k(x')dx'] + \exp[-2i\int_0^l k(x')dx' + i\int_0^x k(x')dx']}{1 - \exp[-2i\int_0^l k(x')dx']}, \tag{3.16}$$

where $p(0)$ is the value of the pressure at the base. The first term of the numerator represents a travelling wave that propagates towards the apex, while the second term describes a wave that originates by reflection of the first wave at the helicotrema ($x = L$) and then propagates toward the base. This last term is significant only for frequencies so low that the pressure $p(x)$ at the apex retains an appreciable value. It has been shown, by numerical integration of the WKB solution (Deepu, 2019), that this reflected wave is much smaller than the forward-travelling wave and that it is important only in a region very near the apex. We can thus simplify the approximate solution in Eq. (3.16) as:

$$p(x) = \frac{p(0)\sqrt{k(0)}}{\sqrt{k(x)}} \exp(\phi). \tag{3.17}$$

where

$$\phi = -\mathrm{i}\int_0^x k(x')\,\mathrm{d}x'. \tag{3.18}$$

The integral above can be solved as outlined in Appendix A. A simplified expression can then be obtained by making the approximation $\omega \ll \omega_b$, since we are interested in the form of the solution for excitation frequencies that are much lower than the natural

frequency at the base. In this case ϕ can be written as:

$$\begin{aligned}\phi = {} & \mathrm{i}C\sqrt{1-2\mathrm{i}V}\Bigg[\frac{1}{Q\sqrt{-1+\frac{16N^2}{C^2}}}\mathrm{F}\left(-\arcsin(\mathrm{i}/Q+\omega_n/\omega),\frac{1}{\sqrt{1-\frac{16N^2}{C^2}}}\right)\\ & +\frac{4\omega^2}{Q}\sqrt{-1+\frac{16N^2}{C^2}}\Pi\left(-Q^2;-\arcsin(\mathrm{i}/Q+\omega_n/\omega),\frac{1}{\sqrt{1-\frac{16N^2}{C^2}}}\right)\\ & +\operatorname{arctanh}\left(\frac{\sqrt{(\mathrm{i}/Q+\omega_n/\omega)^2-1}}{\sqrt{16N^2/C^2-1+(\mathrm{i}/Q+\omega_n/\omega)^2}}\right)\\ & +\sqrt{-1+\frac{16N^2}{C^2}}\arctan\left(\frac{\sqrt{16N^2/C^2-1}\sqrt{(\mathrm{i}/Q+\omega_n/\omega)^2-1}}{\sqrt{16N^2/C^2-1+(\mathrm{i}/Q+\omega_n/\omega)^2}}\right)\Bigg],\end{aligned} \tag{3.19}$$

where F and Π are, respectively, an elliptic integral of the first and third kind. It is interesting to note that although the wavenumber in Eq. (3.11) depends on $C_n = \omega_n l/c_0$, via the term G in Eq. (3.13), the phase term ϕ only depends on the nondimensional compressibility term $C = \omega l/c_0$ defined in Eq. (3.14a) where ω is the excitation frequency, since the term ω_n cancels out in the integration in Eq. (A.3).

From the pressure distribution, given by Eq. (3.17), we can derive the velocity of a point of the BM using Eq. (3.4) and, from this, the corresponding displacement Δ by dividing by $\mathrm{i}\omega$, obtaining:

$$\Delta(x,\omega) = -\frac{\sqrt[4]{1+\frac{16N^2}{C^2\left(\frac{\omega_b^2}{\omega^2}+\frac{\mathrm{i}\omega_b}{Q_0\omega}-1\right)}}}{m_0\omega^2\left(\frac{\mathrm{i}\omega_n}{Q_0\omega}+\frac{\omega_n^2}{\omega^2}-1\right)\sqrt[4]{1+\frac{16N^2}{C^2\left(\frac{\mathrm{i}\omega_n}{Q_0\omega}+\frac{\omega_n^2}{\omega^2}-1\right)}}}p(0)\exp(\phi). \tag{3.20}$$

It is customary to normalize the displacement of the BM with respect to the displacement of the stapes, Δ_s, which can be derived from the fluid volume velocity u at $x = 0$, given by Eq. (3.2), as:

$$\Delta_s = -\frac{u|_{x=0}}{\mathrm{i}\omega} = -\frac{\sqrt{1+\frac{16N^2}{C^2\left(\frac{\mathrm{i}\omega_b}{Q_0\omega}+\frac{\omega_b^2}{\omega^2}-1\right)}}}{2\mathrm{i}\omega\rho c_0\sqrt{1-2\mathrm{i}V}}p(0), \tag{3.21}$$

so that, using $2\rho c_0/\omega m_0 = 4N/C\sqrt{\mu}$, we obtain the BM displacement ratio $D = \Delta/\Delta_s$, as a function of only the nondimensional parameters defined above:

$$D = \frac{4N\mathrm{i}\sqrt{1-2\mathrm{i}V}\exp(\phi)}{C\sqrt{\mu}\left(\frac{\mathrm{i}\omega_n}{Q\omega}+\frac{\omega_n^2}{\omega^2}-1\right)\sqrt{1+\frac{16N^2}{C^2\left(\frac{\omega_b^2}{\omega^2}+\frac{\mathrm{i}\omega_b}{Q\omega}-1\right)}}\sqrt[4]{1+\frac{16N^2}{C^2\left(\frac{\mathrm{i}\omega_n}{Q\omega}+\frac{\omega_n^2}{\omega^2}-1\right)}}}. \tag{3.22}$$

3.4 Parametric variation of the coupled response with nondimensional parameters

We now show how the amplitude and the phase of the normalised BM motion, D, as calculated in the previous section, depends on the nondimensional parameters introduced in Section 3.2 (Q,N,C and V), so that we can clarify their physical significance. In Fig. 3.3 the amplitude and the phase of D are plotted, as a function of the normalised angular frequency ω/ω_n, for different values of the nondimensional compressibility parameter, C, calculated at $\omega/\omega_n = 1$, at which frequency C is equal to C_n.

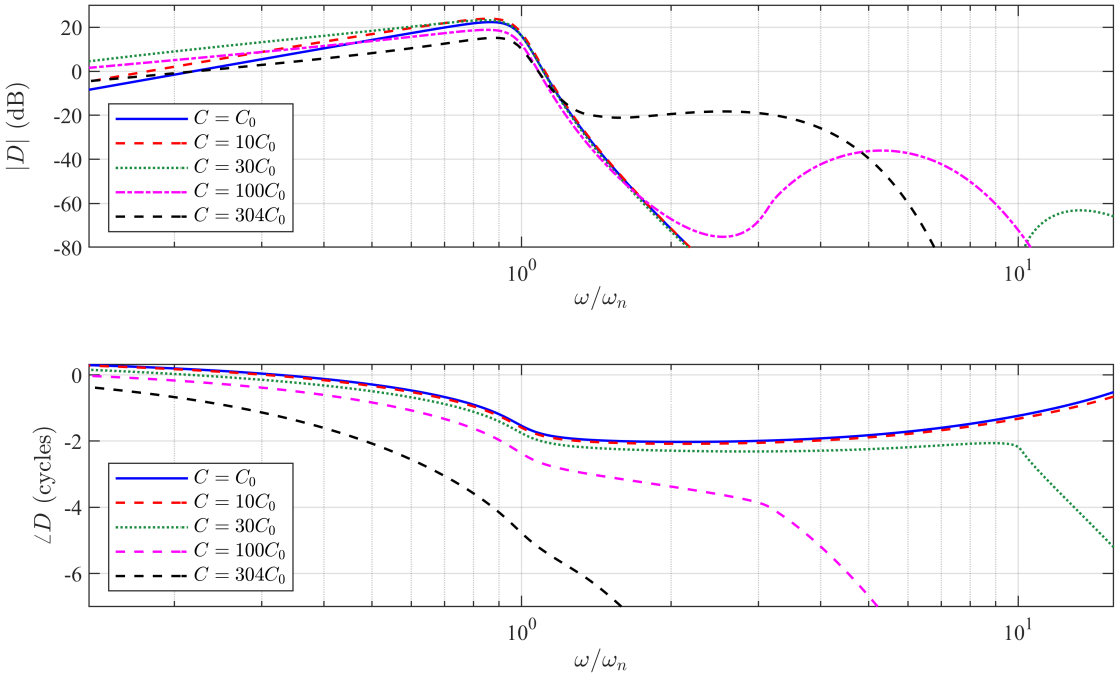

Figure 3.3: Variation of the amplitude (top) and of the phase (bottom) of the normalised BM displacement, for different values of the nondimensional compressibility parameter C, calculated at $\omega/\omega_n = 1$, as a function of normalised excitation frequency.

For C less than C_0 there is no effect on the amplitude and phase of the response, so that fluid compressibility can be neglected in a physiological model of the cochlea. As C is increased above the nominal value C_0, but less than $30C_0$, the amplitude of the displacement ratio increases in the lower pass band. For values of C greater than $100C_0$, the value of D decreases at the characteristic frequency. In the stop band, the response decays rapidly, due to the high losses attributed to the imaginary part of the wavenumber there, as seen in Fig. 3.2a. For larger values of C, a second peak appears in the second pass band, as the wave again starts to propagate. In the phase plot of Fig. 3.3, it can be seen that the phase decreases gradually up to the peak frequency. In the stop band the phase shift is lower. In the second pass band, the phase again decreases due to forward wave propagation. In Fig. 3.4, the amplitude and the phase of D are plotted for different values of the nondimensional viscosity parameter, V, calculated at $\omega/\omega_n = 1$. The nondimensional viscosity term has an appreciable effect only for very

high values ($V > 10^3 V_0$), for which the magnitude of D is reduced, resulting in a lower peak around ω/ω_n. This is related to the increase of the real and imaginary part of the

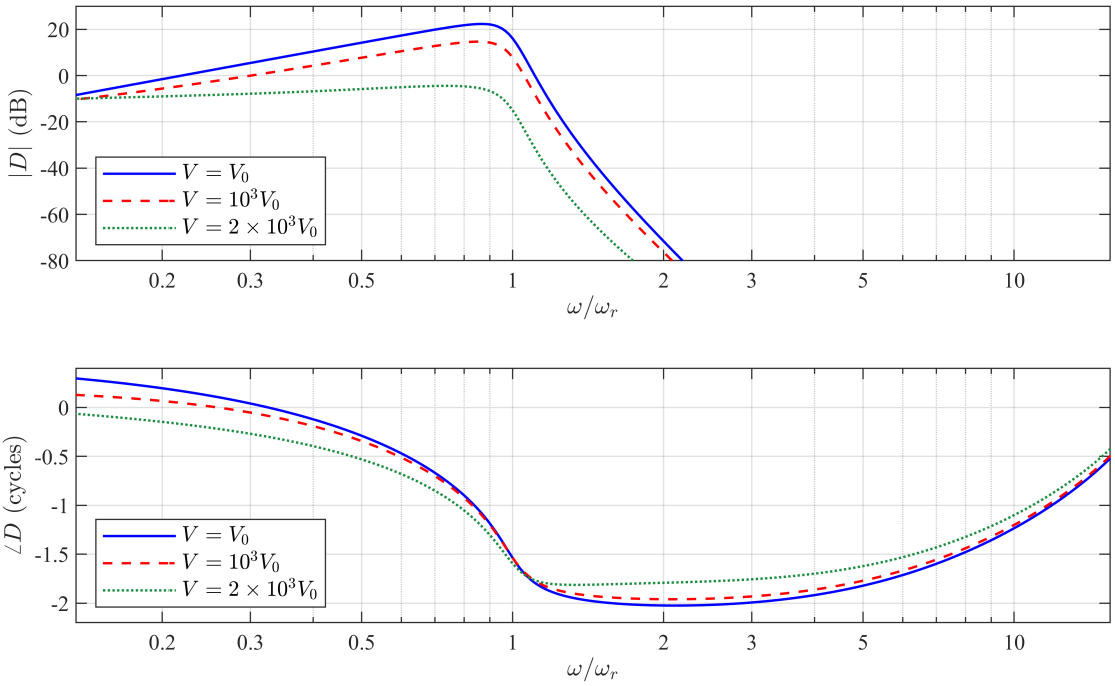

Figure 3.4: Variation of the amplitude (top) and of the phase (bottom) of the normalised BM displacement, for different values of the nondimensional viscosity parameter V, calculated at $\omega/\omega_n = 1$, as a function of normalised excitation frequency.

wavenumber, for high values of V, as seen in Fig. 3.2b. In particular, the high value of the imaginary part at lower frequencies greatly attenuates the wave, thus decreasing the value of D and flattening the curve. This supports a previous study by (Sasmal and Grosh, 2019), in which it is shown that the effect of viscosity is important only at the apex of the cochlea, where the viscous boundary layer thickness becomes comparable to the height of the cochlea. It is also in agreement with experimental results in which it has been shown that an increase in fluid viscosity led to a decrease in the BM amplitude (Tonndorf, 1957) and in the flattening of the response curve (Gan et al., 2007). For values of V less than the nominal value, there is no change in the coupled response thus, apart from its effect at the apex of the cochlea, fluid viscosity can be neglected in the model.

In Fig. 3.5 the amplitude and the phase of D are plotted for different values of the quality factor, Q. The amplitude response becomes sharper around the natural frequency and shifts to higher frequencies with increasing Q. For $\omega/\omega_n > 1$ the response decay becomes steeper as Q is increased, while for $\omega/\omega_n \ll 1$ the amplitude is relatively unaffected. The phase response becomes steeper around the characteristic frequency with increasing Q. This corresponds to the increase of the real part of the wavenumber around $\omega/\omega_n = 1$.

In Fig. 3.6 the amplitude and the phase of D are plotted for different values of the nondimensional phase-shift parameter N. For low values of N, the response of the BM

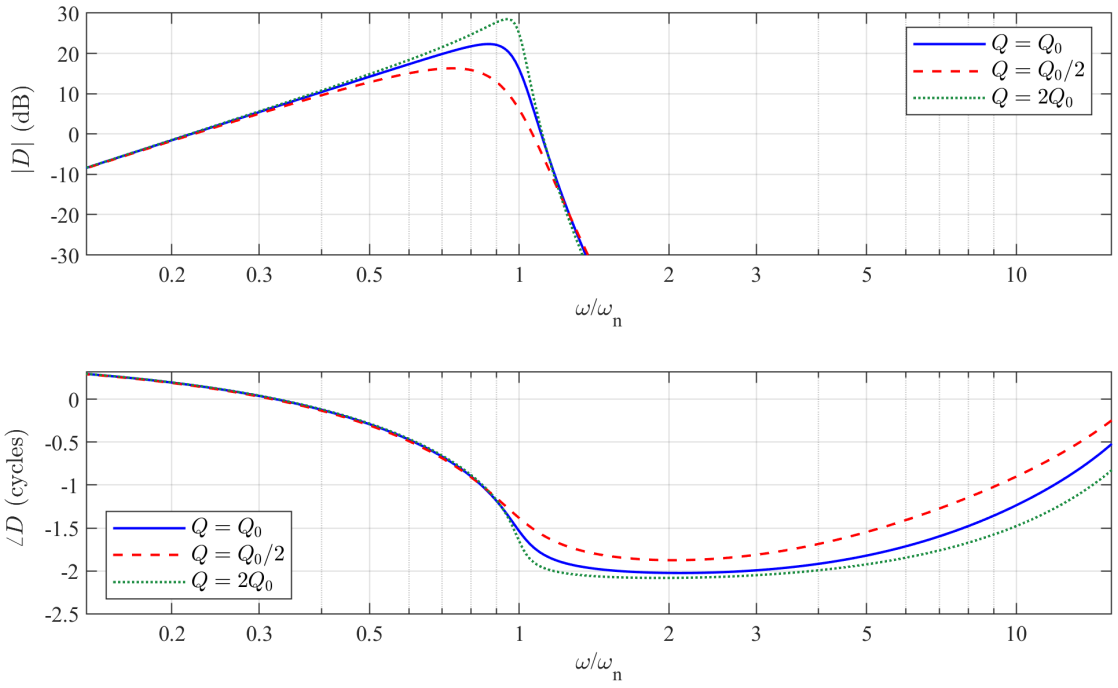

Figure 3.5: Variation of the amplitude (top) and of the phase (bottom) of the normalised BM displacement, for different values of the nondimensional quality factor Q, as a function of normalised excitation frequency.

is almost symmetric on a log frequency axis, indicating weak fluid coupling and a phase shift of about half a cycle only occurs close to the characteristic frequency, implying a local resonance and no wave propagation. With increasing values of N, the phase change is larger and the amplitude response becomes asymmetrical, with a characteristic peak at sightly less than $\omega/\omega_n = 1$, with a steep decrease after this, indicating strong fluid coupling. This is related to the dependence of the wavenumber on N, as shown in Fig. 3.2d. For small values of N, the real part of the wavenumber is small so that the wave speed is high and the pressure becomes almost uniform along the cochlea, driving the BM as a resonant second order system. The phase shift of D is then only $\pi/2$ at the BM resonance, as associated with an isolated resonator. These results are in accordance with (Rapson et al., 2014), where the relationship between the BM mass and the coupled response is discussed. The more complete analysis here illustrates the dependence of the form of the coupled response not just on the BM mass via μ, but on the more complicated nondimensional parameter, N.

In all the cases discussed above, the phase shift of the BM displacement ratio, given by Section 3.3, increases somewhat for frequencies much higher than the characteristic frequency. This is in contrast to what has been observed experimentally, as in (Rhode and Geisler, 1970). However, this phase increase only occurs when the normalised magnitude response is lower than -60 dB, so that it does not affect the overall response in practice.

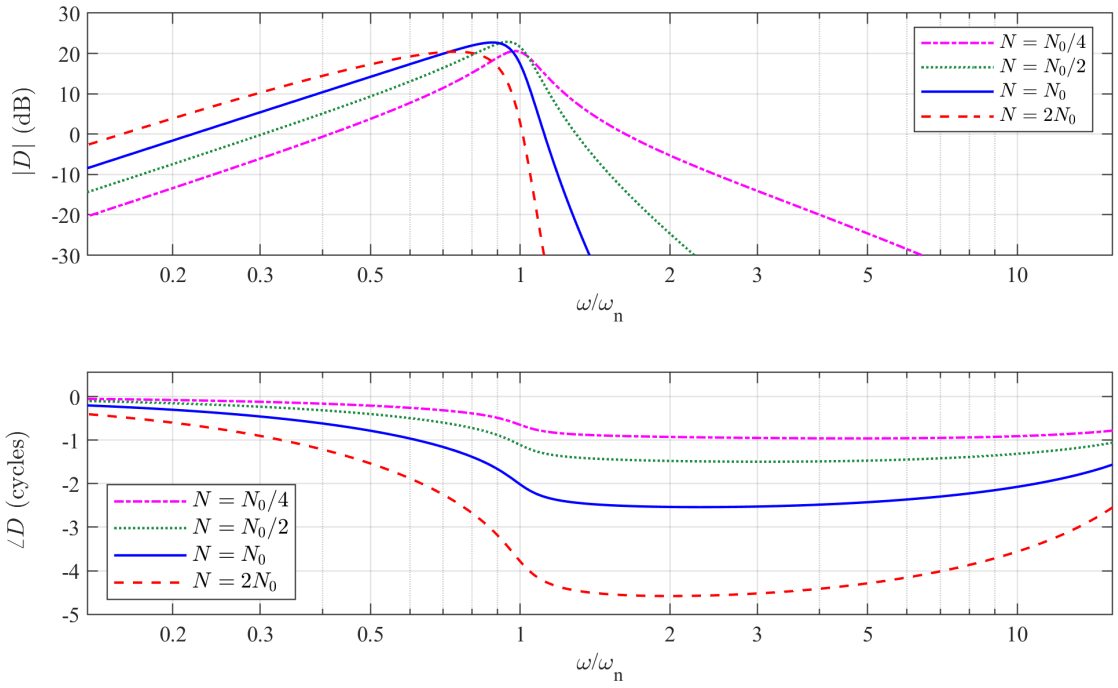

Figure 3.6: Variation of the amplitude (top) and of the phase (bottom) of the normalised BM displacement, for different values of the nondimensional parameter N, as a function of normalised excitation frequency.

3.4.1 Incompressible and inviscid case

The contributions of compressibility and viscosity of the fluid to the displacement ratio can be neglected if V and C are much smaller than unity. This is valid for nominal physiological values of these parameters, as seen in Table 3.2. In this case, the wavenumber in Eq. (3.11) simplifies so that:

$$kl = 4N\sqrt{\frac{\omega^2}{\omega_n^2 + \mathrm{i}\omega_n\omega/Q - \omega^2}} \tag{3.23}$$

i.e. the wavenumber is directly proportional to N as seen in Fig. 3.2d. Section 3.3 for the displacement ratio then reduces to:

$$D = \frac{4N\mathrm{i}\exp\{-\mathrm{i}4N(\arcsin(\omega/\omega_n - \mathrm{i}/(2Q)) - \arcsin(\omega/\omega_b - \mathrm{i}/(2Q))\}}{C\sqrt{\mu}\left(\frac{\mathrm{i}\omega_n}{Q\omega} + \frac{\omega_n^2}{\omega^2} - 1\right)\frac{4N}{C}\sqrt[4]{\frac{1}{\left(\frac{\omega_b^2}{\omega^2} + \frac{\mathrm{i}\omega_b}{Q\omega} - 1\right)}}\sqrt[4]{\frac{1}{\left(\frac{\omega_n^2}{\omega^2} + \frac{\mathrm{i}\omega_n}{Q\omega} - 1\right)}}}, \tag{3.24}$$

which becomes, taking into account the relation $N = l/(4h\sqrt{\mu})$ and making the approximation $\omega \ll \omega_b$:

$$D_{incomp} = \frac{\mathrm{i}\omega\sqrt{\omega_b}\exp\{-\mathrm{i}4N(\arcsin(\omega/\omega_n - \mathrm{i}/(2Q))\}}{\sqrt{\mu}\left(\omega_n^2 - \omega^2 + \mathrm{i}\frac{\omega\omega_n}{Q}\right)^{3/4}}. \tag{3.25}$$

Apart from an additional factor of h and the absence of a factor of $\omega_n^{3/2}$, which give the correct nondimensionality, this expression is equivalent to that derived in (Zweig et al., 1976) for the case of an incompressible and inviscid fluid.

The only direct effect of the mass ratio, μ, on D is to scale the overall response, whose shape is determined by N and Q. Although the nondimensional parameter N is seen to be a function of μ in the definition in Eq. (3.14c), its additional dependence on l and h means that in numerical simulations it can be varied while keeping μ constant, as in Fig. 4.13 of (Karlos, 2020).

3.5 Conclusions

An analytic WKB solution for the wave equation in the passive cochlea has been derived, including the effects of both viscosity and compressibility in the cochlear fluids, which reduces to an earlier result (Zweig et al., 1976), if the effects of viscosity or compressibility are ignored. This allows the response of the cochlea to be expressed in terms of four nondimensional parameters, two dependent on the viscosity and compressibility of the fluid, one dependent on the damping of the basilar membrane, and finally a previously derived nondimensional phase-shift parameter (Zweig et al., 1976). For the parameters found in the normal cochlea, however, the effect of the fluid viscosity and compressibility is very small. A physical interpretation can then be put on the behaviour of the wave by considering the parametric variation of the cochlear response with each of these parameters. It is found that the nondimensional phase-shift parameter determines not only the high frequency phase shift (Zweig et al., 1976) but also the nature of the interaction between the structural dynamics of the BM and the fluid inertia. If this parameter is large, the fluid-structural coupling is strong and a propagating wave is generated for frequencies up to about the natural frequency, with strong attenuation above this, giving a very asymmetrical frequency response. If this parameter is small, the fluid-structural coupling is weak, and the elements of the basilar membrane respond independently, driven by the constant pressure in the fluid, generating an almost symmetrical frequency response function when plotted on a log scale. Although the phase-shift parameter that determines the shape of the response is proportional to the square root of the ratio of the mass per unit length of the fluid in the chambers to the mass per unit length of the BM (Rapson et al., 2014), it also depends on the ratio of the characteristic length of the exponential decay in frequency along the cochlea to the effective height of the fluid chambers. Therefore, the mass ratio by itself only changes the amplitude and not the form of the response if the phase-shift parameter is kept constant, by varying the characteristic length of the cochlea.

In the passive, one dimensional case described in this chapter, only one type of wave dominates the coupled response of the system. When longitudinal coupling due to other forms of fluid coupling or other components of the Organ of Corti is included, an infinite number of wavenumber distribution, associated with various types of waves, are possible.

In Chapter 7 we will present a method to derive the wavenumber distribution associated with different types of waves for active model of the cochlea which includes different types of longitudinal coupling. This model is derived as an extension of the elemental model (Elliott and Ni, 2018) to include the micromechanical structure of the Organ of Corti, based on a detailed Finite Element Model of the cochlea developed by (Sasmal and Grosh, 2019), as described in Chapters 5 and 6. Before we do that, in the next Chapter we review the experimental methods used to measure the passive and active response of the cochlea and, in particular, recent experiments that showed the important contribution of longitudinal coupling to the active response of the cochlea.

Chapter 4

Review of experimental measurements within the active cochlea

4.1 Introduction

As discussed in Chapter 2 , in order to explain the high sensitivity and frequency discrimination of the cochlea, it is necessary to hypothesize the existence of an active feedback system within the Organ of Corti. To understand how this system works, the differential movements of the cells and tissues that compose the Organ need to be measured and distinguished. Until recently, this has not been possible because the resolution limit of the various experimental techniques used to probe the cochlea were greater than the height of the Organ of Corti ($\sim 100\,\mu$m vs $\sim 50\mu$m). Furthermore, in order to obtain a good signal to noise ratio, it was necessary to open the cochlea and to place reflective beads on its surfaces. This has three main consequences. First, once the cochlea is opened, its physiological and mechanical properties, responsible for the good functioning of the cochlear amplifier, degrades over time. Secondly, the reflective components may alter the mechanical properties of the OoC, even if they are designed to be as small and light as possible. Furthermore, because of the spiral structure of the cochlea, the basal region is difficult to access, so that the majority of the experiments have measured the response in the apical region of the cochlea.

However, in 2007, (Chen et al., 2007) introduced the use of the low-coherence interferometer to study the movements within the OoC in a living cochlea. With this technique it is possible to achieve an axial resolution of $\sim 10\,\mu$m so that the movements of the major components of the OoC (RL, BM, OHC, Hensen's cells, TM) can be distinguished. As explained in the previous chapter, it is believed that the cells responsible for the active feedback process are the outer hair cells so it makes sense to use the new technique to measure their motion with respect to the BM, whose motion has been measured in the last 50 years, so that the new data can be connected to the older BM data.

However, a consensus on which cells' or tissues' movements should be measured has not yet been reached. So far, the motion of the RL, the OHCs, the Hensens' cells and the TM have been recorded with respect to the BM. Thanks to these new data it is now possible to test old and develop new models of the cochlea to explain the functioning of the active amplifier. The aim of this chapter is to present the main techniques that have been used to record the movements within the cochlea, underling the contribution of each approach to the understanding of particular features of the Organ of Corti (e.g. passive and mechanics, non-linearity, high frequency selectivity). Furthermore, the advantages and limitations of each technique will be described.

4.2 Stroboscopy

Stroboscopy was first used by Bekesy to study the movements of the basilar membrane in human and animal cadavers (Békésy, 1960). The temporal bone was dissected soon after death and immersed in a saline solution. The round and oval windows were removed and substituted by rubber windows and a mechanical vibrator was attached to one of them (Fig. 4.1). Then the cochlear bone was opened under water and a light microscope, with a magnification of 140x, was used to observe, under a flashing light source, the movements of a specific point of the basilar membrane when it was excited by acoustic stimuli. A reflective material could also be placed on the basilar membrane in order to enhance the signal to noise ratio. The results were reported in two ways: by measuring

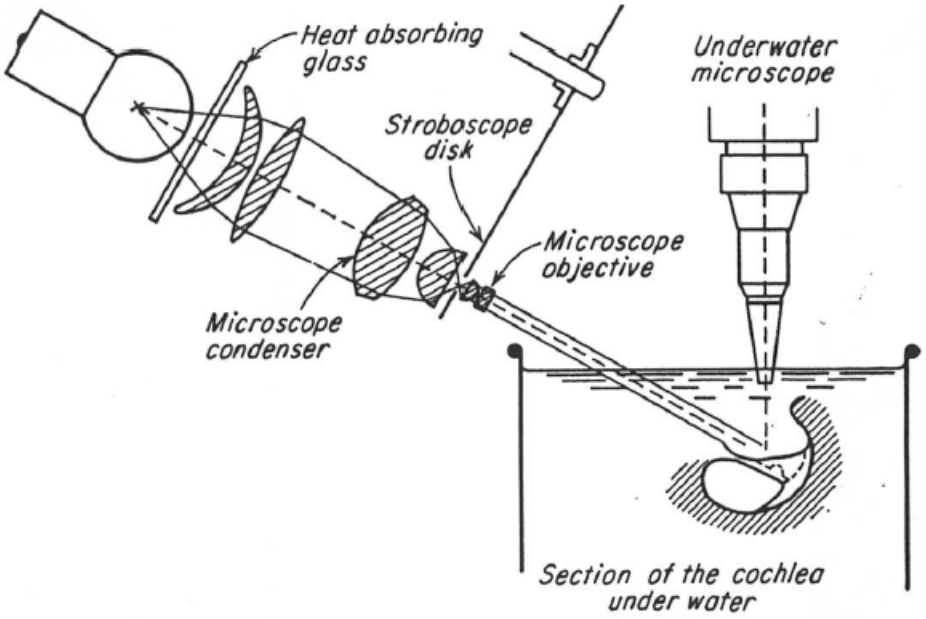

Figure 4.1: A diagram showing the stroboscopy technique used to look at the movements of the basilar membrane. The source is a stroboscopy light, followed by a heat absorbing glass to reduce the heat transmitted by the source. The microscopic condenser lens concentrate the light so that, in the plane of the stroboscope disk, an image of 100 μm is formed. Republished with permission of McGraw Hill LLC, from (Békésy, 1960, p. 441); permission conveyed through Copyright Clearance Center, Inc.

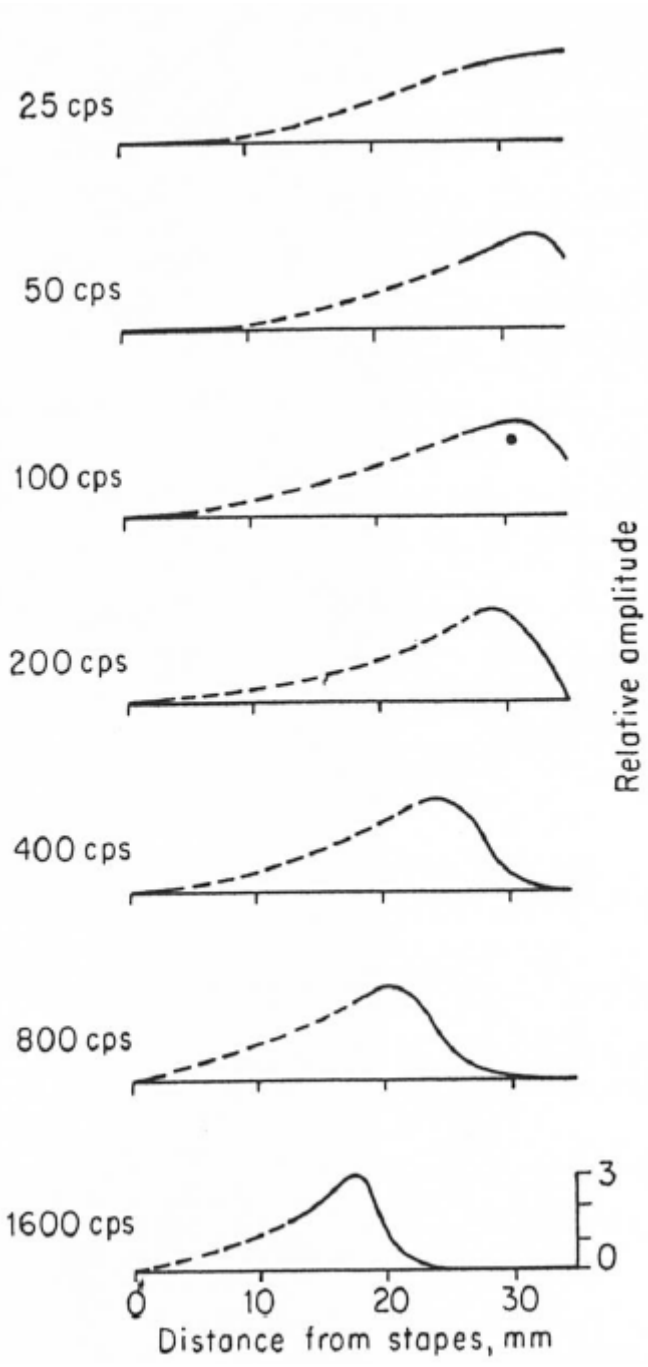

Figure 4.2: Patterns of vibration of the cochlear partition for various frequencies. Republished with permission of McGraw Hill LLC, from (Békésy, 1960, p. 448); permission conveyed through Copyright Clearance Center, Inc.

the vibrations at a fixed point as the frequency was varied, Fig. 4.2 or by plotting the movements along the basilar membrane for a particular frequency, Fig. 4.3. Both type of approaches showed that vibrations of the stapes induce a travelling wave along the basilar membrane which grows in amplitude as it travels towards the apex, decreasing in speed and then decaying after a specific point, which occurs in the basal region for high-frequency tones and in the apical region for low-frequency tones. The axial resolution

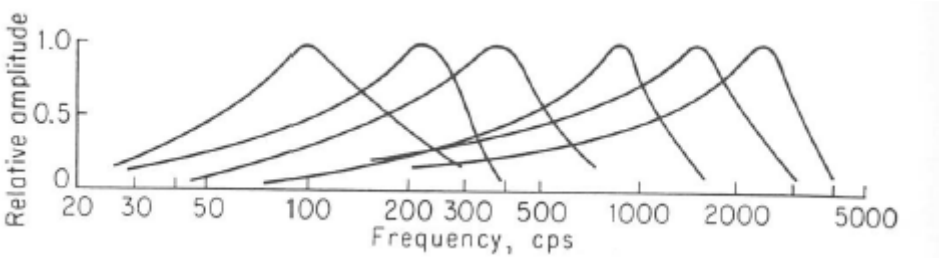

Figure 4.3: Frequency responses for six different positions along the cochlear partition. Republished with permission of McGraw Hill LLC, from (Békésy, 1960, p. 454); permission conveyed through Copyright Clearance Center, Inc.

of this method is about 100 μm (Békésy, 1960) so that only the movement of the basilar membrane can be distinguished. The frequency selectivity of the basilar membrane was observed to be not very sharp ($Q^{-1} < 1.6$), with a sallow slope for frequencies below the CF and a steep slope on the high-frequency side. Bekesy explained his data as a result the interaction between the inertia of the fluid in the chambers and the stiffness of the partition that separates them, which induce a travelling wave on the basilar membrane which peaks at particular positions according to the frequency of excitation.

4.3 Capacitive probes

Bekesy also pioneered the use of capacitive probes, as an alternative technique to stroboscopy, to measure the vibration of the basilar membrane (Békésy, 1960, p. 54-57). In this method, a metal plate is positioned in the vicinity of the basilar membrane, so that together they form a capacitor, whose capacitance varies as the distance between the two objects varies (Fig. 4.4). A circuit is built to obtain a voltage signal that is proportional to the capacitance so that the vibrations of the basilar membrane can be recorded. But Bekesy's probes were not small enough to obtain the required spatial resolution to distinguish the BM movements. (Wilson and Johnstone, 1972), used a mini-probe with a tip of 0.2 mm in diameter and was able to measure the vibrations of the BM down to 0.1 mm.

The main advantage of this technique, respect to the stroboscopic experiments, is that there are no reflective objects that interfere with the movements of the BM. The main disadvantage is that the calibration is not simple because the output depends on the dielectric constant of the tissue facing the probe, which is not known, and on the average distance between the probe and the vibrating surface, so that it is not always possible to obtain absolute measurements. Furthermore, it is necessary to remove the perilymph from the scala tympani, altering the mechanical and physiological properties of the cochlea.

[1] defined as the resonant frequency divided by the half-power band width.

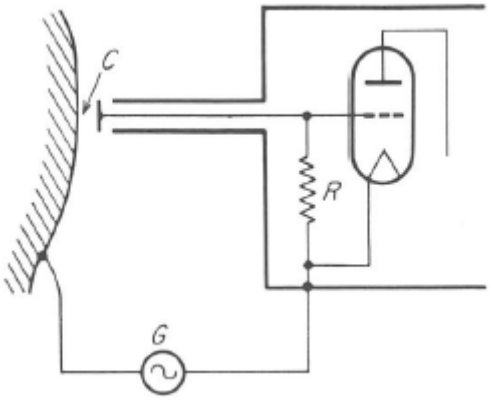

Figure 4.4: The principle of the capacitive probe. The probe capacitance, C, is measured in terms of the alternating voltages across the resistance R , when a current of 100 kHz is passed through R and the condenser C from a source G. When the impedance of C is much grater than that of R, the voltage across R is essentially a measure of the impedance C, if the generator voltage is kept constant. Republished with permission of McGraw Hill LLC, from (Békésy, 1960, p. 54); permission conveyed through Copyright Clearance Center, Inc.

4.4 The Mössbauer technique

Bekesy's measurements were restricted to frequencies below 2 kHz, to amplitude of vibrations in the visible range, to high sound pressure levels ($\sim$ 140 dB) and were performed on excised cochleas. For these reasons, the extrapolation from these data to predict the displacement of the basilar membrane in living cochleas under normal stimuli was not straightforward. In this context, the experiments conducted with the Mössbauer technique by (Johnstone and Boyle, 1967) and Rhode (Rhode, 1971) were revealing. Using this technique it has been possible to measure the velocity of the basilar membrane extending the range of measurements in both frequency and pressure excitation (Johnstone and Boyle, 1967; Rhode, 1971; Sellick et al., 1982; Robles et al., 1986).

In the Mössbauer technique a radioactive element, typically Cobalt-57, is deposed on the basilar membrane.Cobalt-57 decays mainly by electron capture (99.80% of the time), to the excited level (136.47 keV) of Iron-57, with a half-life of 271.81 days. The Iron-57 excited state decays in turn to the stable state of Fe-57 emitting gamma rays, with a half-life of 98.0 ns. A nucleus in the vicinity of the iron nuclei can absorb the emitted gamma radiation if it has an equivalent nuclear level, a phenomenon called nuclear resonance. If this happens, a detector of gamma rays will show a decrease in the counting rate, indicating that resonance has taken place and that the surface of interest is moving. Furthermore, if the absorber and the emitter nuclei are moving one respect to the other, the Doppler effect changes the frequency of the gamma rays, so that the direction of motion can be distinguished.

The first experiments conducted using the Mossbauer technique were performed by Johnstone and Boyle in 1967 (Johnstone and Boyle, 1967) who measured the displacement ratios of the BM to the stapes in living guinea pigs and by Rhode in 1971 (Rhode, 1971) , who measured the ratio of displacement between the BM and the malleus in

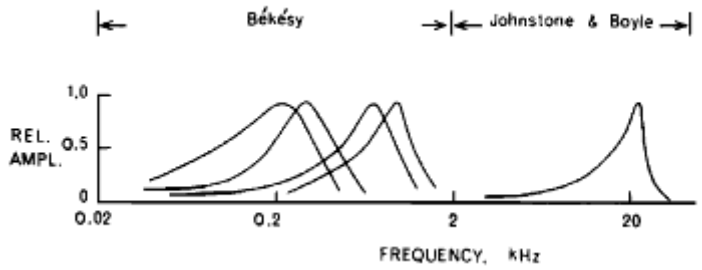

Figure 4.5: Tuning curves from Bekesy's and Johnstone experiments, enhancing the difference in the sharpness of the peaks, measured by the Q-value, and the range of frequency measurements. Reprinted with permission from (Johnstone et al., 1970). Copyright 1968, Acoustic Society of America.

squirrel monkeys. They extended the frequency range of measurements to the basal region ($3 - 25\,\text{kHz}$), measured absolute velocities, and used a wider range of stimuli ($60 - 120\,\text{dB}$) than Bekesy. In both works the frequency response curves were found to be sharper than those obtained by Bekesy: with a positive slope ($\sim 10\,\text{dB/octave}$) for frequencies below the CF and a steep negative slope ($\sim -100\,\text{dB/octave}$) for frequencies above the CF and a greater Q value ($Q \sim 2.5$ compared to $Q < 1.6$ obtained by Bekesy) (Figure Fig. 4.5). Rhode also measured the phase response, showing that it is constant for very low frequencies ($< 0.3\,\text{kHz}$), linear for intermediate frequencies (up to $5.5\,\text{kHz}$) and attains a constant value for greater frequencies Fig. 4.6. The phase results are coherent with the travelling wave theory because in the basal region the wave travels rapidly so that the phase increase is small; near the peak it changes more rapidly with distance because it slows down, and then, beyond the CF, the phase becomes flat as the wave decays. These experiments also showed that the cochlea vibrates non-linearly, that is, as the sound stimulus is increased the amplitude response does not grow linearly, especially around the characteristic frequency. Then the responses obtained by Bekesy at high stimulus intensities cannot be used to extrapolate the response at lower stimulus intensity. Subsequently, (Sellick et al., 1982) confirmed the nonlinear response and the sharp tuning of the BM in the guinea pig showing, for the first time, that the response of the basilar membrane depends on the good physiological conditions of the cochlea because the nonlinear response tends to deteriorate and becomes linear as time passes after the cochlea is opened (Fig. 4.7). Furthermore Robles, (Robles et al., 1986) measured the mechanical response at the base of the BM of the chinchilla confirming the nonlinear response, the sharp tuning and that the nonlinearity disappears after death.

The resolution of this technique is around $10\,\text{nm}$. It can measure velocities as small as $0.2\,\text{mm/sec}$ (Rhode, 1971). The disadvantages of this technique, however, are its nonlinearity, its low signal to noise ratio and the load on the basilar membrane that could alter the properties of the Organ of Corti because of the radioactivity. Furthermore, because of the probabilistic nature of the decay, the measurements require a certain amount of time in order to accumulate sufficient counts for an acceptable statistical

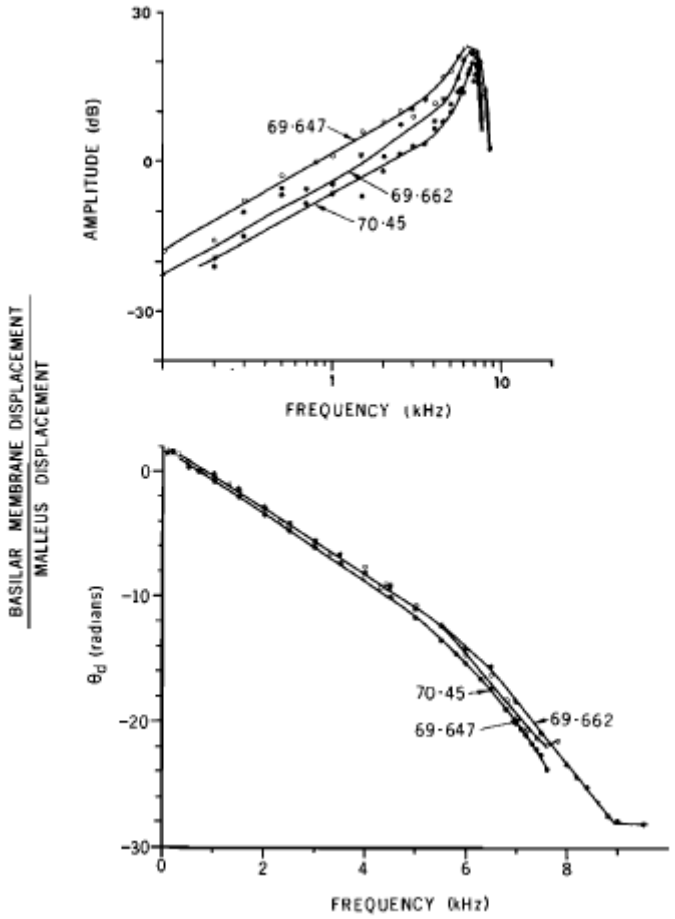

Figure 4.6: Response of the basilar membrane respect to the malleus displacements in amplitude (up) and phase (down). Reprinted with permission from (Rhode, 1971). Copyright 1968, Acoustic Society of America.

error. But because the cochlea is opened, a greater time for measurements results in the degradation of the mechanical properties of the Organ.

4.5 Long-coherence laser Interferometry

The Mössbauer technique lead to the discovery of the nonlinearity and the sharply frequency-tuned response of the basilar membrane but, because of the nonlinear transduction mechanism, the relatively long data-sampling times required by the probabilistic nature of gamma radiation and the possibility of radioactive damage, it was not an ideal technique. Laser interferometry, on the other hand, is faster, linear, not ionizing, with a greater sensitivity ($\sim$ pm), with a wide dynamic range, it is frequency independent, it retains the waveform information and has a simple calibration procedure.

It is a velocity-sensing method, in which the velocity of the BM is derived from the Doppler shift of the frequency of photons reflected from the moving target. There are two main optical arrangements that are used to measure cochlear vibrations: the homodyne and the heterodyne laser interferometer.

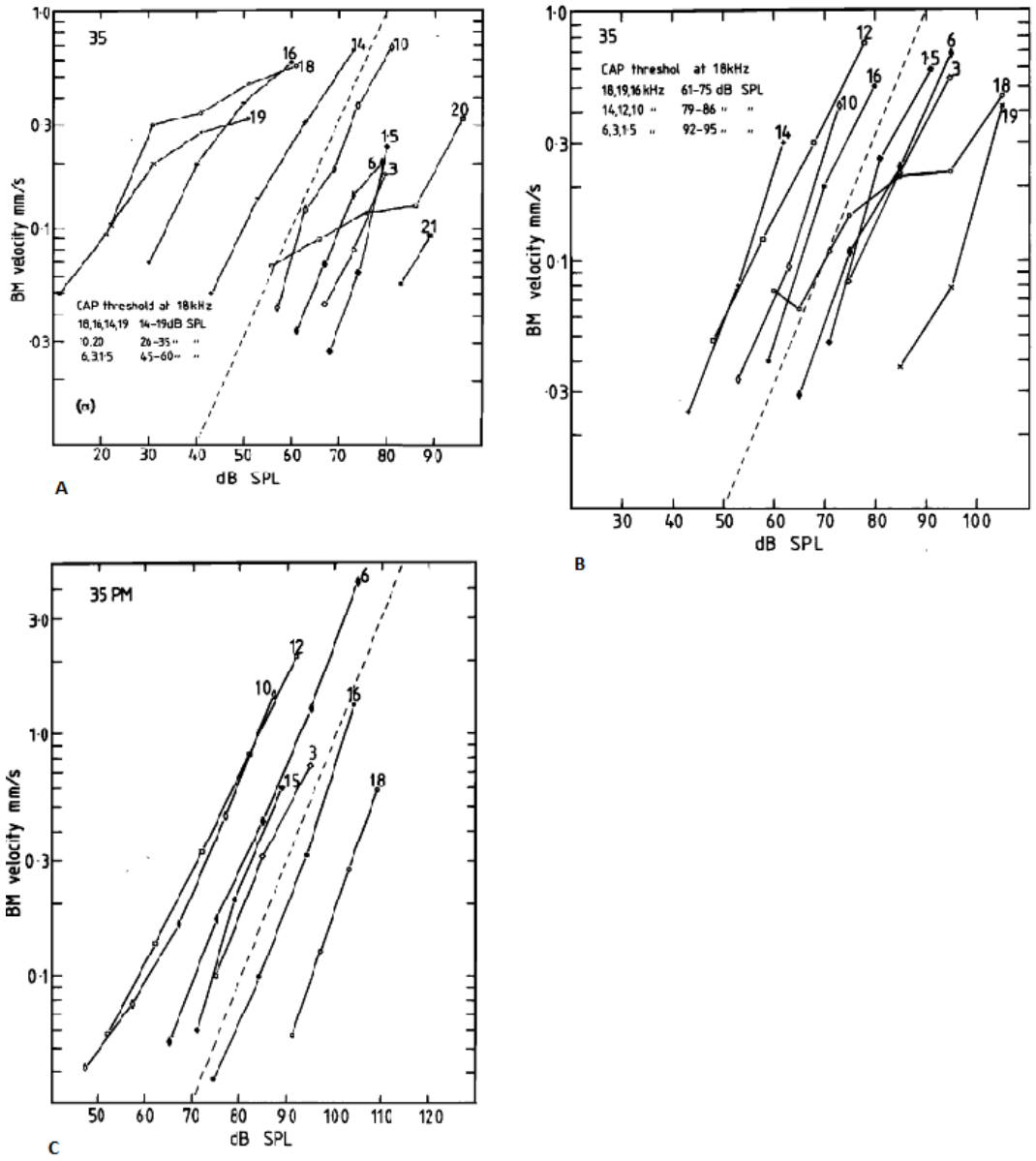

Figure 4.7: Basilar membrane velocity input-output functions for the same animal (guinea pig) at the beginning of the experiment, just after the cochlea was opened (A), after some time when the conditions of the cochlea deteriorated (B) and post mortem (C). The numbers on the curve represents the gross cochlear action potential (CAP) evoked by pure-tone bursts, used as an indication of neural threshold. The shifting from a nonlinear to a linear response is evident. Reprinted with permission from (Sellick et al., 1982). Copyright 1982, Acoustic Society of America.

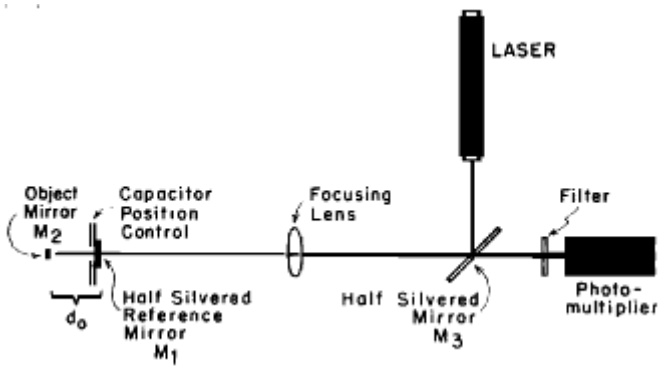

Figure 4.8: Schematic representation of the homodyne interferometer. The light source is a He-Ne laser which is focused on a mirror, M2, fixed on the basilar membrane. A half reflective mirror, M1, is positioned in front of the mirror M2 to obtain two beams and it can be moved by a capacitor in order to modify the distance between the two mirrors and regulate the interference. A photo-multiplier is used to measure the combined intensity of the light reflected from M1 and M2. Reprinted with permission from (Khanna et al., 1968). Copyright 1968, Acoustic Society of America.

4.5.1 Homodyne Interferometer

The homodyne interferometer was developed by Deferrari (Deferrari et al., 1967) and then Khanna for more than 20 years dedicated his experimental work to the adaptation of this technique to the measurement of the vibrations of the inner ear, in which case the narrow confinement of space, the limited access and the low rigidity of the skull, presented special problems that are not encountered when measuring vibrations of inanimate objects. Khanna made some innovations to facilitate the measurements in living animals and to achieve the high sensitivity necessary to measure displacements of the order of 3 pm within the cochlea. The system developed by Khanna is represented in Fig. 4.8. A mirror, M_2, is attached to the basilar membrane. Light from a helium-neon laser is focused on mirror M_2. The light falling on it is reflected back on the face of a photo-multiplier. A focusing lens is used to direct the light onto a selected spot of the photo-multiplier. A partially silvered reference mirror, M_1, is mounted in the path of the laser beam in front of mirror M_2. The position of mirror M_1 is carefully aligned with that of mirror M_2 so that their reflections coincide at the face of the photo-multiplier tube. As the structure to which mirror M_2 is attached vibrates, a time-varying interference is produced between the two beams. This, in turn, results in a time-varying output of the photo-multiplier. When the average distance between the vibrating mirror and the fixed mirror is suitably adjusted, the output waveform of the photo-multiplier is an exact replica of the amplitude of vibration of the object, as (Appendix A):

$$I_\omega = \pm B(4\pi/\lambda)cos\omega t. \tag{4.1}$$

which is valid for vibration amplitudes below $10^{-}6$ cm. The relationship is linear from 3 pm to 10 pm while is nonlinear from 10 pm to 100 pm. Because of the high sensitivity, the response of the BM can be measured in the frequency range of $20 - 20000$ Hz. In

Eq. (4.1) there is still an ambiguity of sign. To eliminate this, the reference mirror, M_1, is vibrated sinusoidally by an electrical reference signal of low amplitude and low frequency ($100Hz$). The $100Hz$ output of the interferometer is observed through a separate filter tuned to $100Hz$. Its phase is displayed on an oscilloscope. As the distance between mirrors M_1 and M_2 is adjusted to obtain maximal output, the phase of the $100Hz$ output flips through 180 deg. However, since the reference mirror is always vibrating with the same known phase, it is easy to select the output with respect to the main signal, which gives the correct phase. This is the so called quadrature condition which eliminates the phase ambiguity.

Despite these advantages, the structures of the OoC are nearly transparent so that it is still necessary to open the cochlea to place on the BM a reflective object to enhance its reflectivity. This was done by (Khanna, 1986), who described the use of tiny gold particles as reflective spots to be placed on the BM. Then he measured the vibrations of the BM (Khanna and Leonard, 1982) in responses to pure tones in the cat cochlea, showing how the sharp tuning of the BM is progressively lost as time passes and the mechanical properties of the opened cochlea deteriorates.

4.5.2 Heterodyne interferometer

All the techniques that we have described so far require opening the cochlea. In the Mössbauer method the cochlear opening is needed in order to place a radioactive source on the BM; in the capacitive probe technique the cochlea is opened to place the probe close to the BM and in the homodyne interferometer the cochlea is opened to deposit reflective beads on the BM.

Then in 1987 Khanna developed a heterodyne interferometer, through which it is possible to obtain a sensitivity of 10 pm without opening the cochlea (Khanna et al., 1987). The system is shown in Fig. 4.9. By means of two acousto-optical modulators a frequency shift $\Delta\omega$ between the optical frequencies ω_1 and ω_2, of the two interfering beams, is introduced. Due to this frequency difference, the interference between the reference beam (RB) and the object beam (OB) has an intensity modulation at the beat frequency $\Delta\omega$. This intensity modulation is detected by a photo-detector (DET in Fig. 4.9). Displacement of the surface of interest changes the optical path length and therefore the phase of the object beam. This is converted directly into a change of phase of the beat frequency. The photo-current at the detector is given by:

$$i(t) = a + bcos[\Delta\omega t + \Phi(t)], \tag{4.2}$$

where a is the direct and b the alternating amplitude of the photo-current and $\Phi(t)$ is the phase difference between the two interfering beams. When the object moves, the phase $\Phi(t)$ is a period function of the form

$$\Phi(t) = \beta ucos(\Omega t + \psi) + \Phi_c \tag{4.3}$$

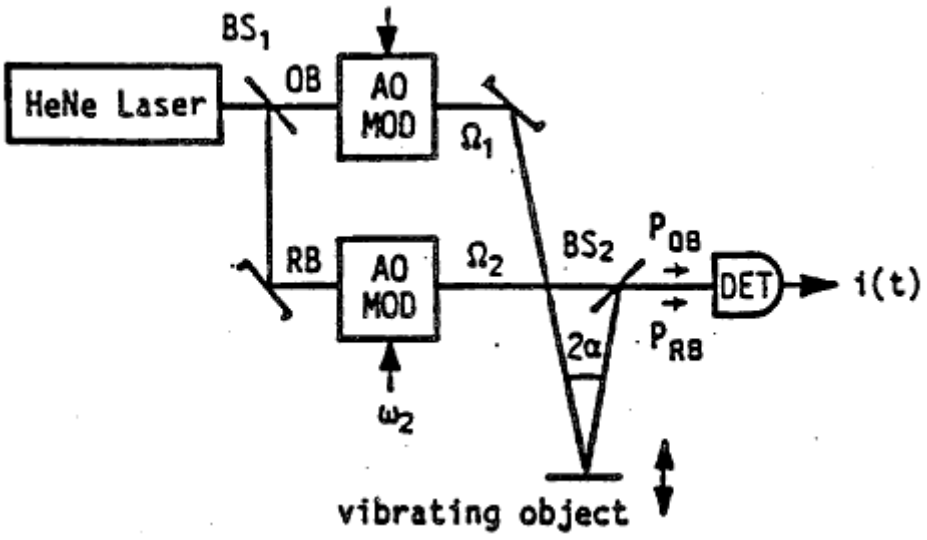

Figure 4.9: Schematic representation of the heterodyne interferometer. The light source is a He-Ne laser, which is splitted in a object (OB) and reference (RB) beam by two beam splitters. The RB is direct to the detector while the OB is directed to the vibrating object and then trough a beam splitter which combines the OB and the RB on a photo-detector (DEC). The current output is proportional to the intensity of the combined beams. Both beams are modulated in frequency by acousto-optical modulators (AO-MOD). From (Khanna et al., 1987).

where u, Ω and ψ are, respectively, the amplitude, the frequency and the phase of the vibration, Φ_c is a constant phase and β a geometrical factor. If 2α is the mutual angle between the illumination and observation directions (as shown in Fig. 4.9) and λ is the wavelength of the laser, then β is given by

$$\beta = \frac{4\pi}{\lambda} cos\alpha. \tag{4.4}$$

Combination of Eq. (4.3) and Eq. (4.4) shows that the detector output is a phase or a frequency-modulated signal with carrier frequency $\Delta\omega$ and modulation frequency Ω. The corresponding spectrum of such a signal is a discrete Bessel spectrum, centred at $\Delta\omega$. For small vibration amplitudes, this spectrum consists of three lines: the carrier and the first upper and lower side-bands. Small vibrations amplitudes are found from the power ratio of the carrier (P_0) and the first side-band (P_1) as

$$\sqrt{\frac{P_0}{P_1}} = J_0(\beta u) \sim \frac{2}{\beta u}, \tag{4.5}$$

where J_0 and J_1 are Bessel functions of integer order. The power P_0 and P_1 can be measured with a spectrum analyser.

The advantage of the heterodyne interferometer when compared to the homodyne interferometer are:

- the linearity of the heterodyne, which is not limited to small vibration amplitudes

because optical phase variations are not converted to intensity variations (according to a sine function) but to phase variations of an electrical AC signal at the beat frequency;

- the quadrature condition which has to be maintained for homodyne techniques is not necessary with heterodying, because sensitivity is independent of the phase difference between the two interfering beams;
- the interference phase, which is completely separated from the interference amplitude and from the other terms resulting from the superposition of the two beams. This means that drifts taking the interferometer away from the quadrature condition does not cause signal fading as in the homodyne interferometer. Thus, problems with the position control of the reference mirror are avoided, and the reference beam path can also be outside the system under study;
- heterodyne interferometry does not need a vibrating reference mirror for calibration because the interference phase, which is proportional to the displacement to be measured depends only on the geometry of the illumination and reflection.

Using a heterodyne interferometer, in 1997 Ruggero (Ruggero et al., 1997) confirmed and extended the results he obtained in 1986 (Robles et al., 1986) with the Mössbauer technique. He measured responses to pure tones at the basal end of the chinchilla cochlea and showed the nonlinearity of responses to CF tones respect to the variation of the stimulus intensity. These results are shown in Figs. 4.11 and 4.12. More recently, Rhode (Rhode and Recio, 2000) showed the non-linearity of the response of the basilar membrane at the most basal region of the opened cochlea of the chinchilla. The increase in amplitude around the CF due to the nonlinearity was measured to be 45 dB. Ren (Ren et al., 2011) measured the response of the BM in the basal region of the guinea pig cochlea. He obtained a peak response amplified up to 50 dB. Nilsen and Russel (Nilsen and Russell, 2000) measured the vibrations of the BM without using reflective particles in the basal turn of the guinea pig cochlea.

Some common points can be inferred from all these studies. If the response is measured at a specific frequency at various locations, at low-intensity tones the basilar membrane is characterised by a high frequency selectivity; only a small region of the basilar membrane peaks for a particular tone frequency; as the intensity of the tones increases, the frequency selectivity decreases and the membrane is excited over a broader region. If the displacement is measured at a fixed point varying the frequency, at low intensities the basilar membrane acts as a band-pass filter while for high intensities as a low pass filter, as shown in Fig. 4.10. To summarize, the results obtained with these techniques showed that the frequency selectivity of the cochlea depends on its physiological conditions and it is absent post-mortem. Then a sharply tuned component is added to a broadly tuned one in the living cochlea. This component is the result of the action of a feedback process, called cochlear amplification, that increase the amplitude of the response and its frequency selectivity.

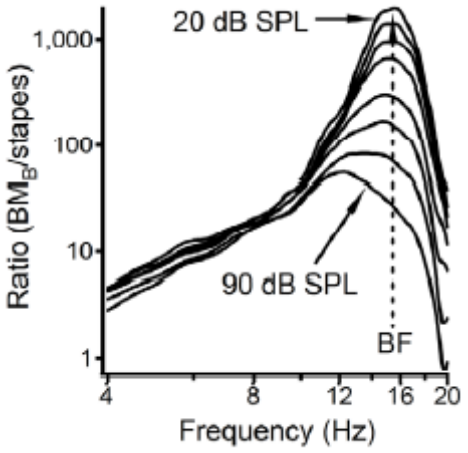

Figure 4.10: Displacement of the basilar membrane, with respect to the stapes, for different sound intensities. As the sound level increases, the peak magnitude decreases, broadens and shifts at lower frequencies. From (Ren et al., 2011), which is published in open access under a Creative Commons Attribution 4.0 International License, https://creativecommons.org/licenses/by/4.0/.

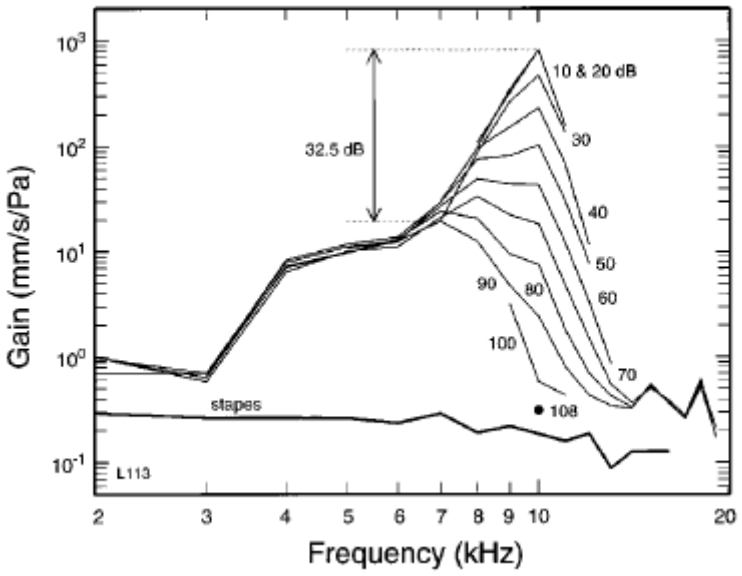

Figure 4.11: Gain of the displacement of the basilar membrane for different sound intensities. Reprinted with permission from (Ruggero et al., 1997). Copyright 1997, Acoustic Society of America.

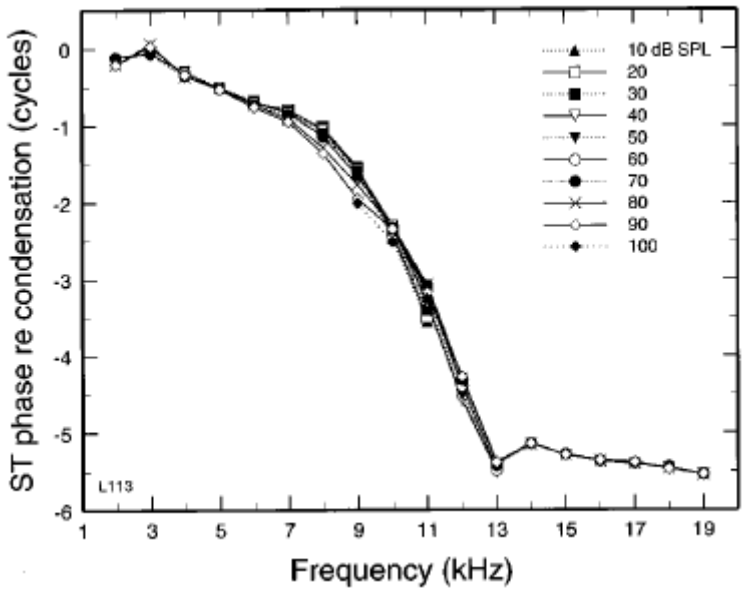

Figure 4.12: Phase of the displacement of the basilar membrane for different sound intensities. Reprinted with permission from (Ruggero et al., 1997). Copyright 1997, Acoustic Society of America.

4.6 Low-coherence interferometry

Even though the heterodyne interferometer can be used without reflective particles, the narrow bandwidth of the source (typically a He-Ne laser) imposes a long coherence length, so that it is not possible to distinguish the reflective signals of the different components of the Organ of Corti and the measurements are then limited to the BM. If a low-coherence light source is used, such as a light-emitting diode, however, the signals from the various components of the OoC (BM, RL, TM, Hensen's cells, OHCs) can be distinguished, because the coherence length sets the axial resolution to tens of μm. Furthermore, the $\sim 10\,\mu$m coherence length acts as a time gate of order of $\sim 10\,$fs that rejects scattered photons that arrive either before or after the time gate of collection, thus reducing the background noise due to multiply scattered photons. The system can also be used to acquire images of the organ of Corti using the Optical Coherence Tomography (OCT) method, assisting in the adjustment of scanning mirrors to localize the vibrating points to be measured within the OoC. Such a system can be operated both in the homodyne (Choudhury et al., 2006; Chen et al., 2011) and heterodyne (He et al., 2018) configuration.

(Chen et al., 2007) demonstrated the use of a custom-built homodyne interferometer to obtain *in vivo* measurements of the vibrations of the BM, RL and TM. The optical system is shown in Fig. 4.13. When scanned as an OCT system, an image of the organ of Corti is obtained from the photons reflected from the tissues. As the pathlength of

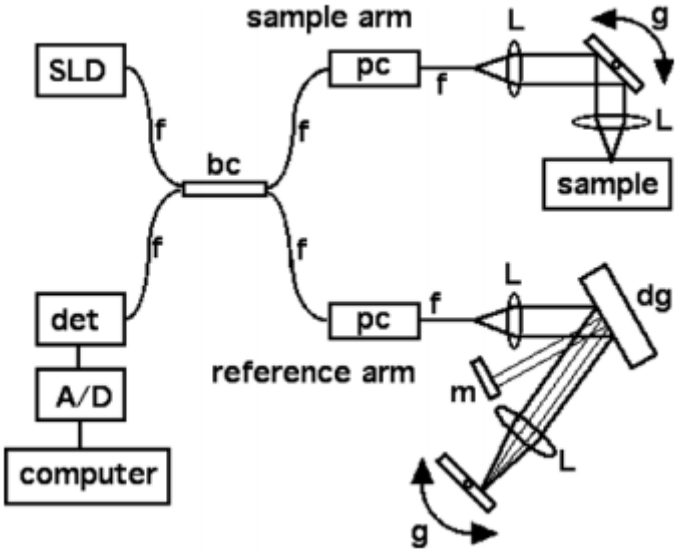

Figure 4.13: Schematic representation of a low-coherence interferometer. The source is a superluminiscent light diode (SLD). The light is transmitted through optical fibres (f) and splitted by a bridge coupler (bc) in a reference and a sample arm. The reference arm is equipped with a galvo-mirror, a mirror (m) and a diffraction grating (dg) to scan the cochlea along the axial direction. In the sample arm there is a galvo-mirror which can be rotated to select the position along the z-axis. Reprinted from (Choudhury et al., 2006). Copyright 2006, with permission from Elsevier.

the reference arm is modulated by a z-axis galvo mirror, the coherence gate of 10 μm is moved axially within the sample. A second galvo-mirror scans laterally along the x-axis. The acquired image presented the reflected intensity, $R(x, z)$, in an x-z plane as shown in Fig. 4.14 (left). While the axial (z) resolution is set by the coherence gate to 10 μm, the lateral (x) resolution is due to the numerical aperture of the optical apparatus and is usually around 20 μm. Figure 4.14 (right) shows the axial scan at one position x, $R(z)$. In this plot, the signals from the BM, the RL, the TM and the RM can be distinguished from each other and from the background as peaks with a signal-to-noise ratio that ranges from 10 to 1000, depending on the structure. From these plots, a location in the image corresponding to the position of the surface of interest can be selected so that the system, controlled by the galvo-mirrors, moves the coherence gate to the selected $x - z$ position and stop the scanning. Then the system operates as a a classical homodyne interferometer that can report the movements of the selected membranes, as the beams from the sample and reference arm are combined on the detector.

4.6.1 Recent experiments

Using an OCT-heterodyne system, He and Ren recently measured (He et al., 2018) the differential motion between the reticular lamina and the basilar membrane *in vivo* in the mouse cochlea. They found that, when excited by sound-induced stimuli, the reticular lamina vibrates with an amplitude that is at least two times greater than

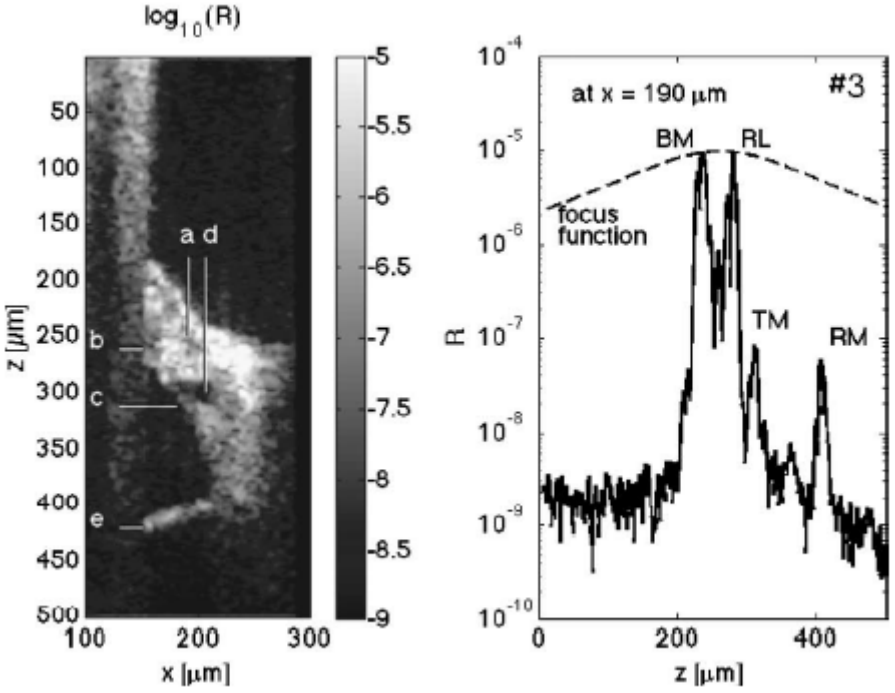

Figure 4.14: On the left, an image of the Organ of Corti, is plotted as a grey scale along the z xis. This is obtained from the values of the reflected intensity $R(x, z)$ as a function of x and z axis. On the right, an axial scan across the z axis is shown, for a specific position x, showing peaks in the reflectance that corresponds to the various structures within the OoC. From (Chen et al., 2007), which is published in open access under a Creative Commons Attribution 4.0 International License, https://creativecommons.org/licenses/by/4.0/.

that of the basilar membrane in all the range of frequencies examined ($5 - 30\,\text{kHz}$) as shown in Fig. 4.15 A, B, G. Furthermore, the two membranes vibrate in opposite directions at the base of the cochlea and in phase at the location of the characteristic frequency (Fig. 4.15 H). These data are consistent with previous experiments of the same group in mice (Ren et al., 2016a) and in gerbils (Ren et al., 2016b). They disagree with some earlier data from Chen's group (Chen et al., 2011) in guinea pigs, however, who also measured the differential motions of the RL and BM using a OCT-homodyne interferometer. While Chen et al. agree that the vibrations of the reticular lamina are two/three times greater than those of the basilar membrane at the characteristic frequency, at lower frequencies the ratio of the movements of the RL and BM are almost the same (Fig. 4.16). Furthermore, the reticular lamina leads the movements of the basilar membrane up to the characteristic frequencies, where a phase difference of 90 deg was measured (Fig. 4.17).

Because the active mechanism in the cochlea of the mouse and the gerbil are assumed to be substantially the same as that in the guinea pig, since they are mammals that belong to the same order, these differences are not expected. Our conclusion is that the discrepancy in the results between He and Ren and Chen could be due to differences in the methods used. The two groups used a different configuration of the optical

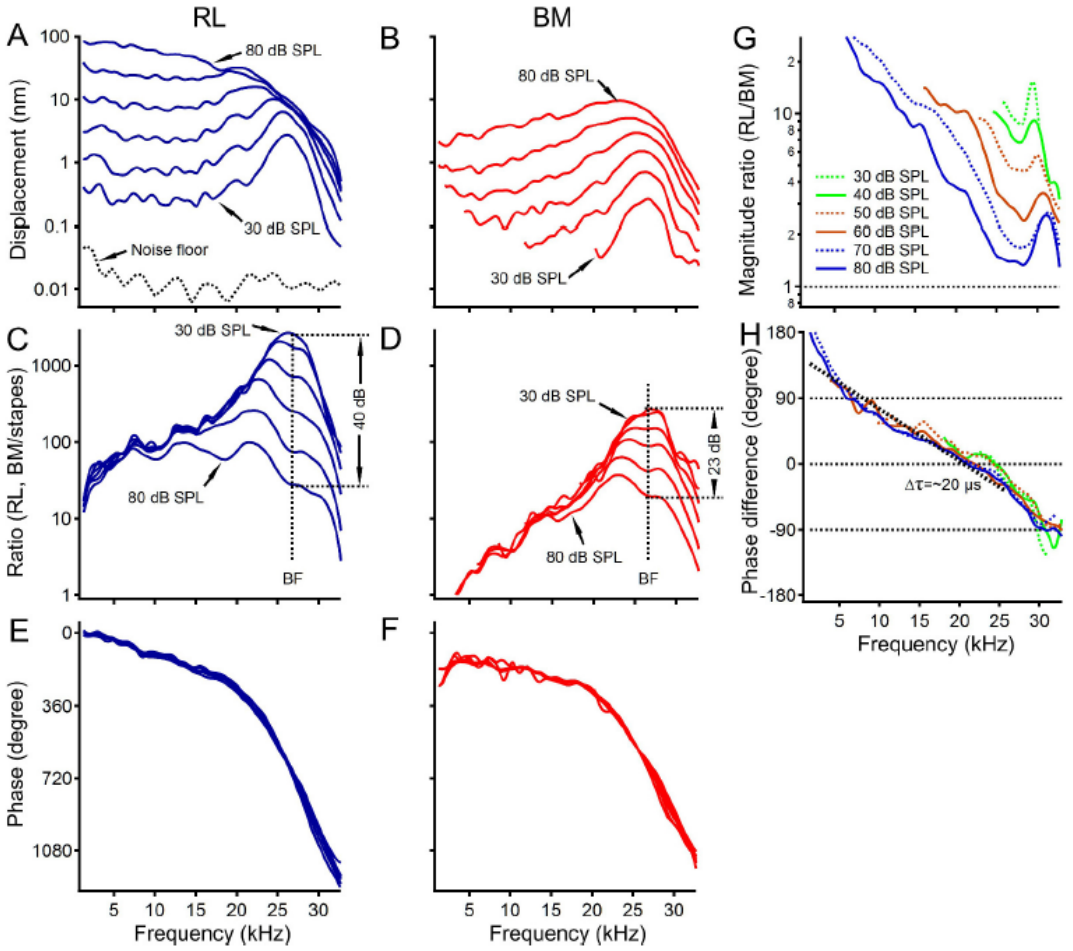

Figure 4.15: Reticular lamina (RL) and basilar membrane (BM) displacement (A,B); displacement ratios respect to the stapes (C,D); phase response (E,F); magnitude ratio (G) and phase difference (H) measured in the mouse. From (He et al., 2018), which is published in open access under a Creative Commons Attribution 4.0 International License, https://creativecommons.org/licenses/by/4.0/.

coherence tomography system: Ren and He used a heterodyne interferometer while Chen et al. a homodyne interferometer. As we explained in Section 4.5 these two systems differ in how they deal with the quadrature problem. In particular, in heterodyne interferometry the interference phase is separated from the interference amplitude while in homodyne interferometry the phase variations are converted to intensity variations, so that the homodyne interferometer is susceptible to noise that drifts the system from the quadrature condition, while the heterodyne system is not.

Another possible explanation that we think could account for the discrepancies in the results is related to the direction of the laser beam respect to the basilar membrane. In all the experiments conducted by Ren and He the laser was directed perpendicular to the BM while in Chen the angle between the beam and the BM can be inferred to be around 30°. These difference in the incident angle can in part explain the phase lag of the RL vibration, considering that the distance between the BM and RL is around

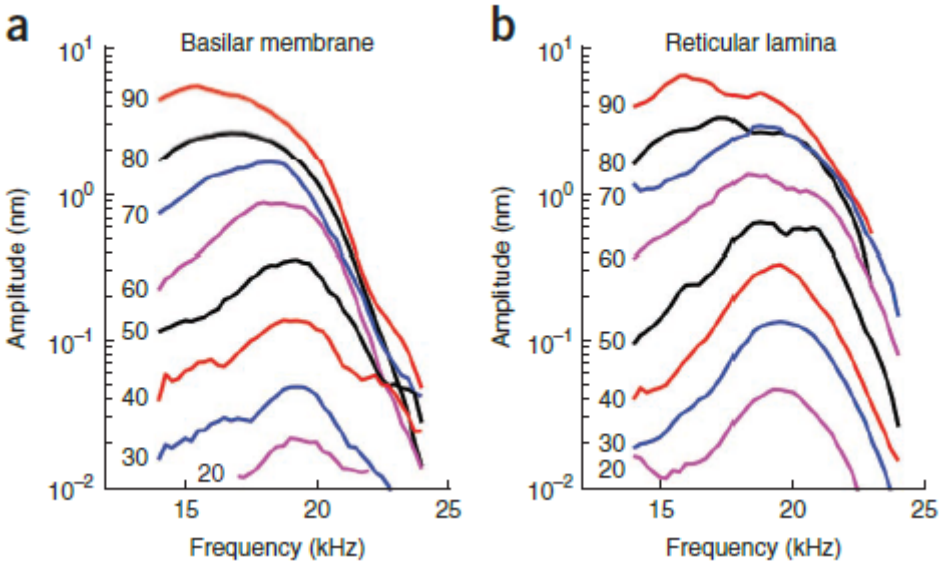

Figure 4.16: Basilar membrane (left) and reticular lamina (right) vibration amplitudes as a function of frequency for different stimulus frequency measured in the guinea pig. From (Chen et al., 2011), which is published in open access under a Creative Commons Attribution 4.0 International License, https://creativecommons.org/licenses/by/4.0/.

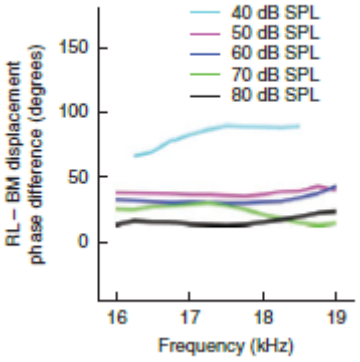

Figure 4.17: Phase difference between the RL and the BM as a function of the frequency for various sound pressure levels. From (Chen et al., 2011), which is published in open access under a Creative Commons Attribution 4.0 International License, https://creativecommons.org/licenses/by/4.0/.

$(20-40)\,\mu$m in the cochleae of the mouse (MacDonald and Rubel, 2008) and the guinea pig (Iyer et al., 2016), while the shortest wavelength of the BM's travelling wave at the characteristic position is around $200\,\mu$m Ren (2002). This explanation is strengthened by the recent OCT results obtained by the Oghalai group (Lee et al., 2016) who showed that there is a difference in the differential motion between the BM and RL if the angle between the BM and the laser beam is taken into account.

Another possible explanation of the different results could be traced to the identification of the points on the BM and RL from which the vibrations are measured. As explained in subsection Section 4.6, this can be done unambiguously by looking at the

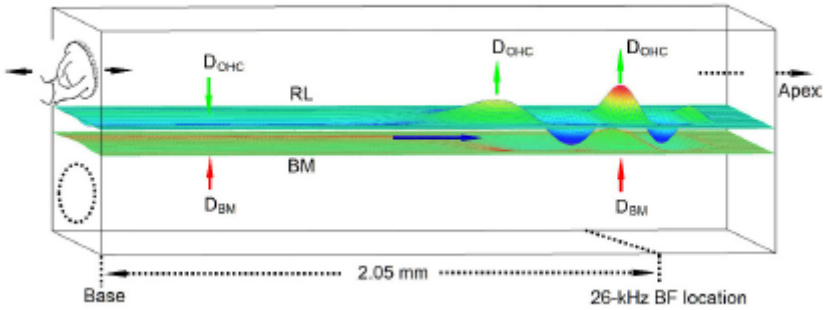

Figure 4.18: Diagrams of time waveforms of the (upper) RL and (lower) BM. From (He et al., 2018), which is published in open access under a Creative Commons Attribution 4.0 International License, https://creativecommons.org/licenses/by/4.0/.

intensity profile of the reflectance in a given longitudinal position. While in (Lee et al., 2016) and Ren (He et al., 2018) this method is used to choose the points to be measured on the BM and RL, in (Chen et al., 2011) the points are identified by looking directly at the images of the Organ obtained from the OCT scan.

Because of the different results, the two groups have suggested different explanations in terms of a possible micromechanical model of the active mechanism in the cochlea. (Chen et al., 2011) suggested that their measurements could help refine a local feedback mechanism model in which outer hair cells are thought to apply an active force directly to the membrane at its generation location. In this case, the phase leading of the reticular lamina over the basilar membrane is thought to ensure the right timing of the outer hair cells for cochlear amplification. On the other hand, (He et al., 2018) proposed a "global hydro-mechanical" model in which the outer hair cells drive the reticular lamina vibrations over a wide longitudinal range which interacts with the travelling wave of the basilar membrane through the cochlear fluid. In particular, when the basilar membrane moves upward toward the scala vestibuli near the cochlear base, (Fig. 4.18), OHCs depolarize and induce a large downward RL displacement. This movement creates a positive fluid pressure between the RL and the BM at the cochlear base. At the same time, the RL at more apical locations moves upward, resulting in a negative fluid pressure inside the cochlea partition. The resulting pressure gradient pumps fluids longitudinally along the OoC, enhancing the travelling wave on the BM as it propagates apically. In phase vibrations at the CF results in constructive interference which further amplify the RL vibrations. A recent experiment by the Oghalai group (Dewey et al., 2019) tested the global hydro-mechanical model proposed by He and Ren mapping the regions of the BM and RL where the amplification of the response forces accumulates. They studied the response of the apical region of the living cochlea of adult mice using a custom-built low-coherence interferometer. The points of interest on the BM and the RL were selected looking at the peaks in the reflectivity versus depth obtained from OCT images. The angle between the laser and the BM was between $60 - 75$ deg. The axial resolution was 9.8 μm and the lateral resolution 11.4 μm. The measurements from the RL then

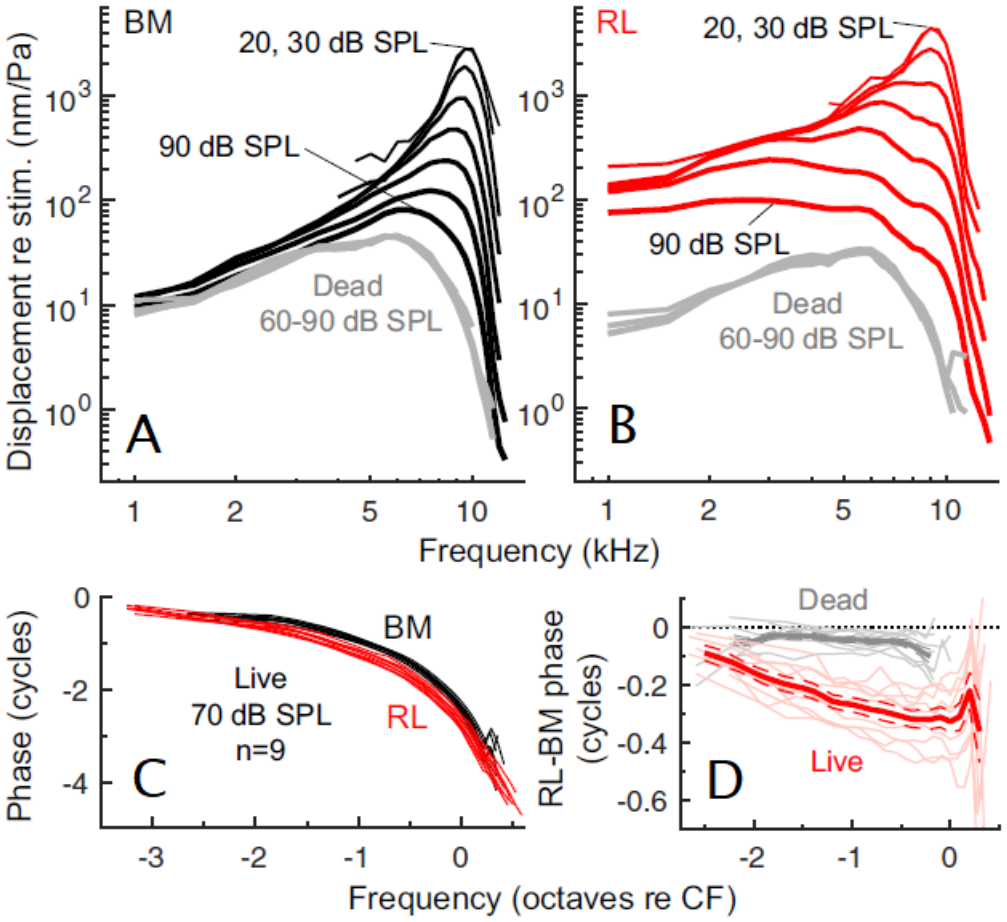

Figure 4.19: Displacement of the BM (A) and RL (B) normalised to the evoking stimulus pressure in Pa, as a function of the frequency, before and after death. BM and RL phase response (C). Phase difference between the RL and the BM before and after death (D). Adapted from (Dewey et al., 2019), which is published in open access under a Creative Commons Attribution 4.0 International License, https://creativecommons.org/licenses/by/4.0/.

actually are a combined motion of the RL and the upper half of the OHC, over the width of one or two OHCs, considering that the OHCs in the apical part of the mouse cochlea are $5-7\,\mu$m in diameter and are spaced $8\,\mu$m apart. First Oghalai et al studied the response of the BM and RL to single tones, reporting the amplitude and phase versus the frequency of excitation (Fig. 4.19). RL responses are generally larger and grew more compressively than the BM responses, particularly at low frequencies (Fig. 4.19 A,B), in accordance to the results of He and Ren but in disagreement with Chen results on the gerbil cochlea, where the responses of RL and BM tends to converge at lower frequencies. About the phase responses, the BM and RL moves in phase at low frequencies; then RL progressively lags BM as the stimulus is increased, up to 120 deg (Figure 4.19 C,D), which is opposite to the phase response observed by He and Ren. After death, the response of the BM and RL becomes linear and the low frequency response of the RL is greatly attenuated; the phase difference also disappears after death. As before, the difference in the phase response between various groups could be attributed to different measurement location and differences in measurement angles.

Dewey et al. then used a second tone to suppress the BM and RL response to the primary tone. Suppression occurs when the response to one tone saturates OHCs mechanotranductor currents, limiting OHC force generation. Varying the suppressor tone frequency, they mapped the regions of the BM and RL where accumulation occurs. It was already believed that the BM travelling-wave is amplified near the CF region. On the other hand, the behaviour of the RL was not clear, especially after He and Ren experiments. Oghalai found out that:

- if the frequency of the suppressor tone is more than an octave above the CF, the suppression is low ($< 1dB$) for both the BM or RL. This means that the amplification of the travelling wave peak does not depend on forces generated by OHCs from far basal regions;
- If the frequency of the suppressor tone is slightly above the first tone, then the response is reduce (up to 30 dB for frequencies with a difference of only 0.1 kHz from the CF), in accordance to the theory that the built up of the amplification occurs just basal to the CF site;

These results shows that even if OHCs forces amplify the motion of the RL along the length of the travelling wave, the amplification accumulates only near the peak of the wave, in the same region where the BM motion is amplified. These results thus contradict the global hydro-dynamical model proposed by He and Ren.

The conclusions drawn by Dewey et al. are in agreement with a previous experiment by (Dong and Olson, 2013). They simultaneously measured the amplitude and the phase of the voltage and the pressure close to the BM at the same position, when the cochlea is excited by pure tones. From the pressure measurements it is possible to derive the BM motion, X_{BM}, while the voltage can be related directly to that of the OHCs, V_{OHC}. Dong et al found that the amplitudes of X_{BM} and V_{OHC} are tuned at about 24 kHz and are nonlinear with increasing SPL. The corresponding phases vary rapidly around the best frequency with a similar phase accumulation. However, the voltage phase exhibits a phase shift just before the CF. Then, at lower frequencies, the voltage is in phase with the displacement, in agreement with a model by (Davis, 1965), in which upward displacement of the BM pivots the hair bundles of the OHCs towards taller stereocilia, leading to channel opening, to OHC depolarization and thus to a positive voltage in the scala timpani. At about 0.7× CF and up to the characteristic frequency, the voltage leads the BM displacement by about a quarter of a cycle, thus being in phase with BM velocity. In this case, the voltage drop across the OHC leads to the contraction of the OHC and to the production of a somatic force. Because this force is in phase with the BM velocity, power is transferred to the travelling wave and the motion is amplified. Thus, as in (Dewey et al., 2019), there is a frequency region just before the peak in which, because of the phase relationship between the OHC voltage and the BM velocity, power is supplied to the travelling wave, resulting in the amplification of the response of the BM in the CF region.

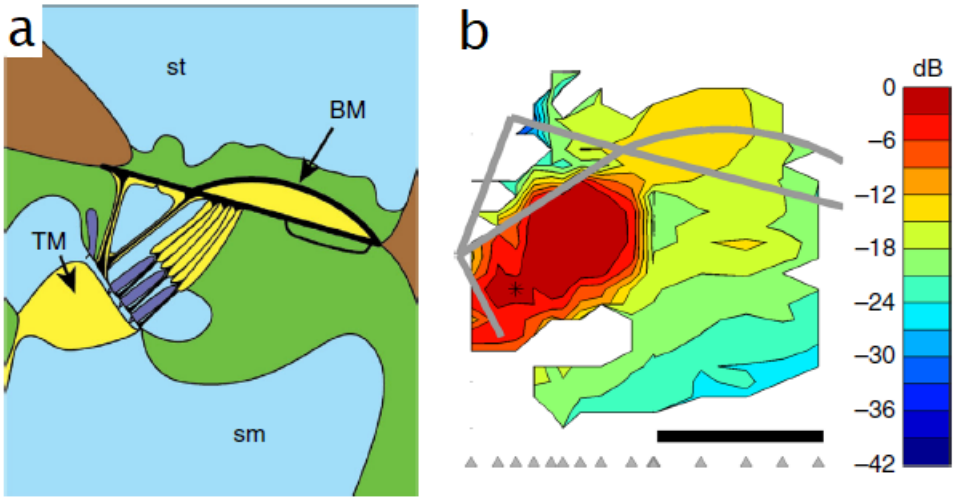

Figure 4.20: Underlying anatomical structure (A) and map of longitudinal vibration magnitudes (B), in the $x - y$ plane, evoked by a 22.6 kHz component of a multi-tone stimulus at 40 dBSPL. Magnitudes are expressed in decibels relative to the $3 unit mm$ maximum observed at the location marked with an asterisk. It is evident that the largest vibrations occur in a well-delimited area that extends from the base of the OHCs to the apexes of the Deiters' cells and, width-wise, from the outer pillar cells to the outer tunnel of Corti. This is the area called hotspot region. From (Cooper et al., 2018), which is published in open access under a Creative Commons Attribution 4.0 International License, https://creativecommons.org/licenses/by/4.0/.

Finally, another recent experiment conducted by Cooper et al. (Cooper et al., 2018) reported simultaneous measurements of the whole Organ of Corti, through the round window of the basal region of the living gerbil cochlea, using an OCT-low-coherence interferometer. Their results agree with those obtained by He and Ren and Oghalai in that the reticular lamina responses are greater, more broadly tuned and non-linear in a wider frequency region than those of the BM. However, Cooper et al. showed that this characteristics are not confined to the reticular lamina but the longitudinal vibration of the whole region between the BM and RL has a greater magnitude and a different phase to the BM. In particular, the largest vibrations occur between the interface of the Deiter's and outer hair cells, which they called the "hotspot" region (Fig. 4.20). These vibrations are less sharply tuned than that of the basilar membrane but more non-linear and exhibit a compression which is greater than that observed in the RL near the CF. Because the BM motion has been observed to be smaller than that of the hotspot and there is also a large phase difference, with the RL leading the BM by about 0.25 cycles, these authors disagree with the local-feedback loop hypothesis. They suggested that, because of the geometrical structure of the OHCs and the Deiters cells, which are inclined with respect to the BM and RL, and because these cells are suspended between the BM and RL, (Fig. 4.21), a large contribution to the amplification of the BM involves a longitudinal motion of the OH-Deiter's cells structure. In order to better understand this idea, it would be necessary to build a model that studies the contribution of the longitudinal coupling to the amplification of the vibrations of the BM and RL in the transverse direction.

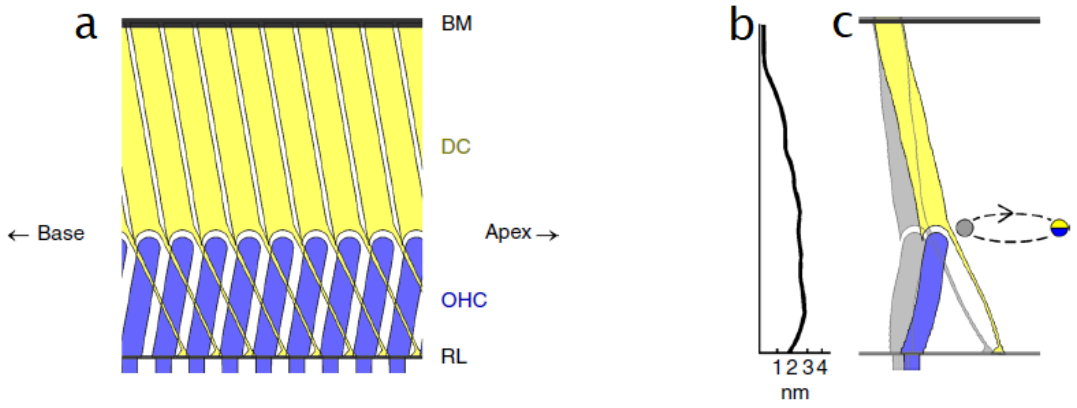

Figure 4.21: Schematised anatomical relationship between the BM, RL, OHC (in blue) and Deiter's cells (in yellow) (A). Proposed longitudinal motion of the Deiter's and outer hair cells (B) to explain the measured vibration amplitude along the transverse direction (B). From (Cooper et al., 2018), which is published in open access under a Creative Commons Attribution 4.0 International License, https://creativecommons.org/licenses/by/4.0/.

4.7 Conclusions

In summary, even though low-coherence interferometry is a powerful method to study the movements within the Organ of Corti with high spatial and temporal resolution, the data obtained from different authors has led them to different conclusions. This is probably due to the fact that even if the data are precise, they are not simple to interpret. We suggest that the discrepancies in the results could be explained in three ways. First, He and Ren and Chen used two different configurations of the optical coherence tomography systems and we showed that the system used by Chen is more susceptible to noise. Secondly, the direction of the laser beam with respect to the basilar membrane is different in various experiments and thus, because of the geometrical structure of the Organ of Corti, this could lead to a difference in the measured phase up to 30 deg. Finally, different groups used different methods to identify the locations of the BM and the RL, which could also contribute to the discrepancy in the phase response.

Nonetheless, all these experiments underlie the importance to understand what exactly is the contribution of the various components of the OoC to the amplification of the BM's motion, both in the transverse and longitudinal direction.

To gain further insight in the active mechanism of the cochlea, an elemental formulation of a detailed Finite Element Model by (Sasmal and Grosh, 2019) is developed in the next two chapters. This is initially carried out for a locally reacting model, to develop the formulation, and is then extended to include different forms of longitudinal coupling in the OoC.

Chapter 5

Elemental formulation of a finite element model of the active cochlea

5.1 Introduction

This chapter develops the formulation of an elemental model for cochlear micromechanics, with a locally reacting basilar membrane, to include an active organ of Corti. One of the aims of developing such a model is to understand the importance of longitudinal coupling and so help to resolve the differences between the explanations that have been put forward for various experimental observations. The details of the longitudinal coupling are postponed until Chapter 6, and this chapter will focus on the case with a locally reacting Organ of Corti.

In Chapter 4 we reviewed recent experimental results, regarding the relative motion of the various tissues and membranes within the Organ of Corti. The data has suggested two possible mechanisms as an explanation of the active amplification of the response observed in the living cochlea. One possibility, put forward by (Chen et al., 2011), is that the outer hair cells act as a local feedback system that applies an active force directly to the basilar membrane at its generation location, while the phase of the reticular lamina ensures the right timing of the OHCs to correctly enhance the BM motion around the characteristic frequency. An alternative mechanism has been proposed by (He et al., 2018), whose experimental results underline the importance of the longitudinal coupling. Furthermore, an experiment by (Cooper et al., 2018), demonstrate that the longitudinal vibrations in the whole region between the RL and the BM, including the OHCs and Deiter's cells, are involved in the amplification of the BM response.

To test these hypotheses, we extend the elemental method of the cochlea, as reviewed in (Elliott and Ni, 2018), to include a micromechanical model of the Organ of Corti as described in the Finite Element model developed by (Sasmal and Grosh, 2019). This Finite Element Model includes mechanical longitudinal coupling in the TM and the BM,

and a cable model for the mechano-eletrical transduction of the OHCs that includes electrical longitudinal coupling along the scalae. By developing an equivalent elemental model of the finite element model by Sasmal and Grosh, we aim to obtain a more transparent model that has a lower computational cost and also to gain further insight in the active mechanism, by studying the variation of the BM admittance and the wavenumber for various types of longitudinal coupling in the Organ of Corti.

In this chapter, we briefly review the elemental and the finite element model. Then we show how it is possible to include a locally reacting model of the Organ of Corti in the elemental model. In Chapter 6 the elemental model is extended to include the effects of the longitudinal coupling by the TM, the BM and the electrical cables.

5.2 Elemental model

In the elemental analysis, described by (Elliott and Ni, 2018) for example, the cochlea is divided into a finite number of elements, N, and the individual physical processes involved in the motion of the fluid and the dynamics of the Organ of Corti are individually characterised and then combined to give a coupled model of the system. Although a Finite Element Model of the cochlea could be characterised as being "elemental", in the sense that the continuous-domain physical processes are made spatially discrete, the number of state variables in such a model is large, typically 4000, and it is difficult to understand the interaction between the components. By combining all the mechanics of the organ of Corti into a single response, there is only a single interaction between this and the fluid dynamics, allowing those two components of the coupled response to be considered individually. This provides a greater degree of intuition about the behaviour of these two components and hence the overall response. The model of the organ of Corti is assumed to be linear, or at least quasi-linear (Kanis and de Boer, 1993), so that superposition holds and linear algebra can be used.

The cochlea is modelled as an uncoiled system with two fluid-chambers, divided by the BM, as shown in Fig. 5.1. The boundaries of these chambers are considered to be rigid and to communicate to the external environment only through the membranes at the round and oval windows, at the base of the cochlea. Furthermore, the two fluid-chambers communicate at the apex through the helicotrema, where the pressure difference between the two fluids is assumed to be zero. The BM motion in the radial direction is represented by a single transverse mode, $\psi(y)$. This is justified by the fact that the fluid coupling is relatively insensitive to the exact form of the radial BM velocity distribution (Ni and Elliott, 2013). Then, the complex velocity of the BM in the longitudinal and transverse direction, $v(x, y)$, at a given frequency, can be represented by a single longitudinal variable, $v(x)$, and is given by

$$v(x) = \frac{1}{W} \int_0^W \psi(y) v(x, y) \, \mathrm{d}y, \tag{5.1}$$

where the mode shape $\psi(y)$ is normalised to 1 with respect to the width, W, of the BM. In a similar way, the longitudinal distribution of the complex pressure difference at this frequency, acting on the BM is defined as

$$p(x) = \frac{1}{W}\int_0^W [p_1(x,y,0) - p_2(x,y,0)]\,\mathrm{d}y, \tag{5.2}$$

where $p_1(x,y,z)$ and $p_2(x,y,z)$ are the three-dimensional pressure distributions in the upper and lower fluid chambers. By dividing the cochlea into N sections, the continuous distributions of BM velocity $v(x)$ and pressure $p(x)$ can be represented by two vectors:

$$\mathbf{p} = [p(1), p(2), ..., p(N)]^T, \tag{5.3a}$$

$$\mathbf{v} = [v(1), v(2), ..., v(N)]^T, \tag{5.3b}$$

which are coupled because of the fluid in the chambers and because of the micromechanical response of the BM. The first and last element are used to represent, respectively, the boundary conditions at the stapes and at the helicotrema. The number of elements N should be such that their length is at least six times greater than the shortest wavelength (Elliott and Ni, 2018). The fluid coupling in the chambers is then described by the matrix equation:

$$\mathbf{p} = \mathbf{Z}_{fc}\mathbf{v}, \tag{5.4}$$

where $\mathbf{Z_{fc}}$ is the fluid coupling matrix. The micromechanical response of the BM is given by

$$\mathbf{v} = \mathbf{v}_s - \mathbf{Y}_{bm}\mathbf{p}, \tag{5.5}$$

where $\mathbf{v}_s$ is the excitation vector due to the stapes, whose motion drives the system and $\mathbf{Y}_{bm}$ is the BM admittance matrix. The first element of $\mathbf{v}_s$ is equal to the stapes velocity, while the remaining elements could represent external velocity excitations of the elements along the BM, but these are considered to be zero here. By combining Eqs. (5.4) and (5.5), and assuming that the matrix $[\mathbf{I} + \mathbf{Y}_{bm}\mathbf{Z}_{fc}]$ is not singular, an

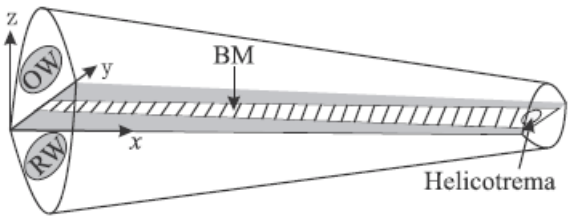

Figure 5.1: Elemental model of the cochlea, with two fluid chambers and the basilar membrane, BM. The oval window driven by the stapes of the middle ear is denoted by OW and the round window as RW, which acts as a pressure release boundary condition. x, y and z are, respectively, the longitudinal, radial and transverse coordinates, with their origin on the BM, at the base of the cochlea. From (Elliott and Ni, 2018), which is published in open access under a Creative Commons Attribution 4.0 International License, https://creativecommons.org/licenses/by/4.0/.

explicit expression for the vector of complex velocities of the BM as a function of the BM admittance matrix, the fluid coupling impedance matrix and the excitation vector is obtained:

$$\mathbf{v} = [\mathbf{I} + \mathbf{Y}_{bm}\mathbf{Z}_{fc}]^{-1}\mathbf{v}_s. \tag{5.6}$$

Substituting Eq. (5.6) into Eq. (5.4) we also obtain an expression for the vector of pressures along the cochlea:

$$\mathbf{p} = [\mathbf{Z}_{fc}^{-1} + \mathbf{Y}_{bm}]^{-1}\mathbf{v}_s. \tag{5.7}$$

These two last equations can be written in matrix form as:

$$\begin{bmatrix} \mathbf{Z}_{fc}^{-1} & \mathbf{1} \\ \mathbf{1} & \mathbf{Y}_{bm}^{-1} \end{bmatrix} \begin{bmatrix} \mathbf{p} \\ \mathbf{v} \end{bmatrix} = \begin{bmatrix} -\mathbf{v_s} \\ \mathbf{0} \end{bmatrix}, \tag{5.8}$$

which can be solved to give the pressure and velocity distributions for a given excitation, $\mathbf{v_s}$, of the system.

All of the physical processes involved in the motion of the fluid in the two chambers are thus reduced to a single fluid matrix, $\mathbf{Z_{fc}}$, and all the physical processes within the Organ of Corti and at the BM are reduced to a single admittance matrix, $\mathbf{Y_{BM}}$, where both matrices have complex elements which depend on the excitation frequency.

5.2.1 Fluid dynamics

The elemental model can be formulated to describe 1D or 3D fluid coupling problems, for fluid-chambers with either constant and non-constant cross-sectional area (Elliott et al., 2011; Ni and Elliott, 2015) . The 1D model is valid under the condition that the shortest wavelength of the slow wave in the cochlea is greater than the cross-sectional dimensions of the fluid chamber. This condition is satisfied for a passive model of the cochlea; however, when the cochlea is active, the shortest wavelength becomes smaller, especially around the characteristic place, where the wavelength of the BM motion becomes comparable with the chamber height. In this case a 3D formulation of the fluid coupling is necessary.

5.2.1.1 1D fluid coupling

In the 1D fluid coupling model, the pressure in each fluid chamber is assumed to be uniform over each cross-section. Then the wave equation for the pressure depends only on the longitudinal coordinate x. This is obtained by combining the laws of conservation of mass and of momentum to an elemental volume of the fluid, as reviewed in Chapter 3 which, in the incompressible and inviscid case gives:

$$\frac{\partial^2 p}{\partial x^2} = \frac{-2i\omega\rho v(x)}{h}, \tag{5.9}$$

which relates the complex pressure difference across the BM, $p(x)$, to the complex BM velocity distribution, $v(x)$. Both of these variables are assumed to have a time dependence described by $\exp(i\omega t)$, under the hypothesis of an excitation of the cochlea at a single frequency. The cross-sectional area of each chamber is initially assumed to be constant along x, with an effective height, h, given by $\pi A/(8B)$ (Elliott et al., 2011), where A is the area of each chamber and B is the width of the BM; ρ is the density of the fluid.

Assuming that the wavelength of the slow wave is small compared with the length of the elements, the second partial derivative of Eq. (5.9) can be approximated using the finite difference approach as:

$$\frac{\partial^2 p}{\partial x^2} \sim \frac{p_{n-1} - 2p_n + p_{n+1}}{\Delta^2} \tag{5.10}$$

where p_n denotes the elemental pressure at position x and $p_{n\pm1}$ denotes that at $x \pm \Delta$, where Δ is the length of an element in Fig. 5.1, equal to L/N. A matrix equation for all the elements can then be constructed using Eq. (5.9) as:

$$i\omega \begin{bmatrix} v_s \\ v_2 \\ . \\ . \\ . \\ v_{N-1} \\ v_N \end{bmatrix} = \frac{h}{-2\rho\Delta^2} \begin{bmatrix} -\frac{\Delta}{h} & +\frac{\Delta}{h} & & & & & \\ 1 & -2 & 1 & & & & \\ 0 & 1 & -2 & 1 & & & \\ & & & . & & & \\ & & & . & & & \\ & & & . & & & \\ & & & 1 & -2 & 1 & \\ & & & 0 & 0 & \frac{\Delta^2}{h^2} & \end{bmatrix} \begin{bmatrix} p_1 \\ p_2 \\ . \\ . \\ . \\ p_{N-1} \\ p_N \end{bmatrix}. \tag{5.11}$$

where $v_1 = v_s$ which is the velocity due to the motion of the stapes. The first row of the matrix on the right hand side takes into account the boundary condition at the base of the cochlea:

$$-2i\omega\rho v_s = \frac{\partial p}{\partial x}|_{x=0} \sim \frac{p_2 - p_1}{\Delta}. \tag{5.12}$$

The last row of the matrix represents the boundary condition at the helicotrema, where the pressure difference across the BM is assumed to be zero:

$$p_N = 0. \tag{5.13}$$

Equation (5.11) can be written in compact form as

$$i\omega(\mathbf{v}) = \mathbf{F}\mathbf{p} \tag{5.14}$$

where $\mathbf{v}$ and $\mathbf{p}$ are the vectors defined in Eq. (5.3) and $\mathbf{F}$ is the matrix of finite difference terms in Eq. (5.11). Assuming that this matrix is not singular, it can be inverted to obtain:

$$\mathbf{p} = i\omega\mathbf{F}^{-1}(\mathbf{v}). \tag{5.15}$$

By comparison with Eq. (5.4) it can be seen that the fluid coupling matrix for the 1D case is given by:

$$\mathbf{Z}_{fc}^{1D} = i\omega\mathbf{F}^{-1}. \tag{5.16}$$

5.2.1.2 3D fluid dynamics

To understand how the fluid-coupling matrix in Equation (5.4) can be represented in the case of 3D fluid coupling, it is important to notice the physical significance of the columns of the matrix $\mathbf{Z_{fc}}$: they give the pressure distribution along the cochlea due to the vibration of a single element of the BM, with all the other elements being fixed. In 1D fluid coupling, $\mathbf{Z_{fc}}$ is given by Eq. (5.16). When 3D fluid coupling is considered, there are significant variations of the pressure close to the BM both along the length of the cochlea and along the cross-section of the fluid chambers. The resulting additional contribution to the pressure is called the near-field component. While the 1D fluid coupling component determines the propagation of the main travelling wave along the cochlea, the near-field component is associated with the evanescent, higher order, modes in the fluid chambers (Elliott et al., 2011). The near-field component does not generally extend to the boundaries of the fluid-chambers so that it does not depend significantly on the cross-sectional shape of the fluid-chambers (Ni and Elliott, 2015). On the other hand, the near-field component depends on the width and the position of the BM across the cochlear partition (Elliott et al., 2011). The longitudinal distribution of the near-field pressure due to the vibration of a single element can be approximated by a decaying exponential function (Ni and Elliott, 2015),

$$p_{NF}(x) = i\omega\rho v_0\Delta\frac{8(a-b)B}{\pi^2\sqrt{b}W}\mathrm{e}^{|x-x_0|/(\sqrt{b}W)}, \tag{5.17}$$

where x_0 is the position of the vibrating element; a and b are fitting coefficients; B and W are the width of the BM and the fluid chambers, respectively; and Δ is the length of a single element. The fluid coupling impedance in the case of 3D fluid coupling, $\mathbf{Z_{fc}}^{3D}$, can be calculated by adding the discrete form of Eq. (5.17) to the columns of the fluid coupling matrix calculated assuming 1D fluid coupling, $\mathbf{Z_{fc}}^{1D}$, given by Eq.(5.16), so that:

$$\mathbf{Z}_{fc}^{3D} = \mathbf{Z}_{fc}^{1D} + \mathbf{Z}_{fc}^{NF}, \tag{5.18}$$

where the n^{th} column of $\mathbf{Z}_{fc}^{NF}$ is given by

$$Z_{fc}^{NF}(n) = i\omega\rho\Delta\frac{8(a-b)B}{\pi^2\sqrt{(b)}W}\mathrm{e}^{|n-n_0|\Delta/(\sqrt{b}W)}. \tag{5.19}$$

5.2.1.3 Spatial representation of the fluid coupling

The simple formulation for 1D fluid coupling in Eq. (5.14), and for the additional near-field fluid coupling in Eq. (5.17), allows the easy calculation of the pressure distribution due to the motion of one element in the cochlea, with all the other elements remaining

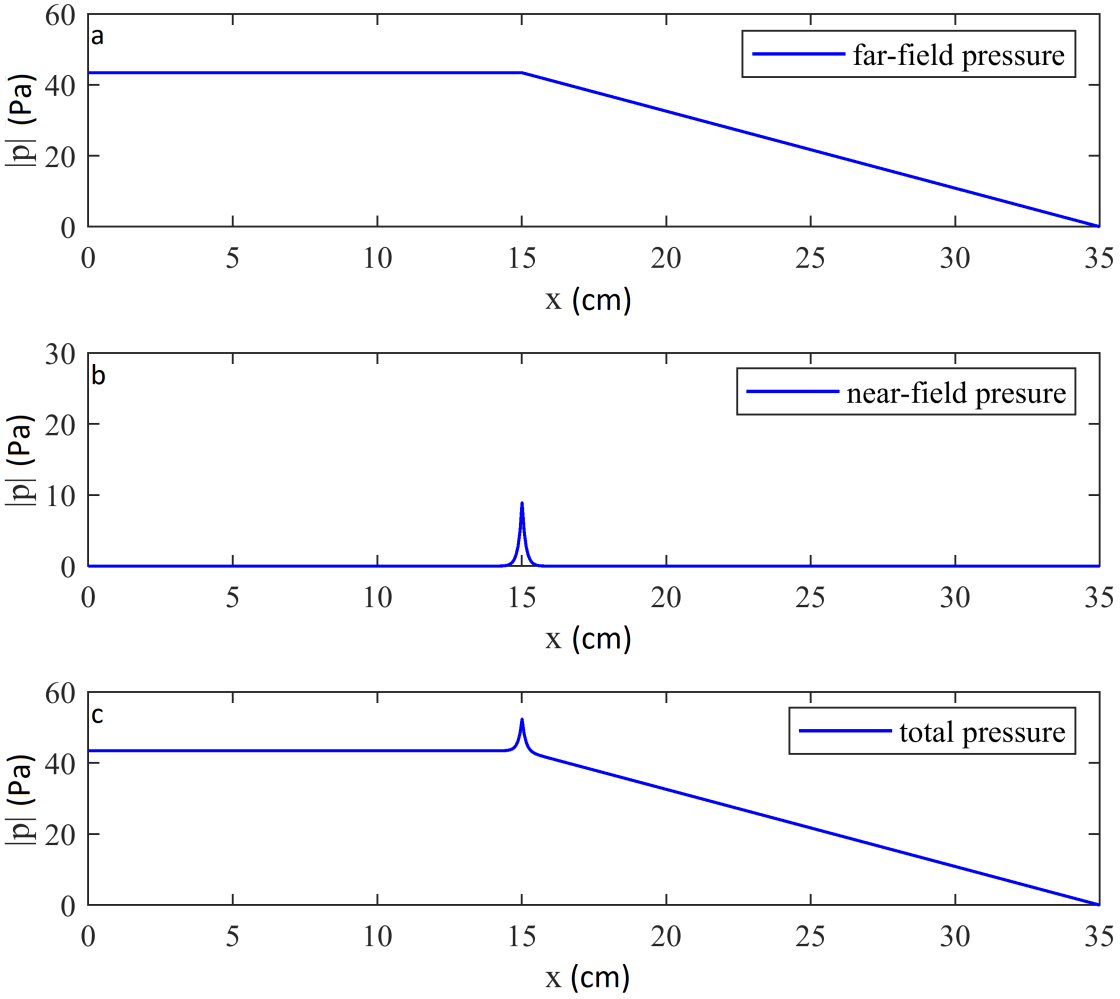

Figure 5.2: Pressure distribution along the length of the uniform cochlea, due to the motion of a single element at $x = 15\,\text{mm}$ with a velocity of $10\,\text{mms}^{-1}$ at a frequency of 1 kHz, showing the far-field pressure distribution due to (a) 1D fluid coupling, (b) the near-field pressure distribution due to 3D fluid coupling and (c) the total pressure distribution due to 3D fluid coupling, which is the sum of (a) and (b).

rigid. This pressure distribution is plotted in Fig. 5.2 for a single moving element at $x = 15\,\text{mm}$ for (a) the 1D fluid coupling model, (b) the 3D near-field component and (c) the total pressure due to 3D fluid coupling. In this example, W and H are assumed to be 1 mm, B to be 0.3 mm and the fitting parameters a and b in Eq. (5.17) to be 1 and 0.0140 (Ni and Elliott, 2015). Pressure distributions like this make up the columns of the matrix $\mathbf{Z}_{\mathbf{fc}}^{\mathbf{3D}}$.

In contrast, fluid coupling in the Finite Element Model, as described by (Ramamoorthy et al., 2007) for example, is modelled as the sum of a certain number of radial acoustic modes. The coupled response with a different number of these acoustic modes is plotted in Fig.18 of (Ramamoorthy et al., 2007). This shows that the peak BM displacement is significantly higher if 5 acoustic modes are used, instead of the 3 modes assumed in the calculation for the other plots in this paper, suggesting incomplete convergence of the series of acoustic modes used to calculate the pressure.

The elemental formulation provides some insight into the coupled response of the cochlea by allowing the physical nature of the fluid coupling, discussed here, and the BM dynamics, discussed in the next section, to be analysed separately. This is in contrast to the Finite Element Model, in which the two components are embedded in the code.

5.2.2 BM dynamics

If the BM is supposed to be locally reacting, the velocity of an element of the BM depends only on the pressure difference at that point, according to the relation:

$$v_n = -Y_{BM}(n)p_n, \tag{5.20}$$

where Y_{BM} is the mechanical admittance of the BM and the negative sign is due to the fact that in the coordinate system described in Fig. 5.1, a positive pressure difference drives the BM in a downward direction, while the elements of $\mathbf{v}$ are defined to be positive in the upward z direction. In a single degree of freedom model of the passive BM, as showed in Chapter 3 for example, its admittance is given by:

$$Y_{BM}(n) = \frac{i\omega}{i\omega r_n - \omega^2 m_n + s_n}, \tag{5.21}$$

where m_n, s_n, and r_n are, respectively, the mass, stiffness and damping, per unit area, of the n^{th} element of the BM. In this case the BM is assumed to be locally reacting, thus the Y_{BM} matrix in Eq. (5.5) is diagonal. In active models of the cochlea, the dynamics of the Organ of Corti, that is situated on the BM, also needs to be accounted for. It is also possible to take into account the mechanism of mechanical longitudinal coupling which derives from the interaction of the structures of the Organ of Corti. The elemental model can be extended to include these cases by assuming that adjacent elements are coupled by a longitudinal stiffness k_l and damping c_l, as for example is done for the BM longitudinal coupling in (Elliott and Ni, 2018). The expression for these latter elements can be derived by writing down the pressure difference on the n^{th} element as a function of the velocities of the n^{th}, $(n-1)^{th}$ and $(n+1)^{th}$ elements of the BM and then rearranging the terms to obtain a tri-diagonal matrix of BM impedance $\mathbf{Z}_{BM}$ such that

$$\mathbf{p} = -\mathbf{Z}_{BM}\mathbf{v}. \tag{5.22}$$

From this equation, the BM admittance matrix $\mathbf{Y_{BM}}$ required in the elemental model can be derived from the inversion of $\mathbf{Z}_{BM}$, while the response of the system is still given by Eq. (5.8). With other forms of longitudinal coupling the matrix $\mathbf{Z_{BM}}$, and hence $\mathbf{Y_{BM}}$, become increasingly non-diagonal, but the form of Eq. (5.5) remains valid.

5.3 Locally reacting organ of Corti model

In this chapter the BM admittance that arises from the equivalent locally reacting, active model, will be discussed, and this will be extended to the longitudinally coupled model in the following chapter. In the full finite element model developed by (Sasmal and Grosh, 2019), the two fluid chambers are modelled as a tapered prismatic box, with a constant width and varying and different height for the SV and the ST. The BM is modelled as an orthotropic plate with variable width and is assumed to vibrate with the mode shape corresponding to the first transverse vibrational mode. The fluid is assumed to be viscous and compressible and its pressure is decomposed in a sum of modes in the radial direction. The TM is modelled as a mass with two degrees of freedom with motion in the radial, y and transverse, z, direction and is longitudinally coupled through elastic stiffness and shear viscosity. Finally, the current flow in the scalae and the mechanoelectrical properties of the OHCs are modelled using cable theory.

To extend the elemental model to include the micromechanical structure of the organ of Corti, however, we do not need to refer to the full finite element model, but it is sufficient to review the differential equations that describe the dynamics of the Organ. Initially, we consider a locally reacting version of the model, which corresponds to the one developed by (Ramamoorthy et al., 2007), but without electrical longitudinal coupling. In this simplified case, the BM is modelled as a set of parallel simply supported beams and the TM as a rigid bar, so that mechanical longitudinal coupling is not included. Furthermore, the chambers are considered to be rectangular and of equal and constant area and the fluid is supposed to be non viscous and incompressible. Finally, to develop the BM admittance part of the the elemental model, we are only interested in the kinematics and dynamics of the Organ of Corti, which is reviewed in the next section.

5.3.1 Micro electro-mechanical model of the Organ of Corti

The micromechanical model of the Organ of Corti (Ramamoorthy et al., 2007), situated on the BM, is shown in Fig. 5.3. The Deiter's cells are assumed to be rigid connections between the OHCs and the BM. The OHCs are modelled as massless electro-motile elastic bars, attached at their apical end to the RL by pin-joint and at the base to the BM. The RL is modelled as a massless rigid bar attached to the pillar cells, PC, by a rotational spring. The hair bundles, HBs, are represented as rigid links, attached by a pin-joint to the TM and by a rotational spring to the RL. The TM is modelled as a rigid bar attached to a rotational spring for bending and a translational spring for shear. The three degrees of freedom of the systems are the displacement of the BM, u_{bm} and the shear u_{tms} and bending u_{tmb} mode of the TM. The equations of motion are derived from the variation of the Lagrangian, L, of the system with respect to the mechanical variables.

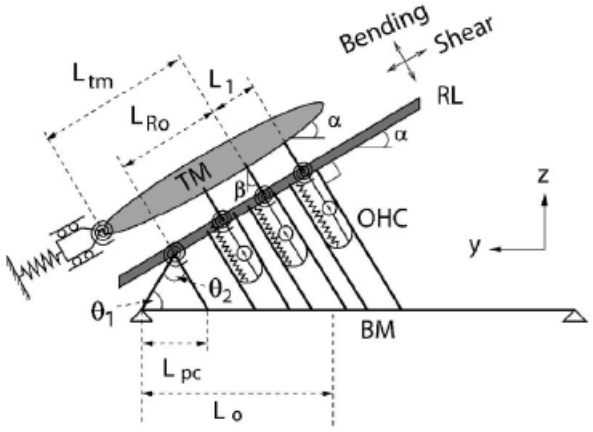

Figure 5.3: Micromechanical model of the Organ of Corti structures. BM: basilar membrane; TM: tectorial membrane; OHC: Outer hair cell; RL: Reticular lamina. L_{ro} is the distance between RL pivot point on the arch of Corti and the middle OHC; L_1 is the radial distance between OHCs along the RL; θ_1 is the acute angle between the inner pillar cell and the BM, θ_2 is the acute angle between the inner and outer pillar cell; L_{pc} is the distance along the BM between the left edge of the BM and the contact point of the outer PC with the BM; L_o is the distance along the BM between the left edge of the BM and the contact point of the middle OHC with the BM, and L_tm is the length of the TM from its pivot to the attachment point of the middle row HBs with the TM. Reprinted with permission from Ramamoorthy et al. (2007). Copyright 2007, Acoustic Society of America.

The Lagrangian is defined as the difference between the total kinetic and potential energy $L = K - V$, given respectively by

$$K = \frac{b}{4} M_{bm} \dot{u}_{bm}^2 + \frac{1}{2} M_{tmb} \dot{u}_{tmb}^2 + \frac{1}{2} M_{tms} \dot{u}_{tms}^2, \tag{5.23}$$

and

$$\begin{aligned} V =& \frac{b}{4} K_{bm} u_{bm}^2 + \frac{1}{2} K_{tms} u_{tms}^2 + \frac{1}{2} K_{tmb} u_{tmb}^2 + \frac{1}{2} \Big((u_{hb,1} + u_{rl,1} \frac{L_{hb}}{L_{Ro} - L1})^2 + (u_{hb,2} \\ &+ u_{rl,2} \frac{L_{hb}}{L_{Ro}})^2 + (u_{hb,3} + u_{rl,3} \frac{L_{hb}}{L_{Ro} + L1})^2 \Big) + \frac{1}{2} K_{rl} (u_{rl,2} + u_{ap} \frac{L_{Ro}}{L_{po}})^2, \end{aligned} \tag{5.24}$$

where b is the width of the BM, and varies along x; K_{tms} and M_{tms} represent the stiffness and mass of the TM shear mode; K_{tmb} and M_{tmb} are the corresponding quantities for the TM bending mode; K_{bm} and M_{bm} refers to the BM; $u_{rl,i}$ is the RL displacement in the z direction away from the $i-th$ row of OHCs; $u_{hb,i}$ is the shear motion between the top and bottom end of the $i-th$ row of HBs in the negative y direction; u_{ap} is the displacement of the apical end of the arch of Corti and the geometrical factors L_{hb}, L_{Ro},L_1 and L_{po} are defined in Fig. 5.3. The generalised work done by external forces, including the electromotile forces from the OHCs, the acoustic pressure and nonconservative viscous

damping, is defined as:

$$\begin{aligned} Q_{\mu mech} = &- \sum_{i=1}^{3} F^a_{ohc,i}\delta u^a_{ohc,i} - \sum_{i=1}^{3} F^b_{ohc,i}\delta u^b_{ohc,i} - p(x,z)\delta u_{bm}\mu_1 - (C_{bm}\dot{u}_{bm})\delta u_{bm} \\ &- (C_{tms}\dot{u}_{tms})\delta u_{tms} - C_{tmb}\dot{u}_{tmb})\delta u_{tmb} \end{aligned} \tag{5.25}$$

where $F^a_{ohc,i}$ and $F^b_{ohc,i}$ are the forces exerted, respectively, by the basal and apical part of the OHCs and C_{bm}, C_{tms} and C_{tmb} represents viscous damping coefficients for BM, TM bending and TM shear modes, respectively. The equations of motion for the Organ of Corti are derived from the variation of the Lagrangian with respect to the three mechanical variables:

$$\begin{aligned} \frac{\partial}{\partial t}\frac{\partial L}{\partial \dot{u_{bm}}} - \frac{\partial L}{\partial u_{bm}} &= \frac{\partial Q}{\partial \delta u_{bm}} \\ \frac{\partial}{\partial t}\frac{\partial L}{\partial \dot{u_{tms}}} - \frac{\partial L}{\partial u_{tms}} &= \frac{\partial Q}{\partial \delta u_{tms}} \\ \frac{\partial}{\partial t}\frac{\partial L}{\partial \dot{u_{tmb}}} - \frac{\partial L}{\partial u_{tmb}} &= \frac{\partial Q}{\partial \delta u_{tmb}} \end{aligned} \tag{5.26}$$

This leads to a set of equations that can be written, in the frequency domain, as:

$$\left(\begin{bmatrix} \mathbf{K_s} & \mathbf{K_{se}} \\ \mathbf{K_{es}} & \mathbf{K_e} \end{bmatrix} + i\omega \begin{bmatrix} \mathbf{C_s} & \mathbf{C_{se}} \\ \mathbf{C_{es}} & \mathbf{C_e} \end{bmatrix} - \omega^2 \begin{bmatrix} \mathbf{M_s} & \mathbf{0} \\ \mathbf{0} & \mathbf{0} \end{bmatrix} \right) \begin{bmatrix} \mathbf{u_{Ooc}} \\ \phi \end{bmatrix} = \begin{bmatrix} -\mu \mathbf{p_{Ooc}} \\ 0 \end{bmatrix}, \tag{5.27}$$

where $\mathbf{u_{Ooc}}$ is the $3N \times 1$ vector of the structural displacements DOFs:

$$\mathbf{u_{Ooc}} = [u_{bm,1}, u_{tms,1}, u_{tmb,1}..., u_{bm,N-1}, u_{tms,N-1}, u_{tmb,1}, u_{bm,N}, u_{tms,N}, u_{tmb,N}]^T, \tag{5.28}$$

where $i = 1, ..., N$ is the index of the element in the model. ϕ is the $4N \times 1$ vector of electrical DOFs:

$$\phi = [\phi_{sv,1}, \phi_{sm,1}, \phi_{ohc,1}, \phi_{st,1}, ..., \phi_{sv,N}, \phi_{sm,N}, \phi_{ohc,N}, \phi_{st,N}]^T, \tag{5.29}$$

where $\phi_{sv,i}$ is the potential in the scala vestibuli, $\phi_{sm,i}$ is the potential in the scala media, $\phi_{ohc,i}$ is the intracellular potential of the i-th OHC and $\phi_{st,i}$ is the potential in the scala tympani. $\mathbf{p_{Ooc}}$ is the vector of pressures of the fluid acting on the BM,

$$\mathbf{p_{Ooc}} = -\mu[p_{bm,1}, 0, 0, p_{bm,2}, 0, 0, ..., p_{bm,N}, 0, 0]^T; \tag{5.30}$$

μ is the coupling coefficient resulting from the integration of the lateral modes for the pressure and the BM displacement. The form of the matrices $\mathbf{K_s}$, $\mathbf{C_s}$ and $\mathbf{M_s}$, as derived from Ramamoorthy et al. (2007) are detailed in the MATLAB program listed in D.2.

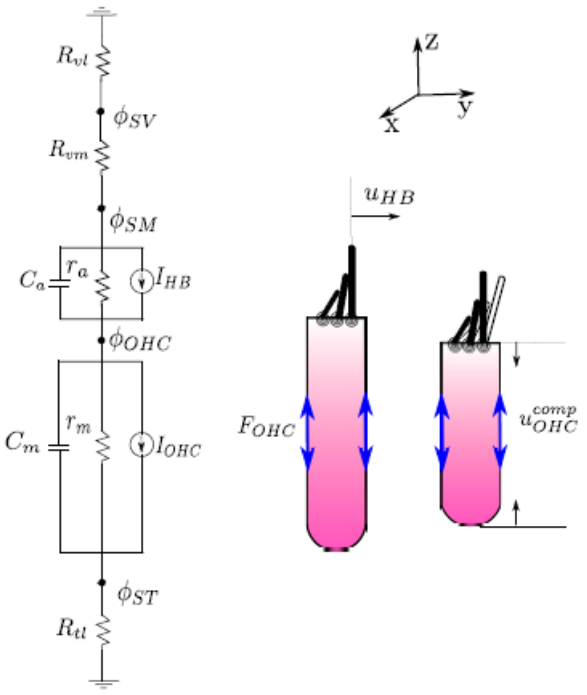

Figure 5.4: Electrical model of the OHCs, the HBs and the spread of current trough the scalae. R_{vm} is the resistance seen by the current flowing from the SV to the SM; R_{vl} is the resistance between SV and the ground; R_{tl} is the resistance between ST and the ground; R_{a0} and C_a are the apical resistance and capacitance of the OHCs, while R_m and C_m are the corresponding variables of the basolateral part. ϕ represent the electrical potential in each zone; I_{OHC} is the current due to the OHC electromotility and I_{HB} the current to the variable HB conductance. Modified from (Sasmal and Grosh, 2019), which is published in open access under a Creative Commons Attribution 4.0 International License, https://creativecommons.org/licenses/by/4.0/.

5.3.1.1 Electrical domain and coupling between mechanical and electrical degrees of freedom

The coupling between the mechanical and the electrical domain is due to the piezoelectric action of the OHCs and the displacement dependent conductance of the HBs. The coupling matrices for the electrical-structure interactions in Eq. (5.27) and the expression for the active force generated by the OHCs in Eq. (5.25) are derived from an electrical model of the OHCs and of the spread of current through the scalae, as shown in Fig. 5.4. Using Kirchhoff's laws, we obtain the model equations (Ramamoorthy et al., 2007):

$$\begin{cases} -i\omega(Y_a + Y_m)\phi_{SM} + (Y_a C_{r2} + Y_m)\phi_{ohc} + I_{hb} + I_{ohc} = 0 \\ Y_m \phi_{sm} - (Y_m + 1/R_{vl})\phi_{ohc} + I_{ohc} = 0, \end{cases} \tag{5.31}$$

where Y_a and Y_m are the admittances at the apical and basal surface of the OHC, respectively, given by:

$$Y_a = \frac{1}{r_a} + i\omega C_a; \tag{5.32a}$$

$$Y_m = \frac{1}{r_m} + i\omega C_m; \tag{5.32b}$$

where r_a and C_a are the apical resistance and capacitance of the OHC, while r_m and C_m are the corresponding quantities of the basal part of the OHC. I_{ohc} is the current due to the electromotility of the OHCs and is given by:

$$I_{ohc} = \sum_{j=1}^{3} \epsilon_3 \dot{u}_{ohc,j}^{comp}, \tag{5.33}$$

where $u_{ohc,j}^{comp}$ is the total inward compression of the j^{th} OHC, and ϵ_3 is the electromechanical coupling coefficient. The force transduced by the j^{th} OHC is given by:

$$F_{ohc,j} = K_{ohc,j} u_{ohc,j}^{comp} + \epsilon(\phi_{ohc} - \phi_{ST}) \tag{5.34}$$

where $K_{ohc,j}$ is the axial stiffness associated with the j^{th} OHC. I_{hb} is the current passing trough the mechano-electrical transduction (MET) channels in the HBs and is given by:

$$I_{hb} = (\phi_{SM} - \phi_{ohc}) G_{MET}, \tag{5.35}$$

where G_{MET} is the HB conductance, which is initially assumed to be a nonlinear function of the HB deflection as:

$$G_{MET} = G_0 P = \frac{G_0}{1 + e^{-(u_{HB} - u_{HB}^0)/\delta_{HB}}}, \tag{5.36}$$

where G_0 is the maximum MET conductance, P is the open probability of a channel, u_{hb} is the HB deflection, u_{HB}^0 is the resting displacement of the HB and δ_{hb} is the MET channel width. To obtain a linear model, the transduction current I_{HB} is linearised with respect to small variations of HB deflections u_{hb}, as:

$$I_{hb} = (G_{MET}^0 + i\omega C_a)(\phi_{sm} - \phi_{ohc}) + (V_{sm} - V_{ohc}) \sum_{j=1}^{3} G_{MET,j}^1 u_{hb,j}, \tag{5.37}$$

where $G_{MET,j}^0 = 1/r_a$ is the conductance at the resting state of the HB; V_{sm} and V_{ohc} are the voltages at resting state in the SM and of the OHC, respectively; G_{MET}^1 is the slop of the change of conductance with respect to the HB deflection, which is supposed to be a function of x. These equations are used to derive the form of the matrices $\mathbf{K_e}$, $\mathbf{K_{es}}$, $\mathbf{C_{es}}$ in Eq. (5.27), as detailed in the MATLAB program in D.2.

5.4 Extension of the elemental model to condense out the electrical degrees of freedom.

The elemental model, reviewed in Section 5.2, can be extended to include the locally reacting micromechanical model of the Organ of Corti, described in Section 5.3, by

deriving an equivalent BM admittance matrix, $\mathbf{Y_{BM}}$. Then this is used within the framework of the elemental model, to derive the response of the system in the case of 3D fluid coupling, using Eq. (5.8). First, we notice that the vector of BM velocities given by Eq. (5.3b) is equal to:

$$\mathbf{v} = i\omega\mathbf{T}\mathbf{u}, \tag{5.38}$$

where $\mathbf{T}$ is a $N \times 7N$ matrix given by:

$$\mathbf{T} = \begin{bmatrix} 1 & 0 & 0 & 0 & 0 & ... \\ 0 & 0 & 0 & 1 & 0 & ... \\ . & & & & & \\ . & & & & & \\ . & & & & & \\ . & & & & & \end{bmatrix}, \tag{5.39}$$

and:

$$\begin{aligned}\mathbf{u} =&[u_{bm,1}, u_{tms,1}, u_{tmb,1}, ..., u_{bm,N}, u_{tms,N}, u_{tmb,N}, ..., \phi_{sv,1}, \phi_{sm,1}, \phi_{ohc,1}, \phi_{st,1}, ..., \\ &\phi_{sv,N}, \phi_{sm,N}, \phi_{ohc,N}, \phi_{st,N}]^T.\end{aligned} \tag{5.40}$$

Furthermore:

$$\tilde{\mathbf{p}} = \mathbf{S}\mathbf{p} \tag{5.41}$$

where:

$$\tilde{\mathbf{p}} = [p_{bm,1}, 0, 0, 0, 0, 0, 0, p_{bm,2}, 0, 0, 0, 0, 0, 0, ..., p_{bm,N}, 0, 0, 0, 0, 0, 0]^T, \tag{5.42}$$

$\mathbf{S}$ is a $7N \times N$ matrix, given by:

$$\mathbf{S} = \begin{bmatrix} 1 & 0 & 0 & 0 & ... \\ 0 & 0 & 0 & 0 & ... \\ 0 & 0 & 0 & 0 & ... \\ 0 & 1 & 0 & 0 & ... \\ 0 & 0 & 0 & 0 & ... \\ 0 & 0 & 0 & 0 & ... \\ 0 & 0 & 1 & 0 & ... \\ . & & & & \\ . & & & & \\ . & & & & \end{bmatrix}, \tag{5.43}$$

and $\mathbf{p}$ is the vector of elemental pressures in Eq. (5.3a). Then, if we define:

$$\mathbf{K_{global}} = \left(\begin{bmatrix} \mathbf{K_s} & \mathbf{K_{se}} \\ \mathbf{K_{es}} & \mathbf{K_e} \end{bmatrix} + i\omega \begin{bmatrix} \mathbf{C_s} & \mathbf{C_{se}} \\ \mathbf{C_{es}} & \mathbf{C_e} \end{bmatrix} - \omega^2 \begin{bmatrix} \mathbf{M_s} & \mathbf{0} \\ \mathbf{0} & \mathbf{0} \end{bmatrix} \right), \tag{5.44}$$

from Eq. (5.27) we can write:

$$\mathbf{v} = -i\omega \mathbf{T}\mathbf{K}_{\mathbf{global}}^{-1}\mathbf{S}\mathbf{p} \tag{5.45}$$

By comparing this equation to the one used in the elemental model:

$$\mathbf{v} = -\mathbf{Y}_{\mathbf{bm}}\mathbf{p}, \tag{5.46}$$

we obtain the expression of the equivalent BM admittance as:

$$\mathbf{Y}_{\mathbf{bm}} = \mathbf{T}\mathbf{K}_{\mathbf{global}}^{-1}\mathbf{S}. \tag{5.47}$$

This admittance can then be used in the elemental model, to obtain the response of the cochlea using Eq. (5.8). The electrical degrees of freedom in Eq. (5.27) contained in ϕ have thus been condensed out of the formulation in this process. This considerably simplifies the interpretation of the BM dynamics, by incorporating the forces due to the OHCs into the elemental mechanical model.

5.4.1 Results

In this section we present the predictions of the BM response in the passive and active case for the elemental model with a locally reacting Organ of Corti, based on the guinea pig parameters used in (Ramamoorthy et al., 2007). The data from the finite element model was kindly made available by Karl Grosh as part of a collaboration with the University of Michigan, as part of this PhD. The results are derived for various positions along the cochlea and for each of them we report the characteristic frequency, the amplification and $Q_{10\,\mathrm{dB}}$, which measures the sharpness of tuning, defined as $f_0/\Delta f$, where f_0 is the frequency where the response peaks and Δf is the full width of the amplitude curve 10 dB down from the maximum response. In all cases 3D fluid coupling is included and the chamber areas are assumed to be uniform.

5.4.1.1 Passive case

Figure 5.5 shows the predicted BM response, relative to the stapes, as a function of the frequency, in the passive case, at different longitudinal locations. The dashed lines are from the finite element model (Ramamoorthy et al., 2007) while the solid lines are from the elemental formulation. There are minor differences between the two models, including the lack of longitudinal electrical coupling in the elemental model and the way the fluid coupling is modelled, as discussed above. With respect to the finite element model, the characteristic frequencies of the elemental model at the various locations are slightly shifted. Furthermore, there is a difference in the slope of the response at the lowest frequencies. The overall form of the passive response is, however, similar for the two models.

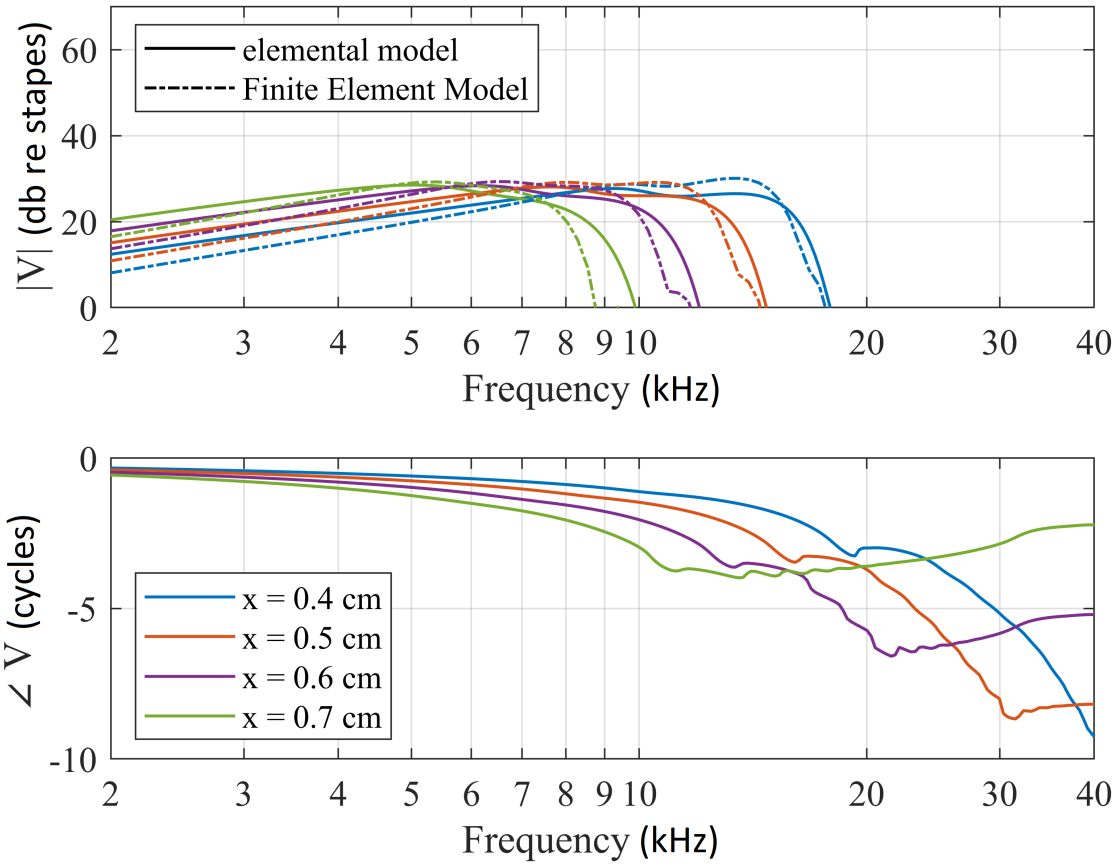

Figure 5.5: Prediction of the locally reacting BM response, relative to the stapes, as a function of the frequency ,in the passive case at different locations along the cochlea. The amplitude response from the elemental model (solid lines) is compared to the response from the elemental model (Ramamoorthy et al., 2007).

5.4.1.2 Active case

Figure 5.6 shows the predicted BM response, in the active locally reacting case. In these simulations, the OHC electromechanical coupling coefficient, was increased until the frequency response began to demonstrate discontinuities, indicating instabilities, and was then reduced by 95%. For comparison, the passive case derived in the previous section is also reported. As we can see, in the active case there is an increase in the amplitude and sharpness of the response and also a shift of the peak to higher frequencies. In this instance we do not have data to make a direct comparison with the finite element model, but these result have a similar form to those of Fig.5 in (Ramamoorthy et al., 2007). If we look at the phases, we can see that, with respect to the passive case, there is a greater phase accumulation, as expected. Table 5.1 shows, for every position, the characteristic frequency, CF, the amplification with respect to the passive case and the value of $Q_{10\,\mathrm{dB}}$ for this active model. The values of the amplification are somewhat lower than those measured for the guinea pig by (Zheng et al., 2007), but this is expected as in (Ramamoorthy et al., 2007) it is shown that, without electrical longitudinal coupling, the amplification of the response is reduced by about 10 dB.

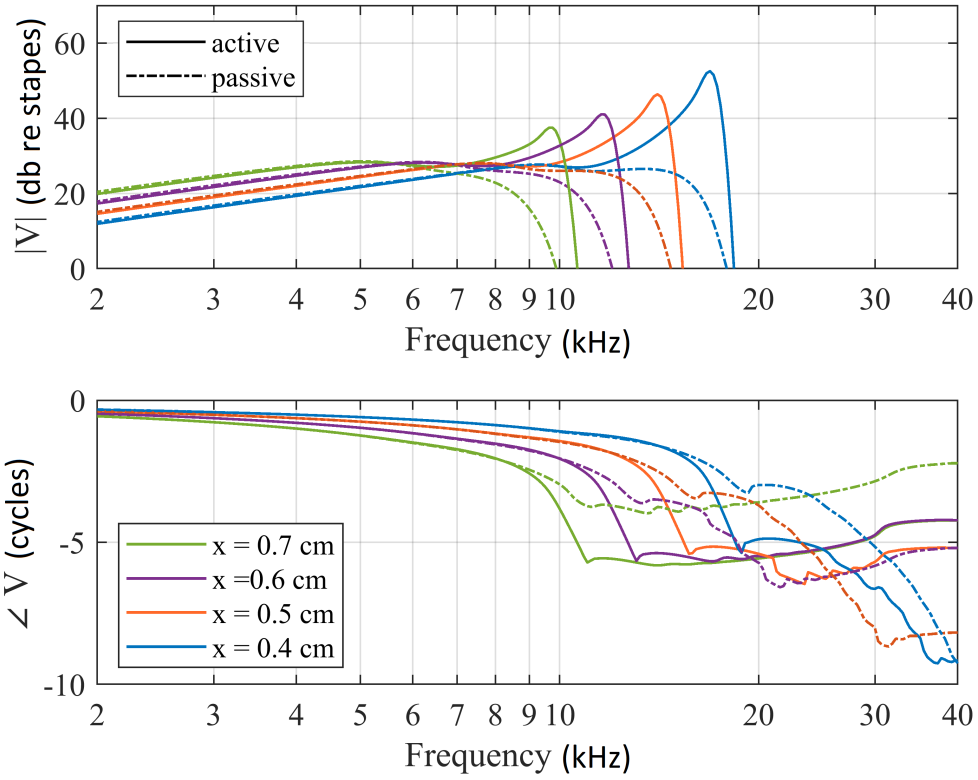

Figure 5.6: Prediction of the BM response relative to the stapes as a function of the frequency in the active, locally reacting case, at different longitudinal locations. The dashdotted lines are from the passive case (Fig. 5.5) while the solid lines are the active case.

Table 5.1: Q_{10dB}, amplification and characteristic frequency at various position in the locally reacting case represented in Fig. 5.6. In square bracket, the experimental values from (Zheng et al., 2007).

Position (cm)	CF (kHz)	Amplification (dB)	$Q_{10\,\mathrm{dB}}$
0.40	16.9 [16.5]	27.0 [35]	8.4 [6.5]
0.50	14.1	20.6	6.4
0.60	11.6	15.8	4.3
0.70	9.7	12.1	3.4

5.4.2 BM admittance

One of the advantages of the elemental model is that the BM admittances that have contributed to the coupled response in Section 5.4.1.1 and 5.4.1.2 can be explicitly calculated. In this active, locally reacting case, this BM admittance includes the electrical and electromechanical behaviour of the OHCs, as discussed in Section 5.4, but not the contribution due to the near-field component of the pressure. Fig. 5.7 shows the BM admittance at the position $x = 4\,\text{mm}$ for the passive and the active model. The BM admittance in the passive case is similar to that expected for the single degree of freedom micromechanics, as described by Eq. (5.21), apart from an increase of the value of the real part at the highest frequencies. The BM admittance in the active case shows a sharper peak before the CF and is negative in a small region before the CF, suggesting that this is the region where the travelling wave is amplified. (Dewey et al., 2019) used an elegant suppression technique to show that amplification of the cochlear wave occurs close to the characteristic frequency, over a region that is about 18% of the cochlear length. This suggests that while this locally reacting model produces realistic coupled responses, the physical description of the cochlear amplifier is incomplete, perhaps due to the lack of longitudinal coupling.

Another advantage of condensing out the electrical degrees of freedom in the elemental formulation is that an equivalent 3DOF mechanical system can be derived, which includes the cochlear amplifier. This is described in Appendix B.

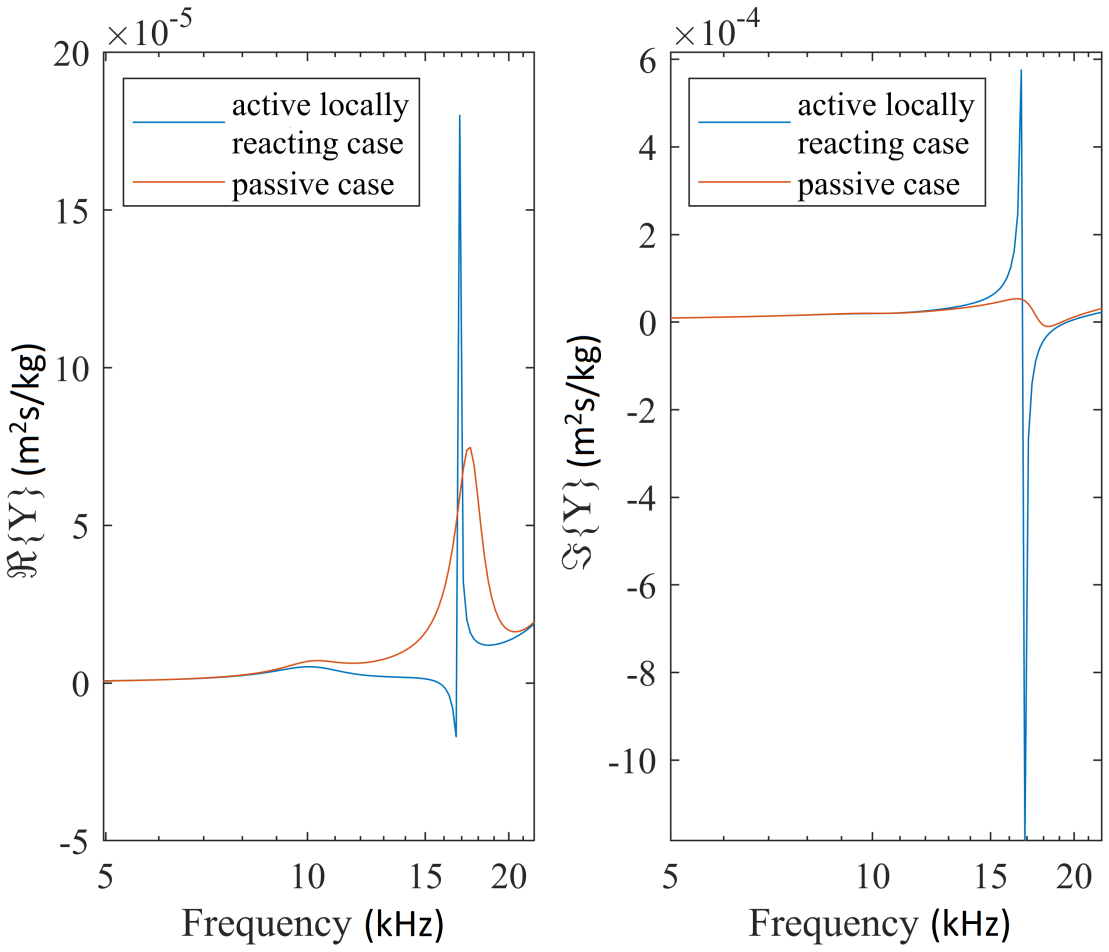

Figure 5.7: Passive and active BM admittance, as a function of the frequency, at the position $x = 4\,\mathrm{mm}$.

5.5 Conclusions

In this chapter, the formulation of the elemental model of the cochlea is reviewed, describing the case with 1D and 3D fluid coupling. The Finite Element Model of the Organ of Corti in the locally reacting case, that is, with no mechanical or electrical longitudinal coupling, as modelled by (Ramamoorthy et al., 2007), is also described. We then showed how the elemental model can be extended to include the micromechanical model of the Organ of Corti and, in particular, how the BM admittance is modified. Finally, we derived the predictions of the BM response for the passive and active case. It is worth noting the relative computational efficiency of the elemental model with respect to the finite element model. By using the same software, MATLAB, and similar hardware, the time required to run the algorithms associated with the finite element model is of 6 hours while the elemental model requires only 15 minutes.

In the next chapter, we show how to include the mechanical and electrical longitudinal coupling in the elemental model and how the responses are modified. The results are compared to the locally reacting case by looking at the amplification of the peak of the response and its sharpness, as measured by $Q_{10\,\mathrm{dB}}$.

Chapter 6

Longitudinal coupling

In the previous chapter the elemental model, reviewed in (Elliott and Ni, 2018), was extended to include the finite element model of the Organ of Corti by (Sasmal and Grosh, 2019), in the simplified case of no mechanical and electrical longitudinal coupling. In this chapter we show how the equivalent BM admittance is modified after the introduction of the mechanical longitudinal coupling of the tectorial membrane, the basilar membrane and the electrical longitudinal coupling along the scalae. Then we compare the effect of the various types of the longitudinal coupling on the active response of the BM, in terms of the amplification of the response and its sharpness, measured by $Q_{10\,\mathrm{dB}}$.

6.1 Longitudinal coupling in the tectorial membrane

When the longitudinal viscoelastic coupling of the TM is included, the governing equation for the shear motion of the TM, u_{tms}, is modified as (Meaud and Grosh, 2010):

$$F_{hb/tms}(x) = K_{tms}u_{tms} + C^f_{sub}\dot{u}_s + M_{tms}\ddot{u}_{tms} - \frac{\partial}{\partial x}\left(A^{eff}_{tm}G_{xy}\frac{\partial u_{tms}}{\partial x} + A^{eff}_{tm}\eta_{xy}\frac{\partial \dot{u}_{tms}}{\partial x}\right) \tag{6.1}$$

where $F_{hb/tms}$ is the force per unit length applied to the TM by the HBs of the OHCs in the shear direction; C^f_{sub} is the damping coefficient due to the viscosity of the fluid in the subtectorial space; u_s is the relative shear displacement between the TM and the RL; A^{eff}_{tm} is an effective cross-sectional area of the TM; G_{xy} is the shear modulus and η_{xy} is the shear viscosity.

To incorporate these extra terms in the matrix formulation given by Eq. (5.27), first we expand out the derivations:

$$\begin{aligned} F_{hb/tms}(x) =& K_{tms}u_{tms} + C^f_{sub}\dot{u}_s + M_{tms}\ddot{u}_{tms} - \left(A^{eff\,\prime}_{tm}G_{xy} + A_{tm}G'_{xy}\right)\frac{\partial u_{tms}}{\partial x} \\ &- \left(A^{eff\,\prime}_{tm}\eta_{xy} + A^{eff}_{tm}\eta'_{xy}\right)\frac{\partial \dot{u}_{tms}}{\partial x} - A^{eff}_{tm}G_{xy}\frac{\partial^2 u_{tms}}{\partial x^2} - A^{eff}_{tm}\eta_{xy}\frac{\partial^2 \dot{u}_{tms}}{\partial x^2}, \end{aligned} \tag{6.2}$$

then we discretise the first and second derivative of u_{tms} so that Eq. (6.2) becomes:

$$\begin{aligned} F_{hb/tms}(x) =& K_{tms}(x)u_{tms}(x) + C^{f}_{sub}(x)\dot{u}_s(x) + M_{tms}\ddot{u}_{tms}(x) - k_{l1}(x+1)u_{tms}(x+1) \\ &+ k_{l1}(x)u_{tms}(x) - c_{l1}(x+1)\dot{u}_{tms}(x+1) + c_{l1}(x)\dot{u}_{tms}(x) \\ &- k_{l2}(x-1)u_{tms}(x-1) + 2k_{l2}(x)u_{tms}(x) - k_{l2}(x+1)u_{tms}(x+1) \\ &- c_{l2}(x-1)\dot{u}_{tms}(x-1) + 2c_{l2}(x)\dot{u}_{tms}(x) - c_{l2}(x+1)\dot{u}_{tms}(x+1), \end{aligned} \tag{6.3}$$

where

$$k_{l1}(x) = \frac{A^{eff'}_{tm}G_{xy}(x) + A^{eff}_{tm}G'_{xy}(x)}{\Delta}, \tag{6.4}$$

$$c_{l1}(x) = \frac{A^{eff'}_{tm}(x)\eta_{xy}(x) + A^{eff}_{tm}(x)\eta'_{xy}(x)}{\Delta}, \tag{6.5}$$

$$k_{l2}(x) = \frac{A^{eff}_{tm}(x)G_{xy}(x)}{\Delta^2}, \tag{6.6}$$

$$c_{l2}(x) = \frac{A^{eff}_{tm}(x)\eta_{xy}(x)}{\Delta^2}. \tag{6.7}$$

Finally, we include these terms, proportional to the first and second derivative of u_{tms}, into the matrix formulation in Eq. (5.27) as extra diagonal and non-diagonal terms into the structural matrices $\mathbf{K_s}$ and $\mathbf{C_s}$. In particular, $\mathbf{K_s}$ becomes:

$$\mathbf{K_s} = \begin{bmatrix} \mathbf{K(1)} & \mathbf{0} & \mathbf{0} & \mathbf{0} & \mathbf{0} & ... & \mathbf{0} \\ \mathbf{K_{l2}} & \mathbf{K(2)} & \mathbf{K_{l1}} & \mathbf{0} & \mathbf{0} & ... & \mathbf{0} \\ \mathbf{0} & \mathbf{K_{l2}} & \mathbf{K(3)} & \mathbf{K_{l1}} & \mathbf{0} & ... & \mathbf{0} \\ . & & & & & & \\ . & & & & & & \\ \mathbf{0} & ... & & & & \mathbf{0} & \mathbf{K(N)} \end{bmatrix} \tag{6.8}$$

where for $i = 2, 3, ..., N-1$

$$\mathbf{K(i)} = \begin{bmatrix} k_{11}(i) & k_{12}(i) & k_{13}(i) \\ k_{21}(i) & k_{22}(i) + k_{l1}(i) + 2k_{l2}(i) & k_{23}(i) \\ k_{31}(i) & k_{32}(i) & k_{33}(i) \end{bmatrix} \tag{6.9}$$

while for $i = 1, N$:

$$\mathbf{K(N)} = \begin{bmatrix} k_{11}(i) & k_{12}(i) & k_{13}(i) \\ k_{21}(i) & k_{22}(i) & k_{23}(i) \\ k_{31}(i) & k_{32}(i) & k_{33}(i) \end{bmatrix} \tag{6.10}$$

and

$$\mathbf{K_{l2}(i)} = \begin{bmatrix} 0 & 0 & 0 \\ 0 & -k_{l2}(i-1) & 0 \\ 0 & 0 & 0 \end{bmatrix} \tag{6.11}$$

and

$$\mathbf{K_{l1}(i)} = \begin{bmatrix} 0 & 0 & 0 \\ 0 & -k_{l1}(i+1) - k_{l2}(i+1) & 0 \\ 0 & 0 & 0 \end{bmatrix} \tag{6.12}$$

A similar expression is obtained for the matrix $\mathbf{C_s}$.

6.2 Longitudinal coupling in the basilar membrane

When the elastic longitudinal coupling of the BM is included, the governing equation for the BM motion becomes (Meaud and Grosh, 2010):

$$\begin{aligned} P_{bm}(x,y) =& \frac{2}{b} C_{bm}\dot{u}_{bm} + M_{bm}\ddot{u}_{bm} - \frac{\partial^2}{\partial x^2}\left(D_{xx}\frac{\partial^2 u_{bm}}{\partial x^2} + D_{xy}\frac{\partial^2}{\partial y^2}\right) - 2\frac{\partial^2}{\partial x \partial y}\left(D_s \frac{\partial^2 u_{bm}}{\partial x \partial y}\right) \\ & - \frac{\partial^2}{\partial y^2}\left(D_{yy}\frac{\partial^2 u_{bm}}{\partial y^2} + D_{xy}\frac{\partial^2 u_{bm}}{\partial x^2}\right), \end{aligned} \tag{6.13}$$

where P_{bm} is the pressure applied by the fluid and the OHC on the BM, C_{bm} is the BM viscous damping per unit area, M_{bm} is the mass of the BM per unit area and b is the width of the BM. D_{xx}, D_{yy}, D_{xy}, and D_s are the orthotropic plate bending stiffness of the BM. $u_{bm}(x,y)$ is the BM displacement and is given by:

$$u_{bm}(x,y) = u_{bm}(x) sin(\pi(y + b/2)/b), \tag{6.14}$$

where $-b/2 \leq y \leq b/2$. If we integrate out the radial dependence of the BM displacement and neglect the longitudinal variation of b, then Eq. (6.13) becomes:

$$\begin{aligned} F_{bm}(x) =& C_{bm}\dot{u}_{bm}(x) + \frac{b}{2} M_{bm}\ddot{u}_{bm}(x) - \frac{b}{2}\left[D_{xx}\frac{\partial^4 u_{bm}}{\partial x^4} - 2(D_{xy} + D_s)\left(\frac{\pi}{b}\right)^2 \frac{\partial^2 u_{bm}}{\partial x^2}\right. \\ & \left. + D_{yy}\left(\frac{\pi}{b}\right)^4 u_{bm}\right], \end{aligned} \tag{6.15}$$

where F_{bm} is the force per unit length applied on the BM. Then, to incorporate these terms into the matrix formulation given by Eq. (5.27), we discretise the derivatives of u_{bm} and include the resulting terms into the matrix $\mathbf{K_s}$, in a similar way in which we have done in the previous section.

6.3 Electrical longitudinal coupling

When the electrical longitudinal coupling is included, the cross-sectional model of the circuit in Figure 5.4 is modified as in Fig. 6.1 (Sasmal and Grosh, 2019) to include the resistances per unit length along the SV, SM and ST. These create two additional potentials in the models, one in the SV and one in the ST, which corresponds to two additional electrical DOFs. The governing equations for the electrical DOFs are modified as (Sasmal and Grosh, 2019):

$$\begin{cases} \frac{1}{r_{sv}}\frac{\partial^2\phi_{sv}}{\partial x^2} - \left(\frac{1}{R_{vl}} + \frac{1}{R_{vm}}\right)\phi_{sv} + \frac{1}{R_{vm}}\phi_{sm} = 0, \\ \frac{1}{R_{vm}}\phi_{sv} + \frac{1}{r_{sm}}\frac{\partial^2\phi_{sm}}{\partial x^2} - \left(\frac{1}{R_{vm}} + 3Y_a\right)\phi_{sm} + 3Y_a\phi_{ohc} - I_{s1} = 0, \\ 3Y_a\phi_{sm} - 3(Y_a + Y_m)\phi_{ohc} + 3Y_m\phi_{st} + I_{s1} - I_{s2} = 0, \\ 3Y_m\phi_{ohc} + \frac{1}{r_{st}}\frac{\partial^2\phi_{st}}{\partial x^2} - \left(\frac{1}{R_{tl}} + 3Y_m\right)\phi_{st} + I_{s2} = 0, \end{cases} \tag{6.16}$$

where $Y_a = 1/R_{a0} + i\omega C_a$ and $Y_m = 1/R_m + i\omega C_m$. I_{s1} is the current due to the variable HB conductance and is given by:

$$I_{s1} = (V_{sm} - V_{ohc})G_a^1 \sum_{j=1}^{3} u_{hb,j}, \tag{6.17}$$

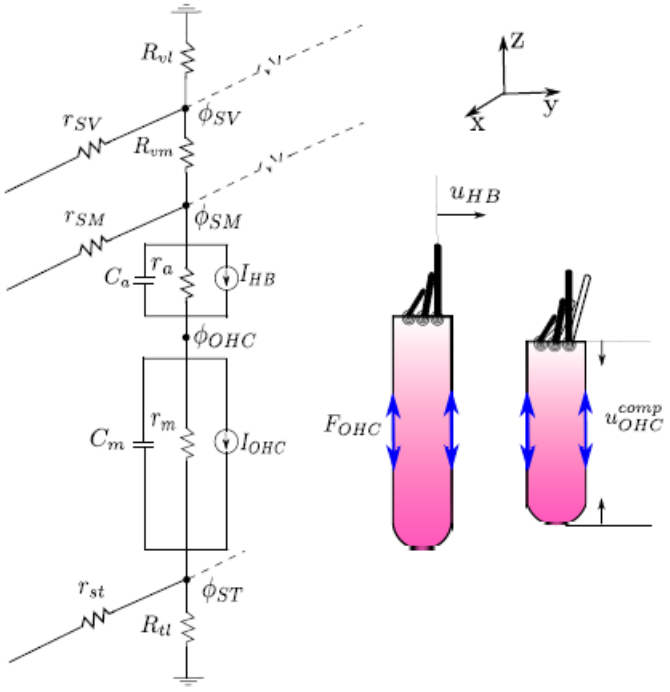

Figure 6.1: Electrical model of the OHCs and of the spread of current trough the scalae. With respect to the locally reacting case, there are additional resistances, r_{sv}, r_{sm} and r_{st} along, respectively, the SV, SM and ST. From (Sasmal and Grosh, 2019), which is published in open access under a Creative Commons Attribution 4.0 International License, https://creativecommons.org/licenses/by/4.0/.

while I_{s2} is the current due to the OHC electromotility:

(6.18)

Then the matrix $\mathbf{C_e}$ in Eq. (5.27) has diagonal blocks of dimension 4×4:

$$\mathbf{C_e(i)} = \begin{bmatrix} 0 & 0 & 0 & 0 \\ 0 & -3C_a & 3C_a & 0 \\ 0 & 3C_a & -3C_a - 3C_m & 3C_m \\ 0 & 0 & 3C_m & -3C_m \end{bmatrix}, \tag{6.19}$$

$\mathbf{K_e}$ can be written as:

$$\mathbf{K_e} = \begin{bmatrix} \mathbf{K_e(1)} & \mathbf{0} & \mathbf{0} & \mathbf{0} & \mathbf{0} & ... & \mathbf{0} \\ \mathbf{K_{e,l2}} & \mathbf{K_e(2)} & \mathbf{K_{e,l1}} & \mathbf{0} & \mathbf{0} & ... & \mathbf{0} \\ \mathbf{0} & \mathbf{K_{e,l2}} & \mathbf{K_e(3)} & \mathbf{K_{e,l1}} & \mathbf{0} & ... & \mathbf{0} \\ . & & & & & & \\ . & & & & & & \\ \mathbf{0} & ... & & & & \mathbf{0} & \mathbf{K_e(N)} \end{bmatrix}, \tag{6.20}$$

where for $i = 2, 3, ..., N-1$:

$$\mathbf{K_e(i)} = \begin{bmatrix} \frac{-1}{R_{vl}} - \frac{1}{R_{vm}} + \frac{2}{r_{sv}\Delta^2} & \frac{1}{R_{vm}} & 0 & 0 \\ \frac{1}{R_{vm}} & \frac{-1}{R_{vm}} - \frac{3}{R_{a0}} + \frac{2}{r_{sm}\Delta^2} & -\frac{3}{R_{a0}} & 0 \\ 0 & \frac{3}{R_{a0}} & -\frac{3}{R_{a0}} - \frac{3}{R_m} & \frac{3}{R_m} \\ 0 & 0 & \frac{3}{R_m} & -\frac{1}{R_{tl}} - \frac{3}{R_m} + \frac{2}{r_{st}\Delta^2} \end{bmatrix} \tag{6.21}$$

while for $i = 1, N$:

$$\mathbf{K_e(i)} = \begin{bmatrix} \frac{-1}{R_{vl}} - \frac{1}{R_{vm}} & \frac{1}{R_{vm}} & 0 & 0 \\ \frac{1}{R_{vm}} & \frac{-1}{R_{vm}} - \frac{3}{R_{a0}} & -\frac{3}{R_{a0}} & 0 \\ 0 & \frac{3}{R_{a0}} & -\frac{3}{R_{a0}} - \frac{3}{R_m} & \frac{3}{R_m} \\ 0 & 0 & \frac{3}{R_m} & -\frac{1}{R_{tl}} - \frac{3}{R_m} \end{bmatrix} \tag{6.22}$$

and:

$$\mathbf{K_{e,l1}(i)} = \begin{bmatrix} -\frac{1}{r_{sv}\Delta^2} & 0 & 0 & 0 \\ 0 & -\frac{1}{r_{sm}\Delta^2} & 0 & 0 \\ 0 & 0 & 0 & 0 \\ 0 & 0 & 0 & -\frac{1}{r_{st}\Delta^2} \end{bmatrix} \tag{6.23}$$

and $\mathbf{K_{e,l2}(i)} = \mathbf{K_{e,l1}(i)}$ because r_{sv}, r_{sm} and r_{st} do not depend on the longitudinal coordinate x. The matrix $\mathbf{C_{es}}$ has diagonal block of dimension 4×3:

$$\mathbf{C_{es}(i)} = -\epsilon \begin{bmatrix} 0 & 0 & 0 \\ 0 & 0 & 0 \\ -C_1 - E_1 & -C_3 & -C_4 \\ C_1 + E_1 & C_3 & C_4 \end{bmatrix}, \tag{6.24}$$

where:

$$C_1 = -3\psi_{1,Lpc}\frac{\sin(\theta_1+\theta_2)}{\sin(\theta_2)}\left(\cos(\theta_1-\alpha) - \frac{\cos(\theta_1-\beta)}{cos(\alpha-\beta)}\right), \tag{6.25a}$$

$$C_3 = -3\tan(\alpha-\beta), \tag{6.25b}$$

$$C_4 = -3, \tag{6.25c}$$

$$E_1 = (\psi_{1,L01} + \psi_{1,L0} + \psi_{1,L10})\cos(\alpha). \tag{6.25d}$$

which are the coefficients that define $u_{ohc,j}$ in Eq. (5.33). The matrix $\mathbf{K_{es}}$ has diagonal blocks of 4×3:

$$\mathbf{K_{es}(i)} = 3iq \begin{bmatrix} 0 & 0 & 0 \\ A_1 & A_3 & A_4 \\ -A_1 & -A_3 & -A_4 \\ 0 & 0 & 0 \end{bmatrix}, \tag{6.26}$$

where:

$$iq = (V_{sm} - V_{ohc})G_a^1, \tag{6.27}$$

and:

$$A_1 = -\psi_{1,Lpc}\frac{\sin(\theta_1+\theta_2)}{\sin(\theta_2)}\frac{\sin(\theta_1-\alpha)}{cos(\alpha-\beta)} - \frac{L_{st}}{L_{ro}}\psi_{1,Lpc}\sin(\theta_1+\theta_2)\frac{\cos(\theta_1-\beta)}{\sin(\theta_2)\cos(\alpha-\beta)}, \tag{6.28a}$$

$$A_3 = \frac{1}{\cos(\alpha-\beta)} + \frac{L_{st}}{L_{ro}}\tan(\alpha-\beta), \tag{6.28b}$$

$$A_4 = \frac{L_{st}}{L_{ro}}. \tag{6.28c}$$

which are the coefficients that define $u_{hb,j}$ in Eq. (5.37). The matrix $\mathbf{K_{se}} = \mathbf{C_{es}^T}$ while $\mathbf{C_{se}} = \mathbf{0}$ because the MET is not a reciprocal function.

6.4 Results

In this section we present the predictions in the active case from the elemental model with a longitudinal coupled Organ of Corti. In the passive case there is found to be a negligible difference between the various cases of longitudinal coupling and the locally reacting case, and so the results are not included. The results are derived for various positions along the cochlea, using parameters based on (Meaud and Grosh, 2010) and listed in the MATLAB program in Appendix D. For each case we report the characteristic frequency, the amplification and $Q_{10\,\mathrm{dB}}$.

6.4.1 Active case with BM longitudinal coupling only

Figure 6.2 shows the prediction of the BM response, in the active case, including BM longitudinal coupling. For comparison, the active locally reacting case, derived in Section 5.4.1.2, is also reported. When the BM longitudinal coupling is included, a greater value of the electromechanical coupling coefficient, ϵ_3, corresponding to an increase of about 6%, compared with the locally reacting case, can be used without incurring in instability in the response. The latter was inferred from discontinuities in the frequency dependence of the amplitude or the phase of the coupled response.

The resulting amplitude of the BM is characterised by a greater amplification, a greater value of $Q_{10\,\mathrm{dB}}$, and the peak of the response is shifted to higher frequencies. This is illustrated in Table 6.1 for this case, which can be compared with Table 5.1 in Chapter 5 for the passive case.

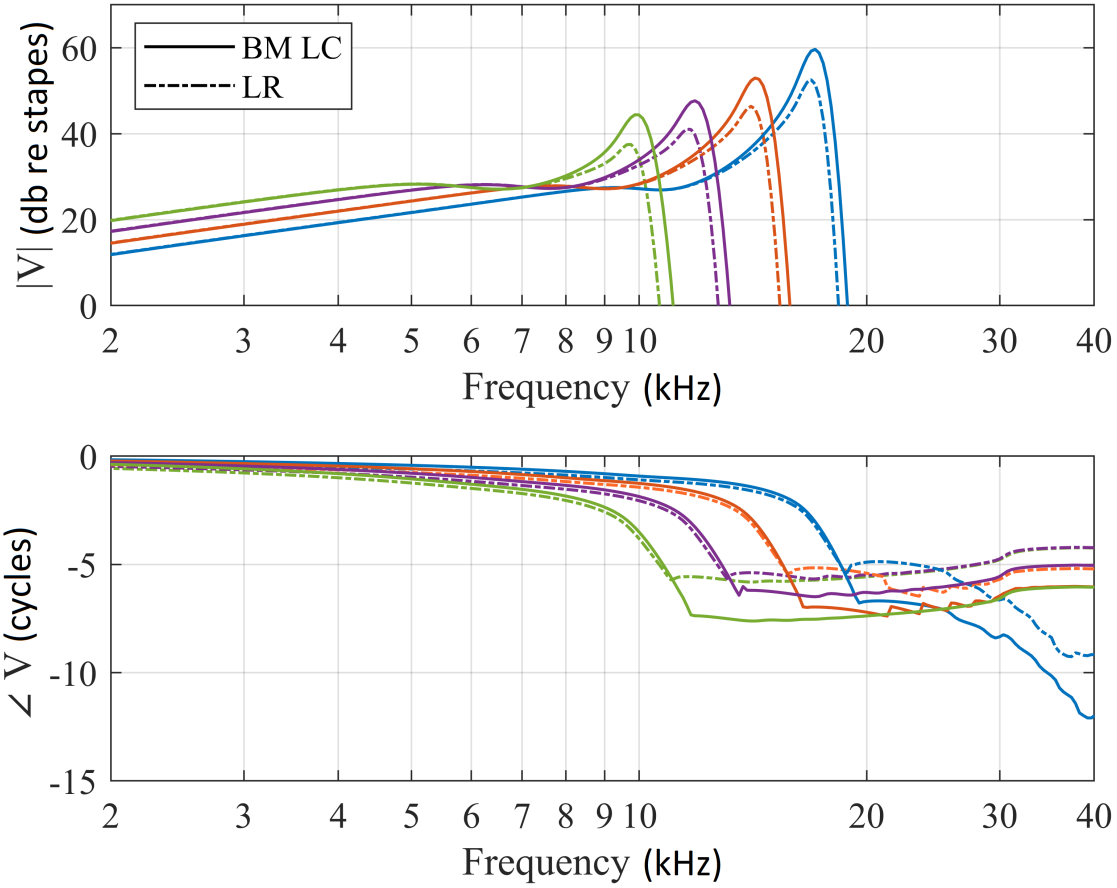

Figure 6.2: Prediction of the BM response relative to the stapes as a function of the frequency in the active case, with BM longitudinal coupling only, at different longitudinal locations. The dashdotted lines are from the active locally reacting case (LR) (Fig. 5.6) while the solid lines are the active case with BM longitudinal coupling only (BM LC).

Table 6.1: Characteristic frequency, amplification and Q_{10dB} at various position in the case with BM longitudinal coupling only, represented in Fig. 6.3.

Position (cm)	CF (kHz)	Amplification (dB)	$Q_{10\,\mathrm{dB}}$
0.40	17.09	32.02	8.9
0.50	14.23	23.82	6.7
0.60	11.85	18.62	6.4
0.70	9.87	15.54	6.1

6.4.2 Active case with TM longitudinal coupling only

Figure 6.3 shows the prediction of the BM response, in the active case, including only TM longitudinal coupling. For comparison, the active locally reacting case, derived in Section 5.4.1.2, is again reported. When the TM longitudinal coupling is included, a greater value of the electromechanical coupling coefficient, ϵ_3, can be used without incurring in instabilities in the response. In particular, in this case, the value of ϵ_3 has been increased by about 40% and, as reported in Table 6.2, the resulting amplitude is characterised by a greater amplification, a greater value of $Q_{10\,\mathrm{dB}}$, compared to the locally reacting case in Table 5.1, and the peak of the response is shifted to lower frequencies.

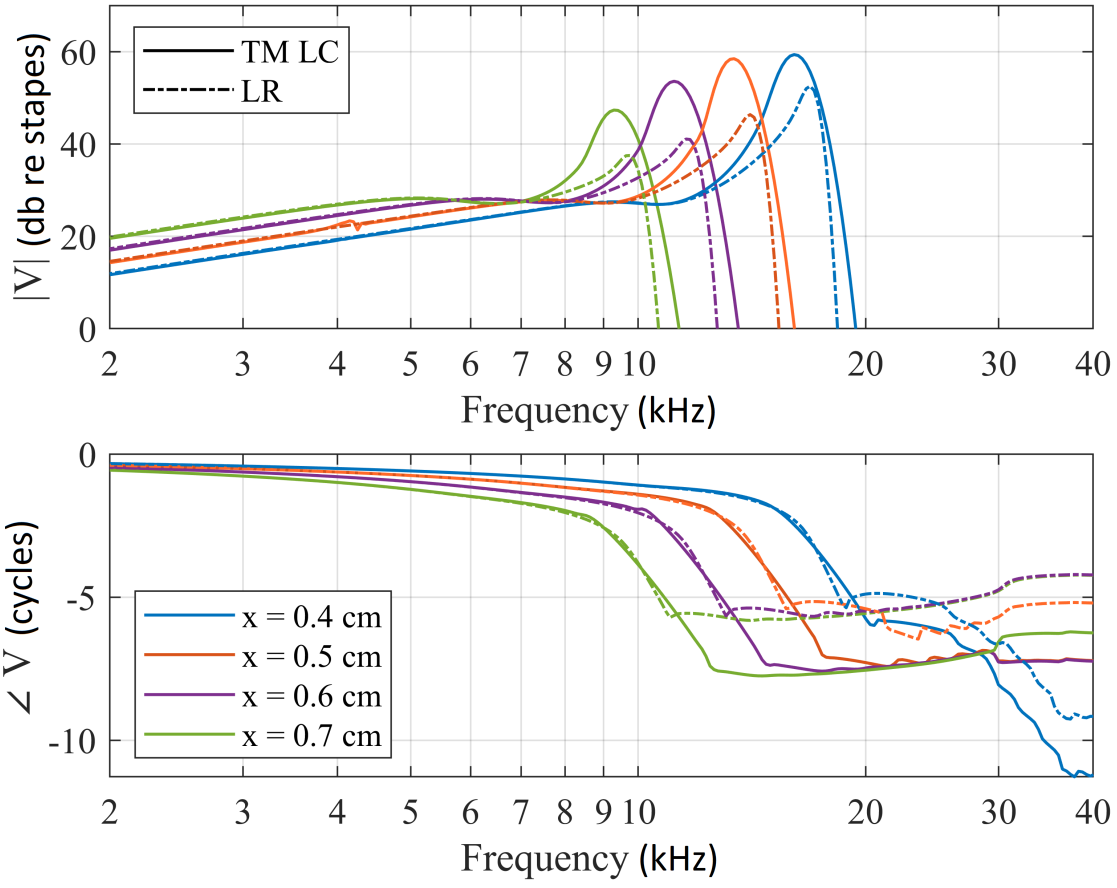

Figure 6.3: Prediction of the BM response relative to the stapes as a function of the frequency in the active case, with TM longitudinal coupling only, at different longitudinal locations. The dashdotted lines are from the active locally reacting case (LR) (Fig. 5.6) while the solid lines are the active case with TM longitudinal coupling only(TM LC).

Table 6.2: Characteristic frequency, amplification and Q_{10dB} at various position in the case with TM longitudinal coupling only, represented in Fig. 6.3.

Position (cm)	CF (kHz)	Amplification (dB)	$Q_{10\,\mathrm{dB}}$
0.40	16.08	31.76	6.00
0.50	13.39	29.44	5.99
0.60	11.02	25.61	5.79
0.70	9.17	18.85	4.75

6.4.3 Active case with both TM and electrical longitudinal coupling

Figure 6.4 shows the prediction of the BM response, in the active case, with both TM and electrical longitudinal coupling. For comparison, the active case with only TM longitudinal coupling, in Table 6.2, derived in the previous section, is also included. As reported in Table 6.3, with respect to the case with only TM longitudinal coupling, we have an increase in both the amplitude and in $Q_{10\,\mathrm{dB}}$ and the peak of the response is shifted to the right. Furthermore, the discontinuity in the amplitude response at about 4 kHz is not present in this case.

Table 6.3: Characteristic frequency, amplification and Q_{10dB} at various position in the case with both TM and electrical longitudinal coupling, represented in Fig. 6.4.

Position (cm)	CF (kHz)	Amplification (dB)	$Q_{10\,\mathrm{dB}}$
0.40	17.3	35.98	5.49
0.50	14.24	34.73	6.17
0.60	11.71	29.41	6.26
0.70	9.75	22.6	6.25

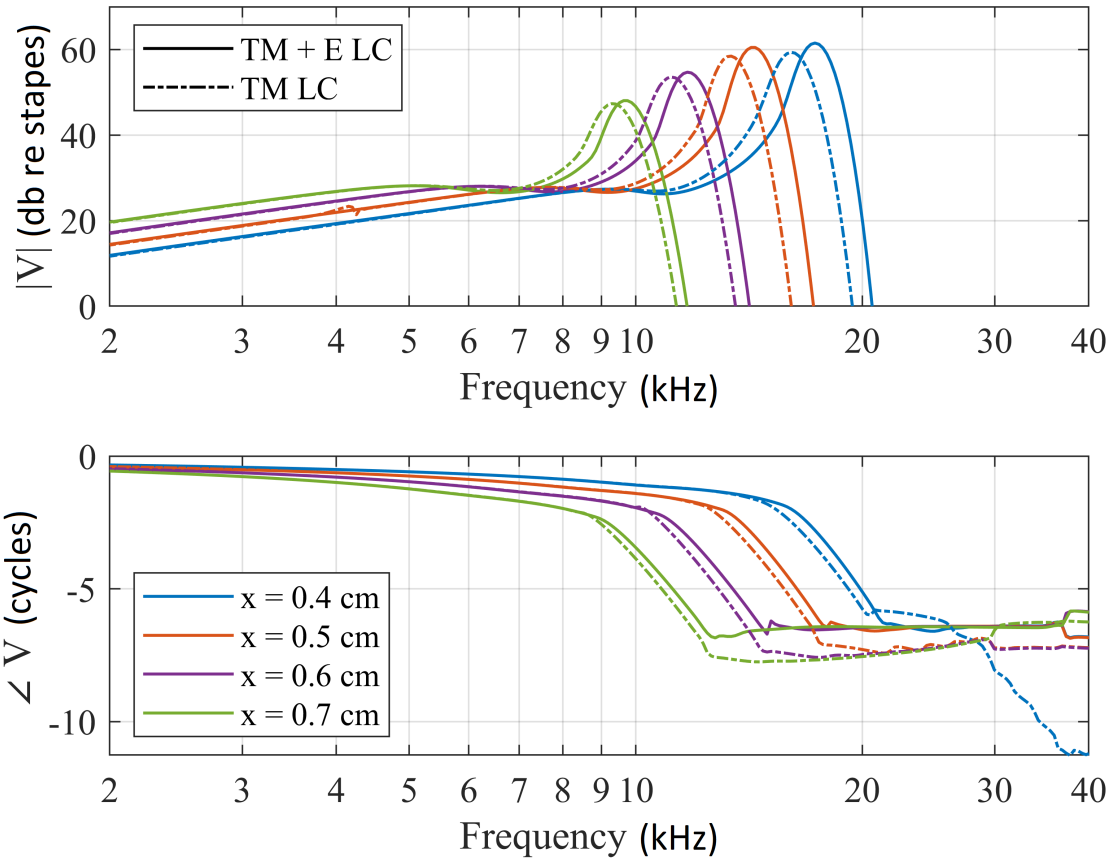

Figure 6.4: Prediction of the BM response relative to the stapes as a function of the frequency in the active case, with TM, BM and electrical longitudinal coupling, at different longitudinal locations. The dashdotted lines are from the active case with TM longitudinal coupling (TM LC) (Fig. 6.3) while the solid lines are the active case with both TM and electrical longitudinal coupling (TM + E LC).

6.4.4 Active case with both TM and BM longitudinal coupling.

Figure 6.5 shows the prediction of the BM response, in the active case, with TM and BM longitudinal coupling. For comparison, the active case with only TM longitudinal coupling, derived in the Section 6.4.2, is also included. The same value of ϵ_3 is used. As reported in Table 6.3, with respect to the case with only TM longitudinal coupling, we have a slightly increase in both the amplitude and in $Q_{10\,\mathrm{dB}}$ and the peak of the response is shifted to the right. However, these increases are less than those observed with electrical longitudinal coupling. As seen in the case of TM and electrical longitudinal coupling, the discontinuity in the amplitude response at about 4 kHz is not present.

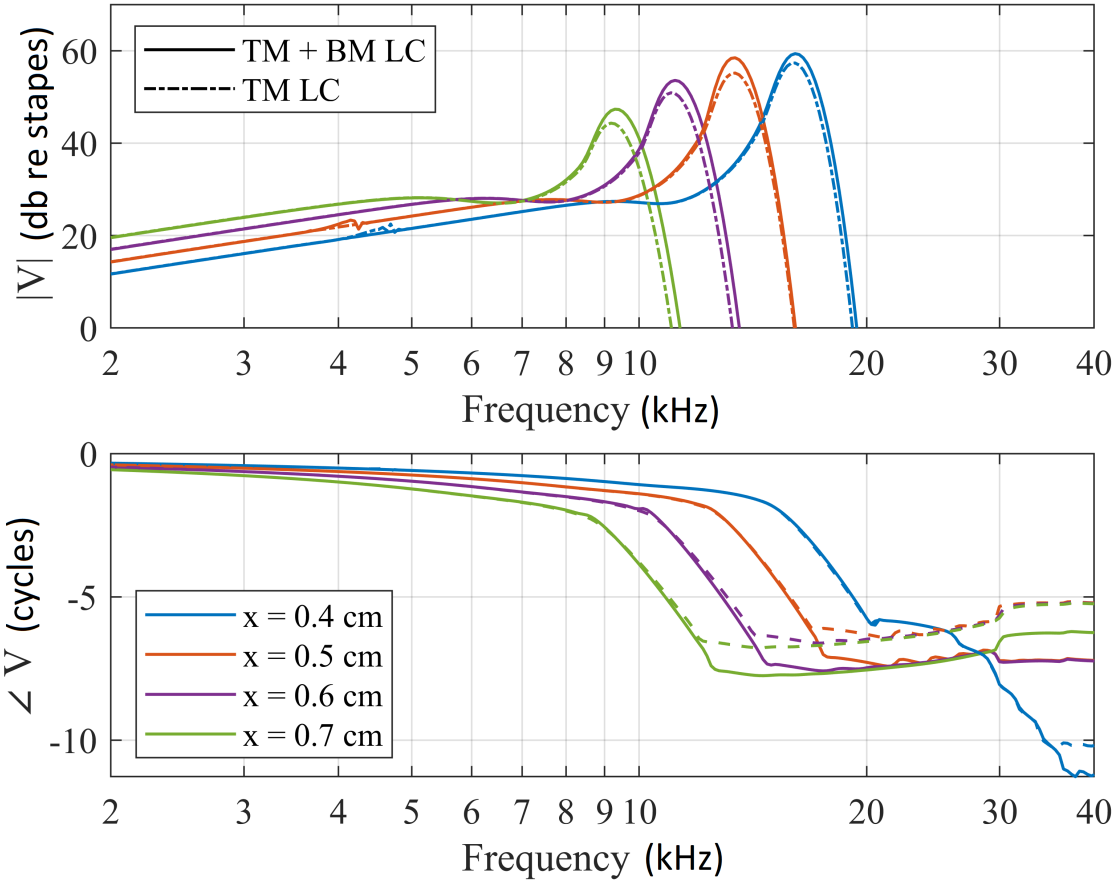

Figure 6.5: Prediction of the BM response relative to the stapes as a function of the frequency in the active case, with TM and BM longitudinal coupling, at different longitudinal locations. The dashdotted lines are from the active case with both TM longitudinal coupling (TM LC) (Fig. 6.3) while the solid lines are the active case with TM and BM longitudinal coupling (TM + BM LC).

Table 6.4: Characteristic frequency, amplification and Q_{10dB} at various position in the case with both TM and BM longitudinal coupling, represented in Fig. 6.5.

Position (cm)	CF (kHz)	Amplification (dB)	$Q_{10\,\mathrm{dB}}$
0.40	16.03	33.82	6.92
0.50	13.39	32.71	6.52
0.60	11.15	28.29	5.67
0.70	9.29	21.89	5.11

6.4.5 Active case with TM, electrical and BM longitudinal coupling.

Figure 6.6 shows the prediction of the BM response, in the active case, with TM, electrical and BM longitudinal coupling. For comparison, the active case with TM and electrical longitudinal coupling, derived in the previous section, is also reported. The corresponding results from the finite element model (Meaud and Grosh, 2010) are also plotted in Fig. 6.6 as dashed lines [1]. If we compare the amplitude response of the elemental formulation to that from the finite element model, we can see that, as in the passive case in Section 2.5.1, the peak of the response is shifted slightly to the right and the slope at the lowest frequencies is slightly different, again possibly due to the different way in which the fluid coupling is calculated in the two models. As we can see, when the BM longitudinal coupling is introduced in this case, there is only a slight difference in the amplitude response. Indeed, all the values of the CF, the amplification and the $Q_{10\,\mathrm{dB}}$ are the same as those reported in Table 6.3.

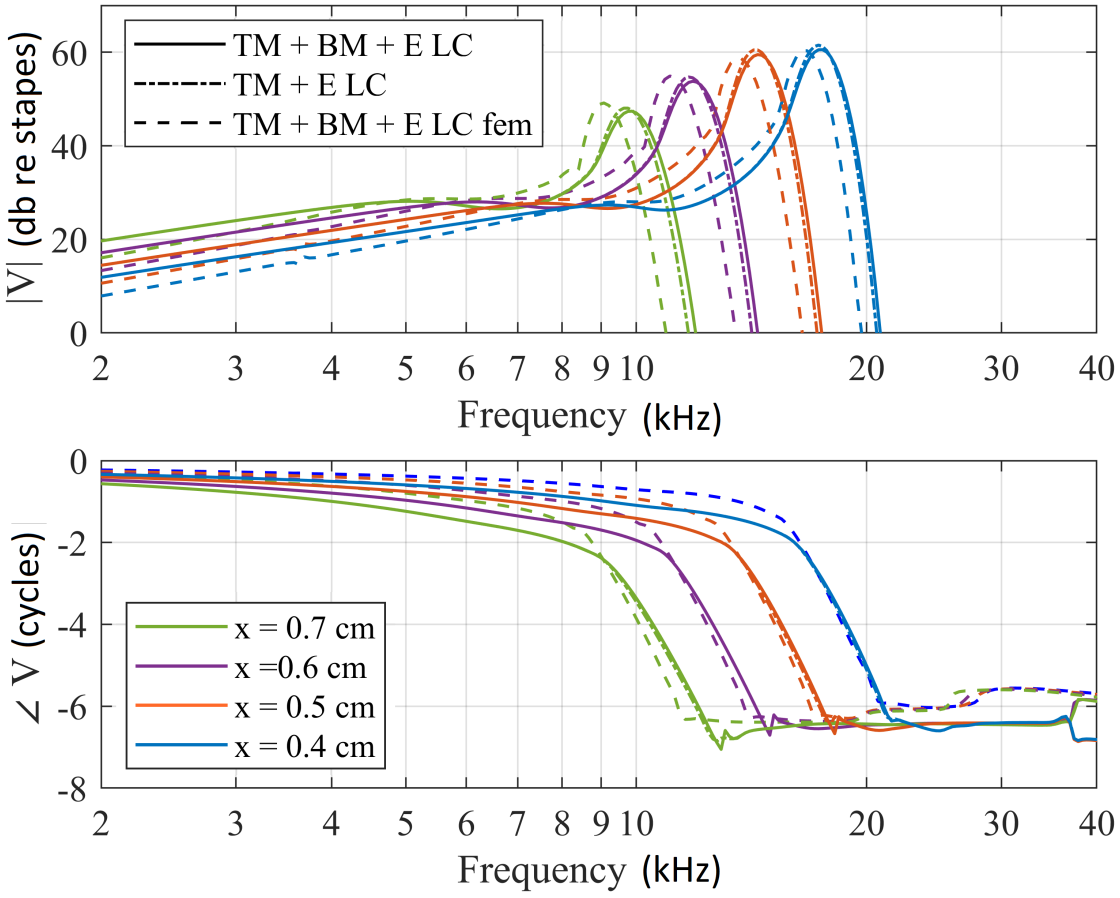

Figure 6.6: Prediction of the BM response relative to the stapes as a function of the frequency in the active case, with BM, TM and electrical longitudinal coupling, at different longitudinal locations. The dashdotted lines are from the active case with TM, BM and electrical longitudinal coupling (TM + BM + E LC) (Fig. 6.4) while the solid lines are the active case with TM and electrical longitudinal coupling (TM + E LC). The dashed lines are those from the corresponding finite element model with TM, BM and electrical longitudinal coupling.

[1] The data for the Finite Element model were kindly provided by Apoorva Khadilkar, from Karl Grosh's laboratory.

6.5 BM response with 1D fluid coupling

In the previous sections and in the locally reacting case discussed in Chapter 5, we have determined the BM response for an elemental model with 3D fluid coupling. To understand the effect of different types of fluid coupling, in this section we derive the response of the BM with 1D fluid coupling. This can be done by using the fluid matrix $\mathbf{Z_{fc}^{1D}}$ in Eq. (5.8) instead of the full 3D fluid matrix. Furthermore, in this case, the mass of the BM is increased, to account for the fluid loading (Ni and Elliott, 2015). The value of ϵ_3 has been chosen, as before, as the maximum before which discontinuities appear in the amplitude and phase response. With respect to the corresponding cases with 3D fluid coupling, ϵ_3 is decreased by 10% in all the cases.

Figures 6.7 and 6.8 show the predictions of the BM response at $x = 4\,\text{mm}$ for the locally reacting case and with different types of longitudinal coupling with 1D fluid coupling, compared to the case with 3D fluid coupling derived in the previous sections and in Chapter 5. In the locally reacting case in Fig. 6.7, the amplitude of the peak and the Q ratio are grater in the 1D case with respect to the 3D case. Furthermore, the phase variation around the characteristic frequency is lower. In the cases with longitudinal coupling in Figs. 6.7 and 6.8 some common features can be noticed: with respect to the 3D case, in the 1D case the amplitude and the position of the peak of the response are similar, while the Q ratio is greater. Furthermore, the phase variation is lower around the characteristic frequency. It can also be noticed that the amplitude has a notch before the peak response and that the phase does not decrease monotonically but increases in the leading phase direction before the characteristic frequency. These two last characteristics have also been notice by (Neely and Kim, 1986), in which an active model of the cochlea with 1D fluid coupling is also used.

As we discussed in Section 5.2.1, the model with 1D fluid coupling is suitable to describe a passive model of the cochlea, because it is valid under the condition that the shortest wavelength of the slow wave is greater than the cross-sectional dimension of the fluid chamber (de Boer, 1996). On the other hand, in the active case, around the CF, the wavelength of the BM motion becomes comparable with the chamber height and a 3D description of the fluid dynamics is necessary.

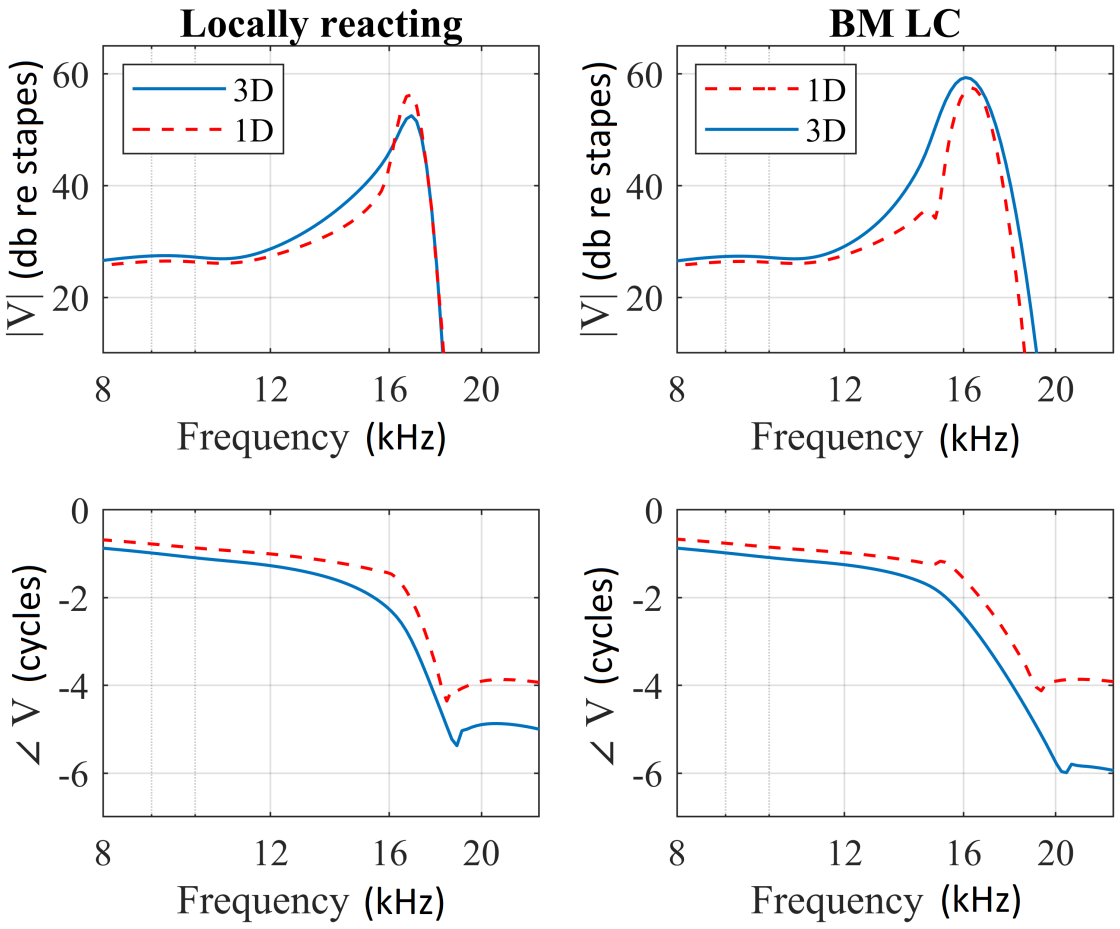

Figure 6.7: Comparison between the BM response, as a function of the frequency,(solid blue) with 1D and (dash-dot) with 3D fluid coupling, in the (left) locally reacting case and (right) with BM longitudinal coupling.

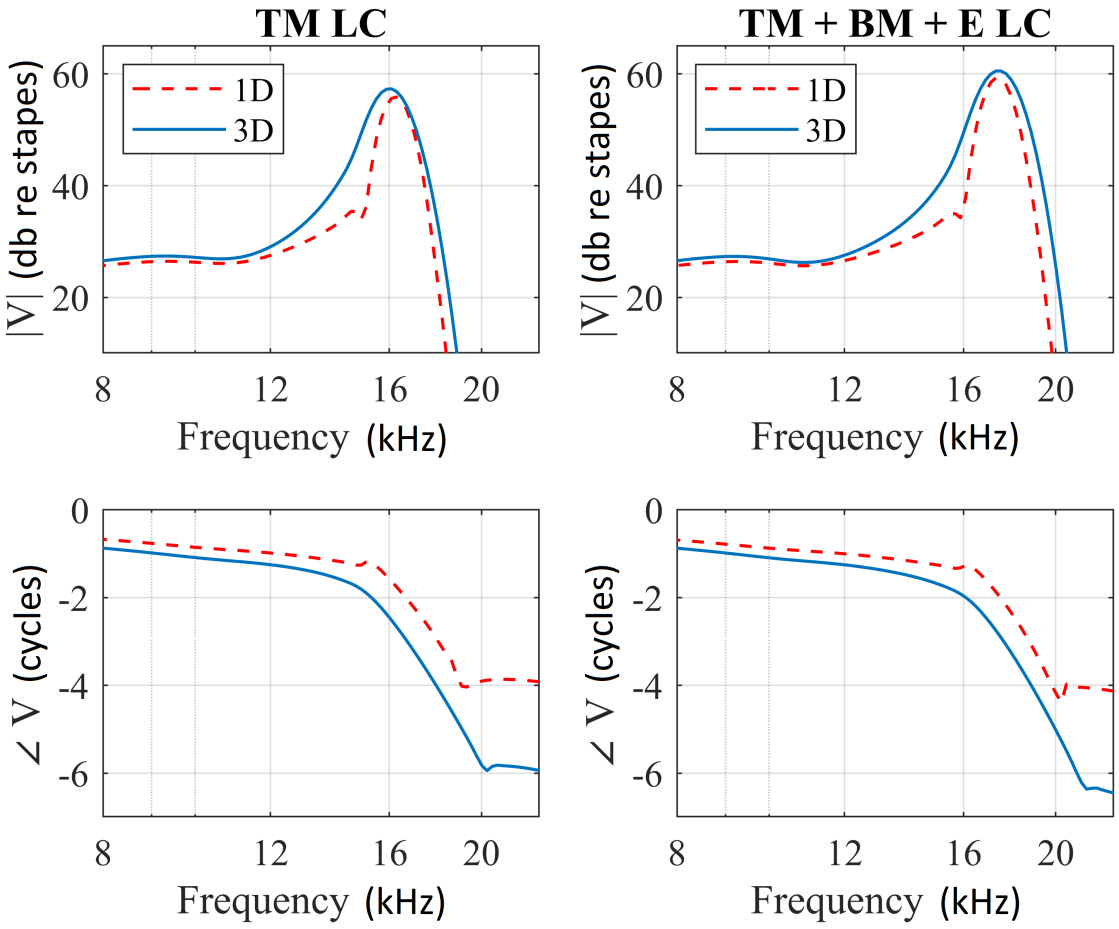

Figure 6.8: Comparison between the BM response, as a function of the frequency,(solid blue) with 1D and (dash-dot) with 3D fluid coupling, (left) with TM longitudinal coupling and (right) with TM, BM and electrical longitudinal coupling.

6.6 Conclusions

The effects of the various type of longitudinal coupling can be seen by comparing the various cases at the position $x = 4\,\mathrm{mm}$, in Fig. 6.9. The mechanical longitudinal coupling by the TM is the most important, both in stabilizing the system and in obtaining an amplification that is similar to that observed in experimental data. Indeed, in this case, we are able to increase the electromechanical coupling coefficient ϵ_3 by 40% and obtain a response that is more similar in amplitude and in sharpness, as measured by $Q_{10\,\mathrm{dB}}$, to that obtained in the data, for example in (Zheng et al., 2007). The electrical longitudinal coupling, on the other hand, shifts the peak frequency of the BM response. The BM longitudinal coupling also helps in stabilizing both the amplitude and phase response, but its effect is not as significant as that due to the electrical and TM longitudinal coupling.

In this chapter the stability of the response was inferred from discontinuities in the frequency dependence of the amplitude or the phase of the coupled response. A more formal method of assessing stability would be to examine the poles of a state space model. (Bowling et al., 2019) for example, using a state space formulation (Meaud and Lemons, 2015) of a finite element model of the gerbil cochlea, studied how the stability of the cochlea depends on the viscoelastic properties of the TM. Their model is based on that by (Meaud and Grosh, 2010), which includes longitudinal coupling by the BM and TM. However, in (Bowling et al., 2019) longitudinal coupling is added also to the TM bending mode. They showed that by reducing either viscous or elastic coupling of the TM, the model exhibits various unstable modes, resulting in a BM frequency response which is not smooth but characterised by many spectral peaks. Furthermore, if cochlear roughness is introduced into the model, in the form of random perturbations to the electromechanical coupling coefficient ϵ_3, the reduction of the viscoelastic coupling by the TM corresponds to an increase in the generation of spontaneous otoacustic emission.

The results presented in this chapter, as summarised in Fig. 6.9 are broadly similar to those from the longitudinal coupling study of (Meaud and Grosh, 2010), who used a finite element model. These authors adjusted the OHC coupling coefficient, ϵ_3, for each of the models to give the same gain the BM response at the characteristic frequency, which was about 25 dB in their case. In the present study the OHC coupling coefficient was increased by about 40% once the TM coupling was introduced, but was otherwise kept constant.

The change of the BM admittance with longitudinal coupling is more difficult to represent than in the locally reacting case, since the BM velocity not only depends on the excitation position along the cochlea, but also on the distance away from the excitation position, since the $\mathbf{Y_{BM}}$ matrix is no longer diagonal. This is discussed for the case of TM longitudinal coupling in the following chapter, which also describes a method of calculating the wavenumber distribution from the spatial distribution of the BM admittance, and so links the model back to the wave description for the passive cochlea in Chapter 3 .

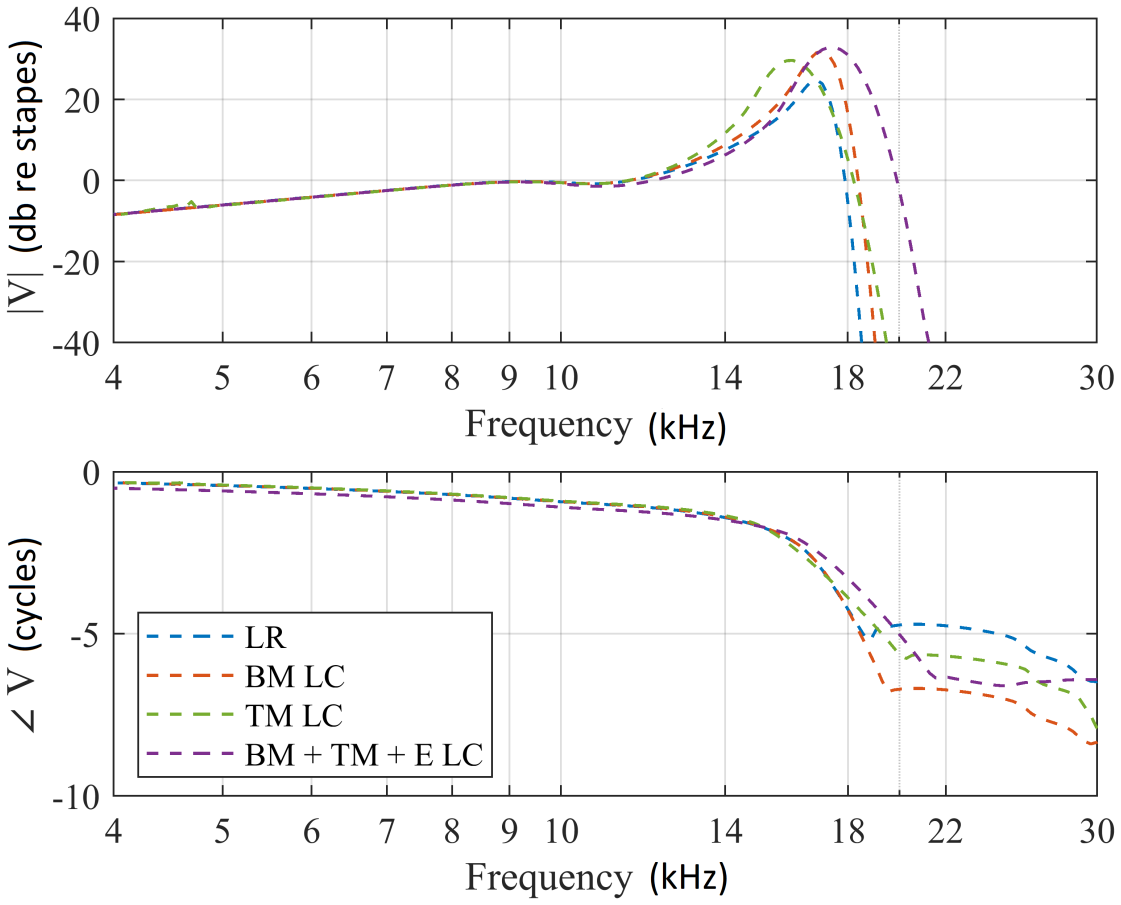

Figure 6.9: Comparison of the BM amplitude (top) and phase (bottom) response at $x = 4\,\text{mm}$ for the locally reacting case (LR), the case with BM longitudinal coupling (BM LC), TM longitudinal coupling (TM), and BM, TM and electrical longitudinal coupling (BM + TM + E LC).

Chapter 7

Wavenumber for propagation with a longitudinally coupled OoC

7.1 Introduction

In this chapter, we present a method to derive the wavenumber distribution in the case of a cochlear model with longitudinal coupling, following on from the discussion of the wavenumber for the locally reacting passive cochlea in Chapter 3 . The method is used to derive the wavenumber distribution of the main travelling wave for the model with TM longitudinal coupling in Section 6.1, but is more general and the wavenumber distribution corresponding to other wave types can be derived.

7.2 Wavenumber derivation

In the wavenumber domain, the modal pressure, $P(k)$, the modal BM velocity, $V(k)$, and the fluid coupling impedance, $Z_{fc}(k)$, are related according to the equation (Steele and Taber, 1981; Elliott et al., 2011):

$$P(k) = Z_{fc}(k)V(k), \tag{7.1}$$

where k is the complex wavenumber. Similarly the BM response can be written in the wavenumber domain as:

$$V(k) = -Y_{BM}(k)P(k), \tag{7.2}$$

where $Y_{BM}(k)$ is the BM admittance transformed into the wavenumber domain, as discussed below for a longitudinally coupled cochlea. Eqs. (7.1) and (7.2) are simultaneously satisfied if a value of k exists for which:

$$Z_{fc}(k) = -\frac{1}{Y_{BM}(k)}. \tag{7.3}$$

In the case of 1D fluid coupling, the fluid coupling impedance can be written as (Ni and Elliott, 2015):

$$Z_{fc}(k) = Z_{1D}(k) = \frac{2i\omega\rho}{k^2 h}, \tag{7.4}$$

and if the BM admittance is only locally reacting then $Y_{BM}(k)$ is independent of k and can be written as Y_{BM}. So Eq. (7.3) is satisfied if:

$$k = \pm\sqrt{\frac{-2i\omega\rho}{h} Y_{BM}}, \tag{7.5}$$

which is equivalent to Eq. (3.6) in Chapter 3 if the fluid is inviscid and incompressible.

More generally, however, Eq. (7.3) is true for 3D fluid coupling and a longitudinally coupled OoC. The fluid coupling impedance in this case can be written as (Elliott et al., 2011):

$$Z_{fc}(k) = Z_{1D}(k) + Z_{nf}(k), \tag{7.6}$$

where $Z_{1D}(k)$ has the simple analytic form of Eq. (7.4), and $Z_{nf}(k)$ is the near fluid component. Substituting this into Eq. (7.3), we obtain:

$$Z_{1D}(k) = -\left(\frac{1}{Y_{BM}(k)} + Z_{nf}(k)\right) := -\frac{1}{Y'_{BM}}, \tag{7.7}$$

where Y'_{BM} is a modified BM impedance that takes into account both the longitudinal coupling within the OoC and the longitudinal coupling due to the near fluid coupling of the pressure, as discussed in Section 5.2.1.3 and can be written as:

$$Y'_{BM} = \left(\frac{1}{Y_{BM}(k)} + Z_{nf}(k)\right)^{-1}. \tag{7.8}$$

Since the near-field pressure is local to the BM it seems more natural to associate this with the BM dynamics than the fluid coupling. Indeed, if the near-field component of the pressure in Section 5.2.1.3 is approximated by a spatial delta function, rather than an exponential distribution, then $Z_{nf}(k)$ is no longer a function of k. If the BM is also locally reacting, so that $Y_{BM}(k)$ is independent of k, then Y'_{BM} in Eq. (7.8) is independent of k and Z_{nf} can be interpreted as an added mass on the BM due to near-fluid motion (Neely, 1985). This added mass is generally larger than the physical mass of the BM and (Elliott et al., 2011) estimated it to be $0.24\,\mathrm{kgm}^{-2}$ compared to the physical mass of the BM, which is about $0.05\,\mathrm{kgm}^{-2}$.

Using Eq. (7.4) for $Z_{1D}(k)$ in Eq. (7.7), the latter can be written as:

$$1 + \frac{2i\omega\rho}{k^2 h} Y'_{BM}(k) = 0. \tag{7.9}$$

By solving this equation for a set of values of ω, we can, in principle, determine the wavenumber as a function of the frequency. The equation can be solved geometrically by determining the intersecting points of the curves given by the real and imaginary

part of this equation:

$$\begin{cases} \Re\{\frac{Y'_{BM}(k)}{k^2}\} = 0 \\ 1 - \frac{2i\omega\rho}{h}\Im\{\frac{Y'_{BM}(k)}{k^2}\} = 0. \end{cases} \tag{7.10}$$

To solve this system of equations, we need to determine the modified BM admittance as a function of the wavenumber, $Y'_{BM}(k)$, from the admittance as a function of ω and x, obtained from the elemental model. This can be done by the following steps:

1. calculate the admittances corresponding to excitation from a pressure difference at the position x_0 and the BM velocity measured at various positions around x_0, i.e. $x = x_0 + x'$ where, in the elemental model, $x' = n\Delta$, with $n = 1, 2, ..., N$:

$$Y_{BM}(\omega, x_0, n\Delta) = \frac{v(x_0 + n\Delta x)}{p(x_0)}; \tag{7.11}$$

2. from $Y_{BM}(\omega, x_0, n\Delta)$ derive, for a particular frequency ω_i, the impedance as a function of the relative position $x' = x - x_0$, $Y_{BM}(\omega_i, x_0, x')$;

3. take the Fourier transform of $Y_{BM}(\omega_i, x_0, x')$ to obtain the admittance as a function of the wavenumber for x_0 and ω_i, $Y(\omega_i, x_0, k)$; this is valid when the imaginary part of the wavenumber, γ, is zero.

4. to obtain the Fourier transform for a non-zero value of γ, multiply $Y_{BM}(\omega_i, x_0, x')$ by $e^{2\pi\gamma x'}$ and then again take the Fourier transform. By repeating this procedure for a range of values of γ, $Y(k)$ for complex values of k is obtained and the curves given by Eq. (7.10) that satisfy Eq. (7.8) can be plotted. Their crossing points gives the real and imaginary part of the wavenumber, k, for the particular frequency chosen, ω_i.

5. steps (2)-(4) are repeated for the whole frequency range of interest.

In general, for a particular frequency, there is more than one solution to Eq. (7.10), corresponding to different type of waves. In the next sections, we will discuss how to choose between these solutions to determine the wavenumber distribution for a particular wave type.

7.3 Passive, locally reacting case, with 1D fluid coupling

To illustrate the procedure to derive the wavenumber, we consider the passive, locally reacting case, which was solved analytically in Chapter 3. We will derive the wavenumber distribution using the procedure outlined in the previous section and then compare it to that derived in Chapter 3 analytically.

In this case the BM admittance is given by Eq. (3.7) and does not depend on the wavenumber, so that Eq. (7.9) becomes:

$$1 + \frac{2i\omega\rho}{k^2 h} Y_{BM}(\omega) = 0. \tag{7.12}$$

At the position $x = 20\,\text{mm}$ and at the angular frequency of $\omega = 2\pi \times 135\,\text{Hz}$, the curves corresponding to the two parts of Eq. (7.10) are shown in Fig. 7.1. Their crossing points corresponds to the solutions of the wavenumber equation for this particular frequency and position. The solution with a positive real part of the wavenumber corresponds to the wave propagating in the positive direction, while the solution with a negative real part of the wavenumber refers to the wave propagating in the opposite direction. As we are interested in the wavenumber distribution of the travelling wave, we choose the solution with a positive value of κ. At the characteristic frequency for this position, which is 1.15 kHz, the two curves of Eq. (7.10), in this case, are shown in Fig. 7.2. At 20 kHz, the corresponding curves are shown in Fig. 7.3.

By repeating this procedure for a set of frequencies, we obtain a set of complex values of k, given by the crossing points of the two curves. These are shown in Fig. 7.4 as blue asterisks, together with the wavenumber distribution obtained analytically from Eq. (7.5). If we solve Eq. (7.10) for all the other frequencies of interest, we can reconstruct the whole wavenumber distribution, and this is identical to the one obtained analytically.

Although this simple example illustrates the method of finding the complex wavenumber for a given position on the cochlea, it also demonstrates the complexity and computational effort involved in this more general method.

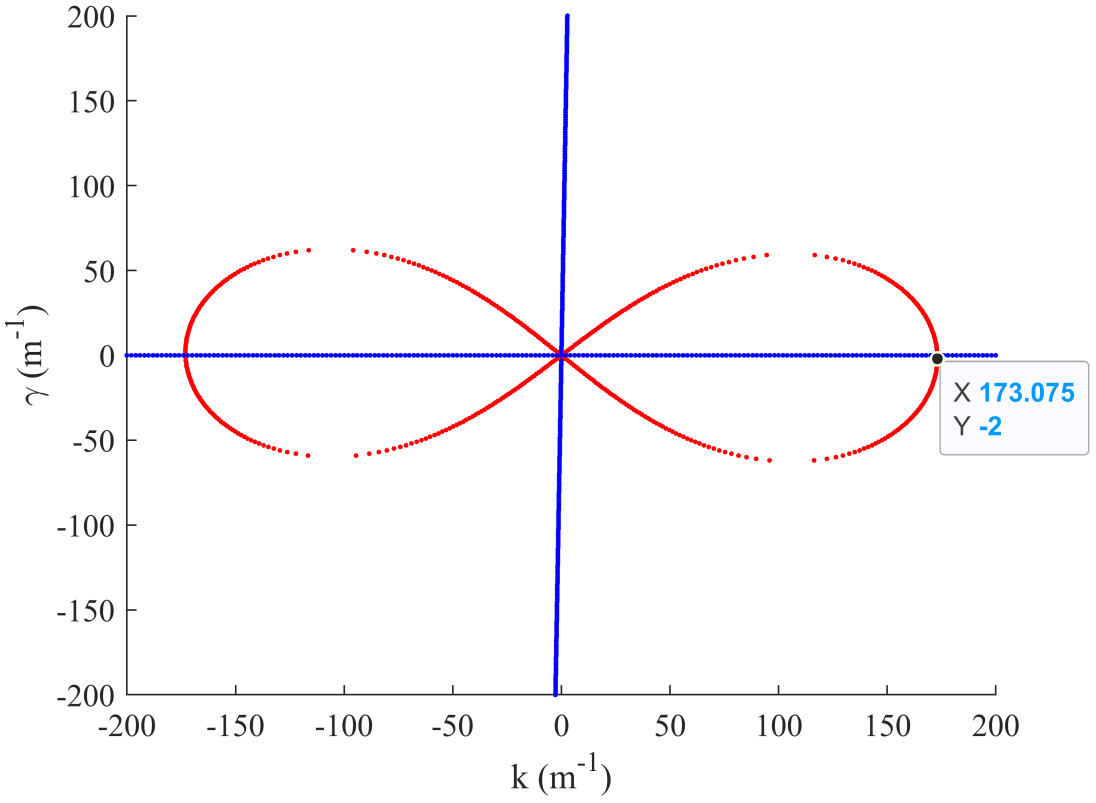

Figure 7.1: Values of the wavenumber for which the real and imaginary part of Eq. (7.12) are zero at a frequency of 135 Hz. The crossing point indicated in the box is the wavenumber solution corresponding to a forward-travelling wave.

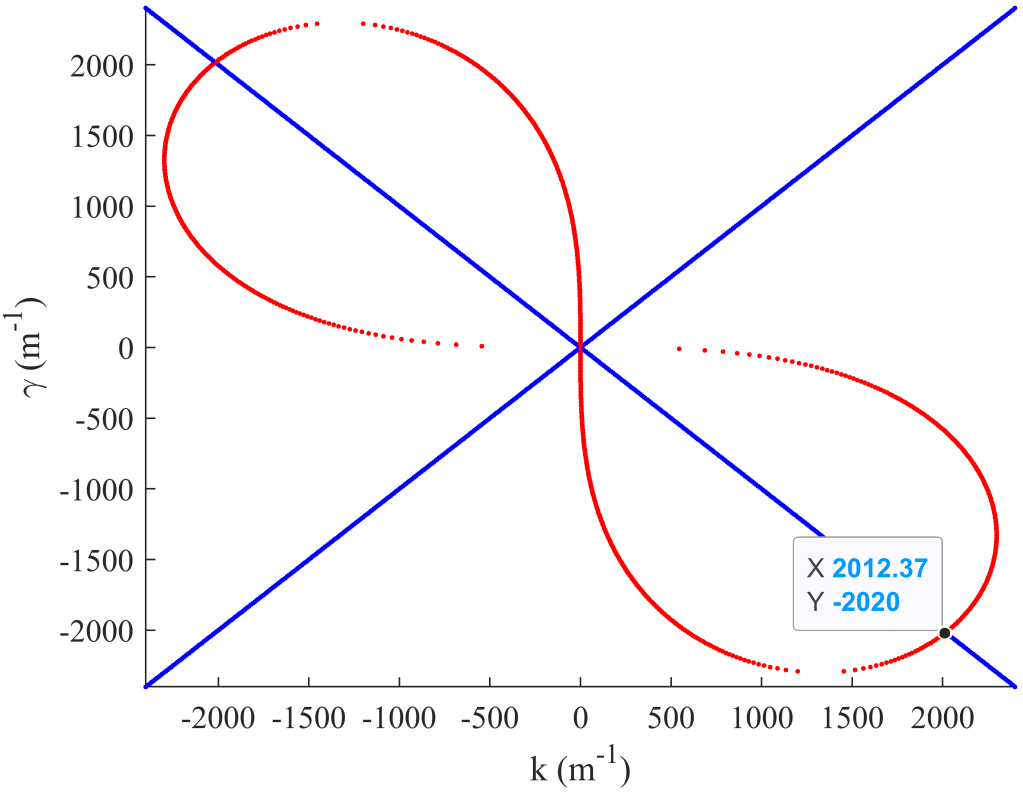

Figure 7.2: Values of the wavenumber for which the real and imaginary part of Eq. (7.12) are zero at the characteristic frequency, 1.15 kHz. The crossing point indicated in the box is the wavenumber solution corresponding to a forward-travelling wave.

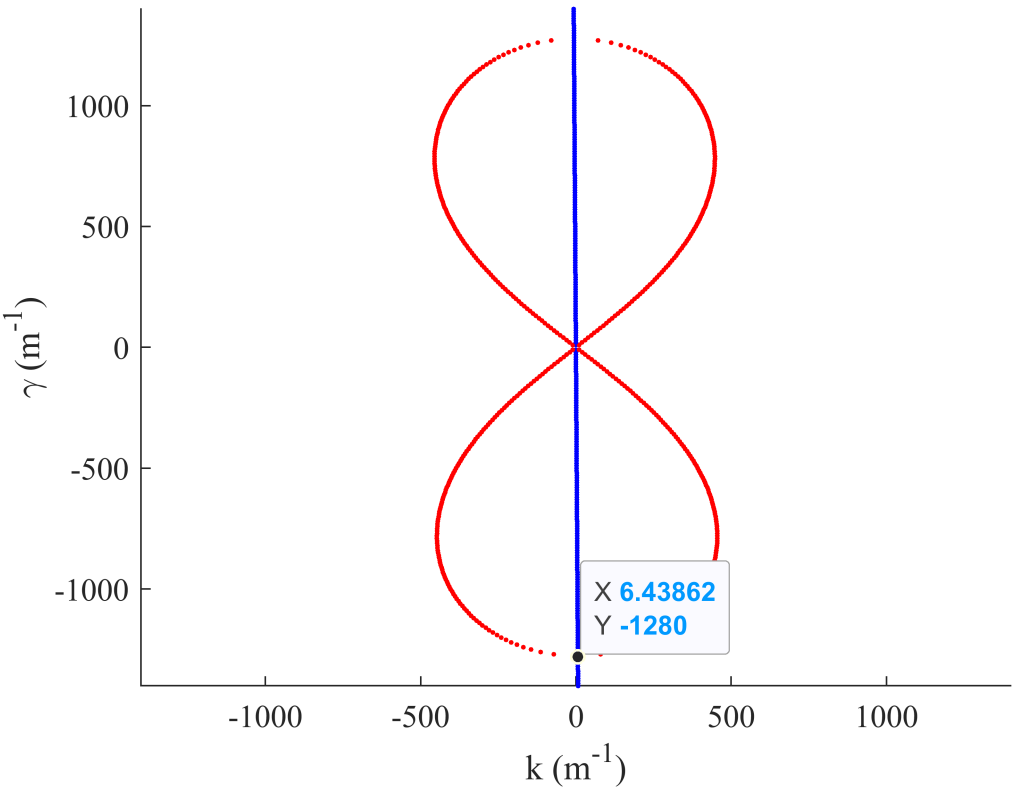

Figure 7.3: Values of the wavenumber for which the real and imaginary part of Eq. (7.12) are zero at a frequency of 20 kHz. The crossing point indicated in the box is the wavenumber solution corresponding to a forward-travelling wave.

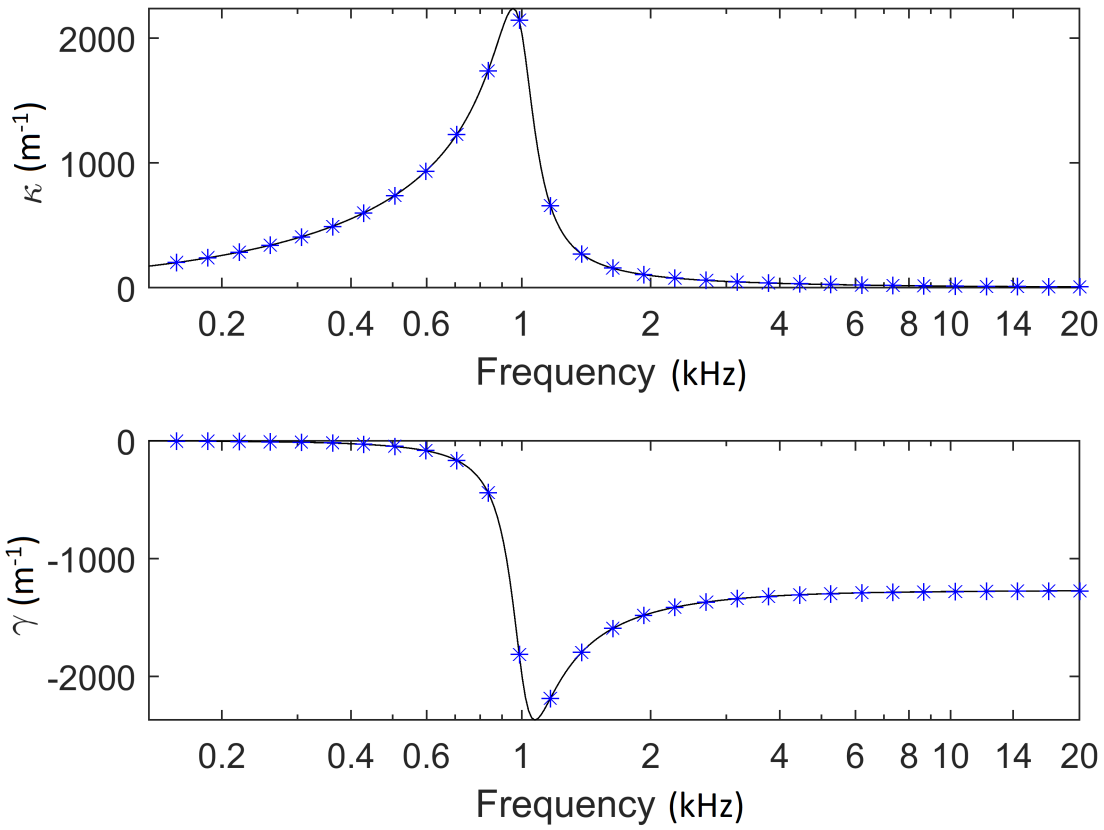

Figure 7.4: The complex wavenumber corresponding to the intersections of the real and imaginary part of Eq. (7.10), shown as blue stars. The analytical solution to the wavenumber, obtained from Eq. (7.5), is plotted as the solid curve over a wider range of frequencies.

7.4 Case with TM longitudinal coupling

In the case of a locally reacting model, the BM admittance matrix, $\mathbf{Y_{BM}}$ in Eq. (5.5), is diagonal. When longitudinal coupling is introduced, this matrix becomes non-diagonal, thus the BM velocity not only depends on the pressure acting on the excitation position x_0, but also on the pressure some distance away. This is shown in Fig. 7.5, where the absolute value and the phase of $Y'_{BM}(\omega, x_0, n\Delta)$ are plotted as a function of the frequency for different values of Δ. As defined in Eq. (7.11), $Y'_{BM}(\omega, x_0, n\Delta)$ corresponds to the ratio of the BM velocity measured at the position $x' = x_0 + n\Delta$ and the pressure difference at the position x_0. It can be seen from Fig. 7.5, calculated for the case with TM longitudinal coupling only, that this admittance has a significant value up to about $x' = x_0 \pm 25\Delta$, that is 1 mm, one side or the other compared with the excitation position.

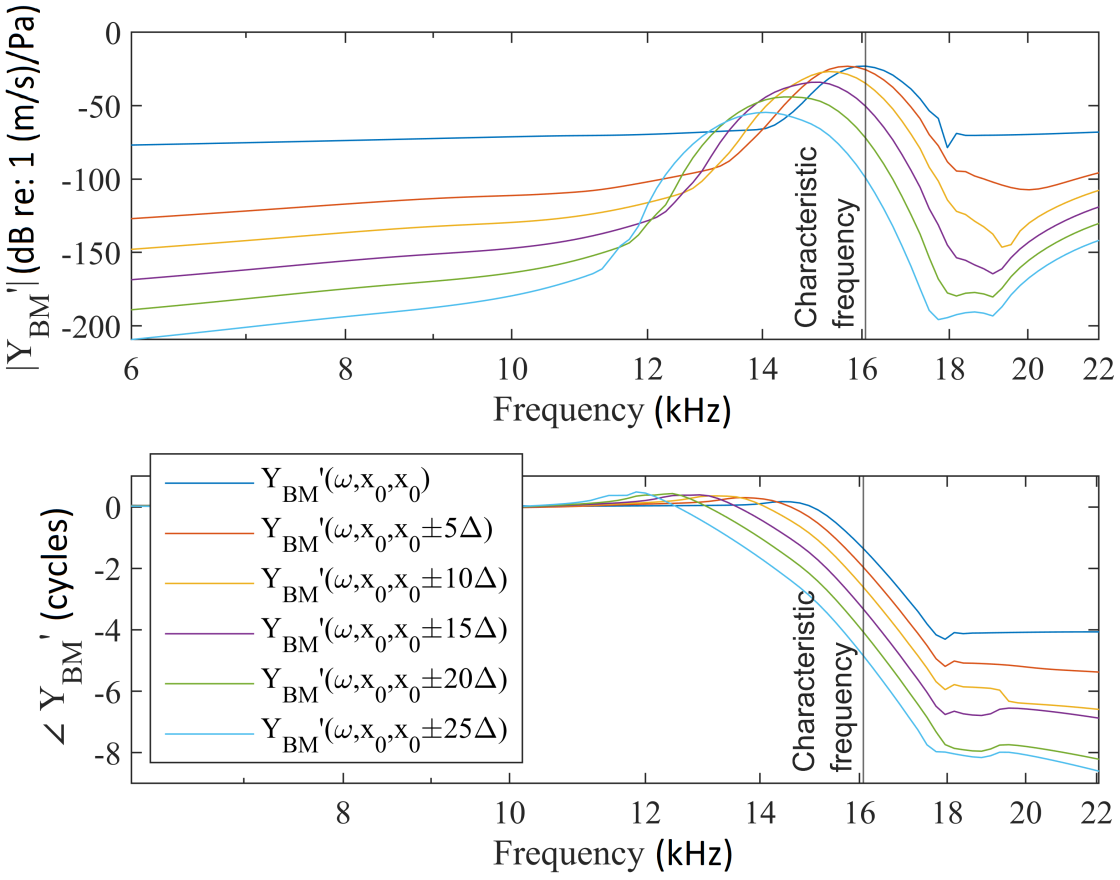

Figure 7.5: Absolute value (upper) and phase (lower) of $Y'_{BM}(\omega, x_0, \pm n\Delta)$, as a function of the frequency. $\Delta = 46\,\mu$m and $x_0 = 4$ mm.

From $Y'_{BM}(\omega, x_0, n\Delta)$, following the procedure outlined in Section 7.2, we derive the impedance as a function of the relative position, x', for a particular frequency ω_i, $Y_{BM}(\omega_i, x_0, x')$. This is shown in Fig. 7.6 for ω_i equal to the characteristic frequency ω_0, shown as a vertical line in Fig. 7.5. In the locally reacting case, $Y'_{BM}(\omega, x_0, x')$ is non-zero only for $x' = 0$. On the other hand, when longitudinal coupling by the TM is introduced, the BM admittance has a significant value up to 1 mm either side of x_0. It

is also worth noticing that $Y_{BM}(\omega_i, x_0, x')$ is symmetric with respect to x_0 in this case, as expected since the longitudinal coupling by the TM is also symmetric.

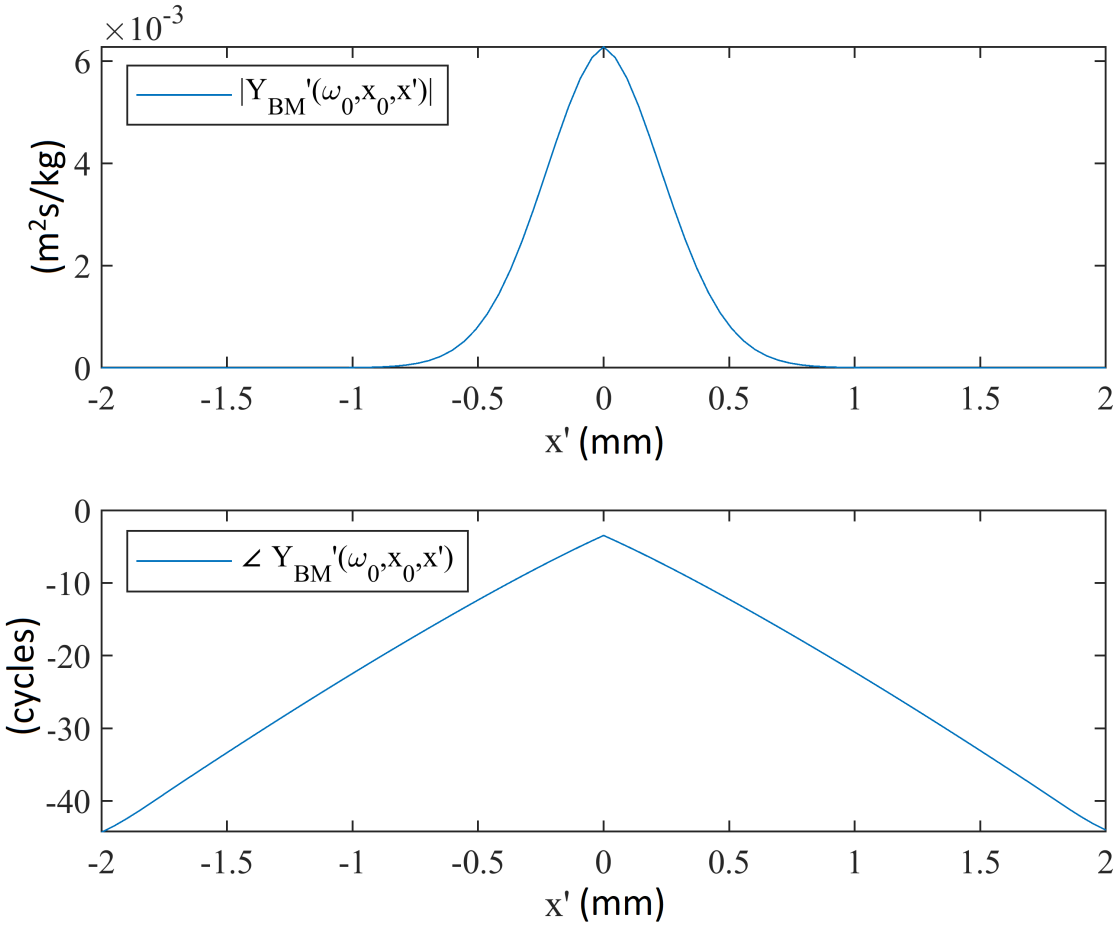

Figure 7.6: Absolute value (upper) and phase (lower) of the BM admittance at the CF, as a function of the relative position x', measured for an excitation position of $x = 4\,\text{mm}$ along the cochlea.

From $Y_{BM}(\omega_0, x_0, x')$ we can derive the admittance as a function of the real part of the wavenumber, $Y(k)$, by taking the discrete Fourier transform:

$$Y_{BM}(\omega_0, x_0, \kappa) = \sum_{l=0}^{N-1} Y_{BM}(\omega_0, x_0, x'(l))\mathrm{e}^{-2\pi\mathrm{i}\kappa l/N}, \tag{7.13}$$

which is performed using the Fast Fourier transform algorithm (FFT) in MATLAB. The result is shown in Fig. 7.7. This is valid when the imaginary part of the wavenumber, γ, is zero. To obtain the Fourier transform for other values of γ, we multiply $Y_{BM}(\omega_0, x')$ by $\mathrm{e}^{2\pi\gamma x'}$ and then again take the Fourier transform, using the FFT. If we repeat this for a range of values of γ, we obtain a set of curves in the $\kappa - \gamma$ plane, which represents the admittance as a function of the complex wavenumber, $Y(k)$. This is shown in Figs. 7.8 and 7.9 for a range of values of κ and γ.

The points for which the real and imaginary parts of $1 + 2i\omega Y'_{BM}/(k^2 h)$ are equal to zero, i.e. satisfy Eq. (7.10), give a set of curves, and their crossing points gives the real

and imaginary part of the wavenumber for the frequency chosen. In general, there are multiple crossing points, corresponding to different types of wave that could exist in the longitudinally-coupled cochlea. As $Y(k)$ is symmetric with respect to κ and γ, for every complex solution with a positive real part, corresponding to a forward travelling wave, there is a corresponding solution with a negative real part, corresponding to a backward travelling wave. This is, as stated before, a consequence of the symmetric nature of the longitudinal coupling.

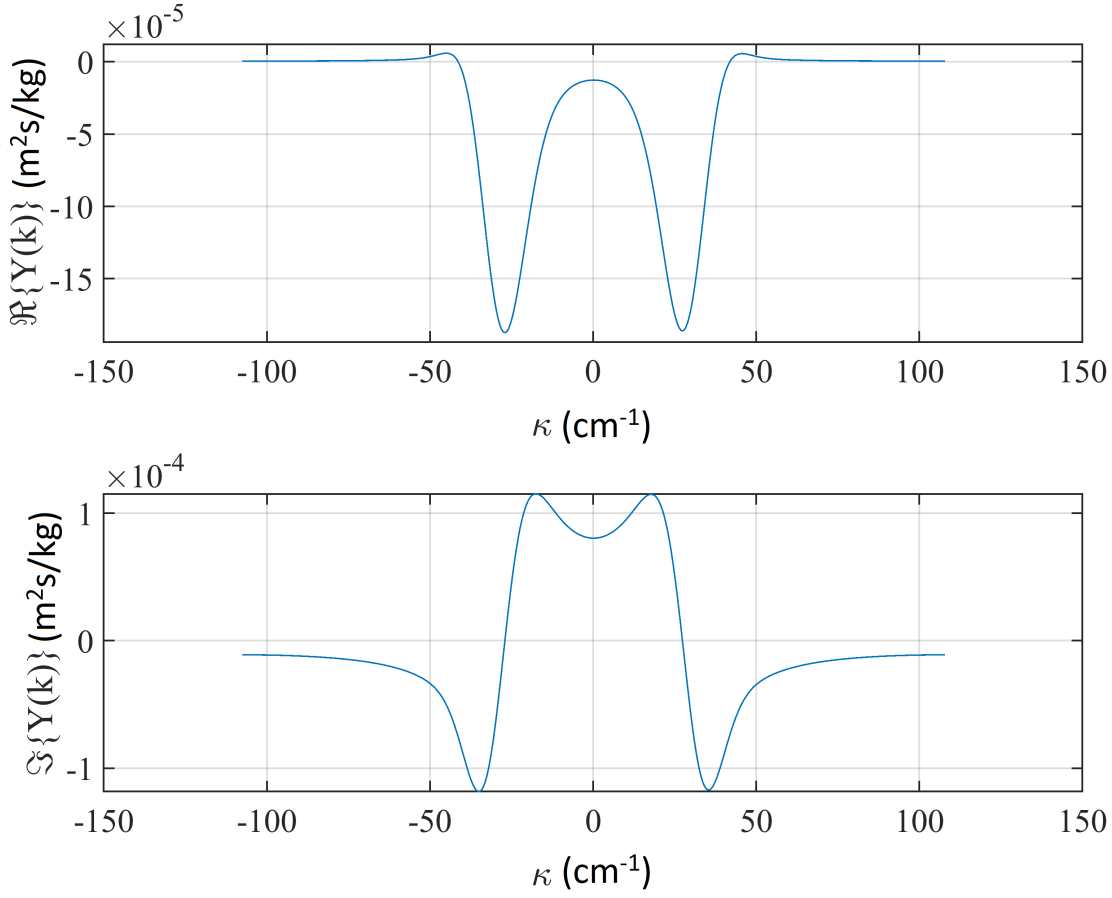

Figure 7.7: Real (upper) and imaginary (bottom) part of $Y_(\omega_0, k)$ for $\gamma = 0$.

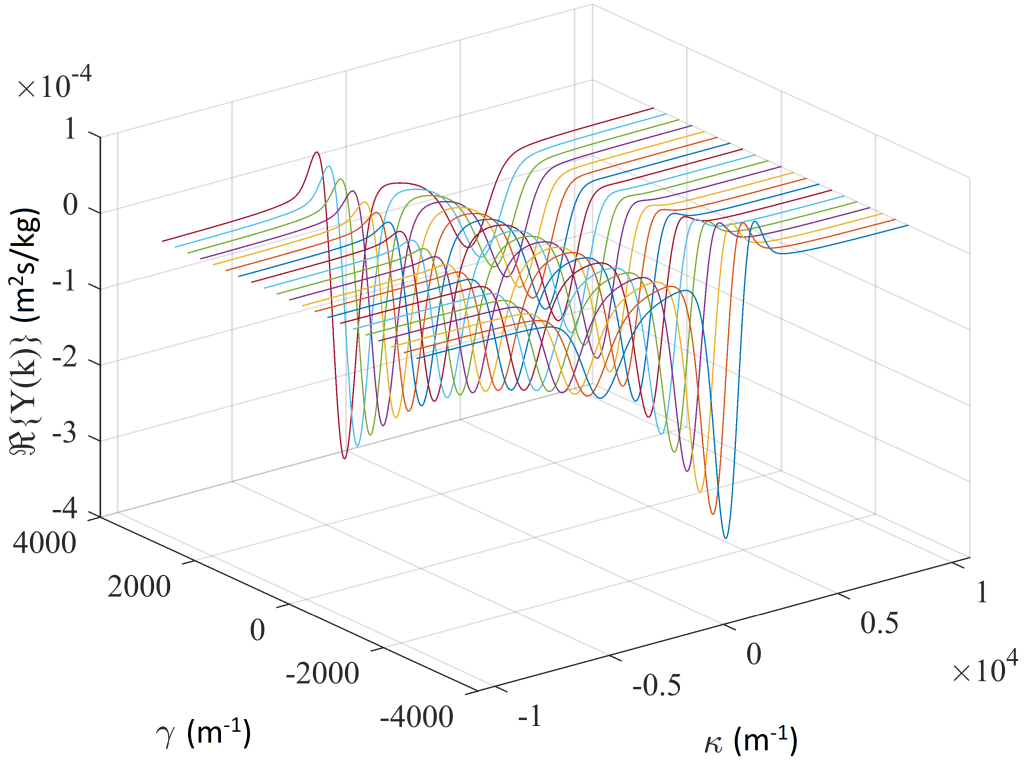

Figure 7.8: Real part of $Y_(\omega_0, k)$ for different values of κ and γ.

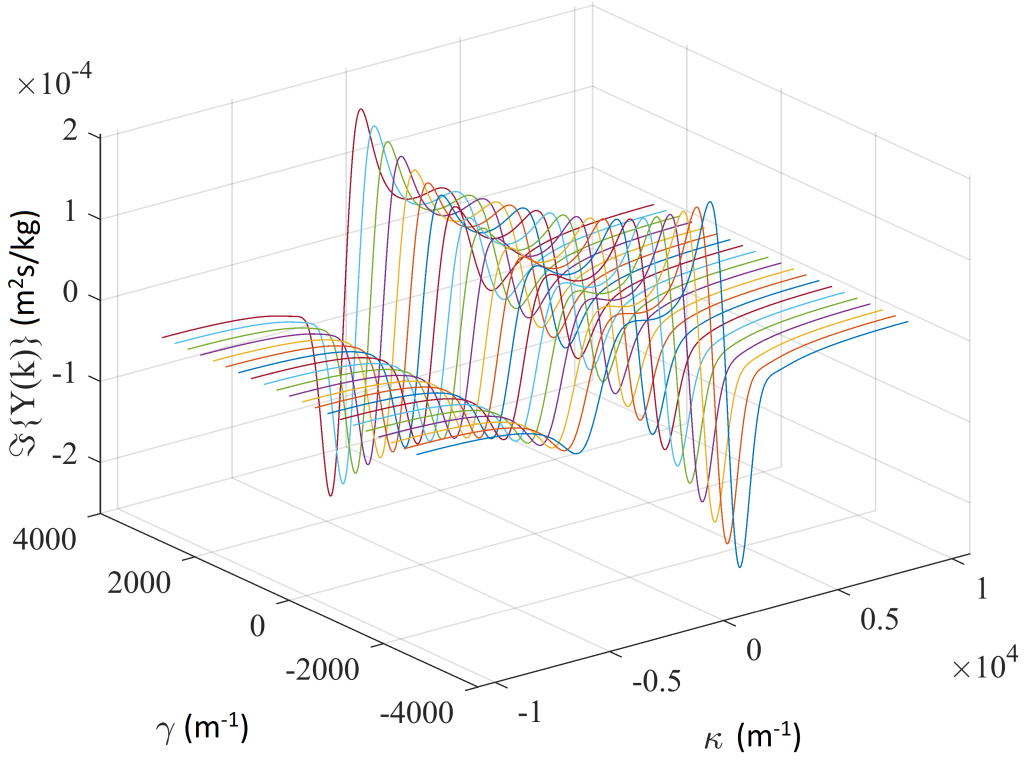

Figure 7.9: Imaginary part of $Y_(\omega_0, k)$ for different values of κ and γ.

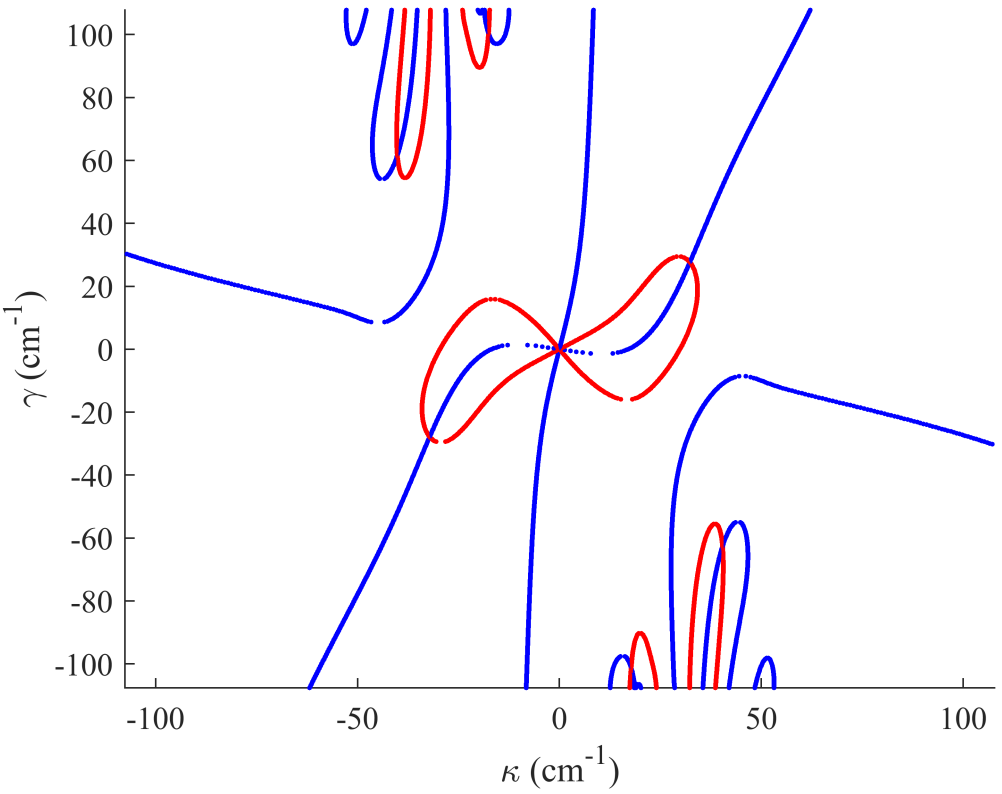

Figure 7.10: Values of the wavenumber for which the real and imaginary part of Eq. (7.12) are zero at a frequency of $\omega = 2\pi \times 13.55\,\text{kHz}$.

To obtain the wavenumber distribution corresponding to the main "slow" travelling wave, we start by deriving the solution of Eq. (7.10) at a low frequency, $\omega = 2\pi \times 554\,\text{Hz}$, by choosing the crossing point with the lowest value of the imaginary part, γ. Then, we follow the solution by solving Eq. (7.10) for the other values of the frequency. In Fig. 7.10, for example, the solution of Eq. (7.10) is shown at a frequency below the CF, i.e. $\omega = 2\pi \times 13.55\,\text{kHz}$. The main "slow" travelling wave corresponds to the crossing point with a positive value of κ and γ at this frequency, where the wave is amplified, while the other crossing points with a positive value of κ have negative values of γ, corresponds to decaying waves.

The wavenumber thus obtained is shown in Fig. 7.11. The real part has a distribution which is similar to the one obtained in the locally reacting case, while the imaginary part is positive in a region before the characteristic frequency. This is in accordance with results previously obtained by Shera (2007), shown in Fig. 1.1 in which the inverse method was used to obtain the wavenumber distribution from experimental measurements of the cochlea. As noted by Shera, a positive value of γ below the characteristic frequency corresponds to a power transfer to the Organ of Corti, thus to the amplification of the travelling wave. This can be verified in our case by calculating the time-averaged power transferred from the BM to the fluid per unit area as:

$$P(x_0, f) = -\frac{1}{2}\Re\{p(x_0, f)\overline{v}(x_0, f)\}, \tag{7.14}$$

where $p(x_0, f)$ and $v(x_0, f)$ are, respectively, the pressure and velocity distributions calculated for the coupled system in this case. The power distribution is shown in Fig. 7.12 and compared to the distribution of the imaginary part of the wavenumber. As expected, the frequency region in which the power is negative is similar to the one in which γ is positive, indicating that the travelling wave is amplified. On the other hand, the region in which the power is positive corresponds to a great negative value of γ, thus to a dissipation of the response.

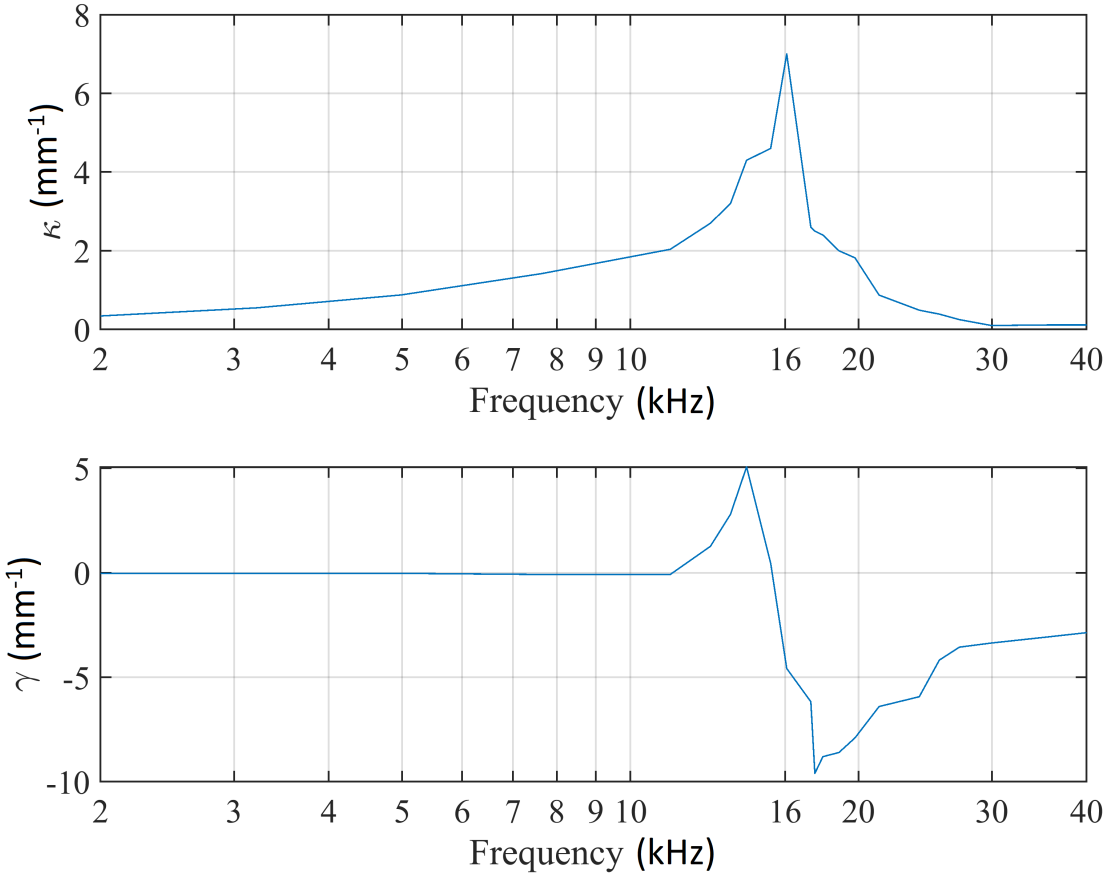

Figure 7.11: (Upper) real and (lower) imaginary part of the wavenumber distribution in the case with TM longitudinal coupling.

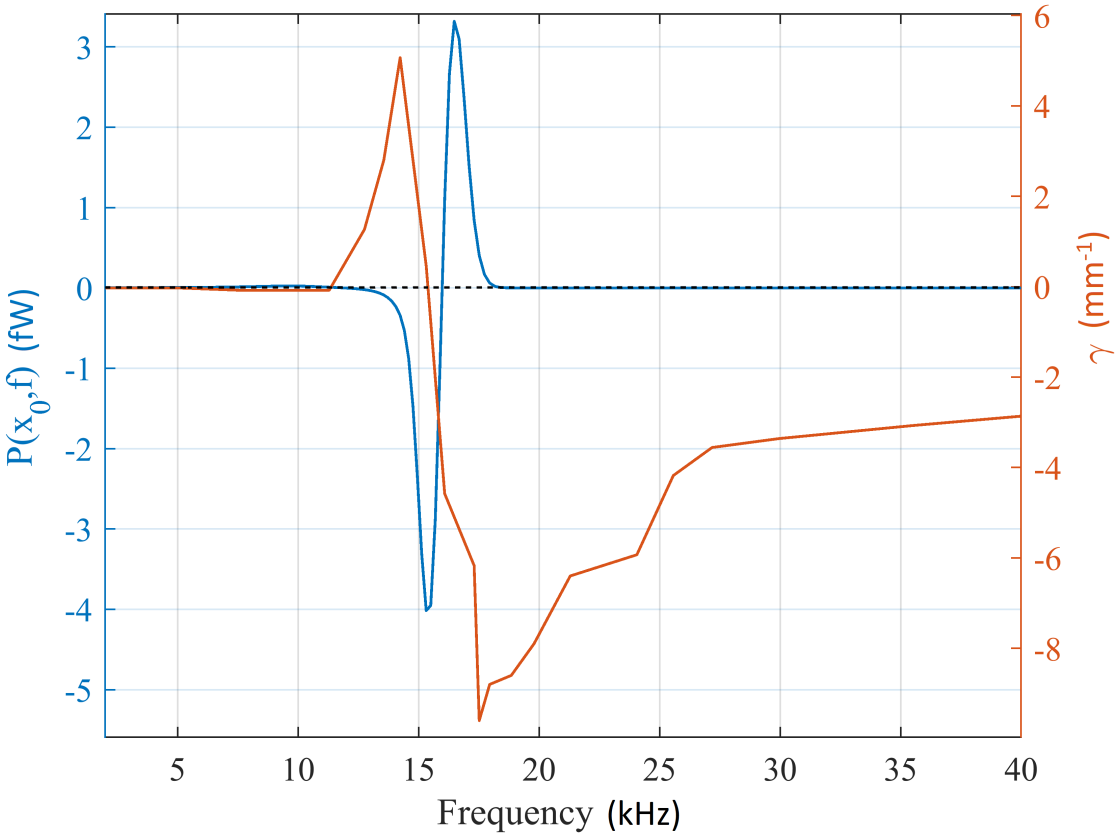

Figure 7.12: Comparison between (blue) power transfer from the BM to the fluid and (red) calculated imaginary part of the wavenumber.

7.5 Conclusions

In this chapter, we presented a method to derive the wavenumber distribution in the case of a cochlear model with longitudinal coupling.

Other methods to derive the wavenumber distribution for a longitudinally coupled organ of Corti have been presented by (Shera, 2007), (Steele and Taber, 1979b) and in the PhD thesis of (Parthasarathi, 2000) and (Cheng, 2007). Shera used an inverse method to derive the wavenumber distribution from experimental measurements of the motion of the basilar membrane. However, this method can be used to derive only the main travelling wave and not other more heavily damped waves. Steele used a Lagrangian approach to derive the eikonal equation, i.e. a relation between the wavenumber and the stiffness of the cochlear partition. His model includes 3D fluid coupling and longitudinal coupling by the partition, which is modelled as a plate. In this case the eikonal equation is a transcendental equation in which the stiffness depends both on the wavenumber and the longitudinal coordinate along the cochlea. By solving this equation, Steele obtained a spectrum of roots for the wavenumber and noticed that only one of these corresponds to the main travelling wave while the others correspond to non-propagating modes. Parthasarathi and Cheng also used the Lagrangian approach to derive the eikonal equation. In their models, they included the longitudinal coupling by the BM and used a Newton-Raphson method to solve the transcendental equation, which requires an initial estimate of the solution. While Steele, Parthasarathi and Cheng focused on the contribution of the nonpropagating modes on the BM response, they did not discuss the wavenumber distribution of the main travelling wave.

In the method presented in this chapter, the eikonal equation depends only on the wavenumber and the frequency of excitation, as the BM admittance is calculated numerically. We derived the wavenumber distribution corresponding to the travelling wave in the case of a model with TM longitudinal coupling. We showed that the real part of the wavenumber has a distribution which is similar to the one for the passive locally reacting case while the imaginary part is characterised by a region with a positive value just before the characteristic frequency. These results, when combined with the derivation of the power transferred from the BM to the fluid, shows that in the region in which the imaginary part is positive the travelling wave is amplified.

The method presented in this chapter can be used to derive the wavenumber distribution associated with different types of waves. To do this however, a more efficient method should be developed to find all the crossing points of the curves given by Eq. (7.10), at all the frequencies. Then, by plotting the set of these points in the complex plane $\kappa - \gamma$, we can follow the wavenumber trajectories associated with different types of waves, as described in (Watts, 2000). The effect of each wave type on the coupled response of the BM can then be determined. This is left as future work.

Chapter 8

Conclusions and suggestions for future work

In this thesis, an existing elemental model has been extended to include the longitudinal coupling by the TM, the BM and the electrical cables, based on the Finite Element Model developed by Grosh's laboratory. The effects of these forms of longitudinal coupling on the BM response have been studied and a method to derive the wavenumber distribution for a cochlear model with a longitudinal coupled OoC has been developed. A summary of conclusions are given in Section 8.1 and suggestions for future work are presented in Section 8.2.

8.1 Summary of conclusions

In Chapter 3 we derived an analytical solution to the cochlear wave equation, in the case of a passive, locally reacting basilar membrane (BM), with fluid compressibility and viscosity. We showed that this solution can be expressed in terms of a few nondimensional parameters: the nondimensional compressibility, C, the nondimensional viscosity, V, the phase-shift constant, N, and the quality factor of the BM, Q. Within the range of nominal values for these parameters, only Q and N have an appreciable effect on the wavenumber distribution and on the response of the BM.

The peak of the real and the imaginary part of the wavenumber becomes sharper as Q is increased. Accordingly, the BM response becomes sharper around the characteristic frequency with increasing values of Q. The real and imaginary parts of the wavenumber are proportional to N. It is shown that the phase-shift parameter determines the nature of the interaction between the structural dynamics of the BM and the fluid inertia. If this parameter is large, the fluid-structural coupling is strong and a travelling wave is generated for frequencies up to about the natural frequency, with strong attenuation above this, giving a very asymmetrical frequency response. If this parameter is small, the fluid-structural coupling is weak, and the elements of the BM responds independently, driven by the constant pressure of the fluid, generating an almost symmetrical frequency response function when plotted on a log scale.

In Chapter 4 we reviewed the experimental measurements that unveiled the main features of the cochlear response to sound stimuli: passive and active mechanics, non-linearity, high sensitivity and frequency selectivity. In particular, we focused on a series of recent experiments, in which the differential movements of various parts of the Organ of Corti have been measured, to help in the understanding of the contribution of longitudinal coupling to the active mechanism of the cochlea. Even if these experiments use an optical technique with high spatial and temporal resolution, the data are difficult to interpret and lead to different conclusions. In particular, (Chen et al., 2011) suggested that a local feedback mechanism is sufficient to explain the active mechanism of the cochlea. On the other hand, (He et al., 2018; Ren et al., 2016a; Lee et al., 2016; Dewey et al., 2019; Cooper et al., 2018) showed that longitudinal coupling plays an important role in the amplification of the BM response.

To better understand the contribution of various types of longitudinal coupling to the active mechanism, we extended the elemental model, as described for example in (Elliott and Ni, 2018), to include the Finite Element Model of the dynamics of the Organ of Corti, developed by (Sasmal and Grosh, 2019). The study of the active mechanism is thus simplified by combining all the mechanics of the OoC into an equivalent BM admittance, and its interaction with the fluid dynamics, so that these two components of the coupled response can be considered individually. The elemental formulation of the Finite Element Model in the locally reacting case is developed in Chapter 5, while the cases with longitudinal coupling by the TM, the BM and the longitudinal cables are discussed in Chapter 6. It is shown that the most important factor in stabilizing the system is the longitudinal coupling by the TM. On the other hand, the electrical longitudinal coupling shifts the BM response to obtain the right map of frequencies along the cochlea. The BM longitudinal coupling is not significant in determining the response expected from experimental measurements.

A method to derive the distribution of the associated with different types of waves is developed Chapter 7. The wavenumber distribution corresponding to the main travelling wave is derived in the case of the model with TM longitudinal coupling. It is shown that while the real part of the wavenumber is similar to the case of a locally reacting model, the imaginary part differs as it is positive just before the characteristic frequency. This results, combined with the derivation of the power transferred to the BM, shows that in the region in which the imaginary part of the wavenumber is positive, the travelling wave is amplified.

8.2 Suggestions for future work

Longitudinal coupling by the reticular lamina

The elemental method can be extended to include the longitudinal coupling by the reticular lamina (RL). The RL can be modelled as an infinite plate, simply supported on one side and free on the other. If we assume that the plate is uniform, the equation

of motion is (Rao, 2006, p.78):

$$D\left(\frac{\partial^4 w}{\partial x^4}+2\frac{\partial^4 w}{\partial x^2\partial y^2}+\frac{\partial^4 w}{\partial y^4}\right)+\rho h_t\frac{\partial^2 w}{\partial t^2}=-P(x,y,t), \tag{8.1}$$

where y is the direction of rotation, x the longitudinal coordinate, w is the transverse displacement, $P(x,y,t)$ is the external pressure per unit length, ρ is the density and h_t the thickness of the plate and D is the flexural rigidity of the plate, give by:

$$D=\frac{Eh_b^3}{12(1-\nu)}, \tag{8.2}$$

where E is Young's modulus, h_b is the thickness associated with bending and ν is Poisson's ratio. Equation (8.1) can be discretised and included in the matrix formulation of the elemental model in a similar way in which we did for the TM, BM, and electrical longitudinal coupling in Sections 6.1 to 6.3, respectively.

If we assume a transverse displacement of the form:

$$w(x,y)=\hat{w}\frac{y}{L}\exp(-\mathrm{i}kx), \tag{8.3}$$

where L is the length of the RL in the y direction and the dependence on time is assumed to be $\exp(\mathrm{i}\omega t)$, then Eq. (8.1) becomes:

$$\left(Dk^4-\omega^2\rho h_t\right)\hat{w}\frac{y}{L}\exp(-\mathrm{i}kx)=-P(x,y,t). \tag{8.4}$$

From this equation we can derive an estimate of the wavelength associated with the wave propagating on the RL. Using $E=3\times10^8\,\mathrm{Pa}$, $\nu=0.45$ (Ni et al., 2016), $\omega=2\pi\times17\,\mathrm{kHz}$ (Sasmal and Grosh, 2019) and assuming an RL thickness of $h_b=2\,\mu\mathrm{m}$, a value of $h_t=20\,\mu\mathrm{m}$, which includes cells underneath, and a density $\rho=10^3\,\mathrm{kg/m^3}$, we obtain $k\sim3\times10^4\,\mathrm{m}^{-1}$ so that:

$$\lambda=\frac{2\pi}{k}\sim200\,\mu\mathrm{m}. \tag{8.5}$$

Study of the power transfer

One important factor in understanding the active mechanism of the cochlea is the power amplification of the travelling wave. In a previous modelling study by (Wang et al., 2016) the power generation by the outer hair cells was for the first time calculated separately from the total power transferred between the BM and the fluid. In this study, a box model of a mouse cochlea with feedforward/feedbackward mechanism has been used. An ideal extension of this work would be the calculation of the power transfer between the OHCs, the BM and the fluid, when different types of longitudinal coupling are included in the Organ of Corti. This can be done with the existing elemental formulation by deriving the response of u_{tms} and u_{tmb}, as the power generated by the OHCs can be expressed in terms of these variables and the motion of the BM, u_{bm}.

Nonlinearity

The nonlinearity of the cochlear amplifier is generally considered to be dominated by the the nonlinear mechanism of the mechano-electrical transduction (MET) in the OHCs (Dallos, 1992; Santos-Sacchi, 1993), in which the HB conductance is a sigmoid function of the HB displacement. For low-level inputs, the values of the HB displacement are such that the HB conductance can be approximated by a linear function. For high-level inputs, the OHCs trans-membrane conductance saturates and the passive mechanism dominate. For intermediate inputs, however, the MET process is nonlinear. In this case, the elemental frequency-domain model can still be used by recurring to the quasi-linear approach developed by (Kanis and de Boer, 1993). This is an iterative method consisting of the following steps:

1. the cochlear model is solved in the frequency domain in the linear case, obtaining the solution $V_{BM}(x, \omega)$;
2. by taking the Fourier transform of $V_{BM}(x, \omega)$, the corresponding solution in the time domain is obtained, $V_{BM}(x, t)$;
3. the assumed functional form of nonlinearity is applied to the time-domain solution;
4. the output of the previous step is approximated by the first Fourier transform in the frequency domain;
5. the admittance of the model is modified according to the output of the previous step;
6. step (1)-(5) are repeated until the relative difference between the outputs is below a chosen tolerance.

Derivation of the wavenumber distribution corresponding to other types of waves

The method presented in Chapter 6 can be used to derive the wavenumber distribution associated to all the wave types within the cochlea. However, as noted in Chapter 6, a more efficient algorithm to derive all the crossing points in a wide frequency range is needed to distinguish the wavenumber trajectories in the complex plane of $\kappa - \gamma$. Then, these wavenumber distributions can be used to determine the effect of the corresponding waves on the coupled response of the BM.

Appendix A

Derivation of the phase integral

The integral in Eq. (3.18) can be written, using Eq. (3.10) and Eq. (3.9), as:

$$\phi = -\mathrm{i}b\frac{w}{c_0}\int_0^x \sqrt{\frac{ac_0^2}{(\omega_b \exp(-x'/l) + i\omega/Q)^2 - \omega^2} + 1}\,\mathrm{d}x', \tag{A.1}$$

where we defined:

$$a = \frac{2\rho}{hm_0}, \tag{A.2a}$$

$$b = \sqrt{1 - \frac{2i\nu}{h^2\omega\rho}}, \tag{A.2b}$$

and at the denominator under the square root of the integrand in Eq. (A.1) we completed the square and assume that $1/Q^2$ is small compared with 1, as in (Zweig et al., 1976). We now change variable by using $\omega_n = \omega_b \exp(-x'/l)$ and obtain:

$$\phi = \mathrm{i}\frac{lb\omega}{c_0}\int_{w_b}^{w_n} \frac{1}{\omega_n}\sqrt{\frac{ac_0^2}{(\omega_n + \mathrm{i}\omega/Q)^2 - \omega^2} + 1}\,\mathrm{d}\omega_n. \tag{A.3}$$

By defining the new variable $t = \left(\omega_n + \frac{i\omega}{Q}\right)$ we have:

$$\phi = \mathrm{i}\frac{lb\omega}{c_0}\int_{(\mathrm{i}\omega/Q+\omega_b)}^{(\mathrm{i}\omega/Q+\omega_n)} \frac{1}{(t - \mathrm{i}\omega/Q)}\frac{\sqrt{ac_0^2 + t^2 - \omega^2}}{\sqrt{t^2 - \omega^2}}\,\mathrm{d}t. \tag{A.4}$$

Taking into account that:

$$\frac{1}{t - \mathrm{i}\omega/Q} = \frac{\mathrm{i}\omega}{Q(t^2 + \omega^2/Q^2)} + \frac{t}{t^2 + \omega^2/Q^2}, \tag{A.5}$$

the integral becomes:

$$\begin{aligned}\phi = \mathrm{i}\frac{lb\omega}{c_0}\Bigg[&\int_{(\mathrm{i}\omega/Q+\omega_b)}^{(\mathrm{i}\omega/Q+\omega_n)} \frac{i\omega\sqrt{ac_0^2 + t^2 - \omega^2}}{Q(t^2 + \omega^2/Q^2)\sqrt{t^2 - \omega^2}}\,\mathrm{d}t \\ &+ \int_{(\mathrm{i}\omega/Q+\omega_b)}^{(\mathrm{i}\omega/Q+\omega_n)} \frac{t}{t^2 + \omega^2/Q^2}\frac{\sqrt{ac_0^2 + t^2 - \omega^2}}{\sqrt{t^2 - \omega^2}}\,\mathrm{d}t\Bigg].\end{aligned} \tag{A.6}$$

Now we consider each integral in the square bracket in turn. We call them respectively I_1 and I_2. Starting from the last one, if we change variable using the substitution $s = t^2$ we obtain:

$$I_2 = \int_{(\mathrm{i}\omega/Q+\omega_b)^2}^{(\mathrm{i}\omega/Q+\omega_n)^2} \frac{1}{2s + 2\omega^2/Q^2} \frac{\sqrt{ac_0^2 + s - \omega^2}}{\sqrt{s-\omega^2}}\,\mathrm{d}s. \tag{A.7}$$

The integrand can be decomposed as:

$$\begin{aligned} I_2 = 1/2 \int_{(\mathrm{i}\omega/Q+\omega_b)^2}^{(\mathrm{i}\omega/Q+\omega_n)^2} & \frac{1}{\sqrt{s-\omega^2}\sqrt{ac_0^2 + s - w^2}}\,\mathrm{d}s \\ +1/2 \int_{(\mathrm{i}\omega/Q+\omega_b)^2}^{(\mathrm{i}\omega/Q+\omega_n)^2} & \frac{4ac_0^2 - (4 + 4/Q^2)\omega^2}{\sqrt{s-\omega^2}\sqrt{ac_0^2 + s - w^2}(4s + 4\omega^2/Q^2)}\,\mathrm{d}s, \end{aligned} \tag{A.8}$$

which we call, respectively, I_{2A} and I_{2B}. If we define $q = \sqrt{s-\omega^2}$ then:

$$I_{2A} = \int_{\sqrt{(\mathrm{i}\omega/Q+\omega_b)^2-\omega^2}}^{\sqrt{(\mathrm{i}\omega/Q+\omega_n)^2-\omega^2}} \frac{1}{\sqrt{ac_0^2 + q^2}}\,\mathrm{d}q, \tag{A.9}$$

and by using $r = q/\sqrt{ac_0^2 + q^2}$:

$$I_{2A} = \int_{\sqrt{(\mathrm{i}\omega/Q+\omega_b)^2-\omega^2}/\sqrt{ac_0^2-\omega^2+(\mathrm{i}\omega/Q+\omega_b)^2}}^{\sqrt{(\mathrm{i}\omega/Q+\omega_n)^2-\omega^2}/\sqrt{ac_0^2-\omega^2+(\mathrm{i}\omega/Q+\omega_n)^2}} \frac{1}{1-r^2}\,\mathrm{d}r, \tag{A.10}$$

so that:

$$\begin{aligned} I_{2A} = & \operatorname{arctanh}\left(\frac{\sqrt{(\mathrm{i}\omega/Q+\omega_n)^2-\omega^2}}{\sqrt{ac_0^2-\omega^2+(\mathrm{i}\omega/Q+\omega_n)^2}}\right) \\ & - \operatorname{arctanh}\left(\frac{\sqrt{(\mathrm{i}\omega/Q+\omega_b)^2-\omega^2}}{\sqrt{ac_0^2-\omega^2+(\mathrm{i}\omega/Q+\omega_b)^2}}\right). \end{aligned} \tag{A.11}$$

Now we go back to the integral I_{2B} in Appendix A for which we use the substitution $m = \sqrt{s-\omega^2}/\sqrt{ac_0^2 + s - \omega^2}$ so that:

$$I_{2B} = \int_\alpha^\beta \frac{4ac_0^2 - (4 + 4/Q^2)\omega^2}{4\omega^2 + 4/Q^2\omega^2 - m^2(4/Q^2\omega^2 - 4(ac_0^2 - \omega^2))}\,\mathrm{d}\mathrm{d}m \tag{A.12}$$

where $\alpha = \sqrt{(\mathrm{i}\omega/Q+\omega_b)^2-\omega^2}/\sqrt{ac_0^2-\omega^2+(\mathrm{i}\omega/Q+\omega_b)^2}$ and $\beta = \sqrt{(\mathrm{i}\omega/Q+\omega_b)^2-\omega^2}/\sqrt{ac_0^2-\omega^2+(\mathrm{i}\omega/Q+\omega_b)^2}$. The result of this integral is:

$$\begin{aligned} I_{2B} = & \frac{\sqrt{4ac_0^2 - (4 + 4/Q^2)\omega^2}}{\omega\sqrt{4 + 4/Q^2}}\Bigg[\operatorname{arctanh}\left(\frac{\sqrt{4ac_0^2 - (4 + 4/Q^2)\omega^2}}{\omega\sqrt{4 + 4/Q^2}}\alpha\right) \\ & - \operatorname{arctanh}\left(\frac{\sqrt{4ac_0^2 - (4 + 4/Q^2)\omega^2}}{\omega\sqrt{4 + 4/Q^2}}\beta\right)\Bigg]. \end{aligned} \tag{A.13}$$

Now going back to I_1 in Appendix A, we can rewrite this as:

$$I_1 = \frac{Q}{4\omega\sqrt{ac_0^2-\omega^2}}\Bigg[\int_{(\mathrm{i}\omega/Q+\omega_b)}^{(\mathrm{i}\omega/Q+\omega_n)} \frac{4\omega^2\sqrt{-ac_0^2+\omega^2}}{Q^2\sqrt{-t^2+\omega^2}\sqrt{-ac_0^2-t^2+\omega^2}}\,\mathrm{d}t$$
$$+\int_{(\mathrm{i}\omega/Q+\omega_b)}^{(\mathrm{i}\omega/Q+\omega_n)} \frac{4\omega^2\sqrt{-ac_0^2+\omega^2}(4ac_0^2-(4+4/Q^2)\omega^2)}{Q^2\sqrt{-t^2+\omega^2}\sqrt{-ac_0^2-t^2+\omega^2}(4t^2+4\omega^2/Q^2)}\,\mathrm{d}t\Bigg]. \tag{A.14}$$

We call the integrals within the square brackets I_{1A} and I_{1B} respectively. Starting from the first one, if we define $\theta = -\arcsin(t/\omega)$, then we obtain:

$$I_{1A} = \frac{4\omega^2}{Q^2}\int_{-\arcsin(\mathrm{i}/Q+\omega_n/\omega)}^{-\arcsin(\mathrm{i}/Q+\omega_n/\omega)} \frac{\mathrm{d}\theta}{\sqrt{1-\frac{\omega^2}{\omega^2-ac_0^2}\sin^2(\theta)}}, \tag{A.15}$$

which is the difference of two elliptic integrals of the first kind, indicated as:

$$I_{1A} = \frac{4\omega^2}{Q^2}\Bigg[\mathrm{F}\left(-\arcsin(\mathrm{i}/Q+\omega_n/\omega), \frac{\omega^2}{\omega^2-ac_0^2}\right) \tag{A.16}$$
$$-\mathrm{F}\left(-\arcsin(\mathrm{i}/Q+\omega_b/\omega), \frac{\omega^2}{\omega^2-ac_0^2}\right)\Bigg]. \tag{A.17}$$

By using the same change of variable, the integral I_{1B} becomes:

$$I_{1B} = 4(ac_0^2-(1+Q^{-2})\omega^2)\int_{-\arcsin(\frac{\mathrm{i}}{Q}+\frac{\omega_n}{\omega})}^{-\arcsin(\frac{\mathrm{i}}{Q}+\frac{\omega_n}{\omega})} \frac{\mathrm{d}\theta}{(1+Q^2\sin^2(\theta))\sqrt{1-\frac{\omega^2}{\omega^2-ac_0^2}\sin^2(\theta)}}, \tag{A.18}$$

which is the difference of two elliptic integrals of the third kind:

$$I_{1B} = (4(ac_0^2-(1+Q^{-2})\omega^2)\Bigg[\Pi\left(-Q^2; -\arcsin(\mathrm{i}/Q+\omega_n/\omega), \frac{\omega^2}{\omega^2-ac_0^2}\right)$$
$$-\Pi\left(-Q^2; -\arcsin(\mathrm{i}/Q+\omega_b/\omega), \frac{\omega^2}{\omega^2-ac_0^2}\right)\Bigg]. \tag{A.19}$$

Then, by putting together all the results above, the integral ϕ becomes:

$$\begin{aligned}\phi = {} & \frac{\mathrm{i}lb\omega}{c_0}\Bigg[\frac{1}{Q\sqrt{-1+\frac{16N^2}{C^2}}}\mathrm{F}\left(-\arcsin(\mathrm{i}/Q+\omega_n/\omega),\frac{\omega^2}{\omega^2-ac_0^2}\right)\\ & +\Pi\left(-Q^2;-\arcsin(\mathrm{i}/Q+\omega_n/\omega),\frac{\omega^2}{\omega^2-ac_0^2}\right)\\ & +\operatorname{arctanh}\left(\frac{\sqrt{(\mathrm{i}\omega/Q+\omega_n)^2-\omega^2}}{\sqrt{ac_0^2-\omega^2+(\mathrm{i}\omega/Q+\omega_n)^2}}\right)\\ & +\frac{\sqrt{4ac_0^2-(4+4/Q^2)\omega^2}}{\omega\sqrt{4+4/Q^2}}\Bigg[\arctan\left(\frac{\sqrt{4ac_0^2-(4+4/Q^2)\omega^2}}{\omega\sqrt{4+4/Q^2}}\right.\\ & \left.\times\frac{\sqrt{(\mathrm{i}\omega/Q+\omega_n)^2-\omega^2}}{\sqrt{ac_0^2-\omega^2+(\mathrm{i}\omega/Q+\omega_n)^2}}\right)\Bigg]+O\left(\frac{\omega}{\omega_b}\right),\end{aligned} \tag{A.20}$$

where $O(\omega/\omega_b)$ include the terms from the lower limit of integration. If we know use the definitions of the nondimensional variables introduced in Eq. (3.14), ϕ can be written as:

$$\begin{aligned}\phi = {} & \mathrm{i}C\sqrt{1-2\mathrm{i}V}\Bigg[\frac{1}{Q\sqrt{-1+\frac{16N^2}{C^2}}}\mathrm{F}\left(-\arcsin(\mathrm{i}/Q+\omega_n/\omega),\frac{1}{\sqrt{1-\frac{16N^2}{C^2}}}\right)\\ & +\frac{4\omega^2}{Q}\sqrt{-1+\frac{16N^2}{C^2}}\Pi\left(-Q^2;-\arcsin(\mathrm{i}/Q+\omega_n/\omega),\frac{1}{\sqrt{1-\frac{16N^2}{C^2}}}\right)\\ & +\operatorname{arctanh}\left(\frac{\sqrt{(\mathrm{i}/Q+\omega_n/\omega)^2-1}}{\sqrt{16N^2/C^2-1+(\mathrm{i}/Q+\omega_n/\omega)^2}}\right)\\ & +\sqrt{-1+\frac{16N^2}{C^2}}\arctan\left(\frac{\sqrt{16N^2/C^2-1}\sqrt{(\mathrm{i}/Q+\omega_n/\omega)^2-1}}{\sqrt{16N^2/C^2-1+(\mathrm{i}/Q+\omega_n/\omega)^2}}\right)\Bigg]\\ & +O\left(\frac{\omega}{\omega_b}\right),\end{aligned} \tag{A.21}$$

where again we assume that $1-1/Q^2$ is small compared with 1. Finally, as we are interested in the form of the solution for excitation frequencies such that $\omega \ll \omega_b$, we can neglect the term of order $O(\omega/\omega_b)$ and we obtain the solution presented in Section 3.3.

Appendix B

Equivalent uni-axial 3DOF system of the locally reacting model

The equivalent 3DOF mechanical system of the locally reacting model is be derived as a special case of that described in Section 5.4. The stiffness and damping parameters

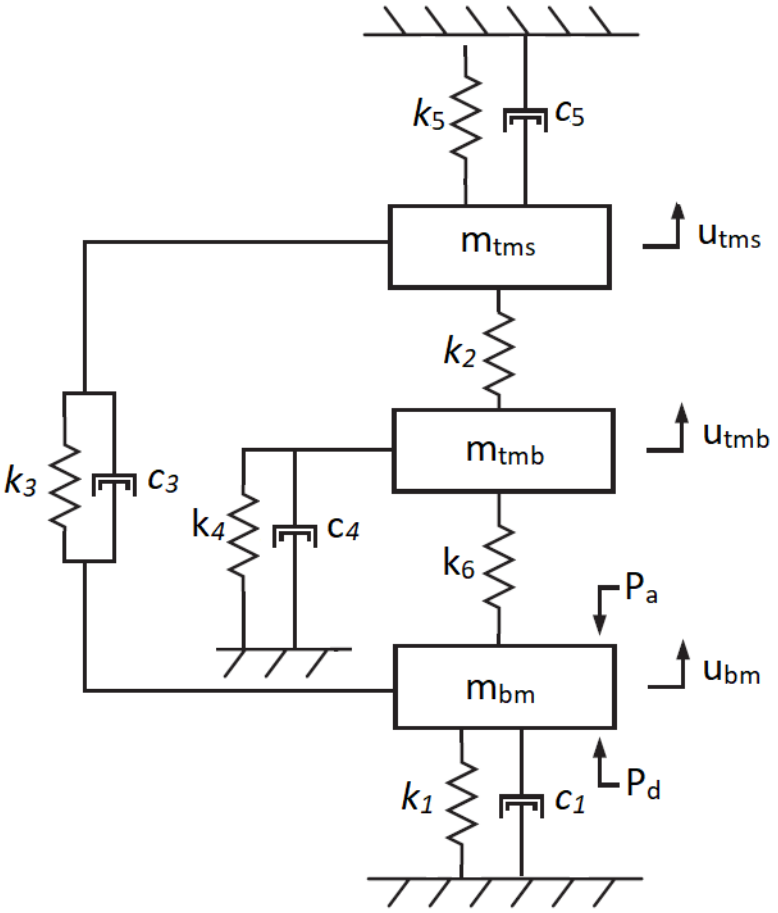

Figure B.1: Equivalent uni-axial 3 DOF system

are given by:

$$\begin{aligned}k_1 =&K_{bm1} + \frac{K_{ohc}}{L_{ro}^2}\Big[(L_{ro}\cos(\beta)\psi_{1,L10} + 2L_1\cos(\theta_2)\psi_{1,Lpc}\cos(\beta-\theta_2))^2 + (L_{ro}\cos(\beta)\psi_{1,L01}\\ &-2L_1\cos(\theta_2)\psi_{1,Lpc}\cos(\beta-\theta_2))^2 - L_{ro}\cos(\beta)\left((L_1+L_{ro})\psi_{1,L10} + (L_{ro}-L_1)\psi_{1,L01}\right.\\ &\left.+L_{ro}\psi_{1,L0}\right) + L_{ro}^2\cos^2(\beta)\psi_{1,L0}^2 - 4L_1^2\cos(\theta_2)\psi_{1,Lpc}\cos(\beta-\theta_2)\Big] + \frac{K_{rl}}{L_{pc}^2}\Big[2\cos(\theta_2)\\ &\times\psi_{1,Lpc}(L_{ro}-L_{pc}\cos(\beta-\theta_2))\left(2\cos(\theta_2)\psi_{1,Lpc}(L_{ro}-L_{pc}\cos(\beta-\theta_2)) + L_{pc}\right)\Big]\\ &+\frac{K_{st}}{L_{ro}^2}\Big[6\cos(\theta_2)\psi_{1,Lpc}(L_{ro}\sin(\beta-\theta_2)+L_{st}\cos(\beta-\theta_2))\left(2L_{ro}\cos(\theta_2)\psi_{1,Lpc}\sin(\beta-\theta_2)\right.\\ &\left.+2L_{st}\cos(\theta_2)\psi_{1,Lpc}\cos(\beta-\theta_2) - L_{ro} - L_{st}\right)\Big]\end{aligned} \tag{B.1}$$

$$k_2 = -K_{st}\frac{3L_{st}}{L_{ro}} \tag{B.2}$$

$$k_3 = K_{st}\frac{6\cos(\theta_2)\psi_{1,Lpc}(L_{ro}\sin(\beta-\theta_2)+L_{st}\cos(\beta-\theta_2))}{L_{ro}} \tag{B.3}$$

$$\begin{aligned}k_4 =&K_{tmb} - \frac{K_{ohc}}{L_{ro}^2}\Big[L_{ro}\cos(\beta)\left((L_1+L_{ro})\psi_{1,L10} + (L_{ro}-L_1)\psi_{1,L01} + L_{ro}\psi_{1,L0}\right) + 4\\ &\times L_1^2\cos(\theta_2)\psi_{1,Lpc}\cos(\beta-\theta_2) - 2L_1^2 - 3L_{ro}^2\Big] + K_{rl}\Big[\frac{1}{L_{pc}}\cos(\theta_2)\psi_{1,Lpc}(L_{pc}\cos(\beta-\theta_2)\\ &- L_{ro}) + 1\Big) - \frac{3K_{st}}{L_{ro}^2}L_{st}\Big[2L_{ro}\cos(\theta_2)\psi_{1,Lpc}\sin(\beta-\theta_2) + 2L_{st}\cos(\theta_2)\psi_{1,Lpc}\cos(\beta-\theta_2)\\ &- L_{ro} - L_{st}\Big]\end{aligned} \tag{B.4}$$

$$\begin{aligned}k_5 =&K_{tms} + K_{st}\Big[-\frac{6L_{st}\cos(\theta_2)\psi_{1,Lpc}\cos(\beta-\theta_2)}{L_{ro}} - 6\cos(\theta_2)\psi_{1,Lpc}\sin(\beta-\theta_2) + \frac{2L_1^2}{L_{tm}^2} +\\ &\frac{3L_{st}}{L_{ro}} + 3\Big]\end{aligned} \tag{B.5}$$

$$\begin{aligned}k_6 =&\frac{K_{ohc}}{L_{ro}^2}\Big[L_{ro}\cos(\beta)\left((L_1+L_{ro})\psi_{1,L10} + (L_{ro}-L_1)\psi_{1,L01} + L_{ro}\psi_{1,L0}\right) + 4L_1^2\cos(\theta_2)\psi_{1,Lpc}\\ &\times\cos(\beta-\theta_2)\Big] + \frac{2K_{rl}}{L_{pc}}\Big[\cos(\theta_2)\psi_{1,Lpc}(L_{pc}\cos(\beta-\theta_2) - L_{ro})\Big] + \frac{6K_{st}}{L_{ro}^2}\Big[L_{st}\cos(\theta_2)\psi_{1,Lpc}\\ &\times(L_{ro}\sin(\beta-\theta_2) + L_{st}\cos(\beta-\theta_2))\Big]\end{aligned} \tag{B.6}$$

$$c_1 = c_{BM} + 2c_{sub}\cos(\theta_2)\psi_{1,Lpc}\sin(\beta-\theta_2)\left(2\cos(\theta_2)\psi_{1,Lpc}\sin(\beta-\theta_2)-1\right) \tag{B.7}$$

$$c_3 = 2c_{sub}\cos(\theta_2)\psi_{1,Lpc}\sin(\beta-\theta_2) \tag{B.8}$$

$$c_4 = c_{tmb} \tag{B.9}$$

$$c_5 = c_{tms} + c_{sub}(1-2\cos(\theta_2)\psi_{1,Lpc}\sin(\beta-\theta_2)) \tag{B.10}$$

As shown in Fig. B.1, in the active case besides P_d, which is the pressure from the fluid on the BM, there is an additional pressure acting on the BM, P_a, resulting from the mechanoeletrical transduction of the OHCs and is given by:

$$P_a = \frac{\epsilon_3}{b\Delta x}R_{tot}(I_{s1}R_{a0} + I_{s2}(R_{a0}(-1-iC_a\omega R_{tot}) - R_{ext})) \tag{B.11}$$

where ϵ_3 is the electromechanical coupling coefficient; $R_{ext} = R_{vl} + R_{tl} + R_{vm}$ and R_{tot} is given by:

$$\begin{aligned} R_{tot} =& R_m/\Big[(R_{a0}(-C_aR_m\omega(C_m\omega R_{ext}-i) + iC_a\omega R_{tot} + iC_mR_m\omega + 1 + iC_mR_m\omega R_{ext} \\ &+ R_m + R_{ext}\Big]; \end{aligned} \tag{B.12}$$

the resistances and capacitances are those defined in Section 5.3.1.1; I_{s1} is the current passing trough the MET channels in the HBs and is given by:

$$I_{s1} = (V_{sm} - V_{ohc})G_a^1\sum_{j=1}^{3}(u_{hb,j} + u_{rl,j}\frac{Lst}{Lro}) \tag{B.13}$$

and I_{s2} is the current due to the piezoelectric action of the OHCs and is given by:

$$I_{s2} = -i\omega\epsilon_3\sum_{j=1}^{3}u_{ohc}^{comp} \tag{B.14}$$

where u_{ohc}^{comp} is the compression of the outer hair cells. The active pressure can be written in terms of two component, one proportional to I_{s1}, given by the MET:

$$P_{Is1} = \frac{\epsilon_3}{b\Delta x}R_{tot}Is_1R_{a0}; \tag{B.15}$$

and another one proportional to I_{s2}, due to the piezoelectric action:

$$P_{Is2} = \frac{\epsilon_3}{b\Delta x}R_{tot}Is_2(-R_{a0}(1+iC_a\omega R_{tot})). \tag{B.16}$$

A comparison of the frequency response of P_a, P_{Is1} and P_{Is2} with the region in which the BM response is nonlinear could help in the understanding of the amplification of the response. This is left as a suggestion for future work.

Appendix C

Derivation of the relationship between the output of the photo-multiplier and the movements of an object in the homodyne interferometer

In this section we review the derivation of the equation that describes the relationship between the output of the photo-multiplier and the movements of an object (M_2) in the homodyne interferometer represented in Fig. 4.8 (Khanna et al., 1968), which we also report here for simplicity . We define the path difference θ between the beams reflected

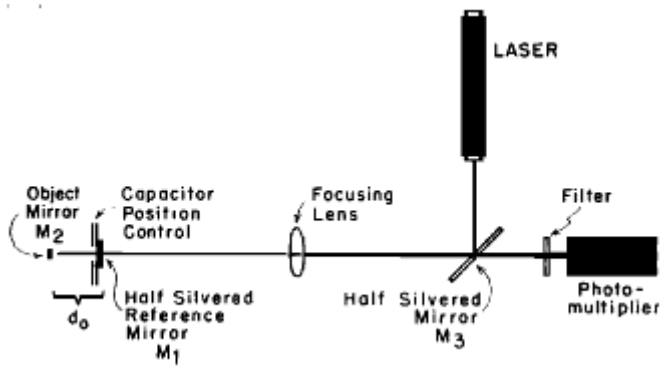

Figure C.1: Schematic representation of the homodyne interferometer. The light source is a He-Ne laser which is focused on a mirror, M2, fixed on the basilar membrane. A half reflective mirror, M1, is positioned in front of the mirror M2 to obtain two beams and it can be moved by a capacitor in order to modify the distance between the two mirrors and regulate the interference. A photo-multiplier is used to measure the combined intensity of the light reflected from M1 and M2. Reprinted with permission from (Khanna et al., 1968). Copyright 1968, Acoustic Society of America.

from mirrors M_1 and M_2 as

$$\theta = 4\pi d_0/\lambda, \tag{C.1}$$

where d_0 is the distance between mirrors $M1$ and $M2$, λ is the wavelength of the laser and θ is measured in radians. If the intensity of the beam reflected from mirror M_1 is I_1 and that of the beam from mirror M_2 is I_2, then the net intensity I is given by

$$I = I_1 + I_2 + 2I_1^{1/2}I_2^{1/2}cos\theta, \tag{C.2}$$

and the resultant photo-multiplier current I_m is

$$I_m = K[I_1 + I_2 + 2(I_1I_2)^{1/2}cos\theta], \tag{C.3}$$

where K is a constant that can be derived from the calibration. The phot-multiplier current has two components, one fixed, A, and one variable, $Bcos\theta$, so that Eq. (C.3) can be written as

$$I_m = A + Bcos\theta. \tag{C.4}$$

If mirror M_2 vibrates with an amplitude $A(t)$, then

$$\theta = (4\pi/\lambda)[d_0 + A(t)], \tag{C.5}$$

and

$$I_m = A + Bcos[4\pi d_0/\lambda + (4\pi/\lambda)A(t)], \tag{C.6}$$

that is

$$I_m = A + B[cos(4\pi d_0/\lambda)cos(4\pi/\lambda)A(t) - sin(4\pi d_0/\lambda)sin(4\pi/\lambda)A(t)] \tag{C.7}$$

If the distance d_0 is adjusted so that

$$d_0 = (2n+1)\lambda/8 \tag{C.8}$$

where $n = 1, 2, 3, ...$ then Eq. (C.7) reduces to

$$I_m = A \pm Bsin[(4\pi/\lambda A(t)]. \tag{C.9}$$

For small angles, $sin\alpha \sim \alpha$ (up to $\alpha = 0.24$ the error is $< 1\%$). Because the wavelength of a helium-neon laser is $\lambda = 6.328 * 10^{-5}$ cm, the small angle condition $\alpha < 0.24$ corresponds to a displacement amplitude less than $1.2 * 10^{-6}$ cm. In this case Eq. (C.9) reduces to

$$I_m = A \pm B(4\pi/\lambda)A(t). \tag{C.10}$$

This equation shows that the output of the interferometer is linearly proportional to the displacement amplitude of M_2 so that the amplitude $A(t)$ is recovered undistorted.

In summary, in order to correctly measure $A(t)$, the separation between mirrors M_1 and M_2 must be precisely adjusted so that Eq. (C.8) is satisfied; the absolute value of the amplitude must be known and it must be maintained below 10^{-6} cm and, finally, the ambiguity of the sign in Eq. (C.10) must be resolved. We will now show how these conditions can be satisfied if mirror M_2 moves with a sinusoidal movements. In this case the amplitude can be written as:

$$A(t) = \delta cos(\omega t), \tag{C.11}$$

where δ is the peak displacement amplitude of M_2 and $\omega = 2\pi f$, then Eq. (C.7) can be rewritten as:

$$I_m = A + Bcos\frac{4\pi d_0}{\lambda}cos(\frac{4\pi\delta}{\lambda}cos\omega t) - sin\frac{4\pi d_0}{\lambda}sin(\frac{4\pi\delta}{\lambda}sin\omega t). \tag{C.12}$$

If we let $4\pi\delta/\lambda = P$, since

$$cos(Pcos\omega t) = J_0(P) - 2J_2(P)cos2\omega t + ..., \tag{C.13}$$

and

$$sin(Pcos\omega t) = 2J_1(P)cos\omega t - 2J_3(P)cos3\omega t + ..., \tag{C.14}$$

where $J_n(P)$ is the Bessel function of the first kind and n^{th} order whose argument is P, then Eq. (C.12) becomes:

$$\begin{aligned} I_m = A + Bcos(4\pi d_0/\lambda)[J_0(P) - 2J_2(P)cos2\omega t + ...] + \\ - sin(4\pi d_0/\lambda)[2J_1(P)cos\omega t - 2J_3(P)cos3\omega t + ...]. \end{aligned} \tag{C.15}$$

The distance between the plates should be adjusted so that

$$sin4\pi d_0/\lambda = \pm 1 \; or \; cos4\pi d_0/\lambda = 0 \; i.e. \; d_0 = (2n+1)\lambda/8. \tag{C.16}$$

This adjustment can be made by observing the output of the photo-multiplier through a filter. If the filter is tuned to the fundamental frequency, the distance between mirrors M_1 and M_2 is adjusted for maximal output at the fundamental. If the filter is tuned to the second harmonic frequency, the distance between the mirrors is adjusted for minimal output at the second harmonic. Then if a filter is used to observe the output of the photo-multiplier at the fundamental frequency of vibration, and the mirror separation is set for maximal output, the output of the filter I_ω is related to the amplitude of vibration by the equation

$$I_\omega = \pm B2J_1(P)cos\omega t = \pm B2J_1(4\pi\delta/\lambda)cos\omega t. \tag{C.17}$$

The amplitude of the fundamental is then related to δ, the amplitude of vibration of mirror M_2. In particular, as the amplitude is slowly increased, I_ω increases and then reaches a maximum; if the amplitude is further increased, I_ω drops sharply. Since the

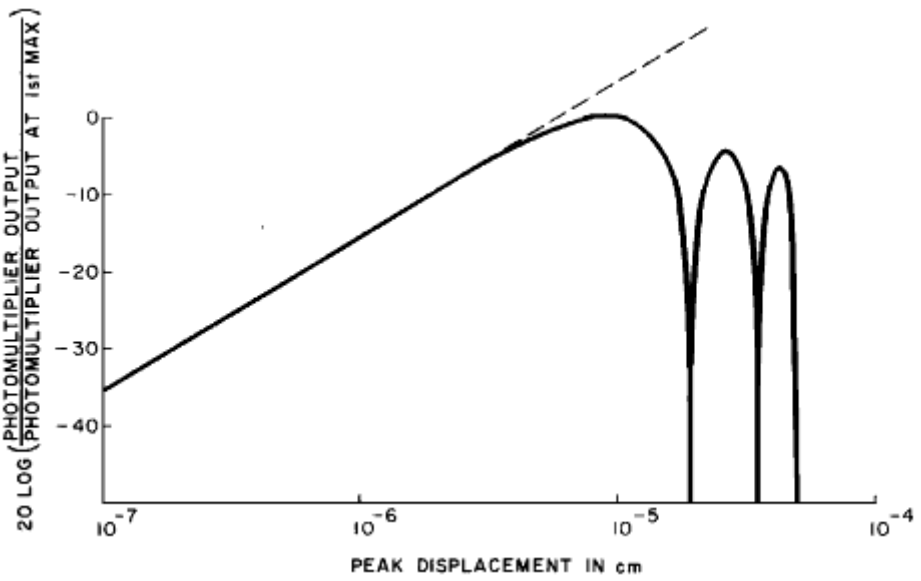

Figure C.2: Output of the interferometer plotted as a function of the vibration of the object mirror as given by Eq. (C.18). Reprinted with permission from (Khanna et al., 1968). Copyright 1968, Acoustic Society of America.

value of $J_1(P)$ is known precisely for all points of maximal and minimal values, the relationship between the photo-multiplier current and the absolute value of vibration it is straightforward. At the first maximum, $P = 1.84\,\text{rad}$ and $\delta = 0.92 * 10^{-5}\,\text{cm}$. At the first minimum, $P = 3.82\,\text{rad}$ and $\delta = 1.92 * 10^{-5}\,\text{cm}$. The amplitude of vibration at any value of the photo-multiplier current is given by the relation

$$\frac{I_\omega}{I_{\omega max}} = \frac{J_1(4\pi\delta/\lambda)}{J_1(1.84)} = \frac{J_1(4\pi\delta/\lambda)}{0.582}, \tag{C.18}$$

where $I_{\omega max}$ is the photo-multiplier current at the first maximum. The relationship between the peak displacement and $20log(I/I_{max})$ is shown in Fig. C.2. Since

$$J_1(P) = P/2 - P^3/16 + P^5/384 - ... \tag{C.19}$$

for values of $P < 0.2$ which corresponds to $\delta < 10^{-6}\,\text{cm}$, $J_1(P) \sim P/2$ with an accuracy of 0.5%. Under this restriction, Eq. (C.17) reduces to

$$I_\omega = \pm B(4\pi/\lambda)cos\omega t. \tag{C.20}$$

Then, for vibration amplitudes below $10^{-6}\,\text{cm}$, a linear relationship exists between the vibration of the object mirror M_2 and the photo-multiplier output. The dynamic is linear from 3 pm to 10 pm but it can actually be extended to 100 nm because in this last region the non-linearity is precisely characterised by Eq. (C.17). Furthermore, because of the high sensitivity, the response of the BM can be measured in the frequency range of $20 - 20000\,\text{Hz}$.

Appendix D

Programs in MATLAB

D.1 Main code for the models without electrical longitudinal coupling

```
clear

%% cochlear parameters

NX =400; %[#] - number of elements
Lc = 1.85; %[cm] - length of the cochlea
Deltab = Lc/(NX-1); %[cm] - length of a single element
Xpos = 0:Deltab:Lc; %[cm] - position along the cochlea
W=0.1; %[cm] width of the chambers
h = 0.1; %[cm] - effective chamber eight
rho = 1; %[g/cm^3] - density of the fluids in each chamber

l5 = 0.38; %[m] - characteristic length
f_b5 = 43.7395e3; %[Hz] - frequency at the base of the cochlea
CF5 = f_b5*exp(-Xpos/l5); %[Hz] - distribution of natural frequencies
w_cf = 2*pi*CF5; %[Hz] - distribution of angular frequencies

%% initialization of fluid matrix and of stapes' velocity vector

I=eye(NX,NX);
v1=ones(NX-1,1);
Iinf=diag(v1,-1);
Isup=diag(v1,1);
F = -2*I+Iinf+Isup;
F(1,:)=0;
F(NX,:)=0;
F(1,1)=-Deltab/h;
F(1,2)=+Deltab/h;
F(NX,NX)=Deltab^2/h;
F = h/Deltab^2 .* F;

vs(NX,1)=0;
vs(1,1)=10;

%% derivation of matrices to be used in the condensation process

modeltype=3; % 1 for 1D fluid coupling, 3 for 3D fluid coupling
```

```
38 epsLevel=1; % maximum value of epsilon_3
39 AL=0.4; %activity level
40
41 for kk=1:1:NX
42     x_gauss=Xpos(kk); %position along the cochlea
43     param_without_el_cables; %code with parameters from the Finite Element Method
44
45     Mglobal(1+3*(kk-1),1+3*(kk-1))=Ms(1,1); %mass matrix
46     Mglobal(1+3*(kk-1),2+3*(kk-1))=Ms(1,2);
47     Mglobal(1+3*(kk-1),3+3*(kk-1))=Ms(1,3);
48     Mglobal(2+3*(kk-1),1+3*(kk-1))=Ms(2,1);
49     Mglobal(2+3*(kk-1),2+3*(kk-1))=Ms(2,2);
50     Mglobal(2+3*(kk-1),3+3*(kk-1))=Ms(2,3);
51     Mglobal(3+3*(kk-1),1+3*(kk-1))=Ms(3,1);
52     Mglobal(3+3*(kk-1),2+3*(kk-1))=Ms(3,2);
53     Mglobal(3+3*(kk-1),3+3*(kk-1))=Ms(3,3);
54
55     Ksglobal(1+3*(kk-1),1+3*(kk-1))=Ks(1,1); %structural stiffness matrix
56     Ksglobal(1+3*(kk-1),2+3*(kk-1))=Ks(1,2);
57     Ksglobal(1+3*(kk-1),3+3*(kk-1))=Ks(1,3);
58     Ksglobal(2+3*(kk-1),1+3*(kk-1))=Ks(2,1);
59     Ksglobal(2+3*(kk-1),2+3*(kk-1))=Ks(2,2);
60     Ksglobal(2+3*(kk-1),3+3*(kk-1))=Ks(2,3);
61     Ksglobal(3+3*(kk-1),1+3*(kk-1))=Ks(3,1);
62     Ksglobal(3+3*(kk-1),2+3*(kk-1))=Ks(3,2);
63     Ksglobal(3+3*(kk-1),3+3*(kk-1))=Ks(3,3);
64
65     Csglobal(1+3*(kk-1),1+3*(kk-1))=Cs(1,1); %structural damping matrix
66     Csglobal(1+3*(kk-1),2+3*(kk-1))=Cs(1,2);
67     Csglobal(1+3*(kk-1),3+3*(kk-1))=Cs(1,3);
68     Csglobal(2+3*(kk-1),1+3*(kk-1))=Cs(2,1);
69     Csglobal(2+3*(kk-1),2+3*(kk-1))=Cs(2,2);
70     Csglobal(2+3*(kk-1),3+3*(kk-1))=Cs(2,3);
71     Csglobal(3+3*(kk-1),1+3*(kk-1))=Cs(3,1);
72     Csglobal(3+3*(kk-1),2+3*(kk-1))=Cs(3,2);
73     Csglobal(3+3*(kk-1),3+3*(kk-1))=Cs(3,3);
74
75     Ceglobal(1+2*(kk-1),1+2*(kk-1))=Ce(1,1); %electrial damping matrix
76     Ceglobal(1+2*(kk-1),2+2*(kk-1))=Ce(1,2);
77     Ceglobal(2+2*(kk-1),1+2*(kk-1))=Ce(2,1);
78     Ceglobal(2+2*(kk-1),2+2*(kk-1))=Ce(2,2);
79
80     Keglobal(1+2*(kk-1),1+2*(kk-1))=Ke(1,1); %electrical stiffness matrix
81     Keglobal(1+2*(kk-1),2+2*(kk-1))=Ke(1,2);
82     Keglobal(2+2*(kk-1),1+2*(kk-1))=Ke(2,1);
83     Keglobal(2+2*(kk-1),2+2*(kk-1))=Ke(2,2);
84
85     Cesglobal(1+2*(kk-1),1+3*(kk-1))=Ces(1,1);%electric-structural damping coupling matrix
86     Cesglobal(1+2*(kk-1),2+3*(kk-1))=Ces(1,2);
87     Cesglobal(1+2*(kk-1),3+3*(kk-1))=Ces(1,3);
88     Cesglobal(2+2*(kk-1),1+3*(kk-1))=Ces(2,1);
89     Cesglobal(2+2*(kk-1),2+3*(kk-1))=Ces(2,2);
90     Cesglobal(2+2*(kk-1),3+3*(kk-1))=Ces(2,3);
91
92     Kesglobal(1+2*(kk-1),1+3*(kk-1))=Kes(1,1);%electric-structural stiffness coupling
93     Kesglobal(1+2*(kk-1),2+3*(kk-1))=Kes(1,2);
94     Kesglobal(1+2*(kk-1),3+3*(kk-1))=Kes(1,3);
95     Kesglobal(2+2*(kk-1),1+3*(kk-1))=Kes(2,1);
96     Kesglobal(2+2*(kk-1),2+3*(kk-1))=Kes(2,2);
```

```
97      Kesglobal(2+2*(kk-1),3+3*(kk-1))=Kes(2,3);
98
99      Cseglobal(1+3*(kk-1),1+2*(kk-1))=Cse(1,1); %structure-electrical damping coupling matrix
100     Cseglobal(1+3*(kk-1),2+2*(kk-1))=Cse(1,2);
101     Cseglobal(2+3*(kk-1),1+2*(kk-1))=Cse(2,1);
102     Cseglobal(2+3*(kk-1),2+2*(kk-1))=Cse(2,2);
103     Cseglobal(3+3*(kk-1),1+2*(kk-1))=Cse(3,1);
104     Cseglobal(3+3*(kk-1),2+2*(kk-1))=Cse(3,2);
105
106     Kseglobal(1+3*(kk-1),1+2*(kk-1))=Kse(1,1); %structure-electrical stiffness coupling matrix
107     Kseglobal(1+3*(kk-1),2+2*(kk-1))=Kse(1,2);
108     Kseglobal(2+3*(kk-1),1+2*(kk-1))=Kse(2,1);
109     Kseglobal(2+3*(kk-1),2+2*(kk-1))=Kse(2,2);
110     Kseglobal(3+3*(kk-1),1+2*(kk-1))=Kse(3,1);
111     Kseglobal(3+3*(kk-1),2+2*(kk-1))=Kse(3,2);
112
113     %contribution to the stiffness and damping matrices by TM longitudinal coupling
114
115     if kk<NX
116         Ksglobal(2+3*(kk-1),2+3*(kk-1))=Ap*G/Deltab+A*Gp/Deltab+Ksglobal(2+3*(kk-1),2+3*(kk-1));
117
118
119         Ksglobal(2+3*(kk-1),2+3+3*(kk-1))=-Applus*Gplus/Deltab-Aplus*Gpplus/Deltab;
120
121
122     end
123
124     if kk<NX && kk>1
125
126         Ksglobal(2+3*(kk-1),2-3+3*(kk-1))=-Am*Gm/Deltab^2;
127
128         Ksglobal(2+3*(kk-1),2+3*(kk-1))=2*A*G/Deltab^2+Ksglobal(2+3*(kk-1),2+3*(kk-1));
129
130         Ksglobal(2+3*(kk-1),2+3+3*(kk-1))=-Aplus*Gplus/Deltab^2+Ksglobal(2+3*(kk-1),2+3+3*(kk-1));
131
132     end
133
134     if kk<NX
135         Csglobal(2+3*(kk-1),2+3*(kk-1))=Ap*eta/Deltab+A*etap/Deltab+Csglobal(2+3*(kk-1),2+3*(kk-1)
        );
136
137
138         Csglobal(2+3*(kk-1),2+3+3*(kk-1))=-Applus*etaplus/Deltab-Aplus*etapplus/Deltab;
139
140     end
141
142     if kk<NX && kk>1
143
144         Csglobal(2+3*(kk-1),2-3+3*(kk-1))=-Am*etam/Deltab^2;
145
146         Csglobal(2+3*(kk-1),2+3*(kk-1))=2*A*eta/Deltab^2+Csglobal(2+3*(kk-1),2+3*(kk-1));
147
148         Csglobal(2+3*(kk-1),2+3+3*(kk-1))=-Aplus*etaplus/Deltab^2+Csglobal(2+3*(kk-1),2+3+3*(kk-1)
        );
149
150     end
151
152
153     %contribution to the stiffness matrix by BM longitudinal coupling
```

```
154
155     if kk<NX && kk>1
156
157         Ksglobal(1+3*(kk-1),1-3+3*(kk-1))=+2*(Dxy+Ds)*bmpar2/Deltab^2;
158
159         Ksglobal(1+3*(kk-1),1+3*(kk-1))=-2*2*(Dxy+Ds)*bmpar2/Deltab^2+Ksglobal(1+3*(kk-1),1+3*(kk
       -1));
160
161         Ksglobal(1+3*(kk-1),1+3+3*(kk-1))=+2*(Dxy+Ds)*bmpar2/Deltab^2+Ksglobal(1+3*(kk-1),1+3+3*(
       kk-1));
162
163     end
164
165     if kk<NX-1 && kk>1+1
166
167         Ksglobal(1+3*(kk-1),1-6+3*(kk-1))=-Dxx/Deltab^4;
168
169         Ksglobal(1+3*(kk-1),1-3+3*(kk-1))=Dxx*(4/Deltab^4)+Ksglobal(1+3*(kk-1),1-3+3*(kk-1));
170
171         Ksglobal(1+3*(kk-1),1+3*(kk-1))=-Dxx*(6/Deltab^4)+Ksglobal(1+3*(kk-1),1+3*(kk-1));
172
173         Ksglobal(1+3*(kk-1),1+3+3*(kk-1))=Dxx*(4/Deltab^4)+Ksglobal(1+3*(kk-1),1+3+3*(kk-1));
174
175         Ksglobal(1+3*(kk-1),1+6+3*(kk-1))=-Dxx/Deltab^4;
176
177     end
178
179     Ksglobal(1+3*(kk-1),1+3*(kk-1))=Dyy+Ksglobal(1+3*(kk-1),1+3*(kk-1));
180
181     b22(kk)=b; %[cm] width of the BM
182 end
183
184 %% initialization of matrices and vectors to calculate the response
185 tic
186 clear S
187 clear T
188
189 T(NX,3*NX)=0;
190 for i=1:1:NX
191     T(i,1+3*(i-1))=1;
192 end
193
194 S(3*NX,NX)=0;
195 for i=1:1:NX
196     S(1+3*(i-1),1+1*(i-1))=1;
197 end
198
199 Yppkk(NX,NX)=0;
200 p_s(NX,NX)=0;
201 p_L(NX,NX)=0;
202 VBM3d(NX,NX)=0;
203 Z_nf(NX,NX)=0;
204
205 %% calculation of the response at each frequency
206 for pp=1:length(w_cf)
207     w_my=w_cf(pp);
208
209     %calculation of the equivalent BM admittance matrix
210
```

```
211     Ks1global=-w_my^2*Mglobal+Ksglobal+1i*w_my*Csglobal;
212     Kaglobal=(Kseglobal+1i*w_my*Cseglobal)*inv(Keglobal+1i*w_my*Ceglobal)*(1i*w_my*Cesglobal+
        Kesglobal);
213     Ksaglobal=(Ks1global-Kaglobal)/(1i*w_my);
214     Y=inv(Ksaglobal);
215     Yabm=T*Y*S.*b22*(1/(2*pi));
216
217     %calculation of fluid coupling matrix
218
219     Z_nf(1:NX,1:NX)=0;
220
221     for ll=1:1:NX
222         for jj=1:1:NX
223             Z_nf(ll,jj) = 1.3958*1i*w_my*rho*Deltab*exp(-abs(jj-ll)*Deltab/(0.0854*W));
224         end
225     end
226
227     %calculation of the response by the elemental method
228
229     Yabm(1,1)=0;
230     Yabm(NX,NX)=0;
231
232     Zfc=-2*1i*w_my*rho.*inv(F)+Z_nf;
233     p_s(:,pp)=Zfc*vs;
234     p_L(:,pp)=(I+Zfc*Yabm)\p_s(:,pp);
235     VBM3d(:,pp)=-(Yabm*p_L(:,pp));
236
237 end
238 toc
239
240 %% plot of the velocity response
241
242 fr=CF5;
243 fr=fr/1000;
244 posit5=88; %x_0
245
246 prt = 2; % #1 for printing
247 doc_type = 1;   % #0 quick print, no document
248 % #1 for papers, reports, theses
249 % #2 presentationsz
250 % #3 posters
251 if epsLevel>0 && AL>=0.00002
252     col = {'--','--k','--g', '--b','--m','--m'};
253 elseif epsLevel==1 && AL==0
254     col = {'-.','-.k','-.g', '-.b','-.m','--m'};
255 elseif epsLevel==0
256     col = {'-','-k','-g', '-b','-m','--m'};
257 end
258 fig_name = {'plot_1'};
259 Ft_size = 12;
260 Ft_name = 'Times New Roman';
261 set(0,'defaulttextinterpreter','tex')
262 set(0,'DefaultTextFontSize', Ft_size)
263 set(0,'DefaultTextFontName', Ft_name)
264 set(0,'DefaultAxesFontSize', Ft_size)
265 set(0,'DefaultAxesFontName', Ft_name)
266
267 figure(13)
268 hold on
```

```
subplot(2,2,1)
semilogx(fr,20*log10(abs(VBM3d(posit5,:))),col{1},'Linewidth',1,'DisplayName','Active', '
    Handlevisibility','on')
hold on
grid on
xlabel('Frequency [kHz] ','interpreter','tex')
ylabel('|V| [db re stapes]','interpreter','tex')
set(gca,'FontSize',Ft_size)
ylim([0 65])
xlim([2 40])
xticks([2:10,20,30,40])

angle_Va=unwrap(angle(VBM3d(posit5,:)))/(2*pi);
subplot(2,2,3)
semilogx(fr,angle_Va-angle_Va(end),col{1},'Linewidth',1,'DisplayName','Active', 'Handlevisibility'
    ,'on')
hold on
grid on
xlabel('Frequency [kHz] ','interpreter','tex')
ylabel('\angle V [cycles]','interpreter','tex')
set(gca,'FontSize',Ft_size)
xlim([2 40])
xticks([2:10,20,30,40])

%
```

D.2 Parameters for code without electrical longitudinal coupling

```
%%param_without_el_cables.m

%geometrical parameters-----------------------------------------------

hbm = 0.0007+(0.00017-0.0007)*x_gauss/Lc;   %[cm] - thickness of the BM
b   = 0.008 +(0.018-0.008)*x_gauss/Lc;       %[cm] - width of the BM
Ltm = 0.006+(0.018-0.006)*x_gauss/Lc; %[cm] - length of TM

alpha = 0.4363 + (0.7856-0.4363)*x_gauss/Lc; %[radians] - RL tilt angle
beta  = alpha;  %[radians] - HB angle
t1    = 60*pi/180; %[radians] - IPC-BM angle
t2    = 60*pi/180; %[radians] - IPC-OPC angle
L0    = b/2; %[cm] - distance to midle OHC
L1    = 0.0013; %[cm] distance between OHC2-3
Lpc   = b/3.0; %[cm]
Lst   = 0.0001 +(0.0006-0.0001)*x_gauss/Lc; %[cm] - length of HB
Lro   = 0.004; %[cm]
%-------------------------------------------------------------------------

% mechanical parameters
% stiffnesses------------------
Kbm1 = 0*1.8e6*exp(-3.6*x_gauss);%[dyn/cm] - stiffness of BM 1st mode
Kst  = 5.8e5*exp(-3.3*x_gauss); %[dyn/cm] - stiffness of stereocilia
Ktms = 1.4e5*exp(-3*x_gauss); %[dyn/cm] - spring at TM for shear mode
Ktmb = 1.4e5*exp(-3*x_gauss); %[dyn/cm] - spring at TM for bending mode
Krl  = 7.6e4*exp(-3.25*x_gauss); %[dyn/cm] - spring at the RL-PC attachment
Kohc = 7.6e4*exp(-3.25*x_gauss); %[dyn/cm] - spring for OHC
```

```
%masses --------------------------
Mbm1 = hbm*1.0*b/2;%[gr/cm] BM mass
Mtm  = 0.9*1.2*2600d-8*exp(0.5*x_gauss); %[gr/cm] TM mass for shear mode
Mtmb = 0.77*1.2*2600d-8*exp(0.5*x_gauss);%[gr/m] TM mass for bending mdoe

if modeltype==1
    Mfluid        =Mbm1*4.6; %[gr/cm] added fluid mass for 1D fluid coupling
else
    Mfluid=0;
end

%damping coefficient
csub = 0.01*Ltm/Lst;%[dyn*s/cm^2] subtectorial space damping
cTMS = 0;%[dyn*s/cm^2] damping for TM shear mode
cBM  = 0.85;%[dyn*s/cm^2] damping for BM
cTMB = 0.5; %[dyn*s/cm^2] damping for TM bending mode
%-------------------------------------------------------------------------
%mechanical/electrical coupling parameters
%MET channel
iq=AL*648*0.001/Lst*exp(-2.15*x_gauss)*(150-10*x_gauss);%[S/cm^2*mV] - HB conductance
eps3=epsLevel*(-0.0104*(1+.1*x_gauss));%[sA/m^2] - electromechanical coupling coefficient

%-------------------------------------------------------------------------
%electrical parameters
Rtl = 4d2; %[Ohm*cm]
Rvm = 2.5d3 ; %[Ohm*cm]
Rvl = 1d3  ; %[Ohm*cm]
Ra0 =1d6/3;%[Ohm*cm]
Rm = 1*(10^6)/(3*(51-(51-3.6)*x_gauss/Lc))/3; %[Ohm*cm]
Ca =0.5d-9*3; %[F/cm]
Cm =3d-9*(18 + (42-18)*x_gauss/Lc)*3; %[F/cm]
rsv = 3d4 ; %[Ohm*cm]
rsm = 5d4  ; %[Ohm*cm]
rst = 1.5d6 ;%[Ohm*cm]

%--------------------------
psi1Lpc = sin(pi*Lpc/b);
psi2Lpc = sin(2*pi*Lpc/b);
psi1L01 = sin(pi*(L0-L1/cos(alpha))/b);
psi2L01 = sin(2*pi*(L0-L1)/b);
psi1L0  = sin(pi*(L0)/b);
psi2L0  = sin(2*pi*(L0)/b);
psi1L10 = sin(pi*(L0+L1/cos(alpha))/b);
psi2L10 = sin(2*pi*(L0+L1/cos(alpha))/b);

%uhb1 coeffs
A11 = psi1Lpc*sin(t1+t2)/sin(t2)*(sin(t1-beta) -(1-L1/Lro)*sin(alpha-beta)*cos(t1-beta)/cos(alpha-
    beta));
A13 = cos(alpha-beta)*(1-L1/Ltm) +  (1-L1/Lro)*sin(alpha-beta)*sin(alpha-beta)/cos(alpha-beta);
A14 = -sin(alpha-beta)*(1-L1/Ltm)+  (1-L1/Lro)*sin(alpha-beta);

%uhb2 coeffs
A21 = psi1Lpc*sin(t1+t2)/sin(t2)*sin(t1-alpha)/cos(alpha-beta);
A23 = 1.0/cos(alpha-beta);
A24 = 0;

%uhb3 coeffs
A31 = psi1Lpc*sin(t1+t2)/sin(t2)*(sin(t1-beta) -   (1+L1/Lro)*sin(alpha-beta)*cos(t1-beta)/cos(
    alpha-beta));
```

```
85  A33 = cos(alpha-beta)*(1+L1/Ltm) +  (1+L1/Lro)*sin(alpha-beta)*sin(alpha-beta)/cos(alpha-beta);
86  A34 = -sin(alpha-beta)*(1+L1/Ltm) +   (1+L1/Lro)*sin(alpha-beta);
87
88  %url1 coeffs
89  B11 = -(1-L1/Lro)*psi1Lpc*sin(t1+t2)*cos(t1-beta)/(sin(t2)*cos(alpha-beta));
90  B13 = (1-L1/Lro)*tan(alpha-beta);
91  B14 = (1-L1/Lro);
92
93  %url2 coeffs
94  B21 = -psi1Lpc*sin(t1+t2)*cos(t1-beta)/(sin(t2)*cos(alpha-beta));
95  B23 = tan(alpha-beta);
96  B24 = 1;
97
98  %url2 coeffs
99  B31 = -(1+L1/Lro)*psi1Lpc*sin(t1+t2)*cos(t1-beta)/(sin(t2)*cos(alpha-beta));
100 B33 = (1+L1/Lro)*tan(alpha-beta);
101 B34 = (1+L1/Lro);
102
103 %ohc1a coefficients
104 C11 = -psi1Lpc*sin(t1+t2)/sin(t2)*(cos(t1-alpha) -(1-L1/Lro)*cos(t1-beta)/cos(alpha-beta));
105 C13 = -(1-L1/Lro)*tan(alpha-beta);
106 C14 = -(1-L1/Lro);
107
108 %ohc2a coefficients
109 C21 = -psi1Lpc*sin(t1+t2)/sin(t2)*(cos(t1-alpha) -cos(t1-beta)/cos(alpha-beta));
110 C23 = -tan(alpha-beta);
111 C24 = -1;
112
113 %ohc3a coefficients
114 C31 = -psi1Lpc*sin(t1+t2)/sin(t2)*(cos(t1-alpha) -(1+L1/Lro)*cos(t1-beta)/cos(alpha-beta));
115 C33 = -(1+L1/Lro)*tan(alpha-beta);
116 C34 = -(1+L1/Lro);
117
118 %ap coefficients (top of the pillar cells)
119 D1 = psi1Lpc*sin(t1+t2)/sin(t2);
120 D3 = 0;
121 D4 = 0;
122
123 %ohc2a coefficients
124 E11 = psi1L01*cos(alpha);
125 E12 = psi2L01*cos(alpha);
126
127 %ohc2b coefficients
128 E21 = psi1L0*cos(alpha);
129 E22 = psi2L0*cos(alpha);
130
131 %ohc2c coefficients
132 E31 = psi1L10*cos(alpha);
133 E32 = psi2L10*cos(alpha);
134
135 %ohc3a coefficients
136 C1 = -3*psi1Lpc*sin(t1+t2)/sin(t2)*(cos(t1-alpha)-cos(t1-beta)/cos(alpha-beta));
137 C3 = -3*tan(alpha-beta);
138 C4 = -3;
139
140 %ohc3b coeffs
141 E1 = (psi1L01+psi1L0+psi1L10)*cos(alpha);
142 E2 = 0;
143
```

```
%ohc3b coeffs
A1 = A21+B21*Lst/(Lro);
A3 = A23+B23*Lst/Lro;
A4 = A24+B24*Lst/(Lro);
%-------------------------------------------------------------------------
%stiffnessess corresponding to the difference dof (and coupling terms) [dyn/cm]

k11 = Kbm1+Kst*((A11+B11*Lst/(Lro-L1))^2+(A21+B21*Lst/Lro)^2+(A31+B31*Lst/(Lro+L1))^2) + Krl*(B21+
    D1*Lro/Lpc)^2+Kohc*((C11+E11)^2+(C21+E21)^2+(C31+E31)^2);

k13 = Kohc*(C13*(E11+C11)+C23*(E21+C21)+C33*(E31+C31))+ Kst*((A13+B13*Lst/(Lro-L1))*(A11+B11*Lst/(
    Lro-L1))+(A23+B23*Lst/Lro)*(A21+B21*Lst/Lro) ...
    +(A33+B33*Lst/(Lro+L1))*(A31+B31*Lst/(Lro+L1)))+Krl*B23*(B21+D1*Lro/Lpc);

k14 = Kohc*(C14*(E11+C11)+C24*(C21+E21)+C34*(C31+E31))+Kst*((A14+B14*Lst/(Lro-L1))*(A11+B11*Lst/(
    Lro-L1))...
    +(A24+B24*Lst/Lro)*(A21+B21*Lst/Lro)+(A34+B34*Lst/(Lro+L1))*(A31+B31*Lst/(Lro+L1)))+Krl*B24*(
    B21+D1*Lro/Lpc);

k33 = Ktms + Kohc*(C13^2+C23^2+C33^2)+Kst*((A13+B13*Lst/(Lro-L1))^2+(A23+B23*Lst/Lro)^2+(A33+B33*
    Lst/(Lro+L1))^2) + Krl*B23^2;

k34 = Kohc*(C14*C13+C24*C23+C34*C33) + Kst*((A14+B14*Lst/(Lro-L1))*(A13+B13*Lst/(Lro-L1))+(A24+B24
    *Lst/Lro)*(A23+B23*Lst/Lro)...
    +(A34+B34*Lst/(Lro+L1))*(A33+B33*Lst/(Lro+L1))) + Krl*B24*B23;

k44 = Ktmb + Kst*((A14+B14*Lst/(Lro-L1))^2+(A24+B24*Lst/Lro)^2 +(A34+B34*Lst/(Lro+L1))^2) + Krl*
    B24^2+ Kohc*(C14^2+C34^2+C24^2);

%damping terms in corresponding matrix ------------------------------------------------------
c13 = csub*A21*A23;
c14 = 0;
c34 = 0;
c11 = cBM+csub*A21^2;
c33 = csub*A23^2+cTMS;
c44 = cTMB;
%-------------------------------------------------------------------------
%mass terms
Mbm  = Mbm1+Mfluid ;
Mtms = Mtm;
Ms   = [Mbm 0 0 ;0 Mtms 0;0 0 Mtmb];%Structural Mass
Ks   = [k11 k13 k14; k13 k33 k34; k14 k34 k44] ;% Structural Stiffness
Cs   = [c11 c13 c14; c13 c33 c34; c14 c34 c44] ;% Structural Deltabmping

%-------------------------------------
% Electrical equations with **no longitudinal cables**
Cr1 = (1/Rvm)/(1/Rvl+1/Rvm);
Cr2 = (1/Rtl)/((Cr1-1)/Rvm);
Ce   = [-Ca-Cm Ca*Cr2+Cm ; Cm -Cm];
Ke   = [-1/Ra0-1/Rm Cr2/Ra0+1/Rm ; 1/Rm -1/Rtl-1/Rm];

% coupling matrices
Cse  = zeros(3,2);
Kse=[(C1+E1)*eps3 -(C1+E1)*eps3; C3*eps3 -C3*eps3; C4*eps3 -C4*eps3]; %somatic force generation
Ces  = [eps3*(C1+E1) eps3*C3 eps3*C4; -eps3*(C1+E1) -eps3*C3 -C4*eps3];
Kes  = 3*iq*[A1 A3 A4 ; 0 0 0];

Mse = zeros(3,2);
Mes = zeros(2,3);
```

```
196 Me  = zeros(2,2);
197
198 % longitudinal parameters for TM
199
200 eta=0.5; % [g/(cm*s)]
201 G=7d4*exp(-3*x_gauss); %[g/(cm*s^2)]
202 A=2600d-8*exp(0.5*x_gauss); %[cm^2]
203
204 %parameters derived
205 Ap=A*0.5;
206 Gp=G*(-3);
207 etap=0;
208
209 %paramters at position x+Deltab
210 xminus=x_gauss-Deltab;
211 Gm=7d4*exp(-3*xminus);
212 Am=2600d-8*exp(0.5*xminus);
213 Apm=Am*0.5;
214 Gpm=Gm*(-3);
215 etam=0.5;
216
217 %paramters at position x-Deltab
218 xplus=x_gauss+Deltab;
219 Gplus=7d4*exp(-3*xplus);
220 Aplus=2600d-8*exp(0.5*xplus);
221 Applus=Aplus*0.5;
222 Gpplus=Gplus*(-3);
223 etaplus=eta;
224 etapplus=0;
225
226 % longitudinal parameters for BM
227 Dxx=-b/2*6.5*1e-4;%[dyne/cm]
228 Dxy=-b/2*3.1*1e-4;%[dyne/cm]
229 Ds=-b/2*4.3*1e-4;%[dyne/cm]
230 Dyy=1.8e6*exp(-3.6*x_gauss);%[dyne/cm]
231 %
```

D.3 Main code for the models with electrical longitudinal coupling

```
1  clear
2
3  %% cochlear parameters
4
5  NX =400; %[#] - number of elements
6  Lc = 1.85; %[cm] - length of the cochlea
7  Deltab = Lc/(NX-1); %[cm] - length of a single element
8  Xpos = 0:Deltab:Lc; %[cm] - position along the cochlea
9  W=0.1; %[cm] width of the chambers
10 h = 0.1; %[cm] - effective chamber eight
11 rho = 1; %[g/cm^3] - density of the fluids in each chamber
12
13 l5 = 0.38; %[m] - characteristic length
14 f_b5 = 43.7395e3; %[Hz] - frequency at the base of the cochlea
15 CF5 = f_b5*exp(-Xpos/l5); %[Hz] - distribution of natural frequencies
16 w_cf = 2*pi*CF5; %[Hz] - distribution of angular frequencies
```

```
17
18 %% initialization of fluid matrix and of stapes' velocity vector
19
20 I=eye(NX,NX);
21 v1=ones(NX-1,1);
22 Iinf=diag(v1,-1);
23 Isup=diag(v1,1);
24 F = -2*I+Iinf+Isup;
25 F(1,:)=0;
26 F(NX,:)=0;
27 F(1,1)=-Deltab/h;
28 F(1,2)=+Deltab/h;
29 F(NX,NX)=Deltab^2/h;
30 F = h/Deltab^2 .* F;
31
32 vs(NX,1)=0;
33 vs(1,1)=10;
34
35 %% derivation of matrices to be used in the condensation process
36
37 modeltype=3; %1 for 1D fluid coupling, 3 for 3D fluid coupling
38 epsLevel=0.9; %maximum value of epsilon_3
39 AL=0.3; %activity level
40
41 for kk=1:1:NX %576 %66 or 88
42     x_gauss=Xpos(kk);
43     param_with_el_cables;
44
45     Mglobal(1+3*(kk-1),1+3*(kk-1))=Ms(1,1); %mass matrix
46     Mglobal(1+3*(kk-1),2+3*(kk-1))=Ms(1,2);
47     Mglobal(1+3*(kk-1),3+3*(kk-1))=Ms(1,3);
48     Mglobal(2+3*(kk-1),1+3*(kk-1))=Ms(2,1);
49     Mglobal(2+3*(kk-1),2+3*(kk-1))=Ms(2,2);
50     Mglobal(2+3*(kk-1),3+3*(kk-1))=Ms(2,3);
51     Mglobal(3+3*(kk-1),1+3*(kk-1))=Ms(3,1);
52     Mglobal(3+3*(kk-1),2+3*(kk-1))=Ms(3,2);
53     Mglobal(3+3*(kk-1),3+3*(kk-1))=Ms(3,3);
54
55     Ksglobal(1+3*(kk-1),1+3*(kk-1))=Ks(1,1); %structural stiffness matrix
56     Ksglobal(1+3*(kk-1),2+3*(kk-1))=Ks(1,2);
57     Ksglobal(1+3*(kk-1),3+3*(kk-1))=Ks(1,3);
58     Ksglobal(2+3*(kk-1),1+3*(kk-1))=Ks(2,1);
59     Ksglobal(2+3*(kk-1),2+3*(kk-1))=Ks(2,2);
60     Ksglobal(2+3*(kk-1),3+3*(kk-1))=Ks(2,3);
61     Ksglobal(3+3*(kk-1),1+3*(kk-1))=Ks(3,1);
62     Ksglobal(3+3*(kk-1),2+3*(kk-1))=Ks(3,2);
63     Ksglobal(3+3*(kk-1),3+3*(kk-1))=Ks(3,3);
64
65     Csglobal(1+3*(kk-1),1+3*(kk-1))=Cs(1,1); %structural damping matrix
66     Csglobal(1+3*(kk-1),2+3*(kk-1))=Cs(1,2);
67     Csglobal(1+3*(kk-1),3+3*(kk-1))=Cs(1,3);
68     Csglobal(2+3*(kk-1),1+3*(kk-1))=Cs(2,1);
69     Csglobal(2+3*(kk-1),2+3*(kk-1))=Cs(2,2);
70     Csglobal(2+3*(kk-1),3+3*(kk-1))=Cs(2,3);
71     Csglobal(3+3*(kk-1),1+3*(kk-1))=Cs(3,1);
72     Csglobal(3+3*(kk-1),2+3*(kk-1))=Cs(3,2);
73     Csglobal(3+3*(kk-1),3+3*(kk-1))=Cs(3,3);
74
75     % contribution by TM longitudinal coupling
```

```
76      if kk<NX
77          Csglobal(2+3*(kk-1),2+3*(kk-1))=Ap*eta/Deltab+A*etap/Deltab+Csglobal(2+3*(kk-1),2+3*(kk-1)
        );
78
79
80          Csglobal(2+3*(kk-1),2+3+3*(kk-1))=-Applus*etaplus/Deltab-Aplus*etapplus/Deltab;
81
82      end
83
84      if kk<NX && kk>1
85
86          Csglobal(2+3*(kk-1),2-3+3*(kk-1))=-Am*etam/Deltab^2;
87
88          Csglobal(2+3*(kk-1),2+3*(kk-1))=2*A*eta/Deltab^2+Csglobal(2+3*(kk-1),2+3*(kk-1));
89
90          Csglobal(2+3*(kk-1),2+3+3*(kk-1))=-Aplus*etaplus/Deltab^2+Csglobal(2+3*(kk-1),2+3+3*(kk-1)
        );
91
92      end
93
94      if kk<NX
95          Ksglobal(2+3*(kk-1),2+3*(kk-1))=Ap*G/Deltab+A*Gp/Deltab+Ksglobal(2+3*(kk-1),2+3*(kk-1));
96
97
98          Ksglobal(2+3*(kk-1),2+3+3*(kk-1))=-Applus*Gplus/Deltab-Aplus*Gpplus/Deltab;
99
100
101     end
102
103     if kk<NX && kk>1
104
105         Ksglobal(2+3*(kk-1),2-3+3*(kk-1))=-Am*Gm/Deltab^2;
106
107         Ksglobal(2+3*(kk-1),2+3*(kk-1))=2*A*G/Deltab^2+Ksglobal(2+3*(kk-1),2+3*(kk-1));
108
109         Ksglobal(2+3*(kk-1),2+3+3*(kk-1))=-Aplus*Gplus/Deltab^2+Ksglobal(2+3*(kk-1),2+3+3*(kk-1));
110
111     end
112
113
114     % contirbution by BM longitudinal coupling
115     if kk<NX && kk>1
116
117         Ksglobal(1+3*(kk-1),1-3+3*(kk-1))=+2*(Dxy+Ds)*bmpar2/Deltab^2;
118
119         Ksglobal(1+3*(kk-1),1+3*(kk-1))=-2*2*(Dxy+Ds)*bmpar2/Deltab^2+Ksglobal(1+3*(kk-1),1+3*(kk
        -1));
120
121         Ksglobal(1+3*(kk-1),1+3+3*(kk-1))=+2*(Dxy+Ds)*bmpar2/Deltab^2+Ksglobal(1+3*(kk-1),1+3+3*(
        kk-1));
122
123     end
124
125     if kk<NX-1 && kk>1+1
126
127         Ksglobal(1+3*(kk-1),1-6+3*(kk-1))=-Dxx/Deltab^4;
128
129         Ksglobal(1+3*(kk-1),1-3+3*(kk-1))=Dxx*(4/Deltab^4)+Ksglobal(1+3*(kk-1),1-3+3*(kk-1));
130
```

```
131         Ksglobal(1+3*(kk-1),1+3*(kk-1))=-Dxx*(6/Deltab^4)+Ksglobal(1+3*(kk-1),1+3*(kk-1));
132
133         Ksglobal(1+3*(kk-1),1+3+3*(kk-1))=Dxx*(4/Deltab^4)+Ksglobal(1+3*(kk-1),1+3+3*(kk-1));
134
135         Ksglobal(1+3*(kk-1),1+6+3*(kk-1))=-Dxx/Deltab^4;
136
137     end
138
139     Ksglobal(1+3*(kk-1),1+3*(kk-1))=Dyy+Ksglobal(1+3*(kk-1),1+3*(kk-1)); %0th derivative-Dyy*pi^4/
        b^4
140
141     %electrical damping and stiffness matrices with longitudinal coupling by cables
142
143     Ceglobal(1+4*(kk-1),1+4*(kk-1))=0;
144     Ceglobal(1+4*(kk-1),2+4*(kk-1))=0;
145     Ceglobal(1+4*(kk-1),3+4*(kk-1))=0;
146     Ceglobal(1+4*(kk-1),4+4*(kk-1))=0;
147
148     Ceglobal(2+4*(kk-1),1+4*(kk-1))=0;
149     Ceglobal(2+4*(kk-1),2+4*(kk-1))=-3*Ca;
150     Ceglobal(2+4*(kk-1),3+4*(kk-1))=3*Ca;
151     Ceglobal(2+4*(kk-1),4+4*(kk-1))=0;
152
153     Ceglobal(3+4*(kk-1),1+4*(kk-1))=0;
154     Ceglobal(3+4*(kk-1),2+4*(kk-1))=3*Ca;
155     Ceglobal(3+4*(kk-1),3+4*(kk-1))=-3*Ca-3*Cm;
156     Ceglobal(3+4*(kk-1),4+4*(kk-1))=3*Cm;
157
158     Ceglobal(4+4*(kk-1),1+4*(kk-1))=0;
159     Ceglobal(4+4*(kk-1),2+4*(kk-1))=0;
160     Ceglobal(4+4*(kk-1),3+4*(kk-1))=3*Cm;
161     Ceglobal(4+4*(kk-1),4+4*(kk-1))=-3*Cm;
162
163     Keglobal(1+4*(kk-1),1+4*(kk-1))=-1/Rvl-1/Rvm;
164     Keglobal(1+4*(kk-1),2+4*(kk-1))=1/Rvm;
165     Keglobal(1+4*(kk-1),3+4*(kk-1))=0;
166     Keglobal(1+4*(kk-1),4+4*(kk-1))=0;
167
168     Keglobal(2+4*(kk-1),1+4*(kk-1))=1/Rvm;
169     Keglobal(2+4*(kk-1),2+4*(kk-1))=-1/Rvm-3/Ra0;
170     Keglobal(2+4*(kk-1),3+4*(kk-1))=3/Ra0;
171     Keglobal(2+4*(kk-1),4+4*(kk-1))=0;
172
173     Keglobal(3+4*(kk-1),1+4*(kk-1))=0;
174     Keglobal(3+4*(kk-1),2+4*(kk-1))=3/Ra0;
175     Keglobal(3+4*(kk-1),3+4*(kk-1))=-3/Ra0-3/Rm;
176     Keglobal(3+4*(kk-1),4+4*(kk-1))=3/Rm;
177
178     Keglobal(4+4*(kk-1),1+4*(kk-1))=0;
179     Keglobal(4+4*(kk-1),2+4*(kk-1))=0;
180     Keglobal(4+4*(kk-1),3+4*(kk-1))=3/Rm;
181     Keglobal(4+4*(kk-1),4+4*(kk-1))=-1/Rtl-3/Rm;
182
183
184     if kk<NX && kk>1
185
186         Keglobal(1+4*(kk-1),1-4+4*(kk-1))=1/(rsv*Deltab^2);
187         Keglobal(2+4*(kk-1),2-4+4*(kk-1))=1/(rsm*Deltab^2);
188         Keglobal(4+4*(kk-1),4-4+4*(kk-1))=1/(rst*Deltab^2);
```

```
189
190         Keglobal(1+4*(kk-1),1+4*(kk-1))=-2/(rsv*Deltab^2)+Keglobal(1+4*(kk-1),1+4*(kk-1));
191         Keglobal(2+4*(kk-1),2+4*(kk-1))=-2/(rsm*Deltab^2)+Keglobal(2+4*(kk-1),2+4*(kk-1));
192         Keglobal(4+4*(kk-1),4+4*(kk-1))=-2/(rst*Deltab^2)+Keglobal(4+4*(kk-1),4+4*(kk-1));
193
194         Keglobal(1+4*(kk-1),1+4+4*(kk-1))=1/(rsv*Deltab^2);
195         Keglobal(2+4*(kk-1),2+4+4*(kk-1))=1/(rsm*Deltab^2);
196         Keglobal(4+4*(kk-1),4+4+4*(kk-1))=1/(rst*Deltab^2);
197
198     end
199
200     %electric-structural matrices with longitudinal coupling by cables
201
202     Cesglobal(1+4*(kk-1),1+3*(kk-1))=0;
203     Cesglobal(1+4*(kk-1),2+3*(kk-1))=0;
204     Cesglobal(1+4*(kk-1),3+3*(kk-1))=0;
205     Cesglobal(2+4*(kk-1),1+3*(kk-1))=0;
206     Cesglobal(2+4*(kk-1),2+3*(kk-1))=0;
207     Cesglobal(2+4*(kk-1),3+3*(kk-1))=0;
208     Cesglobal(3+4*(kk-1),1+3*(kk-1))=-eps3*(C1+E1);
209     Cesglobal(3+4*(kk-1),2+3*(kk-1))=-eps3*C3;
210     Cesglobal(3+4*(kk-1),3+3*(kk-1))=-eps3*C4;
211     Cesglobal(4+4*(kk-1),1+3*(kk-1))=eps3*(C1+E1);
212     Cesglobal(4+4*(kk-1),2+3*(kk-1))=eps3*C3;
213     Cesglobal(4+4*(kk-1),3+3*(kk-1))=eps3*C4;
214
215     Kesglobal(1+4*(kk-1),1+3*(kk-1))=0;
216     Kesglobal(1+4*(kk-1),2+3*(kk-1))=0;
217     Kesglobal(1+4*(kk-1),3+3*(kk-1))=0;
218     Kesglobal(2+4*(kk-1),1+3*(kk-1))=+3*iq*A1;
219     Kesglobal(2+4*(kk-1),2+3*(kk-1))=+3*iq*A3;
220     Kesglobal(2+4*(kk-1),3+3*(kk-1))=+3*iq*A4;
221     Kesglobal(3+4*(kk-1),1+3*(kk-1))=-3*iq*A1;
222     Kesglobal(3+4*(kk-1),2+3*(kk-1))=-3*iq*A3;
223     Kesglobal(3+4*(kk-1),3+3*(kk-1))=-3*iq*A4;
224     Kesglobal(4+4*(kk-1),1+3*(kk-1))=0;
225     Kesglobal(4+4*(kk-1),2+3*(kk-1))=0;
226     Kesglobal(4+4*(kk-1),3+3*(kk-1))=0;
227
228     %structure-electrical matrices with longitudinal coupling by cables
229     %zeros as MET is not reciprocal
230
231     Cseglobal(1+3*(kk-1),1+4*(kk-1))=0;
232     Cseglobal(1+3*(kk-1),2+4*(kk-1))=0;
233     Cseglobal(1+3*(kk-1),3+4*(kk-1))=0;
234     Cseglobal(1+3*(kk-1),4+4*(kk-1))=0;
235     Cseglobal(2+3*(kk-1),1+4*(kk-1))=0;
236     Cseglobal(2+3*(kk-1),2+4*(kk-1))=0;
237     Cseglobal(2+3*(kk-1),3+4*(kk-1))=0;
238     Cseglobal(2+3*(kk-1),4+4*(kk-1))=0;
239     Cseglobal(3+3*(kk-1),1+4*(kk-1))=0;
240     Cseglobal(3+3*(kk-1),2+4*(kk-1))=0;
241     Cseglobal(3+3*(kk-1),3+4*(kk-1))=0;
242     Cseglobal(3+3*(kk-1),4+4*(kk-1))=0;
243
244     b22(kk)=b; %[cm] width of the BM
245 end
246
247 Kseglobal=transpose(Cesglobal);
```

```
248
249 %% initialization of matrices and vectors to calculate the response
250 tic
251 clear S
252 clear T
253
254 T(NX,7*NX)=0;
255 for i=1:1:NX
256     T(i,1+3*(i-1))=1;
257 end
258
259 S(7*NX,NX)=0;
260 for i=1:1:NX
261     S(1+3*(i-1),1+1*(i-1))=1;
262 end
263
264 Yppkk(NX,NX)=0;
265 p_s(NX,NX)=0;
266 p_L(NX,NX)=0;
267 VBM3d(NX,NX)=0;
268 Z_nf(NX,NX)=0;
269
270 %% calculation of the response at each frequency
271 for pp=1:length(w_cf)
272     w_my=w_cf(pp);
273
274     %calculation of the equivalent BM admittance matrix
275
276     Ks1global=-w_myˆ2*Mglobal+Ksglobal+1i*w_my*Csglobal;
277     Kse1=Kseglobal+1i*w_my*Cseglobal;
278     Kes1=1i*w_my*Cesglobal+Kesglobal;
279     Ke1=Keglobal+1i*w_my*Ceglobal;
280     Ksaglobal=[Ks1global Kse1; Kes1 Ke1];
281     Y=inv(Ksaglobal/(1i*w_my));
282     Yabm=T*Y*S.*b22*(1/(2*pi));
283
284     %calculation of fluid coupling matrix
285     Z_nf(1:NX,1:NX)=0;
286
287     for ll=1:1:NX
288         for jj=1:1:NX
289             Z_nf(ll,jj) = 1.3958*1i*w_my*rho*Deltab*exp(-abs(jj-ll)*Deltab/(0.0854*W));
290         end
291     end
292
293     %calculation of the response by the elemental method
294
295     Yabm(1,1)=0;
296     Yabm(NX,NX)=0;
297     Zfc=-2*1i*w_my*rho.*inv(F)+Z_nf;
298     p_s(:,pp)=Zfc*vs;
299     p_L(:,pp)=(I+Zfc*Yabm)\p_s(:,pp);
300     VBM3d(:,pp)=-(Yabm*p_L(:,pp));
301
302 end
303 toc
304
305 %% plot of the velocity response
306
```

```
fr=CF5;
fr=fr/1000;
posit5=88; %x_0

prt = 2; % #1 for printing
doc_type = 1;   % #0 quick print, no document
% #1 for papers, reports, theses
% #2 presentationsz
% #3 posters
if epsLevel>0 && AL>=0.00002
    col = {'--','--k','--g', '--b','--m','--m'};
elseif epsLevel==1 && AL==0
    col = {'-.','-.k','-.g', '-.b','-.m','--m'};
elseif epsLevel==0
    col = {'-','-k','-g', '-b','-m','--m'};
end
fig_name = {'plot_1'};
Ft_size = 12;
Ft_name = 'Times New Roman';
set(0,'defaulttextinterpreter','tex')
set(0,'DefaultTextFontSize', Ft_size)
set(0,'DefaultTextFontName', Ft_name)
set(0,'DefaultAxesFontSize', Ft_size)
set(0,'DefaultAxesFontName', Ft_name)

figure(13)
hold on
subplot(2,2,1)
semilogx(fr,20*log10(abs(VBM3d(posit5,:))),col{1},'Linewidth',1,'DisplayName','Active', '
    Handlevisibility','on')
hold on
grid on
xlabel('Frequency [kHz] ','interpreter','tex')
ylabel('|V| [db re stapes]','interpreter','tex')
set(gca,'FontSize',Ft_size)
ylim([0 65])
xlim([2 40])
xticks([2:10,20,30,40])

angle_Va=unwrap(angle(VBM3d(posit5,:)))/(2*pi);
subplot(2,2,3)
semilogx(fr,angle_Va-angle_Va(end),col{1},'Linewidth',1,'DisplayName','Active', 'Handlevisibility'
    ,'on')
hold on
grid on
xlabel('Frequency [kHz] ','interpreter','tex')
ylabel('\angle V [cycles]','interpreter','tex')
set(gca,'FontSize',Ft_size)
xlim([2 40])
xticks([2:10,20,30,40])
%
```

D.4 Parameters for code with electrical longitudinal coupling

In this case, the code is the same as that reported in Appendix D.2, apart from lines 55 to 58, which are modified as:

```
1 %%param_with_el_cables.m
2
3 Ra0 =1d6;%[Ohm*cm]
4 Rm = 1*(10^6)/(3*(51-(51-3.6)*x_gauss/Lc)); %[Ohm*cm]
5 Ca =0.5d-9; %[F/cm]
6 Cm =3d-9*(18 + (42-18)*x_gauss/Lc); %[F/cm]
7
8 %
```

References

J.B. Allen. Cochlear micromechanics—A physical model of transduction. *The Journal of the Acoustical Society of America*, 68(6):1660–1670, dec 1980. ISSN 0001-4966. . URL http://asa.scitation.org/doi/10.1121/1.385198.

G. Békésy. *Experiments in Hearing*, volume McGraw-Hil. American Institute of Physics, 1960. ISBN 0883186306.

R.M. Berne, B.M. Koeppen, and B.A. Stanton. *Berne & Levy Physiology*. Mosby, 2008. ISBN 0323045820.

T. Bowling, C. Lemons, and J. Meaud. Reducing tectorial membrane viscoelasticity enhances spontaneous otoacoustic emissions and compromises the detection of low level sound. *Scientific Reports*, 9(1):7494, dec 2019. ISSN 2045-2322. . URL http://www.nature.com/articles/s41598-019-43970-5.

F. Chen, N. Choudhury, J. Zheng, S. Matthews, A.L. Nutall, and S.L. Jacques. In vivo imaging and low-coherence interferometry of organ of Corti vibration. *Journal of Biomedical Optics*, 12(2):021006, 2007. ISSN 10833668. . URL http://biomedicaloptics.spiedigitallibrary.org/article.aspx?doi=10.1117/1.2717134.

F. Chen, D. Zha, A. Fridberger, J. Zheng, N. Choudhury, S.L. Jacques, R.K. Wang, X. Shi, and A.L. Nuttall. A differentially amplified motion in the ear for near-threshold sound detection. *Nature Neuroscience*, 14(6):770–774, jun 2011. ISSN 1097-6256. . URL http://www.nature.com/articles/nn.2827.

L. Cheng. *Cochlear -based transducers: Modeling and design.* PhD thesis, University of Michigan, 2007. URL https://deepblue.lib.umich.edu/handle/2027.42/126897.

N. Choudhury, G. Song, F. Chen, S. Matthews, T. Tschinkel, J. Zheng, S.L. Jacques, and A.L. Nuttall. Low coherence interferometry of the cochlear partition. *Hearing Research*, 220(1-2):1–9, oct 2006. ISSN 03785955. . URL http://linkinghub.elsevier.com/retrieve/pii/S0378595506001523.

N. P. Cooper, A. Vavakou, and M. van der Heijden. Vibration hotspots reveal longitudinal funneling of sound-evoked motion in the mammalian cochlea. *Nature Communications*, 9(1):3054, dec 2018. ISSN 2041-1723. . URL http://www.nature.com/articles/s41467-018-05483-z.

N.P. Cooper and W.S. Rhode. Basilar membrane mechanics in the hook region of cat and guinea-pig cochleae: Sharp tuning and nonlinearity in the absence of baseline position shifts. *Hearing Research*, 63(1-2):163–190, nov 1992. ISSN 03785955. . URL http://linkinghub.elsevier.com/retrieve/pii/037859559290083Y.

P. Dallos. The active cochlea. *The Journal of Neuroscience*, 12(12):4575–4585, dec 1992. ISSN 0270-6474. . URL https://www.jneurosci.org/lookup/doi/10.1523/JNEUROSCI.12-12-04575.1992.

H. Davis. A Model for Transducer Action in the Cochlea. *Cold Spring Harbor Symposia on Quantitative Biology*, 30:181–190, jan 1965. ISSN 0091-7451. . URL http://symposium.cshlp.org/cgi/doi/10.1101/SQB.1965.030.01.020.

H. Davis. An active process in cochlear mechanics. *Hearing Research*, 9(1):79–90, jan 1983. ISSN 03785955. . URL http://linkinghub.elsevier.com/retrieve/pii/0378595583901363.

S.R. Davis, H.; Silverman. *Hearing and deafness*. Holt, Rinehart and Winston, New York, 1970.

E. de Boer. Mechanics of the Cochlea: Modeling Efforts. In R. Richard Dallos , Peter ; Popper, N. Arthur; Fay, editor, *The Cochlea*, chapter 5, pages 258–317. Springer, 1996 edition, 1996. . URL http://link.springer.com/10.1007/978-1-4612-0757-3{_}5.

E. de Boer and M.A. Viergever. Validity of the Liouville-Green (or WKB) method for cochlear mechanics. *Hearing Research*, 8(2):131–155, oct 1982. ISSN 03785955. . URL https://linkinghub.elsevier.com/retrieve/pii/0378595582900715.

P. Deepu. Cochlear mechanics with fluid viscosity and compressibility. *Physical Review E*, 99(3):032417, mar 2019. ISSN 2470-0045. . URL https://link.aps.org/doi/10.1103/PhysRevE.99.032417.

H.A. Deferrari, R.A. Darby, and F.A. Andrews. Vibrational Displacement and Mode-Shape Measurement by a Laser Interferometer. *The Journal of the Acoustical Society of America*, 42(5):982–990, nov 1967. ISSN 0001-4966. . URL http://asa.scitation.org/doi/10.1121/1.1910707.

J.B. Dewey, B.E. Applegate, and J.S. Oghalai. Amplification and Suppression of Traveling Waves along the Mouse Organ of Corti: Evidence for Spatial Variation in the Longitudinal Coupling of Outer Hair Cell-Generated Forces. *The Journal*

of Neuroscience, 39(10):1805–1816, mar 2019. ISSN 0270-6474. . URL https://www.jneurosci.org/lookup/doi/10.1523/JNEUROSCI.2608-18.2019.

W. Dong and E.S. Olson. Detection of Cochlear Amplification and Its Activation. *Biophysical Journal*, 105(4):1067–1078, aug 2013. ISSN 00063495. . URL https://linkinghub.elsevier.com/retrieve/pii/S000634951300800X.

S.J. Elliott and G. Ni. An elemental approach to modelling the mechanics of the cochlea. *Hearing Research*, 360:14–24, mar 2018. ISSN 03785955. . URL https://linkinghub.elsevier.com/retrieve/pii/S0378595517303465.

S.J. Elliott, B. Lineton, and G. Ni. Fluid coupling in a discrete model of cochlear mechanics. *The Journal of the Acoustical Society of America*, 130(3):1441–1451, sep 2011. ISSN 0001-4966. . URL http://asa.scitation.org/doi/10.1121/1.3607420.

S.J. Elliott, G. Ni, B.R. Mace, and B. Lineton. A wave finite element analysis of the passive cochlea. *The Journal of the Acoustical Society of America*, 133(3):1535–1545, mar 2013. ISSN 0001-4966. . URL http://asa.scitation.org/doi/10.1121/1.4790350.

R. Fettiplace. Hair Cell Transduction, Tuning, and Synaptic Transmission in the Mammalian Cochlea. In *Comprehensive Physiology*, pages 1197–1227. John Wiley & Sons, Inc., Hoboken, NJ, USA, sep 2017. ISBN 9780470650714. . URL https://onlinelibrary.wiley.com/doi/abs/10.1002/cphy.c160049.

R.Z. Gan, B.P. Reeves, and X. Wang. Modeling of Sound Transmission from Ear Canal to Cochlea. *Annals of Biomedical Engineering*, 35(12):2180–2195, nov 2007. ISSN 0090-6964. . URL http://link.springer.com/10.1007/s10439-007-9366-y.

T. Gold. Hearing. II. The Physical Basis of the Action of the Cochlea. *Proceedings of the Royal Society of London. Series B - Biological Sciences*, 135(881):492–498, dec 1948. ISSN 2053-9193. . URL http://www.royalsocietypublishing.org/doi/10.1098/rspb.1948.0025.

W. He, D. Kemp, and T. Ren. Timing of the reticular lamina and basilar membrane vibration in living gerbil cochleae. *eLife*, 7, sep 2018. ISSN 2050-084X. . URL https://elifesciences.org/articles/37625.

J.S. Iyer, S.A. Batts, K.K. Chu, M.I. Sahin, H.M. Leung, G.J. Tearney, and K.M. Stankovic. Micro-optical coherence tomography of the mammalian cochlea. *Scientific Reports*, 6(1):33288, dec 2016. ISSN 2045-2322. . URL http://www.nature.com/articles/srep33288.

B.M. Johnstone and A.J.F. Boyle. Basilar Membrane Vibration Examined with the Mossbauer Technique. *Science*, 158(3799):389–390, oct 1967. ISSN 0036-8075. . URL http://www.sciencemag.org/cgi/doi/10.1126/science.158.3799.389.

B.M. Johnstone, K.J. Taylor, and A.J. Boyle. Mechanics of the Guinea Pig Cochlea. *The Journal of the Acoustical Society of America*, 47(2B):504–509, feb 1970. ISSN 0001-4966. . URL http://asa.scitation.org/doi/10.1121/1.1911921.

L.J. Kanis and E. de Boer. Self-suppression in a locally active nonlinear model of the cochlea: A quasilinear approach. *The Journal of the Acoustical Society of America*, 94(6):3199–3206, dec 1993. ISSN 0001-4966. . URL http://asa.scitation.org/doi/10.1121/1.407225.

A. Karlos. *Wave propagation in non-uniform waveguides*. PhD thesis, University of Southampton, 2020. URL http://eprints.soton.ac.uk/id/eprint/441961.

S. Khanna and D. Leonard. Basilar membrane tuning in the cat cochlea. *Science*, 215 (4530):305–306, jan 1982. ISSN 0036-8075. . URL http://www.sciencemag.org/cgi/doi/10.1126/science.7053580.

S. M. Khanna, J.F. Willemin, and R. Dandliker. Heterodyne interferometer, 1987. URL https://patentimages.storage.googleapis.com/c4/13/bd/cccb69f5b70f10/US4834111.pdf.

S.M. Khanna. Homodyne interferometer for basilar membrane measurements. *Hearing Research*, 23(1):9–26, jan 1986. ISSN 03785955. . URL https://www.sciencedirect.com/science/article/pii/0378595586901723.

S.M. Khanna, J. Tonndorf, and W.W. Walcott. Laser Interferometer for the Measurement of Submicroscopic Displacement Amplitudes and Their Phases in Small Biological Structures. *The Journal of the Acoustical Society of America*, 44(6):1555–1565, dec 1968. ISSN 0001-4966. . URL http://asa.scitation.org/doi/10.1121/1.1911296.

H.Y. Lee, P.D. Raphael, A. Xia, J. Kim, N. Grillet, B.E. Applegate, A. K. Ellerbee Bowden, and J.S. Oghalai. Two-Dimensional Cochlear Micromechanics Measured In Vivo Demonstrate Radial Tuning within the Mouse Organ of Corti. *Journal of Neuroscience*, 36(31):8160–8173, aug 2016. ISSN 0270-6474. . URL http://www.jneurosci.org/cgi/doi/10.1523/JNEUROSCI.1157-16.2016.

G.H. MacDonald and E.W. Rubel. Three-dimensional imaging of the intact mouse cochlea by fluorescent laser scanning confocal microscopy. *Hearing Research*, 243 (1-2):1–10, sep 2008. ISSN 03785955. . URL http://linkinghub.elsevier.com/retrieve/pii/S0378595508001068.

F. Martini and J. L. Nath. *Fundamentals of anatomy & physiology*. Pearson/Benjamin Cummings, San Francisco, 8 edition, 2009.

R. Mathews, R.; Walker. *Mathematical Methods of Physics*. Benjamin, New York, 1964.

J. Meaud and K. Grosh. The effect of tectorial membrane and basilar membrane longitudinal coupling in cochlear mechanics. *The Journal of the Acoustical Society of America*, 127(3):1411–1421, mar 2010. ISSN 0001-4966. . URL http://asa.scitation.org/doi/10.1121/1.3290995.

J. Meaud and C. Lemons. Nonlinear response to a click in a time-domain model of the mammalian ear. *The Journal of the Acoustical Society of America*, 138(1):193–207, jul 2015. ISSN 0001-4966. . URL http://asa.scitation.org/doi/10.1121/1.4921282.

S.T. Neely. Finite difference solution of a two-dimensional mathematical model of the cochlea. *The Journal of the Acoustical Society of America*, 69(5):1386–1393, may 1981. ISSN 0001-4966. . URL http://asa.scitation.org/doi/10.1121/1.385820.

S.T. Neely. Mathematical modeling of cochlear mechanics. *The Journal of the Acoustical Society of America*, 78(1):345–352, jul 1985. ISSN 0001-4966. . URL http://asa.scitation.org/doi/10.1121/1.392497.

S.T. Neely. A model of cochlear mechanics with outer hair cell motility. *The Journal of the Acoustical Society of America*, 94(1):137–146, jul 1993. ISSN 0001-4966. . URL http://asa.scitation.org/doi/10.1121/1.407091.

S.T. Neely and D.O. Kim. A model for active elements in cochlear biomechanics. *The Journal of the Acoustical Society of America*, 79(5):1472–1480, may 1986. ISSN 0001-4966. . URL http://asa.scitation.org/doi/10.1121/1.393674.

G. Ni and S.J. Elliott. Effect of basilar membrane radial velocity profile on fluid coupling in the cochlea. *The Journal of the Acoustical Society of America*, 133(3):EL181–EL187, mar 2013. ISSN 0001-4966. . URL http://asa.scitation.org/doi/10.1121/1.4789863.

G. Ni and S.J. Elliott. Comparing methods of modeling near field fluid coupling in the cochlea. *The Journal of the Acoustical Society of America*, 137(3):1309–1317, mar 2015. ISSN 0001-4966. . URL http://asa.scitation.org/doi/10.1121/1.4908242.

G. Ni, S.J. Elliott, and J. Baumgart. Finite-element model of the active organ of Corti. *Journal of The Royal Society Interface*, 13(115):20150913, feb 2016. ISSN 1742-5689. . URL http://rsif.royalsocietypublishing.org/lookup/doi/10.1098/rsif.2015.0913.

K.E. Nilsen and I.J. Russell. The spatial and temporal representation of a tone on the guinea pig basilar membrane. *Proceedings of the National Academy of Sciences*, 97(22):11751–11758, oct 2000. ISSN 0027-8424. . URL https://www.pnas.org/content/97/22/11751.

A.A. Parthasarathi. *Numerical modeling and electro -acoustic stimulus response analysis for cochlear mechanics.* PhD thesis, University of Michigan, 2000. URL https://deepblue.lib.umich.edu/handle/2027.42/132656.

J.O. Pickles. *Introduction to the Physiology of Hearing.* Bingley : Emerald, 2012.

D. Purves, GJ Augustine, and D Fitzpatrick, editors. *Neuroscience.* Sinauer Associates, Sunderland (MA), 2 edition, 2001. URL https://www.ncbi.nlm.nih.gov/books/NBK10867/.

S. Ramamoorthy, N.V. Deo, and K. Grosh. A mechano-electro-acoustical model for the cochlea: Response to acoustic stimuli. *The Journal of the Acoustical Society of America*, 121(5):2758–2773, may 2007. ISSN 0001-4966. . URL http://asa.scitation.org/doi/10.1121/1.2713725.

S.S. Rao. *Vibration of Continuous Systems.* John Wiley & Sons, Inc., Hoboken, NJ, USA, dec 2006. ISBN 9780470117866. . URL http://doi.wiley.com/10.1002/9780470117866.

M.J. Rapson, T.J. Hamilton, and J.C. Tapson. On the fluid-structure interaction in the cochlea. *The Journal of the Acoustical Society of America*, 136(1):284–300, jul 2014. ISSN 0001-4966. . URL http://asa.scitation.org/doi/10.1121/1.4883382.

A. Recio-Spinoso and J.S. Oghalai. Mechanical tuning and amplification within the apex of the guinea pig cochlea. *The Journal of Physiology*, 595(13):4549–4561, jul 2017. ISSN 00223751. . URL http://doi.wiley.com/10.1113/JP273881.

T. Ren. Longitudinal pattern of basilar membrane vibration in the sensitive cochlea. *Proceedings of the National Academy of Sciences*, 99(26):17101–17106, dec 2002. ISSN 0027-8424. . URL http://www.pnas.org/cgi/doi/10.1073/pnas.262663699.

T. Ren, W. He, and E. Porsov. Localization of the Cochlear Amplifier in Living Sensitive Ears. *PLoS ONE*, 6(5):e20149, may 2011. ISSN 1932-6203. . URL https://dx.plos.org/10.1371/journal.pone.0020149.

T. Ren, W. He, and P.G. Barr-Gillespie. Reverse transduction measured in the living cochlea by low-coherence heterodyne interferometry. *Nature Communications*, 7(1):10282, dec 2016a. ISSN 2041-1723. . URL http://www.nature.com/articles/ncomms10282.

T. Ren, W. He, and D. Kemp. Reticular lamina and basilar membrane vibrations in living mouse cochleae. *Proceedings of the National Academy of Sciences*, 113(35):9910–9915, aug 2016b. ISSN 0027-8424. . URL http://www.pnas.org/lookup/doi/10.1073/pnas.1607428113.

W.S. Rhode. Observations of the Vibration of the Basilar Membrane in Squirrel Monkeys using the Mössbauer Technique. *The Journal of the Acoustical Society of America*,

49(4B):1218–1231, apr 1971. ISSN 0001-4966. . URL http://asa.scitation.org/doi/10.1121/1.1912485.

W.S. Rhode and C.D. Geisler. Measurement of the Amplitude and Phase of Vibration of the Basilar Membrane Using the Mössbauer Effect. *The Journal of the Acoustical Society of America*, 47(1A):60–60, jan 1970. ISSN 0001-4966. . URL http://asa.scitation.org/doi/10.1121/1.1974630.

W.S. Rhode and A. Recio. Study of mechanical motions in the basal region of the chinchilla cochlea. *The Journal of the Acoustical Society of America*, 107(6):3317–3332, jun 2000. ISSN 0001-4966. . URL http://asa.scitation.org/doi/10.1121/1.429404.

L. Robles and M.A. Ruggero. Mechanics of the Mammalian Cochlea. *Physiological Reviews*, 81(3):1305–1352, jul 2001. ISSN 0031-9333. . URL https://www.physiology.org/doi/10.1152/physrev.2001.81.3.1305.

L. Robles, M.A. Ruggero, and N.C. Rich. Basilar membrane mechanics at the base of the chinchilla cochlea. I. Input–output functions, tuning curves, and response phases. *The Journal of the Acoustical Society of America*, 80(5):1364–1374, nov 1986. ISSN 0001-4966. . URL http://asa.scitation.org/doi/10.1121/1.394389.

M.A. Ruggero, N.C. Rich, A. Recio, S.S. Narayan, and L. Robles. Basilar-membrane responses to tones at the base of the chinchilla cochlea. *The Journal of the Acoustical Society of America*, 101(4):2151–2163, apr 1997. ISSN 0001-4966. . URL http://asa.scitation.org/doi/10.1121/1.418265.

J. Santos-Sacchi. Harmonics of outer hair cell motility. *Biophysical Journal*, 65(5):2217–2227, nov 1993. ISSN 00063495. . URL https://linkinghub.elsevier.com/retrieve/pii/S0006349593812475.

A. Sasmal and K. Grosh. Unified cochlear model for low- and high-frequency mammalian hearing. *Proceedings of the National Academy of Sciences*, 116(28):13983–13988, jul 2019. ISSN 0027-8424. . URL http://www.pnas.org/lookup/doi/10.1073/pnas.1900695116.

P.M. Sellick, R. Patuzzi, and B.M. Johnstone. Measurement of basilar membrane motion in the guinea pig using the Mössbauer technique. *The Journal of the Acoustical Society of America*, 72(1):131–141, jul 1982. ISSN 0001-4966. . URL http://asa.scitation.org/doi/10.1121/1.387996.

C.A. Shera. Laser amplification with a twist: Traveling-wave propagation and gain functions from throughout the cochlea. *The Journal of the Acoustical Society of America*, 122(5):2738, 2007. ISSN 00014966. . URL http://scitation.aip.org/content/asa/journal/jasa/122/5/10.1121/1.2783205.

C.R. Steele and C.E. Miller. An improved WKB calculation for a two-dimensional cochlear model. *The Journal of the Acoustical Society of America*, 68(1):147–148, jul 1980. ISSN 0001-4966. . URL http://asa.scitation.org/doi/10.1121/1.384640.

C.R. Steele and L. A. Taber. Three-dimensional model calculations for guinea pig cochlea. *The Journal of the Acoustical Society of America*, 69(4):1107–1111, apr 1981. ISSN 0001-4966. . URL http://asa.scitation.org/doi/10.1121/1.385679.

C.R. Steele and L.A. Taber. Comparison of WKB and finite difference calculations for a two-dimensional cochlear model. *The Journal of the Acoustical Society of America*, 65(4):1001–1006, apr 1979a. ISSN 0001-4966. . URL http://asa.scitation.org/doi/10.1121/1.382569.

C.R. Steele and L.A. Taber. Comparison of WKB calculations and experimental results for three-dimensional cochlear models. *The Journal of the Acoustical Society of America*, 65(4):1007–1018, apr 1979b. ISSN 0001-4966. . URL http://asa.scitation.org/doi/10.1121/1.382570.

L.A. Taber and C.R. Steele. Cochlear model including three-dimensional fluid and four modes of partition flexibility. *The Journal of the Acoustical Society of America*, 70 (2):426–436, aug 1981. ISSN 0001-4966. . URL http://asa.scitation.org/doi/10.1121/1.386785.

J. Tonndorf. Fluid Motion in Cochlear Models. *The Journal of the Acoustical Society of America*, 29(5):558–568, may 1957. ISSN 0001-4966. . URL http://asa.scitation.org/doi/10.1121/1.1908965.

H.F. von Helmoltz. *Théorie Physiologique de la Musique*. Masson G. Ed., Paris, 1874.

Y. Wang, C. R. Steele, and S. Puria. Cochlear Outer-Hair-Cell Power Generation and Viscous Fluid Loss. *Scientific Reports*, 6(1):19475, may 2016. ISSN 2045-2322. . URL http://www.nature.com/articles/srep19475.

L. Watts. The mode-coupling Liouville–Green approximation for a two-dimensional cochlear model. *The Journal of the Acoustical Society of America*, 108(5):2266–2271, nov 2000. ISSN 0001-4966. . URL http://asa.scitation.org/doi/10.1121/1.1310194.

J.P. Wilson and J.R. Johnstone. Capacitive probe measures of basilar membrane vibrations. In *Symposium on Hearing Theory, IPO Eidhoven*, pages 172–181. Netherlands, The, 1972.

J. Zheng, N. Deo, Y. Zou, K. Grosh, and A.L. Nuttall. Chlorpromazine Alters Cochlear Mechanics and Amplification: In Vivo Evidence for a Role of Stiffness Modulation in the Organ of Corti. *Journal of Neurophysiology*, 97(2):994–1004, feb 2007. ISSN 0022-3077. . URL https://www.physiology.org/doi/10.1152/jn.00774.2006.

G. Zweig, R. Lipes, and J. R. Pierce. The cochlear compromise. *The Journal of the Acoustical Society of America*, 59(4):975–982, apr 1976. ISSN 0001-4966. . URL http://asa.scitation.org/doi/10.1121/1.380956.